Computational design of heat resistant steels with evolving and time-independent strengthening factors

PhD thesis
September, 2015

Qi LU

Computational design of heat resistant steels with evolving and time-independent strengthening factors

Proefschrift

ter verkrijging van de graad van doctor
aan de Technische Universiteit Delft,
op gezag van de Rector Magnificus prof. ir. K.C.A.M. Luyben,
voorzitter van het College voor Promoties,
in het openbaar te verdedigen op
woensdag 02 september 2015 om 12:30 uur

door

Qi LU
Master of Engineering In Materials Science
Institute of Metal Reserach, Chinese Acadamy of Science, Shenyang, China
geboren te Taizhou, China

This dissertation has been approved by the

promotor: Prof. S. van der Zwaag and
copromotor: Dr. W. Xu

Composition of the doctoral committee:

Rector Magnificus
Prof. S. van der Zwaag promotor
Dr. W. Xu copromotor

Independent members:

Prof. dr. ir. F. van Keulen	3ME, TU Delft
Prof. dr. A. Borgenstam	KTH Royal Institute of Technology, Sweden
Prof. dr. S. Claessens	University of Gent, Belgium
Prof. dr. S.G. Fries	Ruhr-Universität-Bochum , Germany
Prof. dr. R. Thackray	University of Sheffield, UK
Prof. dr. ir. E.H. Brück	TNW, TU Delft, reserved

Keywords: alloy design, heat resistant steel, computational modelling, precipitation hardening, solid solution strengthening, genetic algorithm, thermodynamic, kinetics, coarsening

Printed in the Netherlands by Ipskamp Drukkers, Enschede.
ISBN: 978-94-6259-795-2

Author email: q.lu@tudelft.nl; Yihengson@gamil.com; luqi181@163.com

To Dou and my daughter

Contents

1 Introduction 1

1.1 Alloy design approaches....1

1.2 Introduction to existing heat resistant steels....2

1.3 Scope of this thesis....5

References....6

2 Computational design of precipitation strengthened austenitic heat resistant steels 9

2.1 Introduction....9

2.2 Model description....12

2.2.1 Heat treatment....12

2.2.2 Translator: from properties to microstructure....13

2.2.3 Optimisation criteria....15

2.2.4 Go/no-go criteria....16

2.2.5 Optimization framework....17

2.2.6 Searching condition....18

2.3 Model applications....19

2.4 Discussion ….....21

2.4.1 Analysis of the effect of composition on the design criteria 21
2.4.2 Coarsening /stability of the MX carbonitrides…….....24
2.4.3 Validation of the model.....27
2.5 Conclusions.....30
References.....31

3 Designing new corrosion resistant ferritic heat resistant steels based on optimal solid solution strengthening and minimisation of undesirable microstructural components 35
3.1 Introduction 35
3.2 Model description.....36
3.2.1 Design methodology.....36
3.2.2 Defining the go/no-go criteria 37
3.2.3 Optimisation criterion / Solid solution strengthening contribution.....38
3.2.4 Searching condition and optimization framework.....41
3.3 Validation of solid solution strengthening contribution.....41
3.4 Optimised new steel compositions.....45
3.5 Discussion 47
3.5.1 Validations of go/no go criteria.....47
3.5.2 Compositional effects.....49
3.5.3 Comparison of the predicted strength of the new alloys with existing steel grades.....52
3.6 Conclusions 53
References.....54

4 The design of a compositionally robust martensitic creep resistant steel with an optimised combination of precipitation hardening and solid solution strengthening for high temperature use 57
4.1 Introduction.....57
4.2 Methodology 60
4.2.1 Design methodology.....60
4.2.2 Defining the optimization criterion: PH factor and SSS factor 61
4.2.3 Defining the go/no-go criteria.....62
4.2.4 Search ranges and genetic algorithm 63
4.3 Validation 63
4.3.1 Validation of PH and SSS factors 63
4.3.2 Validation of the go/no-go criteria 66

4.4 Model application 66
4.5 Discussion 69
4.5.1 Properties of the Pareto front 69
4.5.2 Compositional robustness 73
4.5.3 A new alloy optimization scheme taking into account the compositional robustness.....75
4.5.4 Comparison of the newly designed alloys and existing 9-12% Cr martensitic steels.....77
4.6 Conclusions.....78
References 79

5 A strain based computational design of creep resistant steel 81
5.1 Introduction.....82
5.2 Model description 83
5.2.1 Design methodology 83
5.2.2 Defining the go/no-go criteria.....87
5.2.3 Searching condition and optimization framework 87
5.3 Validation and application.....88
5.3.1 Validation against reported experimental data.....88
5.3.2 Design results.....90
5.3.3 Compositional effect.....92
5.3.4 The evolution of threshold stress with time 94
5.3.5 The comparison of designed alloys and existing commercial steel grades96
5.4 Conclusions.....98
References.....99

6 The computational design of W and Co containing creep resistant steels with barely coarsening Laves phase and $M_{23}C_6$ as the strengthening precipitates 101
6.1 Introduction.....101
6.2 Model descriptions.....102
6.3 Model predictions 105
6.4 Discussion 107
6.4.1 Effects of alloying elements on the precipitate configuration 107
6.4.2 Comparison of designed alloys and existing alloys. 110
6.4.3 Combining $M_{23}C_6$ and Laves phase in one alloy 112
6.5 Conclusions.....114
References.....114

7 A comparison of the design space for creep resistant steels with an austenitic, ferritic or martensitic matrix 117
7.1 Introduction 117
7.2 Alloy by design Methodology 118
7.3 Results and discussion 121
7.4 Conclusions 125
References....125

8 Experimental validations 127
8.1 Alloy compositions....127
8.2 Experimental procedures 129
8.3 Results 130
8.3.1 Solution treatment....130
8.3.2 Hardness and microstructure evolution during ageing treatment 136
8.4 Discussion....143
8.4.1 Effect of composition and heat treatment temperature deviations on phase constitution and coarsening rates of strengthening precipitates....143
8.4.2 Precipitates identification in alloys MPHS, MSSI and MPHI....145
8.4.3 A comparison between the new alloy MPHI and the existing steel P92 .148
8.5 Summary and Conclusions....149
References....150

9 Process-time optimisation of vacuum degassing using a genetic alloy design approach 151
9.1 Introduction....151
9.2 Model Description 152
9.2.1 Thermodynamic calculations....153
9.2.2 Kinetic considerations....155
9.2.3 Constraints/go/no-go criteria....156
9.2.4 Parameter settings 158
9.3 Results and Discussion….....159
9.4 Conclusion 164
References 165

Summary 167

Samenvatting **173**

A The impact of intended service temperature on the optimal composi-tion of Laves and $M_{23}C_6$ precipitate strengthened ferritic creep resistant steels **177**

A.1 Introduction 177
A.2 Model description 178
A.3 Model validation....181
A.4 Model application....181
A.5 Discussion. 182
A.5.1 Effect of service temperature on the optimization results 183
A.5.2 Comparison of newly designed alloys and the existing 15Cr alloy....185
A.5.3 Combining $M_{23}C_6$ with Laves phase at three service temperatures....185
A.6 Conclusions....189
References....189

Acknowledgments **193**

Curriculum Vitae **195**

List of Publications **197**

Chapter 1

Introduction

1.1 Alloy design approaches

For over a century, novel alloys with specific properties have been developed to meet the ever rising performance demands from industries. Traditionally, alloy development involves process-structure experiments, much later to be followed by model based studies to understand the structure and properties of candidate microstructures in a more quantitative sense [1]. The experimental 'trial and error' approach generally starts from a set of reference alloys and this approach may (only) realize small stepwise improvements at best. It generally has a low success rate [2-4], since changes in the composition and thermal treatment not only can lead to improvements but also can displace the alloy from its optimal state [5]. Moreover, the design cycle may be extremely long and costly for a new material or alloy system, especially for creep resistant steels, owing to the complex interactions among alloying elements and necessarily long evaluation times.

On the other hand, the remarkable development of computational techniques during the last decades has made the computational design of new alloys feasible, both technically and economically [6, 7]. Use of computational modelling to assist the alloy design process can be traced back to the mid-1980's at Northwestern University [8, 9], recently

culminating in a 500 M$ “material genome initiative” program in the USA, aiming to halve the development time for new materials by dedicated use of computational models in all stages of the material development program. The programmatic ‘material by design’ approach is now copied in other countries such as China and Japan. From a computational perspective, the performance of a material is determined by both its ‘genome’ (inherent property, e.g. composition) and its ‘experience’ (external interactions-processing-condition during usage) [10]. Various computational approaches aiming to accelerate the design of new alloy systems have been explored successfully, for instance, computational thermodynamics, artificial neural networks (ANN) and ab initio calculations. Thermo-Calc is a powerful thermodynamic software package based on the CALPHAD method and is linked to various databases and interfaces, where all the elementary thermodynamic information is stored. With the help of these thermodynamic models some features of the equilibrium microstructure of materials can be predicted as a function of composition and temperature [11-13]. On the other hand statistical models fed with experimentally obtained combinations of composition and properties can also be used to identify opportunities for material improvement. For example, neural network models have been used to simulate the creep rupture life, rupture strength as a function of composition and temperature [14-17]. The ultimate bottom-up design approach based on *ab initio* calculations has also been used successfully in the design of very simple binary or ternary alloys [18-21]. All these computational methods can provide very valuable information and hence guide and accelerate the exploration of new alloy systems.

Genetic algorithms (GAs) are biology- inspired computing techniques, which tend to mimic the basic Darwinian concepts of natural selection [22]. They are highly robust and efficient for most engineering optimising studies. Although a late entrant in the materials arena, GA based studies are increasingly making their presence felt in many different aspects of this discipline. In recent times, in a ‘metals by design’ project at the TU Delft GAs have been successfully combined with thermodynamics to design advanced ultra-high strength stainless steels for room temperature applications using either one or several types of precipitates (MC carbides, Cu clusters and Ni_3Ti/NiAl intermetallics), as the main strengthening factor [23-28]. Although this project lasted only four years the newly designed alloys outperformed those of related commercial alloys with a typical development time of more than 10 years.

1.2 Introduction to existing heat resistant steels

Heat resistant steels combining superior creep strength and great corrosion resistance at high temperatures are widely used in automotive, aerospace, fossil and nuclear power plants applications. Generally, these steels are classified into ferritic (α) and austenitic (γ) heat resistant steels, depending on the crystallographic nature of the matrix, but can be further sub-divided according to Cr or/and Ni concentrations [29]. **Figure 1.1** maps the conventional creep steels on the Fe–Cr–Ni ternary phase diagram. High Cr ferritic heat resistant steels come in two families, the 9-12% Cr ferritic/martensitic steels and 12–29% Cr ferritic steels. They do not contain Ni and are located along the Fe-Cr axis. 9-12% Cr ferritic/martensitic steels will be called "Martensitic steels" for simplicity in this thesis. The other group, austenitic heat resistant steels, are along the boundary between the full γ phase and the γ phase containing α and/or σ, such as 18%Cr–8%Ni steels, 21%Cr–32%Ni steels et. al.. The full γ phase steels contain a relatively high Ni content. The high cost is typically offset by the high creep strength and the improved corrosion resistance.

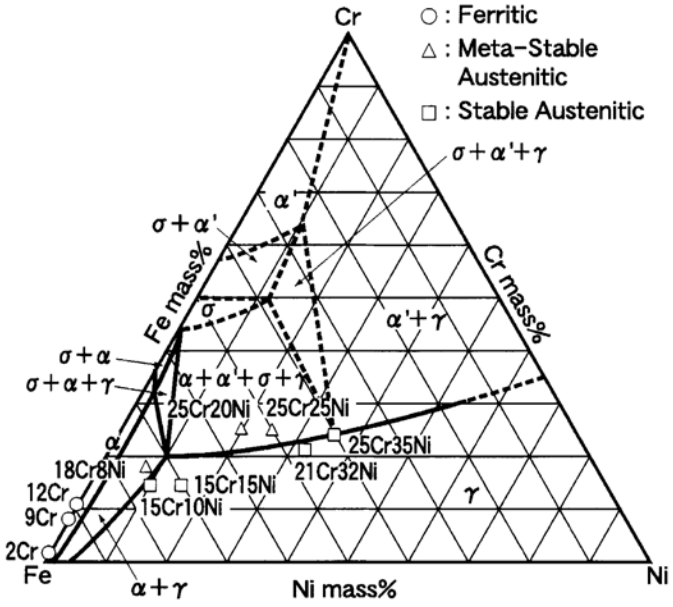

Figure 1.1 Compositions of heat resistant steels in Fe–Cr–Ni ternary phase diagram at 800°C [29].

The differences in composition and matrices also lead to differences in creep strength. In power plant applications, 10^5 h creep rupture strength is an important parameter to judge the performance of steels. **Figure 1.2** shows the 10^5 h creep rupture strength at different temperatures for different heat resistant steel grades. At temperatures lower than 600 ^oC 9-12% Cr martensitic creep resistant steels have the highest creep strength. Stable austenitic steels are a better choice when the use temperature is higher. 12-29% Cr ferritic

steels have inferior creep strength but a higher corrosion resistance than other steel grades, and hence are widely used in the area of low strength, high temperature components.

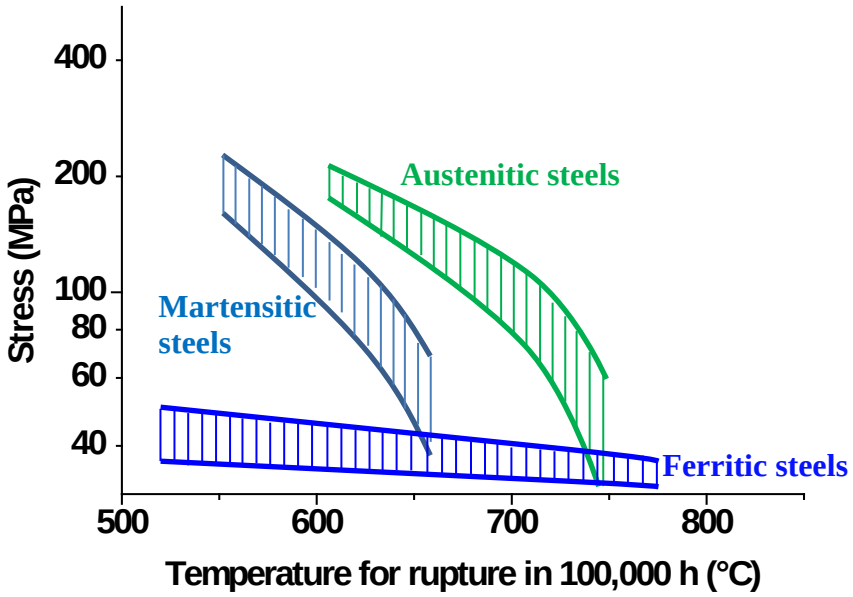

Figure 1.2 The 10^5 h creep rupture strength of austenitic, martensitic and ferritic creep resistant steels at different temperature [29-32]

In new power plants, the design loads and the target operation temperature are set to ever higher values to increase the efficiency of electricity generation. The existing heat resistant steels do not meet the requirements and new alloys with higher strengths or higher use temperatures are necessary. Precipitation hardening and solid solution strengthening are mostly effective ways to improve the creep strength of heat resistant steels. Conventionally, a distinction is made between desirable precipitates, such as MX carbonitride, Cu particle, NiAl, $Ni_3(Al,Ti)$, which contains precipitates which are stable during long period service and have no negative side reactions, and undesirable precipitates, such as $M_{23}C_6$ carbides, Z Phase, Laves Phase and Sigma phase, which coarsen rapidly and in doing so deplete the matrix from important solute atoms. Recently, this definition has become not so precise since the border of undesirable and undesirable is becoming more and more vague. By tuning the precipitate forming elements, the precipitation size, volume fraction, coarsening rate and distribution of precipitates can be modified. Hence desirable precipitates can become even more favourable [2, 13, 33, 34], and previous undesirable phases can be tailored so as to improve creep strength and become attractive as well [35-38]. While precipitation hardening clearly is an effective way to increase the creep strength of steels, the unavoidable precipitate coarsening

process invariably leads to a lowering of the creep strength with time and temperature. In contrast, solid solution strengthening depends on temperature but is essentially time independent. W and Mo are the common elements to increase the solid solution strength of martensitic creep resistant steels [29, 39]. Addition of 2.3 wt.% W in an α iron solution with 0.001 wt.% C can decrease the creep strain rate by a factor 100 or more [39].

1.3 Scope of this thesis

In this thesis, the genetic alloy design approach developed at the TU Delft for the design of ultra-high strength stainless steels for room temperature applications is further extended to design non-corroding ferritic, martensitic and austenitic heat resistant steels for high service temperature. Unlike the previous approach which only focussed on the effect of composition and processing conditions, the new approach directly considers the effect of service time and temperature on the choice of alloy composition and heat treatment conditions. The coarsening of the precipitates at high temperatures is considered as the key optimisation parameter in the design for precipitation hardening. However, solid solution strengthening is also considered.

In Chapter 2, the alloy design approach is applied to the design of austenitic heat resistant steels. Three alloys dedicated to service times of 10, 10^3 and 10^5 hours respectively are designed so as to have the best MX carbonitride precipitation hardening contribution at their intended use times. Different combinations of volume fraction and coarsening rate of MX carbonitrides in these three alloy are found to be the main reason for the different performances of the new alloys. Unlike precipitation hardening, solid solution strengthening is stable once thermodynamic equilibrium is achieved. Consequently, ferritic heat resistant steels with optimal solid solution strengthening and minimised undesirable microstructural components are developed in Chapter 3. The strengthening factor of the designed ferritic alloys has been compared to those of existing ferritic steels and is shown to be higher. In Chapter 4, precipitation hardening of MX carbonitrides and solid solution strengthening are simultaneously optimised in a martensitic heat resistant steels by constructing a “Pareto front” of precipitation hardening and solid solution strengthening contributions of all qualified solutions. The effect of composition on the Pareto front is discussed. The robustness of the optimal composition is also considered and optimised by adding a new criteria. In the previous chapters, the actual deformation during use, the creep strain culminating in creep failure, is not considered. To address this important omission, the austenitic steels developed in Chapter 2 are further optimised by

introducing a relationship between the strain-rate and the precipitate size and volumetric density in Chapter 5. 1% creep strain is taken as the maximum strain and alloys with the highest applied stress for different service time are identified. In Chapter 6, undesirable Laves phase and $M_{23}C_6$ precipitates are tuned by optimising the alloy composition so as to optimise martensitic heat resistant steels. The alloy composition with optimal combination of Laves phase and $M_{23}C_6$ is found by constructing a Pareto front. Similar to martensitic steels, in Chapter 7, ferritic and austenitic steels are optimised with both precipitation hardening and solid solution strengthening. The constructed Pareto fronts and other qualified solutions of all three types of alloys are described. In Chapter 8, the production, microstructural evaluation and hardness evolution at elevated temperatures of five ferritic, martensitic and austenitic alloys, developed in chapters 2 to 5 are described. The behaviour of the newly designed alloys is compared with an existing high-end commercial alloy having received the same heat treatment.

In Chapter 9 the GA-Thermodyamics optimisation approach for the development of new creep steels is generalised and applied to liquid steel making. It is applied to the minimisation of the steel degassing process time, while making sure the chemical composition meets the pre-set target values.

Finally, the main results as reported in this thesis are presented in the Summary. The appendix presents the additional results of the design of ferritic steels as a function of the use temperature.

References

[1] McDowell DL, Olson GB. Concurrent design of hierarchical materials and structures. In: Yip S, de la Rubia TD, editors, vol. 68 LNCSE, 2009. p.207.
[2] Taneike M, Abe F, Sawada K. Creep-strengthening of steel at high temperatures using nano-sized carbonitride dispersions. Nature 2003;424:294.
[3] Sawada K, Taneike M, Kimura K, Abe F. Effect of nitrogen content on microstructural aspects and creep behavior in extremely low carbon 9Cr heat-resistant steel. ISIJ Int. 2004;44:1243.
[4] Horiuchi T, Igarashi M, Abe F. Improved utilization of added B in 9Cr heat-resistant steels containing W. ISIJ Int. 2002;42:S67.
[5] Sandström R. An approach to systematic materials selection. Materials & Design 1985;6:328.
[6] Asta M. Computational materials discovery and design. JOM 2014;66:364.
[7] Sinnott SB. Material design and discovery with computational materials science. Journal of Vacuum Science and Technology A: Vacuum, Surfaces and Films 2013;31.

[8] Olson GB. Computational design of hierarchically structured materials. Science 1997;277:1237.
[9] Olson GB. Brains of Steel: Mind melding with materials. International Journal of Engineering Education 2001;17:468.
[10] Kaufman L, Ågren J. CALPHAD, first and second generation – Birth of the materials genome. Scr. Mater. 2014;70:3.
[11] Michaud P, Delagnes D, Lamesle P, Mathon MH, Levaillant C. The effect of the addition of alloying elements on carbide precipitation and mechanical properties in 5% chromium martensitic steels. Acta Materialia 2007;55:4877.
[12] Teng ZK, Zhang F, Miller MK, Liu CT, Huang S, Chou YT, Tien RH, Chang YA, Liaw PK. New NiAl-strengthened ferritic steels with balanced creep resistance and ductility designed by coupling thermodynamic calculations with focused experiments. Intermetallics 2012;29:110.
[13] Knežević V, Balun J, Sauthoff G, Inden G, Schneider A. Design of martensitic/ferritic heat-resistant steels for application at 650 °C with supporting thermodynamic modelling. Mater. Sci. Eng., A 2008;477:334.
[14] Brun F, Yoshida T, Robson JD, Narayan V, Bhadeshia HKDH, MacKay DJC. Theoretical design of ferritic creep resistant steels using neural network, kinetic, and thermodynamic models. Mater. Sci. Technol. 1999;15:547.
[15] Guo Z, Sha W. Modelling the correlation between processing parameters and properties of maraging steels using artificial neural network. Computational Materials Science 2004;29:12.
[16] Bhadeshia HKDH. Design of ferritic creep-resistant steels. ISIJ Int. 2001;41:626.
[17] Mandal S, Sivaprasad PV, Venugopal S, Murthy KPN, Raj B. Artificial neural network modeling of composition-process-property correlations in austenitic stainless steels. Mater. Sci. Eng., A 2008;485:571.
[18] Vitos L, Korzhavyi PA, Johansson B. Stainless steel optimization from quantum mechanical calculations. Nat. Mater. 2003;2:25.
[19] Leyson GPM, Hector Jr LG, Curtin WA. Solute strengthening from first principles and application to aluminum alloys. Acta Mater. 2012;60:3873.
[20] Raabe D, Sander B, Friák M, Ma D, Neugebauer J. Theory-guided bottom-up design of β-titanium alloys as biomaterials based on first principles calculations: Theory and experiments. Acta Mater. 2007;55:4475.
[21] Hao S, Liu WK, Moran B, Vernerey F, Olson GB. Multi-scale constitutive model and computational framework for the design of ultra-high strength, high toughness steels. Computer Methods in Applied Mechanics and Engineering 2004;193:1865.
[22] Chakraborti N. Genetic algorithms in materials design and processing. Int. Mater. Rev. 2004;49:246.
[23] Xu W, Rivera-Díaz-del-Castillo PEJ, van der Zwaag S. Designing nanoprecipitation strengthened UHS stainless steels combining genetic algorithms and thermodynamics. Comput. Mater. Sci. 2008;44:678.
[24] Xu W, Rivera-Díaz-Del-Castillo PEJ, van der Zwaag S. Genetic alloy design based on thermodynamics and kinetics. Philos. Mag. 2008;88:1825.
[25] Xu W, Rivera-Díaz-del-Castillo PEJ, van der Zwaag S. A combined optimization of alloy composition and aging temperature in designing new UHS precipitation hardenable stainless steels. Computational Materials Science 2009;45:467.

[26] Xu W, Rivera-Díaz-Del-Castillo PEJ, van der Zwaag S. Computational design of UHS maraging stainless steels incorporating composition as well as austenitisation and ageing temperatures as optimisation parameters. Philos. Mag. 2009;89:1647.
[27] Xu W, Rivera-Díaz-del-Castillo PEJ, Wang W, Yang K, Bliznuk V, Kestens LAI, van der Zwaag S. Genetic design and characterization of novel ultra-high-strength stainless steels strengthened by Ni3Ti intermetallic nanoprecipitates. Acta Mater. 2010;58:3582.
[28] Xu W, Rivera-Díaz-del-Castillo PEJ, Yan W, Yang K, San Martín D, Kestens LAI, van der Zwaag S. A new ultrahigh-strength stainless steel strengthened by various coexisting nanoprecipitates. Acta Mater. 2010;58:4067.
[29] Masuyama F. History of power plants and progress in heat resistant steels. ISIJ Int. 2001;41:612.
[30] Shingledecker J, Purgert R, Rawls P. Current status of the U.S. DOE/OCDO A-USC materials technology research and development program. Advances in Materials Technology for Fossil Power Plants - Proceedings from the 7th International Conference, 2014. p.41.
[31] ASM metals handbook, properties and selection irons - irons, steels, and high performance alloys, Specialty steels and heat-resistant alloys. Ohio: ASM International, Materials Park, 2005.
[32] NIMS creep data sheet, National institute for materials science, http://smds.nims.go.jp/creep/index_en.html.
[33] Abe F, Taneike M, Sawada K. Alloy design of creep resistant 9Cr steel using a dispersion of nano-sized carbonitrides. Int. J. Press. Vessels Pip. 2007;84:3.
[34] Yin FS, Tian LQ, Xue B, Jiang XB, Zhou L. Effect of carbon content on microstructure and mechanical properties of 9 to 12 pct Cr ferritic/martensitic heat-resistant steels. Metall. Mater. Trans. A 2012;43:2203.
[35] Rojas D, Garcia J, Prat O, Carrasco C, Sauthoff G, Kaysser-Pyzalla AR. Design and characterization of microstructure evolution during creep of 12% Cr heat resistant steels. Mater. Sci. Eng., A 2010;527:3864.
[36] Hald J, Danielsen HK. Z-phase strenghtened martensitic 9-12%Cr steels. 3rd Symposium on heat resistant steels and alloys for high efficiency USC power plants. Tsukuba, Japan: National Institute for Materials Science, 2009.
[37] Bhandarkar MD, Bhat MS, Parker ER, Zackay VF. Creep and fracture of a Laves phase strengthened ferritic alloy. Metall. Trans. A 1976;7:753.
[38] Abe F. Creep rates and strengthening mechanisms in tungsten-strengthened 9Cr steels. Mater. Sci. Eng., A 2001;319-321:770.
[39] Maruyama K, Sawada K, Koike J. Strengthening mechanisms of creep resistant tempered martensitic steel. ISIJ Int. 2001;41:641.

Chapter 2

Computational design of precipitation strengthened austenitic heat resistant steels

2.1 Introduction

Austenitic heat resistant steels are in great demand in power plants, aerospace and other industrial applications operating at elevated temperatures because of their superior creep strength, corrosion and oxidation resistances. The austenite family of temperature resistant steels predictably contains high amounts of austenite stabilizer, Ni, and various alloying elements to strengthen and stabilise the alloys. On top of the solid solution strengthening effect, alloys can be further and more effectively strengthened by different types of precipitates, such as MX carbonitrides (as in high strength low alloy steels [1], creep resistant steels: 347H, TEMPALOYA-1 and NF 709[2, 3]), Cu particles (as in Super 304H [4]), and Ni_3Ti (as in A286[5]). In order to promote the formation of MX carbonitrides, carbonitride-forming elements, such as Ti and Nb, are added to the system. The formation of carbonitrides also prevents the depletion of Cr in the matrix by suppressing the precipitation of Cr-rich $M_{23}C_6$, and thus helps to sustain a good corrosion resistance without intra-granular corrosion [6]. Taneike [7] and Feng [8] studied strengthening effects of nano-sized carbonitrides and achieved high creep strength values. Hald et. al. focused on the thermal stability of the precipitates and discovered that the coarsening rate of MX carbonitrides is about 3 order of magnitudes less than that of

$M_{23}C_6$ [9]. Thus, MX carbonitrides represent a desirable family of strengthening precipitates in austenitic heat resistant steels, because of their large strengthening effect and their superior stability over time and are used as the principal and only strengthening precipitate type in the current analysis.

The traditional way to design steel grades is to select the most important elements from a wide range, such as C, Cr, Ni, Ti, Mo, Cu, Nb, N, V, Mn, Si, and to optimize the composition via a systematic 'trial and error' approach. With an increasing number of alloying elements and increasing complexity of element interactions, the conventional 'trial and error' approach becomes a very costly and time inefficient route. Inspired by persistent demands from industries and academia, various computational guided alloy design approaches have been developed, including but not limited to computational thermodynamics aided approaches [10-13], artificial neural networks (ANN) [14-17] and even ab initio models [18, 19]. Recently, a genetic algorithm (GA) optimisation protocol has been successfully combined with thermodynamics to design new Ultra High Strength (UHS) stainless steel grades [20-25], in which alloy compositions and heat treatment parameters (austenitisation and ageing temperatures) are optimized simultaneously so as to obtain desirable microstructural components and avoid undesirable phases throughout the entire heat treatment process. Genetic algorithms are biologically inspired optimization techniques, which tends to mimic the basic Darwinian concepts of natural evolution [26]. Like DNA in biological systems, all information of a steel grade including its composition, critical processing temperature and cost price can be contained in a single numerical string, which is then fed to metallurgical calculations and evaluations so as to achieve desired microstructures, represented by a quantified optimization factor and various go/nogo criteria.

Unlike the previous design routes for UHS stainless to be used in room temperature applications only, the design of heat resistant steels not only has to look for maximal amounts of strengthening precipitates at the end of the quench and tempering treatment but also has to consider effects of use temperature and service time on the precipitate dimensions and their effect on the remaining tensile strength. Extensive research has been carried out to predict the creep rupture time through employing various stress-strain correlations in the secondary stage or all three stages during creep loading [27-33]. These correlations are known as constitutive equations [34, 35], wherein parameters are obtained via fitting experimental creep data without considering underlying microstructural evolutions. However, the microstructural evolution is eventually responsible for the high temperature strength degradation with time. Therefore, it is of

great importance to identify the main degradation mechanisms and to incorporate their effects as a function of time and temperature in the design of heat resistant steels. In the present work, the recent GA based model for UHS precipitation strengthened steels for room temperature applications is extended to the design of austenitic heat resistant steels strengthened by MX carbonitrides precipitates and to optimise for the expected strength contribution at the foreseen holding time at the foreseen holding temperature. Hence, the new alloys are designed to give optimal precipitation strength for predefined combinations of application temperature and time. In order to validate the model, strength degradation kinetics of existing precipitation strengthened austenitic steel grades are calculated using the same methodology as used for the alloy optimisation and the predicted strength degradation as a function of time and temperature is compared to experimental results from literature.

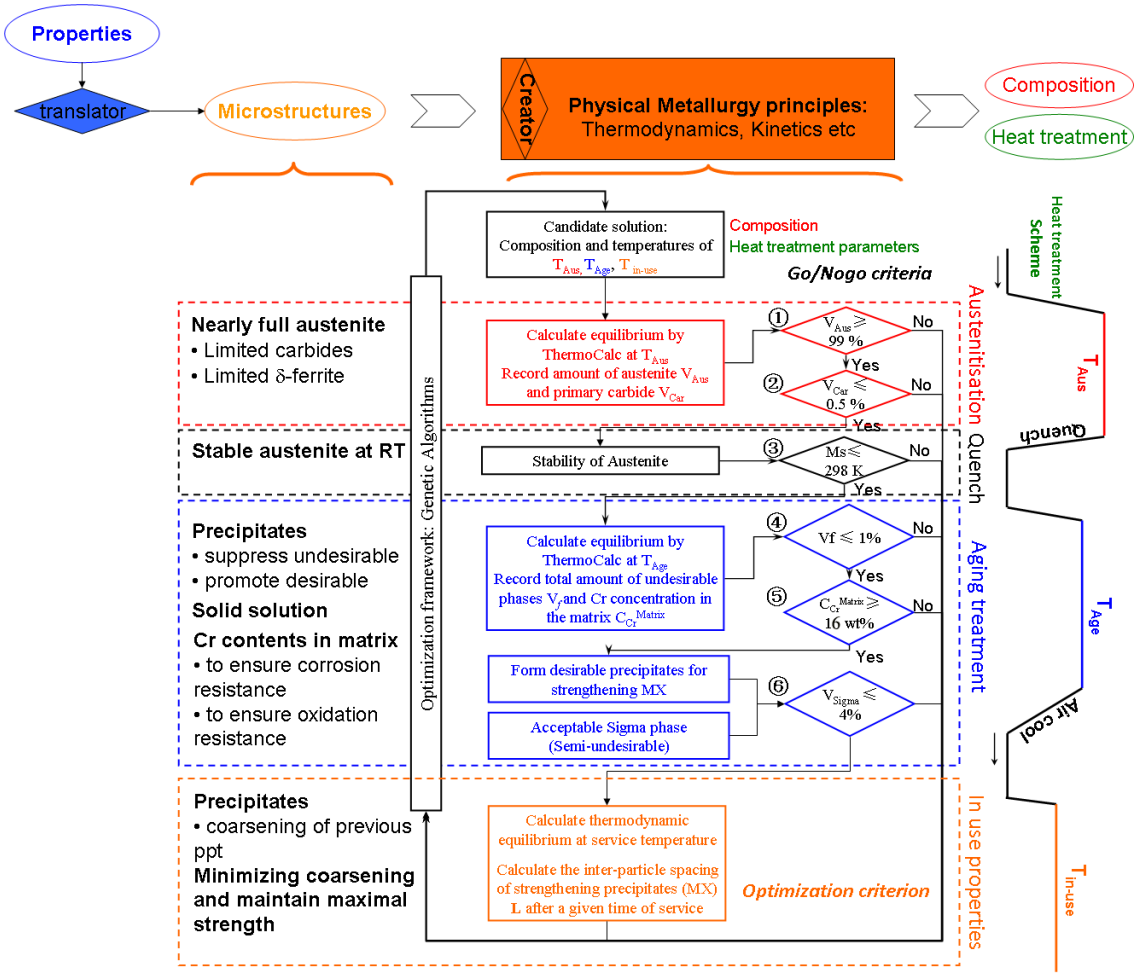

Figure 2.1 Alloy design strategy and criteria evaluation of high strength austenitic heat resistant steels

2.2 Model description

The design methodology follows the 'goal-means' design philosophy proposed by Olson [36], which involves three chains linking the performance, properties, microstructures and eventually the composition/processing. First, a set of required properties for heat resistant steels are determined according to the application in mind [37]. In the second step, the required property combination is translated to metallurgical variants, i.e. microstructural features, and this conversion is termed 'translator'. The last chain is the other transition named 'creator', in which the tailored microstructural features are linked to a specific composition and associated heat treatment conditions. Each step will be discussed in detail in the following sections and is linked to the steps in the computer program shown schematically in **Figure 2.1**

2.2.1 Heat treatment

For MX carbonitrides precipitation strengthened heat resistant steels, the size, density and spatial distribution of precipitates greatly influence the high temperature strength. In the present work we will group high temperature resistant steels (i.e. steel exposed to high temperatures but not continuously loaded to a (constant) stress) and creep resistant steels (i.e. steels loaded at high temperature for extended periods of time to a (constant) load) together and consider their strength after a certain combination of time and temperature. Research has shown that there is a good linear correlation between logarithm of rupture strength and high temperature strength at the same temperature for various types of austenitic stainless steels in the annealed and cold-worked conditions at temperatures range from 538 to 816 ^{o}C and for test times approaching 10^4 h [38]. Hence, in the present first order approach damage evolution due to the actual creep deformation is ignored and the high temperature strength degradation is taken as a good indication of change in creep strength. In order to achieve the most desirable combination of strength and stability of MX carbonitrides, a proper heat treatment scheme is necessary. MX carbonitrides generally have two types of size distribution corresponding to primary and secondary carbides, respectively. Primary carbonitrides are usually formed during solidification, are coarse (1-10 μm) and are not effective in strengthening, while secondary carbonitrides are formed during ageing/service, are nanosized and finely dispersed and hence beneficial to the strength. Therefore, a typical heat treatment of creep resistant steels with MX carbonitrides includes an austenitisation/solution treatment for dissolving undesirable primary carbonitrides and achieving compositional homogeneity, followed by a proper ageing treatment to form desirable secondary strengthening carbonitrides.

2.2.2 **Translator: from properties to microstructure**

Generally, heat resistant steels can be divided into creep resistant steels and fire resistant steels. Creep resistant steels usually serve at intermediate temperatures (500-800 ^{o}C) for a long time up to 10^5 h, while the fire resistant ones serve at similar temperatures but for a much shorter time (around 1~10 h). Both fire resistant steels and creep resistant steels can be further classified into ferritic (martensitic) and austenitic steel, and the latter one is usually used at temperatures higher than 600 ^{o}C.

Compared to steels with a ferritic/martensitic matrix and a BCC lattice structure, steels with the FCC austenitic matrix possesses higher strength levels at elevated temperatures. Moreover, microstructures present in an austenitic matrix are more stable because the diffusion coefficients in FCC are significantly lower [39] and the recrystallization temperature is higher (γ-Fe > 800 ^{o}C and α-Fe ~ 450-650 ^{o}C) [40]. Therefore, an austenitic matrix is preferred for high strength – high temperature applications. At room temperature, alloys with fine austenitic grains usually display high strength according to Hall-Patch relationship [41, 42]. However, such a grain size dependence does not hold true at elevated temperatures A fine grain size implies a larger number of grain boundaries which can function as fast diffusion paths and thereby decrease the creep resistance [43]. In the present work the minor strength reduction as a result of grain growth is not taken into account. Similarly, strength loss due to recovery [44] is minimal and is ignored in the present work.

Given the high concentrations of alloying elements, solid solution strengthening plays some role in the strength of austenite alloys. However, the present work focuses on strengthening by MX carbonitrides precipitation only and compositional effects on the solid solution strengthening contribution are ignored, In principle, the effects of solid solution hardening can easily be included in the optimisation scheme as will be demonstrated in subsequent chapters of this thesis.

The main cause for strength loss at high temperatures for precipitation strengthened austenitic steels is the coarsening of the precipitates [45]. Therefore, to obtain a good high temperature strength for longer periods of time the desirable precipitates not only should have a proper initial population (volume, size and distribution), but also have a good dimensional stability during service to prevent the coarsening of precipitates and a loss in strength. In addition to strength loss due to coarsening of desirable precipitates,

additional strength loss can be due to the in-service formation of undesirable phases, such as sigma and Z phase [46, 47]. To design stable high temperature resistant steels, compositions should be chosen such that the formation of undesirable phase is suppressed.

Finally, to have steels with a decent corrosion and oxidation resistance at high temperatures, a Cr-oxide passive film is necessary to protect the surface from the environment. Hence, an adequate amount of Cr must be present. In the present work the finer details of corrosion resistivity are ignored and corrosion resistance is simply linked to a minimal Cr level in solid solution in the matrix taking into account all Cr consuming formation of precipitates and second phase particles.

In conclusion, in order to obtain high temperature austenitic steels with a high initial strength and a good stability over time, as well as a decent corrosion and oxidation resistance, the ideal steel microstructure is defined as a stable fully austenite matrix strengthened by precipitation of MX carbonitrides without detrimental second phases being present and containing a minimal Cr level in solid solutions.

The target microstructures during all stages of the heat treatment and during final use are summarized below and can also be found in **Figure 2.1**.
(A) During the austenitisation, a homogenous austenite matrix with minimal quantities of detrimental primary carbides and δ-ferrite should exist.

(B) The stability of austenite should be such that it remains stable throughout the entire heat treatment including the intended time of service, i.e. no martensite formation during cooling and no additional phase changes take place during high temperature use.

(C) The as-quenched austenite is strengthened by MX carbonitrides at the intended use temperatures, while undesirable phases do not form. Tempering temperature (if any) should be higher than or equal to the in-use temperature so that the precipitation strengthening obtained by tempering treatment is not lost significantly during service.

(D) The strengthening precipitates should remain stable and not undergo significant coarsening during use at the operating temperature.

(E) The Cr concentration in the matrix upon the completion of precipitation should be sufficient to obtain adequate corrosion and oxidation resistances.

2.3 Creator: converting microstructure to quantifiable criteria

To create targeted microstructures as described above, the next step is to convert the targeted microstructures to multiple quantifiable criteria representing metallurgical descriptions of each microstructural feature under consideration. As demonstrated in **Figure 2.1**, various criteria are built in and quantified via thermodynamic and kinetic calculations, and are treated either as optimization or go/no-go criteria.

2.2.3 **Optimisation criteria**

In the present work, the coarsening of precipitates in taken as the sole mechanism for the degradation of high temperature strength in precipitation strengthened austenitic steels (meeting the requirement of sufficient corrosion resistance and absence of undesirable phases) [45, 48]. The precipitation strengthening is determined by the particle size and its distribution [49]. In the early stages of precipitation, particles are likely to be coherent with the matrix and can be cut by the dislocations, known as the shear mechanism. When the number and size of precipitate particles increase, it becomes increasingly difficult for a dislocation to shear the precipitate. Instead, the dislocation will bow around them and leave dislocation loops, which is called the by-pass mechanism. There is a critical size for the transition of two mechanisms at which the strengthening contribution reaches the maximum, normally about 5-25 nm depending on the interfacial energy and driving force [50]. For heat resistant alloys, the temperature and service time are usually high and long. Then, the by-pass mechanism is the most relevant and its contribution can be estimated as [51]:

$$\sigma_p = \alpha G b / L \tag{2.1}$$

Where σ_p is the precipitation strengthening contribution for the by-pass mechanism, α is a constant, G is precipitate modulus, b is Burges' vector, and L is average inter-particle spacing. At very high temperatures the precipitation strengthening mechanism may change from dislocation bypass to dislocation climb. However, regardless which of the two mechanisms is dominant, the precipitation strengthening contribution is always inversely proportional to the inter-particle spacing [34]. The value of α changes with the mechanism of dislocation passing the particle, either loop or climb, but should be identical for one single mechanism. In order to compare the precipitation strengthening contribution of designed and existing alloys at the same temperature and service time, dimensionless factor α is regarded as a constant and is effectively left out of the calculations.

Even MX carbonitrides in heat resistant steels will grow and coarsen during exposure at high temperatures, and hence the inter-particle spacing will increase. Only at the early stages of high temperature exposure growth and coarsening stages will overlap. Considering the long service time (up to 10^5 h), the effect of coarsening is much greater than the growth stage. Therefore, the inter-particle spacing is estimated by considering the coarsening kinetics only, [50-52]

$$\sigma_p \propto 1/L = \sqrt{f_p}/r = \sqrt{f_p}/\sqrt[3]{r_0^3 + Kt} \tag{2.2}$$

in which

$$r_0 = 2\gamma/\Delta G_v \tag{2.3}$$

and

$$K = 8\gamma V_m{}^p / \sum_{i=1}^{n} \frac{9(x_i^p - x_i^{mp})^2}{x_i^{mp} D_i / RT} \tag{2.4}$$

where L is the average inter-particle spacing, f_p is the equilibrium volume fraction of the strengthening precipitate MX carbonitrides at the service temperature, r_0 is the critical precipitate nucleus size, γ is matrix-precipitate interfacial energy, ΔG_v is volume thermodynamic driving force for the precipitation. V_m^p is the molar volume of precipitate. K is the factor of coarsening rate and t is the exposure time at the high temperature. x is equilibrium interface mole fraction of the MX carbonitrides former elements on both matrix (m) and precipitate (p) sides. T is service temperature and D is corresponding diffusion coefficient. In the calculations the interfacial energy is arbitrarily set at a fixed value of 1 J/m^2 irrespective of the precipitate size. This is a slight simplification but helps in illustrating the effect of precipitate coarsening. All thermodynamic parameter values including f_p, ΔG_v, x_i^p, x_i^{mp}, D_i and V_m^p required during the calculations were calculated via Thermo-Calc using the TCFE6 and Mob2 databases.

In conclusion: in our design of precipitation strengthened austenitic oxidation resistant high temperature steels the precipitation strengthening contribution, being inversely proportional to the time and temperature dependant inter particle spacing, is taken as the sole optimisation parameter in the alloy composition search. The factor $1/L$ is called 'precipitation strengthening factor'.

2.2.4 **Go/no-go criteria**

For simplification, in the optimisation studies the ageing temperature and service temperature are considered to be the same. This assumption is in agreement with existing

procedures showing that existing commercial steel grades employing MX carbonitrides for strengthening do not need a specific tempering treatment prior to be put to use at high temperatures. The various go/no-go criteria reflecting the microstructural considerations discussed above are implemented in the following manner in the simulations:

(A) The thermodynamic calculation is performed at the austenitisation temperature T_{aus}. In the thermodynamic calculations of the state of the steel at this temperature two go/no-go criteria are imposed (1) the equilibrium austenite volume fraction at that temperature is larger than 99% and (2) the maximum level of primary carbides is limited to 0.5% in volume.

(B) The austenite should remain stable upon cooling to room temperature. Therefore, a new go/no-go criterion (3) of the Martensite start (Ms) temperature of the alloy being considered being lower than 25 ^{o}C is imposed. The Ms temperature is calculated according to formula proposed by Ishida[53]:

$$T_{Ms}(^{o}\mathrm{C})=545 - 33000W_C + 200W_{Al} + 700W_{Co} - 1400W_{Cr} - 1300W_{Cu} - 2300W_{Mn} - 500W_{Mo} - 400W_{Nb} - 1300W_{Ni} - 700W_{Si} + 300W_{Ti} + 400W_V \quad (2.5)$$

where W_i is the mass fraction for element “i.

(C) Thermodynamic calculations are performed at the intended service temperature and three go/no-go criteria are enforced: (4) the maximum allowed volume fraction for all undesirable phases (sigma phase excluded) together was set at 1 vol%, (5) a minimum Chromium concentration of 16 mass% in solid solution in the matrix upon completion of the precipitation reactions was imposed to yield adequate corrosion and oxidation resistance, and (6), the maximal allowed sigma phase (not functioning as strengthening precipitates) is set at 4 vol%.

Only candidate solutions which fulfil all go/no-go criteria (1)–(6), were evaluated by the optimisation criterion maximising the precipitation strengthening factor (minimizing the inter-particle spacing) at the intended temperature and for the desired length of time.

2.2.5 **Optimization framework**

A genetic algorithm is applied as the optimization scheme, taking into account 9 variables (8 alloying element concentration and the austenitisation temperature) while setting 32 levels (between present minimal and maximal levels) for each variable, yielding in total 32^9 candidate solutions. The genetic algorithm mimics evolutionary processes in natural systems, following the survival of the fittest principle. The heuristic evolution is controlled by probabilistic operators such as selection, crossover, and mutation rather than deterministic functions. Each candidate solution is coded as a binary string (chromosome) by concatenating the concentration of each element expressed in base-2 (genes). 5 binary bits are linked to each component wherein 00000 stands for the minimum concentration and 11111 refers to the upper boundary as given in Table 2.1. In this way, there are 2^5=32 candidate concentrations for each component distributed equally between the concentration limits of each element and represented by 5 bits. Thus, composition and heat treatment parameter are coded in a 45 (5x9) bits binary string. Details of the genetic algorithm can be found in a previous publication [20]. The calculation time required to find the optimal solution in this design is usually around 2 weeks using a high-end PC.

2.2.6 **Searching condition**

The composition ranges, heat treatment parameters and service time applied in the design exercise are summarized in Table 2.1. The composition ranges take into account practical constraints. Unless specified differently the service temperature is set at a fixed value of 650 ^{o}C. For this temperature, three scenarios are considered, corresponding to intended exposure times of 0, 10 and 10^5 h respectively.

Table 2.1 Search ranges of composition (in mass%) and austenitisation temperature T_{aus} (in ^{o}C), service temperature T_{ser} = Ageing temperature T_{Age} (in ^{o}C) and different service / coarsening time (in h) considered. Mn level and Si level are fixed at 1.00 and 0.5 mass% respectively

	C	Cr	Ni	Ti	Mo	Cu	Nb	N	T_{aus}	Fe	T_{age}=T_{ser}	Service/coarsening time
MIN	0,01	15.00	8.00	0,01	0,10	0,01	0,01	0,01	1000	Bal.	650	0/10/10^5
MAX	0,15	25.00	25.00	1.00	3.00	5.00	1.00	0,15	1250			

2.3 **Model applications**

To design alloys that are suitable for different service times, three exposure times of 0, 10 and 10^5 h are selected. An exposure time of 0 h implies that only the initial strength is optimised without considering the loss of precipitation strengthening due to coarsening. The other two exposure times reflect two principally different application fields, a) fire resistant steels requiring a service time of only 10 h and b) creep resistant steel requiring a service time of 10^5 h. The resulting optimized alloy compositions for the three scenarios are labelled alloy 1, 2 and 3, and their values are shown in Table 2.2.

Table 2.2 The composition (in mass%), austenitisation temperature T_{aus} (in ^oC), Service temperature T_{age} = Ageing temperature T_{ser} (in ^oC), service time (in h) of the designed alloys.

	C	Cr	Ni	Ti	Mo	Cu	Nb	N	Mn	Si	T_{aus}	$T_{age}=T_{ser}$	Service/coarsening time
Alloy 1	0.060	15.97	22.26	0.23	0.10	0.57	0.30	0.040	1.00	0.50	1241	650	0
Alloy 2	0.041	15.97	21.16	0.20	0.10	0.42	0.39	0.069	1.00	0.50	1250	650	10
Alloy 3	0.047	16.61	18.97	0.20	0.10	0.26	0.01	0.064	1.00	0.50	1217	650	10^5

Interestingly the compositional differences between the three solutions are not constrained to one or two alloying elements but show subtle shifts over almost all alloying elements and the austenitisation temperature. Such multi parameter shifts clearly are impossible to be found via a trial and error method. Furthermore, it should be pointed out that the predicted optimal compositions are all well within the search domain, with the exception of the Mo level which is at the lowest pre-defined level (see Table 2.1).

In order to visualize systematic differences in strength degradation behavior due to coarsening of precipitates for the three alloys optimized to different criteria, the precipitation strengthening factors (1/L) as a function of service/coarsening time are calculated according to equation 2.2 and the results are plotted in **Figure 2.2**. It can be observed that each alloy displays a higher precipitation strengthening level at its intended service time than the others (and for that matter any other of the grades explored) grades, as indicated by the arrows, which demonstrates the effectiveness of the optimisation. Remarkably, the precipitation strengthening factors of new alloys 1 and 2 remain at a more or less stable level till the intended service time is reached, and then decrease sharply. For alloy 3, its precipitation strengthening factor remains constant for a much longer time (1000 h), and then drops slowly to its intended service time. Alloy 1 designed without considering the coarsening kinetics shows the fastest softening as a function of service time due to coarsening. The strength of alloy 2 remains high until 10 h, and then

decreases rapidly. Alloy 3 is the most stable and keeps its original strength up to 10^4 h and only slowly loses its strength at 10^5 h. The predicted time dependences of the three steel grades are in perfect agreement with their respective design targets.

Newly designed alloys 2 and 3 are used to explore the effect of service temperature on the strength degradation. The precipitation strengthening factors as a function of time are calculated at different temperatures from 600 to 950 ^oC according to equation 2.2 and results are shown in **Figure 2.3**. For both alloys, the precipitation strengthening factor at a certain time decreases with an increase in service temperature and the rate of degradation becomes higher at higher temperatures. It can also be observed that the turning point where the coarsening softening becomes pronounced appears at an earlier time for a higher temperature. Compared to alloy 2, the degradation rate of precipitation strengthening in alloy 3 at the same temperature is much slower and the turning point appears later. This demonstrates that alloy 3 is a superior creep resistant steel at higher temperatures or for longer times, while alloy 2 possesses a higher strength at a lower temperatures or at shorter service times.

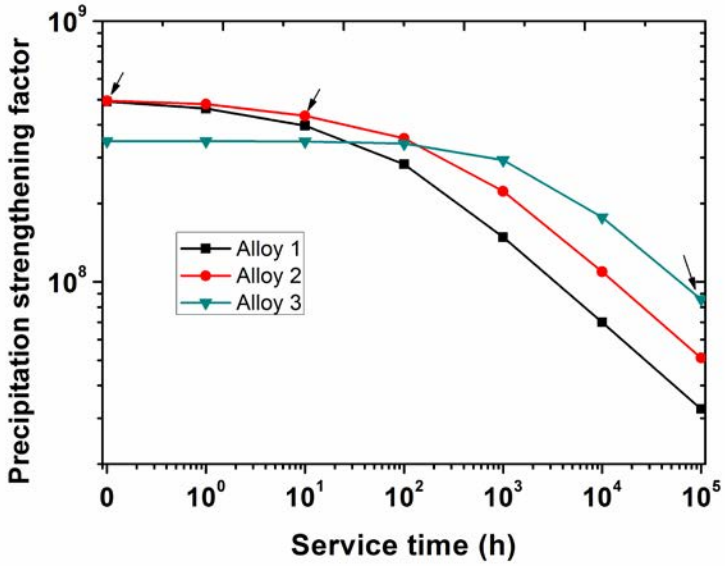

Figure 2.2 The precipitation strengthening factor versus service time for the three alloys designed to give optimal strength at 0, 10 and 10^5 h at 650 ^oC respectively

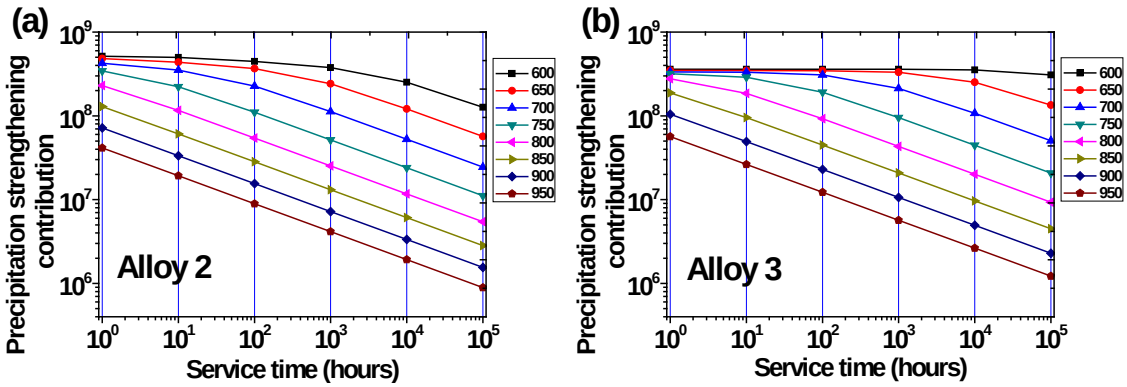

Figure 2.3 The degradation of precipitation strengthening factor with service time for Alloy 2 (a) and Alloy 3 (b) at various temperatures (in °C).

2.4 Discussion

2.4.1 Analysis of the effect of composition on the design criteria

The optimisation factor, i.e. the precipitation strengthening effect is inversely proportional to the average inter-particle spacing, which is a function of the volume fraction of precipitates and the time dependent mean particle radius (equation 2.2). To illustrate the influence of composition on each factor, the volume fraction of MX carbonitrides, the coarsening rate of MX carbonitrides (rate of change of the mean particle radius), the total precipitation strengthening factor and the volume fractions of all equilibrium phases are plotted in **Figure 2.4** as a function of Ti concentration, taking alloy 3 as the baseline composition. It can be seen in **Figure 2.4a** that the volume fraction of MX carbonitrides increases with an increase of Ti (up to Ti~0.0045 mass fraction) when the C and N levels are sufficient, then it increases slowly and finally becomes constant due to a lack of free C and N. **Figure 2.4b** shows that coarsening rate of MX carbonitrides continuously increases with increasing Ti concentration. Two transitions in the coarsening rate can be observed, which are caused by the disappearances of HCP (Cr_2N) and $M_{23}C_6$ respectively (**Figure 2.4d**). When these phases disappear, an extra amount of Ti is released into the matrix which accelerates the coarsening rate. The precipitation strengthening factor is optimized at a Ti concentration ~ 0.002 (mass fraction), where the coarsening rate is small and the optimal combination of volume fraction and mean particle radius is achieved. If the precipitation strengthening factors are calculated for other times other than the 10^5 h for which this alloy is designed, **Figure 2.4c** indicates that precipitation strengthening factors reach the optimum at different Ti concentrations. The optimal Ti concentration decreases with increasing intended service

time. This is because the optimal compromise between the volume fraction and the coarsening rate varies with the intended service time: when the service time is short, the volume fraction of MX carbonitrides would be more important to achieve a high initial precipitation strengthening factor as indicated by equation 2.2; for a longer exposure time, the coarsening effect plays increasingly important role and becomes the dominant feature. Therefore, for different service times, different optimal compositions are predicted, which display different time dependences in the strength degradation behaviour (see **Figure 2.2**).

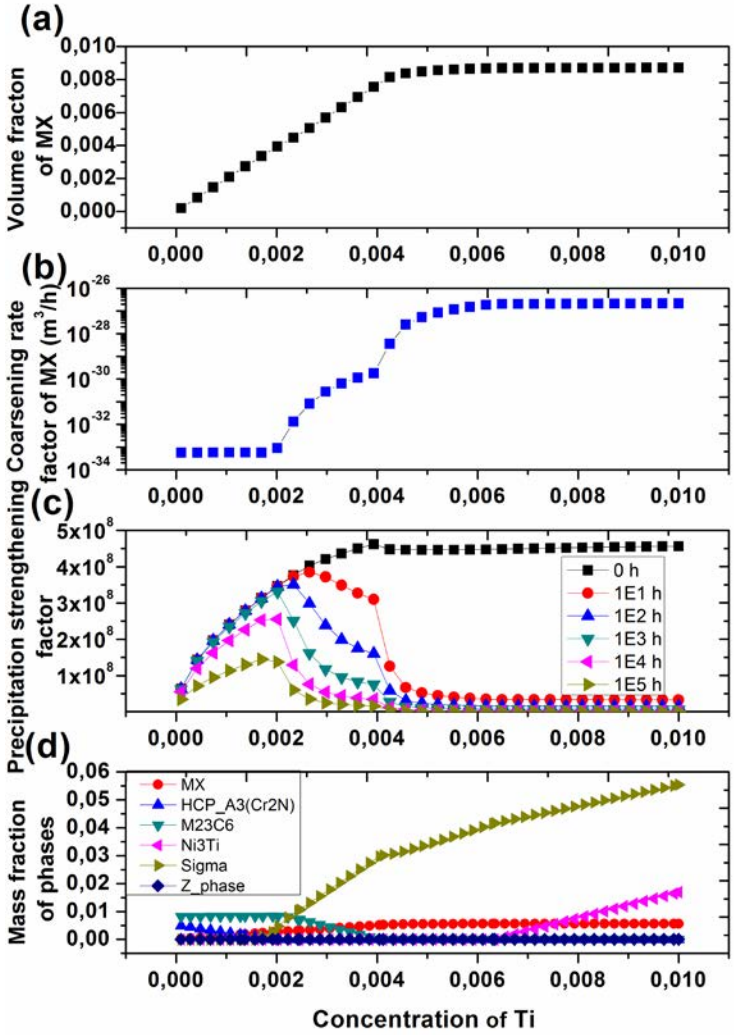

Figure 2.4 The compositional effect on the volume fraction of MX carbonitrides (a), coarsening rate of MX carbonitrides (b), precipitation strengthening factor at different service time (0, 10, 10^2, 10^3, 10^4 and10^5 h respectively) (c) and Mass fraction of all equilibrium phases in the alloy(d). The calculation is taken composition of alloy 3 as a baseline and varies the Ti concentration. Concentration of Ti is in mass fraction.

Figure 2.5 demonstrates the effects of two go/no-go criteria: the Cr concentration in the matrix and the sigma volume fraction, again taking alloy 3 as the baseline. When the overall Cr concentration of the alloy is less than 16 mass%, the Cr concentration in the matrix will increase rapidly with an increase in Cr concentration of the alloy and in the absence of sigma phase (**Figure 2.6a**). However, upon a further increase in the Cr concentration, the amount of sigma increases considerably, and a new compromise between an adequate Cr concentration and a maximal permitted sigma phase volume fraction is to be found. **Figure 2.5b** shows a declining precipitation strengthening factor with increasing Cr levels. In the final optimisations a Cr concentration in the matrix is set to be greater than 16 mass%, and a sigma phase volume fraction < 4vol% is enforced.

To demonstrate the effects/constraints of all criteria on composition and austenitisation temperature, alloy 3 is taken as a baseline to explore the effects of C and Ti and of C and T_{aus} (keeping the levels of all other components constant and only varying C and Ti or C and T_{aus} levels), and the results are shown in **Figure 2.6**. The colour contour of the background indicates the degree of precipitation strengthening factor (1/L) at the intended service time of 10^5 h. As shown in **Figure 2.6a**, the available region in the Ti-C domain which satisfies all the go/no-go criteria is a small slit, with a narrow Ti range and a relatively wide range of C levels. The narrow available area for Ti indicates the sensitivity of Ti and also the difficulty in finding an optimal composition. The region decorated with the horizontal line pattern in the upper part of **Figure 2.6a** stands for the area not fulfilling the go/no-go criteria for the homogenization process, because a too high Ti concentration will cause the volume fraction of the primary carbide to exceed 0.5% (see **Figure 2.1**). The region decorated with the vertical pattern in the lower part of **Figure 2. 6a** masks the (forbidden) area where the go/no-go criteria related to ageing/service (undesirable phase, sigma phase, Cr in the matrix) are not fulfilled. Clearly, the Ti concentration should be carefully controlled. Furthermore, as is obvious from **Figure 2.6a**, it should be pointed out that the composition with the highest precipitation strengthening factor is not located at the place where C and Ti reach their maximum value but at an intermediate level due to the compromise between volume fraction and coarsening rate. The optimal precipitation strengthening factor is achieved in a horizontal band where the concentration of Ti is around 0.002 (mass fraction). Both a higher or lower concentration of Ti will decrease the precipitation strengthening factor. The reason for this can be explained by considering the effect of C and Ti on the coarsening rate as discussed in the next section. **Figure 2.6b** shows that the austenitisation temperature itself does not influence the precipitation strengthening factor, while variations in carbon concentration do play a modest role. A high carbon

concentration promotes the formation of primary carbides and other undesirable carbides, while a low carbon concentration results in the go/no-go criteria of Ms<25 ^{o}C and Cr in the matrix>16% not being met. As a result, the available region should be a vertical band with a relative wide carbon range.

2.4.2 **Coarsening /stability of the MX carbonitrides**

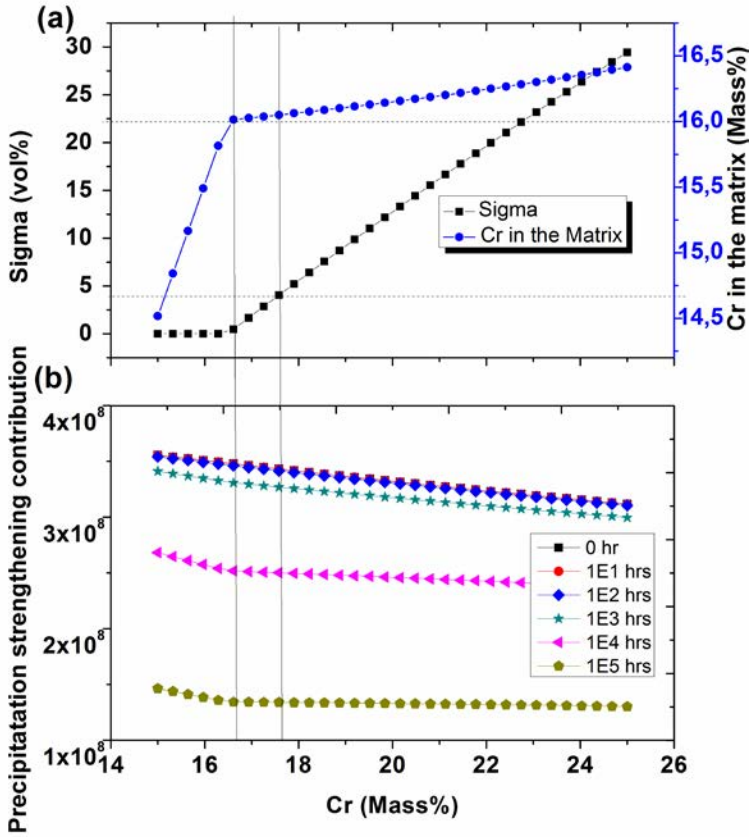

Figure 2.5 Effect of Cr concentration on the volume fraction of sigma phase and Cr concentration in the matrix(a) and on precipitation strengthening factor at various time(b). The 6 curves in **Figure 2.5b** mean the precipitation strengthening factor at 0, 10, 10^2, 10^3, 10^4, 10^5 h respectively

The coarsening rate of the MX carbonitrides is of great importance since it determines the degradation of the precipitation strengthening factor. According to equation 2.4, the factor *K* of coarsening rate is a function of the concentration difference of MX carbonitrides forming elements (Ti, Nb, C, N) at the interface (austenitic matrix/MX carbonitride) and the temperature. Others parameters like interfacial energy (fixed at 1 J/m^2 in all calculations), diffusion coefficient, molar volume of MX carbonitrides do not change when the service temperature is fixed. In order to illustrate the effect of MX

carbonitrides forming elements on the coarsening rate, the binary compositional effects of C-Ti levels on the coarsening rate are calculated taking alloy 3 as a baseline (keeping the levels of other components constant only vary C and Ti levels), and results are shown in **Figure 2.7**. The binary effects of C-Nb, N-Ti and N-Nb are similar to those of C-Ti. Three regions can be distinguished and are marked region I, II and III separated by the two dashed lines in **Figure 2.7**. As indicated by the black arrows, the coarsening rate decreases in three different directions, in which region II is the transition region. In region I, it is interesting to note that the coarsening rate is the same along a line/band with the slope of about 5:1 in the C-Ti plot. In region II, the behaviour of coarsening rate changes more continuously with composition and the carbon play a gradually less role on the coarsening rate. And finally in region III where the Ti concentration is less than ~0.0025 (mass fraction), the coarsening rate of MX carbonitrides depends almost exclusively on the Ti concentration while the C level has little effect. In order to clarify the three coarsening behaviours in the three regions, additional Thermo-Calc calculations were performed. Calculation show that the phases in region I, II and III are sigma+Ti(C,N)+Ni_3Ti, $M_{23}C_6$+Ti(C,N)+Nb(C,N) and $M_{23}C_6$+Cr_2N+Ti(C,N)+Z phase respectively. This means, all C would be tied by Ti to form TiX carbonitrides in region I; while in region II, some C would also be tied by Cr and Nb; in region III almost all C is in $M_{23}C_6$ since the existing N(0.064 mass%) is enough to combine with Ti to form TiN, thus addition of C will go to $M_{23}C_6$ and has no influence on coarsening rate of TiX carbonitrides. The coarsening behaviour in region I is linked to the stoichiometry of the MX carbonitrides precipitates, which for TiC is 1:1 on an atomic fraction ratio and about 5:1 for Ti and C on a mass basis. Compositions A and B located on the same line/band with a slope of 5:1, (see **Figure 2.7**), are chosen to further illustrate this phenomenon. The Ti and C concentrations of composition B are greater than that of A, yet the differences are such that the final equilibrium concentrations Ti and C in the matrix are equal and the alloys only differ in the volume fraction (stoichiometric) of TiC. Hence the gradient in Ti and C compositions at the interface of matrix and precipitate (equation 2.4) should be the same so as to obtain the same coarsening rate. While in region II and III, more C is needed not only to tie Ti to form TiC but also to combine with Cr to form $M_{23}C_6$, as well as to keep final equilibrium concentrations of Ti and C in the matrix equal, thus the slope of contour line of equal coarsening rate drops. Moreover, if the Ti level is fixed yet less than 0.0025 (mass fraction, region III), additions of C would not increase the volume fraction nor the coarsening rate of MX carbonitrides. In this domain variations of Ti levels result in different volume fractions and coarsening rates of MX carbonitrides. At Ti=0.002 (mass fraction) the optimal combination precipitation strengthening factor is achieved (as already mentioned in section 2.4.2).

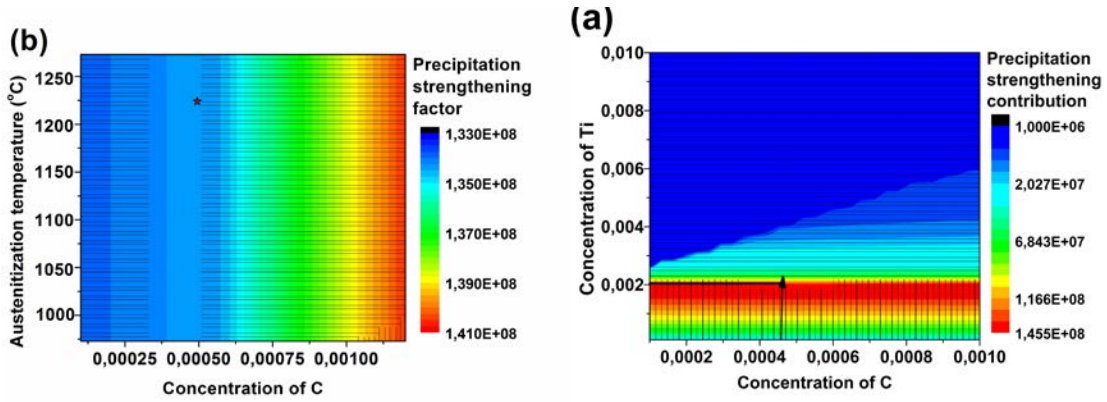

Figure 2.6 Binary effects of C-Ti (a), C-T_{aus} (b). The background contour shows the MX carbonitrides precipitation strengthening factor at a service time of 10^5 h. The horizontal patterns demonstrate the area not fulfilled the go/no-go criteria for homogenization (Ms temperature, primary carbide, austenite of austenitisation, liquid). The vertical patterns show the area not fulfilled the go/no-go criteria during ageing/service (undesirable phase, sigma phase, Cr in the matrix). All concentrations are given in mass fraction.

New optimizations of the alloy compositions are performed for two higher service temperatures yet for the same three intended service times. The resulting carbonitride compositions for each condition are listed in Table 2.3. It can be observed that the optimal MX carbonitride levels change with temperature and service time. For alloys designed for a long service time or a high temperature, the optimal alloys tend to be strengthened by TiX carbonitrides rather than by NbX carbonitrides. This is directly linked to the coarsening rate of MX carbonitride, because the alloy design for 0 h does not consider the coarsening effect, hence the optimal alloy contains both Niobium and Titanium carbonitrides. At longer service times, the TiX carbonitrides are more stable than the NbX carbonitrides and the alloys are strengthened by TiX carbonitrides only.

Table 2.3 MX carbonitrides type for different optimisations at various service time and temperature

Service time(h) / *Temperature(°C)*	*0*	*10*	*10^5*
650	TiX+NbX	TiX+NbX	TiX
750	TiX+NbX	TiX	TiX
850	TiX+NbX	TiX	TiX

2.4.3 **Validation of the model**

To validate the model we analysed the compositions of commercial creep resistant steels and determined the degree to which they met the various go/no-go criteria defined in the model. **Figure 2.8a** shows the comparison of various go/no-go criteria (for each parameter shown as a horizontal blue line) and corresponding values obtained from existing steels grades calculated by Thermo-Calc. The figures show that the compositions of the commercial steels are such that they meet or almost meet the go/no-go criteria. Some commercial steels grades do not match the set go/no-go criteria for the Martensite Start temperature and the volume fraction of sigma phase. It seems we set the criterion for the Ms too sharp and the presence of some martensite is not as detrimental as assumed. This also applies for the sigma phase which in practice can be higher than we set as being desirable. In the lowest graph of **Figure 2.8a**, the calculated strengthening factors for the commercial steels grades are compared to those of the newly designed alloy 3 (red line). The calculations suggest that notwithstanding stricter go/no-go criteria, the new alloy should have higher long term strength values than the existing creep resistant steels.

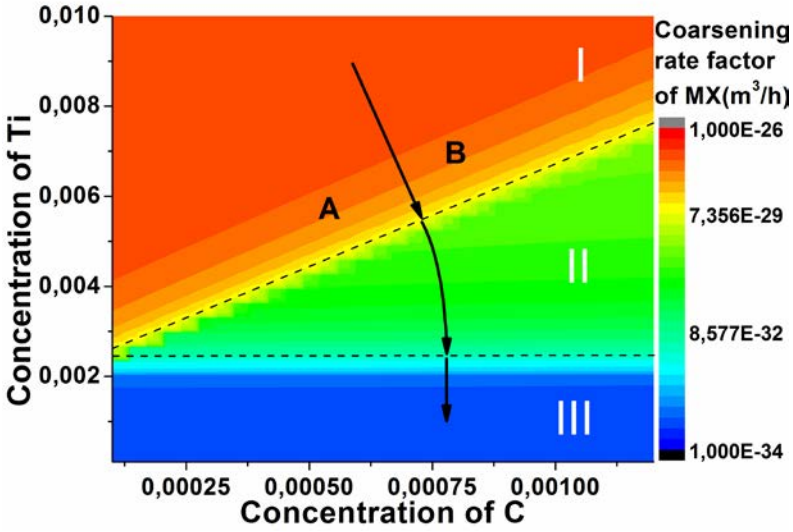

Figure 2.7 The binary compositional effects of C-Ti on the coarsening rate (base on the composition of alloy 3). The background contour shows the coarsening rate of MX carbonitride. All concentration are given in mass fraction.

A comparison of the chemical compositions of the three newly designed alloys and the commercial steel grades is shown in **Figure 2.8b**. Concentrations of Mn and Si of the designed alloys are quite similar to those of existing steels grades, while the elements

required for precipitation strengthening, such as C, N, Ti, Nb, are quite different thus resulting in different precipitation strengthening factors (in the bottom of **Figure 2.8a**). The designed Alloy 3 is similar to the high end creep resistant steel NF709 (most advanced existing steel grade), except lower concentrations of Cr, Mo and N, because the solid solution strengthening effect (applies to Mo and N) is not taken into account and a lower sigma phase fraction (applies to Cr, and Mo) is allowed. Moreover, N will combine with Ti or Nb to form primary carbides during austenitisation, hence its concentration in the designed alloys is limited and not as high as in NF709.

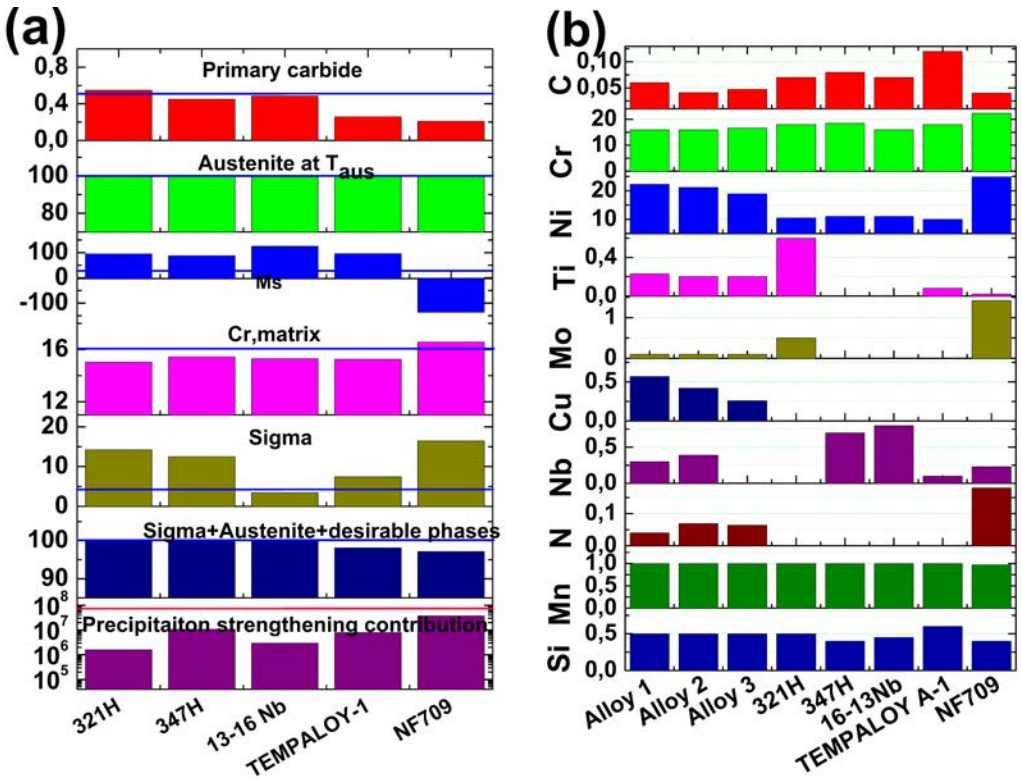

Figure 2.8 Fulfilments of go/no-go criteria, on various existing MX carbonitrides precipitation strengthening steel grades and the comparsion of precipitation strengthening contribution of 10^5 h at 650 ^oC (a), and the comparison of compositions of designed alloys and existing steel grades (b). The blue lines in **Figure 2.8**a are values of go/no-go criteria. The bottom red line indicates the precipitation strengthening contribution predicted for Alloy 3.

Finally, for two commercial steel grades, the calculated precipitation strengthening factor as a function of time is compared against the reported experimental creep strength values and results are shown in **Figure 2.9**. Alloy 347H (a traditional steel grade) and NF709 (a recent advanced steel grade) were selected because of significant differences in reported

creep strength behaviour. A very good qualitative agreement between predictions and actual creep strength behaviour is obtained for both alloys. As shown in **Figure 2.9a**, for both alloys the transition point to a more rapid loss of creep strength (related to precipitate coarsening) is very well predicted. This correspondence leads credibility to our simplifying assumption stated in section 2.2.1 that we base our calculation on the coarsening of precipitates only and ignore the damage due to creep elongation as such. This relation will be addressed in a next design study.

In **Figure 2.9b** the calculated changes in precipitate strengthening contribution as a function of time and temperature are plotted, which can be compared qualitatively with the reported creep strength data for alloy NF709. A very good agreement is shown, indicating that the model indeed captures the relevant metallurgical processes controlling creep strength.

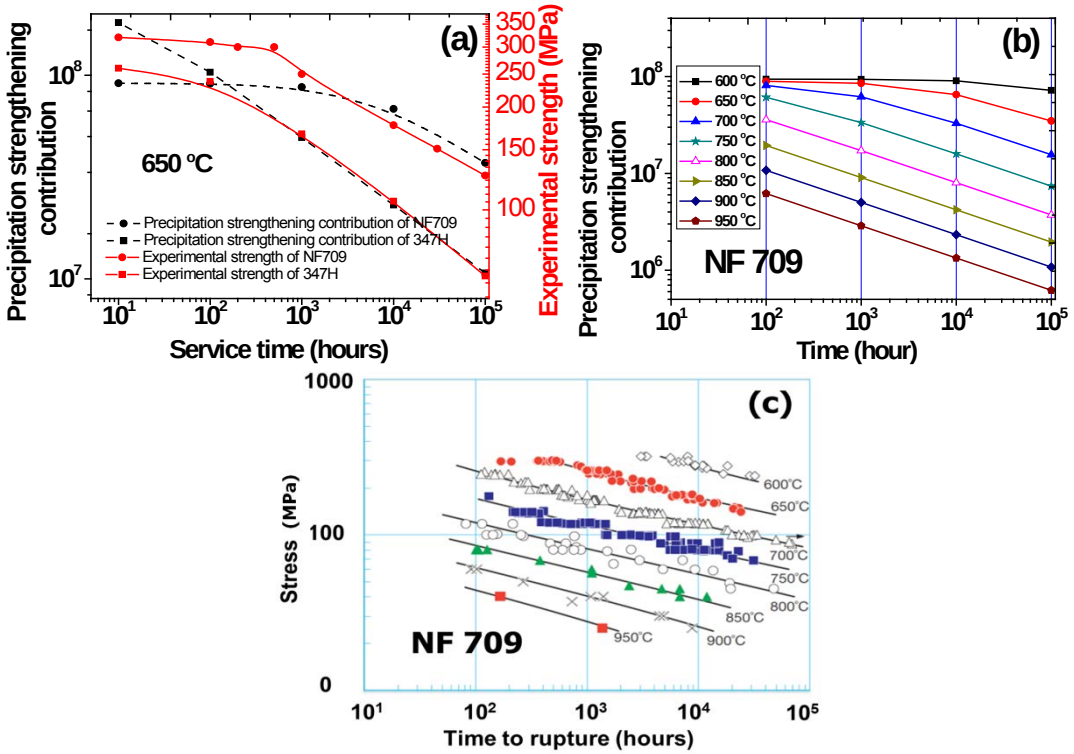

Figure 2.9 (a) Comparison of precipitation strengthening factor degradation of model and experimental creep strength degradation at 650 °C for the existing alloys; The calculated (b) and experimental [54] (c) creep strength versus time for NF709 at different temperatures.

In order to validate the model even further, the connection between the calculated precipitation strengthening factor and the experimental creep strength values at 650 and 750 ^{o}C for existing steel grades is shown in **Figure 2.10**. All commercial steel grades chosen here are MX carbonitrides precipitation strengthened grades. Each curve presents the creep strength evolution from 10 up to 10^5 h. The lower left part of each curve linked to lower strength values is the strength at longer times. For service times larger than 100 h, all alloys are located in the same band, confirming again that the model seems intrinsically sound. It is appropriate to point out that the precipitation strengthening factor for service times less than 10~100 h agree less with experimental creep strength values. The main reason for that is in the current model we intentionally ignored the growth stage of the precipitate evolution.

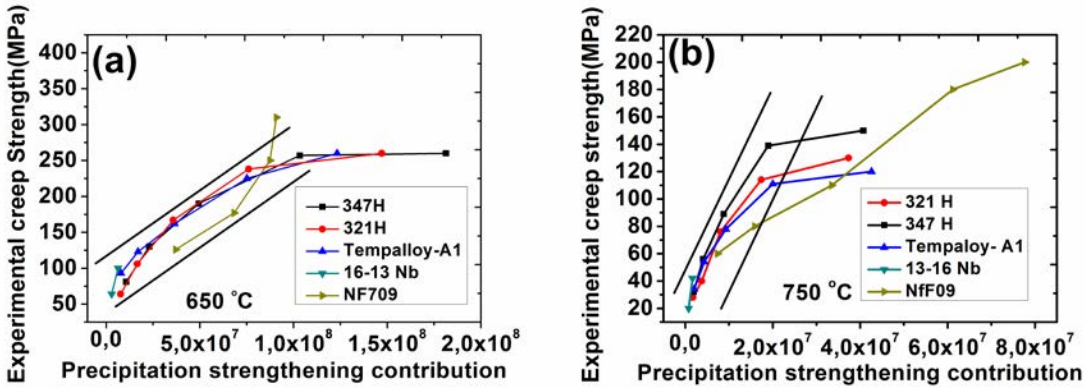

Figure 2.10 The calculated precipitation strengthening factor versus experimental creep strength at 650 (a) and 750 ^{o}C (b) for existing austenitic MX carbonitrides precipitation strengthened) creep resistant steels [55]

2.5 Conclusions

A thermokinetics-based computational alloy design model incorporating the time and temperature effects on precipitation related high temperature strength is developed to design heat resistant alloys. Three alloys are designed for service time of 0 h (for comparison), 10 h (optimised for fire resistance) and 10^5 h (optimised for creep resistance). The kinetics of precipitate coarsening forms the basis for the time and temperature dependence of the creep strength for MX carbonitrides precipitation strengthening corrosion resistance austenitic steels.

The calculations clearly show that the optimal composition for a high initial high temperature strength are quite different from that for a maximal strength after a long service time. For example, the alloy designed for 0 h service has a high initial strength but a low stability (high degradation rate of strength). While the alloy designed for 10^5 h has a relative low initial strength but a much reduced strength degradation rate.

Various comparisons made between the newly designed alloys and existing commercial precipitation strengthened austenitic steels indicate that the model is quite reliable and suggests that the newly defined alloy compositions are likely to be stronger at longer use times than existing creep steels.

References

[1] Charleux M, Poole WJ, Militzer M, Deschamps A. Precipitation behavior and its effect on strengthening of an HSLA-Nb/Ti steel. Metall. Mater. Trans. A 2001;32:1635.
[2] Takahashi T, Sakakibara M, Kikuchi M, Ogawa T, Sakurai H, Araki S, Nagao K, Yasuda H. Development of high-strength 20Cr-25Ni (NF 709) steel for USC boiler tubes. Nippon Steel Technical Report 1988:26.
[3] Minami Y, Kimura H, Tanimura M. Creep rupture properties of 18 Pct Cr-8 Pct Ni-Ti-Nb and Type 347H austenitic stainless steels. J. Mater. Energy Syst. 1985;7:45.
[4] Sawaragi Y, Otsuka N, Senba H, Yamamoto S. Properties of a new 18-8 austenitic steel tube (SUPER 304H) for fossil fired boilers after service exposure with high elevated temperature strength. Sumitomo Search 1994:34.
[5] Pickering FB. The metallurgical evolution of stainless steels. London: The Metals Society, 1979.
[6] Sourmail T. Precipitation in creep resistant austenitic stainless steels. Mater. Sci. Technol. 2001;17:1.
[7] Taneike M, Abe F, Sawada K. Creep-strengthening of steel at high temperatures using nano-sized carbonitride dispersions. Nature 2003;424:294.
[8] Yin FS, Jung W-S. Nanosized MX Precipitates in Ultra-Low-Carbon Ferritic/Martensitic Heat-Resistant Steels. Metall. Mater. Trans. A 2008;40A:302.
[9] Hald J, Korcakova L. Precipitate stability in creep resistant ferritic steels - Experimental investigations and modelling. ISIJ Int. 2003;43:420.
[10] Campbell CE, Olson GB. Systems design of high performance stainless steels I. Conceptual and computational design. J. Comput. Aided Mater. Des. 2000;7:145.
[11] Trabadelo V, Giménez S, Gómez-Acebo T, Iturriza I. Critical assessment of computational thermodynamics in the alloy design of PM high speed steels. Scripta Materialia 2005;53:287.
[12] Agren J. Thermodynamics and heat treatment. Materials Science Forum 1994;163-6:3.
[13] Lee BJ, Kim HD, Hong JH. Calculation of α/γ equilibria in SA508 grade 3 steels for intercritical heat treatment. Metallurgical and Materials Transactions A: Physical Metallurgy and Materials Science 1998;29:1441.

[14] Venkatesh V, Rack HJ. A neural network approach to elevated temperature creep-fatigue life prediction. Int. J. Fatigue 1999;21:225.
[15] Sourmail T, Bhadeshia HKDH, MacKay DJC. Neural network model of creep strength of austenitic stainless steels. Mater. Sci. Technol. 2002;18:655.
[16] Guo Z, Sha W. Modelling the correlation between processing parameters and properties of maraging steels using artificial neural network. Computational Materials Science 2004;29:12.
[17] Bhadeshia HKDH. Neural networks in materials science. ISIJ International 1999;39:966.
[18] Ghosh G, Olson GB. Integrated design of Nb-based superalloys: Ab initio calculations, computational thermodynamics and kinetics, and experimental results. Acta Mater. 2007;55:3281.
[19] Jones TE, Eberhart ME, Imlay S, MacKey C, Olson GB. Better alloys with quantum design. Phys. Rev. Lett. 2012;109.
[20] Xu W, Rivera-Díaz-del-Castillo PEJ, van der Zwaag S. Designing nanoprecipitation strengthened UHS stainless steels combining genetic algorithms and thermodynamics. Comput. Mater. Sci. 2008;44:678.
[21] Xu W, Rivera-Díaz-Del-Castillo PEJ, van der Zwaag S. Genetic alloy design based on thermodynamics and kinetics. Philos. Mag. 2008;88:1825.
[22] Xu W, Rivera-Díaz-Del-Castillo PEJ, van der Zwaag S. Computational design of UHS maraging stainless steels incorporating composition as well as austenitisation and ageing temperatures as optimisation parameters. Philos. Mag. 2009;89:1647.
[23] Xu W, Rivera-Díaz-Del-Castillo PEJ, van der Zwaag S. A combined optimization of alloy composition and aging temperature in designing new UHS precipitation hardenable stainless steels. Comput. Mater. Sci. 2009;45:467.
[24] Xu W, Rivera-Díaz-del-Castillo PEJ, Yan W, Yang K, San Martín D, Kestens LAI, van der Zwaag S. A new ultrahigh-strength stainless steel strengthened by various coexisting nanoprecipitates. Acta Mater. 2010;58:4067.
[25] Xu W, Rivera-Díaz-del-Castillo PEJ, Wang W, Yang K, Bliznuk V, Kestens LAI, van der Zwaag S. Genetic design and characterization of novel ultra-high-strength stainless steels strengthened by Ni3Ti intermetallic nanoprecipitates. Acta Mater. 2010;58:3582.
[26] Chakraborti N. Genetic algorithms in materials design and processing. Int. Mater. Rev. 2004;49:246.
[27] Wolf H, Mathew MD, Mannan SL, Rodriguez P. Prediction of creep parameters of type 316 stainless steel under service conditions using the θ-projection concept. Mater. Sci. Eng., A 1992;159:199.
[28] Evans RW, Parker, J. D. and Wilshire B. Recent Advances in Creep and Fracture of Engineering Materials and Structures. Swansea: Pineridge Press, 1982.
[29] Ahmadieh A, Mukherjee AK. Stress-temperature-time correlation for high temperature creep curves. Mater. Sci. Eng. 1975;21:115.
[30] Haupt A, Munz D, Scheibe W, Schinke B, Schmitt R, Sklenicka V. High temperature creep and cyclic deformation behaviour of AISI 316 L(N) austenitic steel and its modelling with unified constitutive equations. Nucl. Eng. Des. 1996;162:13.
[31] Holdsworth S. Developments in the assessment of creep strain and ductility data. Mater. High Temp. 2004;21:25.

[32] Holdsworth SR, Askins M, Baker A, Gariboldi E, Holmström S, Klenk A, Ringel M, Merckling G, Sandstrom R, Schwienheer M, Spigarelli S. Factors influencing creep model equation selection. Int. J. Press. Vessels Pip. 2008;85:80.
[33] Sustek V, Pahutova M, Acadek J. An investigation of creep behaviour of a low carbon 18Cr-12Ni (304L type) stainless steel at 873-1173 K. Mater. Sci. Eng., A 1994;177:75.
[34] Kassner ME, Pérez-Prado M-T. Fundamentals of creep in metals and alloys. Amsterdam,: Elsevier, 2004.
[35] Naumenko K, Altenbach, Holm. Modeling of Creep for Structural Analysis, 2007.
[36] Olson GB. Computational design of hierarchically structured materials. Science 1997;277:1237.
[37] Xu W, Lu Q, Xu X, van der Zwaag S. The structure of a general materials genome approach to the design of new steel grades for specific properties. Comput. Methods in Mater. Sci. 2013;13:382.
[38] ASM metals handbook, properties and selection irons - irons, steels, and high performance alloys, Specialty steels and heat-resistant alloys. Ohio: ASM International, Materials Park, 2005.
[39] Carter GF. Principles of Physical & Chemical Metallurgy: American Society for Metals, 1979.
[40] Huang QX, Li, H.K. Superalloy (in Chinese), Metallurgical Industry Press, 2000.
[41] Hall EO. The deformation and ageing of mild steel: III Discussion of results. Proc. Phys. Soc. B 1951;64: 747.
[42] Petch NJ. The cleavage strength of crystals. J. Iron and Steel Institute 1953:25.
[43] Lasalmonie A, Strudel JL. Influence of grain size on the mechanical behaviour of some high strength materials. J. Mater. Sci. 1986;21:1837.
[44] Maruyama K, Sawada K, Koike J. Strengthening mechanisms of creep resistant tempered martensitic steel. ISIJ Int. 2001;41:641.
[45] Peng B, Zhang H, Hong J, Gao J, Li J, Wang Q. The evolution of precipitates of 22Cr-25Ni-Mo-Nb-N heat-resistant austenitic steel in long-term creep. Mater. Sci. Eng., A 2010;527:4424.
[46] Lai JK, Wickens A. Microstructural changes and variations in creep ductility of 3 casts of type 316 stainless steel. Acta Metall. 1979;27:217.
[47] Lo KH, Shek CH, Lai JKL. Recent developments in stainless steels. Materials Science and Engineering R: Reports 2009;65:39.
[48] Oruganti R. A new approach to dislocation creep. Acta Mater. 2012;60:1695.
[49] Orowan E. Theory of dislocation bowing. London: Institute of Metals Symposium on Internal Stresses in Metals and alloys, 1948.
[50] Cahn RW, Haasen P. Physical Metallurgy: Elsevier, 1996.
[51] Kelly A. The strength of aluminium silver alloys. Philos. Mag. 1958;3:1472.
[52] Ågren J, Clavaguera-Mora MT, Golczewski J, Inden G, Kumar H, Sigli C. Applications of Computational Thermodynamics: Group 3: Application of computational thermodynamics to phase transformation nucleation and coarsening. Calphad-Computer Coupling of Phase Diagrams and Thermochemistry 2000;24:41.
[53] Ishida K. Calculation of the effect of alloying elements on the Ms temperature in steels. J. Alloys Compd. 1995;220:126.
[54] Nippon Steel Corporation: Nippon Steel Creep Database 2000.

[55] NIMS creep data sheet, National institute for materials science, http://smds.nims.go.jp/creep/index_en.html.

Chapter 3

Designing new corrosion resistant ferritic heat resistant steels based on optimal solid solution strengthening and minimisation of undesirable microstructural components

3.1 Introduction

In Chapter 2, optimisation of precipitation hardening by MX carbonitride is used to design austenitic heat resistant steels. However, for precipitation strengthened alloys, a drop in the strengthening contribution of precipitates is inevitable over very long service times due to precipitate coarsening. Unlike precipitation strengthening, solid solution strengthening is in principle time independent once the equilibrium state is achieved. Alloys based on a high solid solution strengthening contribution will probably have a combination of a lower initial creep strength but a superior stability over very long use times.

Ferritic heat resistant steels have been widely used in high temperature components in power plant applications. One of the main advantages of ferritic steels is its lower thermal-expansion coefficient compared to that of austenitic steels leading to a better thermal fatigue resistance [1]. However, the relatively low strength of ferritic grades at high service temperatures significantly limits their application. Design of new ferritic heat resistant steels with an intrinsically higher strength can significantly expand their

application and increase their relevance for the construction of next generation power plants.

Solid solution strengthening arises from the interaction of dislocations and solutes in the solid solution due the size and modulus misfit of solutes with the solvent. It has been extensively studied both theoretically and experimentally during the last century [2-8]. In recent years, ab initio methods have been used to predict the solid solution strengthening taking into account the size and electronic structure of individual alloying elements [9-13]. In-situ observations of the interaction of dislocation with solutes made it possible to investigate the solid solution behavior at the nano level [14-16].

Given the existing knowledge on solid solution strengthening and relatively new mathematical tools, computational design of high solid solution strengthened alloys involving many strengthening elements at the same time has become possible. In the present work, a genetic alloy design approach coupled with thermodynamics is developed to obtain high strength ferritic heat resistant steels containing 11 alloying elements using solid solution strengthening at a fixed service temperature of 650 ^{o}C as the optimisation target. As the final strength of an alloy not only depends on the optimised presence of the strengthening mechanism, but also on the absence of undesirable microstructural components, in the optimisation both the desirable and the to-be-avoided components are taken into account. Furthermore, the model also takes into account all relevant microstructural changes at the various heat treatment temperatures. The effect of grain size, being a parameter not captured by thermodynamics, is ignored.

3.2 Model description

3.2.1 Design methodology

Using a similar approach as in the design of precipitation strengthened austenitic steel presented in Chapter 2, the flow chart for the design of new ferritic steels is shown in the **Figure 3.1**. For the ferritic creep resistant steel grades studied in the current work, only solid solution strengthening is considered and maximized to safeguard the intrinsic stability of the alloy. The target matrix microstructure is defined as being ferritic (i.e. not martensitic) in combination with a limited precipitate volume fraction (since some precipitates are unavoidable). As before, the creator links the tailored microstructural features to a specific composition and related heat treatment parameters by employing

various quantitative criteria related to thermodynamic and kinetics considerations. Finally, all qualified solutions are ranked according to a properly defined solid solution strengthening factor. Considering the large space of the pre-defined compositional domain, a Genetic Algorithm is employed to make sure the solution space is searched effectively and efficiently. The metallurgical justification of the various steps in the program are given below. The intended use temperature of the new alloy is fixed at 650 ^{0}C.

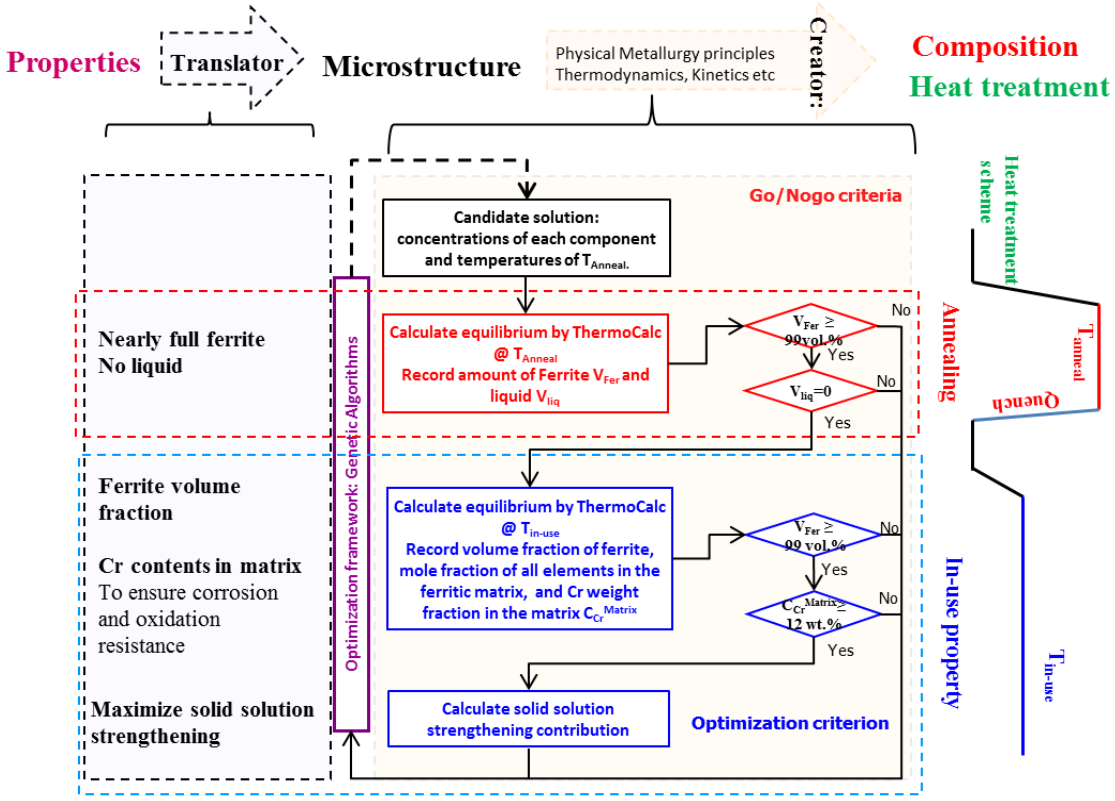

Figure 3.1 Alloy design strategy and criteria evaluation of high solid solution strengthening ferritic heat resistant steels.

3.2.2 Defining the go/no-go criteria

To obtain the desirable microstructure (a fully ferritic matrix with maximal solid solution strengthening, a minimal precipitation volume fraction and an absence of detrimental phases), various go/no-go criteria are defined. Following the order of a conventional heat treatment route for existing ferritic heat resistant steels, candidate solutions are first evaluated at the annealing condition by performing the thermodynamic equilibrium

calculation at the annealing temperature T_{Anneal}. Two go/no-go criteria are imposed at this step, being

(1) the equilibrium ferrite volume fraction at homogenisation temperature should be larger than 99%.
(2) the liquid phase should be absent at this temperature.

After homogenisation, the alloy is cooled down to room temperature before it beubg used at a high temperature. Unlike annealing in the austenitic state, a fully ferritic matrix at the end of the annealing temperature will not undergo a phase transformation during cooling to room temperature. Yet during service, the themodynamic equlibrium may vary and some precipitates may form. Therefore, the second set of themodynamic calculations is performed at the intended service temperature. Two additional go/no-go criteria are enforced:

(3) the volume fraction of ferrite at 650 ^{o}C is set at no less 99 vol.%, i.e. a maximal volume fraction of undesirable phase of 1 vol% is tolerated.
(4) a minimum of 12 wt.% Cr in the ferritic matrix upon completion of the precipitation reactions to ascertain adequate corrosion and oxidation resistance.

Candidate solutions which fulfil all go/no-go criteria (1)–(4), are further evaluated by the optimisation criterion, the solid solution strengthening factor at the pre-defined service temperature.

3.2.3 Optimisation criterion / Solid solution strengthening contribution

Solid solution strengthening in alloys arises from the interaction of dislocations and solutes. Generally, solid solution strengthening can be described as a function of atomic concentration of solutes[17]. However, the interaction mechanisms between solutes and dislocations may differ depending on the (FCC or BCC) crystal structure of the matrix.

In dilute high purity binary FCC systems [18] at modest temperatures [19], the solid solution strengthening contribution $\Delta\sigma_{ss}$ can be expressed by the following relation [4, 5, 20-22],

$$\Delta\sigma_{ss} = (K_i C_i)^{1/2} \tag{3.1}$$

where K_i is strengthening coefficient for 1 at.% of alloying element i, C_i is atomic percent of alloying element i in the solution.

For more concentrated solutions in an FCC matrix Labusch [2, 3] developed a statistical theory of solid solution strengthening, which was further extended by Nabarro [23]. Then the solid (atomic) concentration dependence of the solution strengthening in binary alloys changes from $C^{1/2}$ to $C^{2/3}$,

$$\Delta\sigma_{ss} = (K_i C_i)^{2/3} \tag{3.2}$$

Equation 3.1 and 3.2 have been shown to describe the experimental results in FCC Au-based and Cu-based systems [24, 25] and HCP Ma-based systems [26] equally well.

However, in some FCC solutions, such as austenitic steel system, these two equations do not fit experimental data very well [17]. The same situation also applies to BCC alloys. Suziki and Mott [27, 28] proposed a linear dependence to describe solid solution strengthening better and obtained a good agreement with experimental results for both BCC binary iron systems and FCC multicomponent iron systems. Their linear dependence model yielded

$$\Delta\sigma_{ss} = K_i C_i \tag{3.3}$$

Equation 3.3 has been experimentally validated both for substitutional binary systems [29, 30] and interstitial binary systems [31, 32].

The above three equations all have some credibility within their matrix and concentration constraints. In the present study, Equation 3.3 is chosen to calculate the solid solution strengthening contribution as the ferritic steel has a BCC matrix. In Equation 3.3, the atomic fraction C_i is in the ferritic matrix can be determined by thermodynamic calculation using alloy composition. The strengthening factor K_i, combines both size misfit and modulus misfit effects [2, 8, 30, 33, 34] and it has been found to be difficult to separate the two contributions. The amount of experimental data of modulus misfit for Fe-M binary alloy is rather limited in comparison to the large amount of size misfit data. The recent developments in ab-initio modelling may offer new possibilities to obtain values of modulus misfit and size misfit contributions [9, 13, 35-39]. However, right now the reliability of the ab-initio results remains a problem.

As a result of insufficiently precise theoretical estimates, K_i is normally fiited to experimental data and effects of size misfit and modulus misfit are not evaluated

separately. For the substitutional elements considered in this work, the strengthening coefficients at room temperature (MPa per at.% shown in Table 3.1) were determined from ferritic binary Fe-M system [40, 41]. For the interstitial elements C and N, the strengthening factors at room temperature were determined from the properties of low carbon ferritic steels [17].

Table 3.1 Strengthening coefficient for alloying elements at room temperature (MPa per at.%) [17, 40, 41].

Element	C	N	Si	Ni	Ti	Mn	Mo	Al	Cr	Co	V
K_i	1103.45	1103.45	25.80	19.20	17.90	16.90	15.90	9.00	2.60	2.10	2.00

In the present study, the optimization criterion is the total solid solution strengthening contribution in a multi component system at the intended elevated service temperature i.e. 650 °C. However, K_i values as reported in Table 3.1 were determined for binary systems at room temperature. Therefore, two simplifying assumptions were imposed:

a. ternary and high order interactions between different alloying elements are ignored, and the effect of each alloying element is considered to be additive.
b. The strengthening coefficient at 650 ^{0}C, is proportional to that at room temperature, i. e. the room temperature strengthening coefficient values can be used to describe high temperature strength but with a simple scalar. The effect of solute atom diffusion on their interactions with dislocations [46] may become important at high temperature, depending on the alloy composition, temperature, applied stress, the strain evolution, and the development of microstructures. However, the effect of such diffusion is a second order effect and its impact on the absolute value of solid solution strengthen is relatively limited. Therefore, this effect is neglected in the current version of the model.

Now, the solid solution strengthening contribution in the multi-component ferritic matrix can be reformulated as

$$\Delta\sigma_{ss} = a\sum_i K_i C_i \tag{3.4}$$

where a is temperature dependent scalar. At room temperature, the scalar a is delegated as a_{RT}. and its value is equal to 1 (neglecting cross-term effects). When the temperature is 650 ^{o}C, a new scalar, $a_{650,}$ applies. In case a potential new alloy composition is not fully

ferritic, the solid solution strengthening contribution is scaled to the ferrite volume fraction of the steel grade concerned. A justification of assumptions a) and b) as well as the use of scale factors a_{RT} and a_{650} is presented in Section 3.3.

3.2.4 Searching condition and optimization framework

The range of concentrations for the 11 alloying elements taken into account in the design optimalisation as well as the range of annealing temperature ranges to be applied are summarized in Table 3.2. As said before, the service temperature is set at 650 ^{0}C.

Table 3.2 Search ranges of composition (in at.%), and annealing temperature (in ^{0}C).

	C	*N*	*Si*	*Ni*	*Ti*	*Mn*	*Mo*	*Al*	*Cr*	*Co*	*V*	*Fe*	T_{anneal}
Min.	0	0	0	0	0	0	0	0	8	0	0	Bal.	800
Max.	0.15	0.15	10	10	2	10	3	15	16	10	5		1150

A Genetic Algorithm is applied as the optimization scheme, taking into account 12 variables (11 alloying elements and the annealing temperature). Details can be found in section 2.2.5 in Chapter 2.

3.3 Validation of solid solution strengthening contribution

To validate the use of the solid solution strengthening factor as defined by Equation 3.4 as the optimisation factor in combination with the go/no-go criteria defined for candidate alloys, the experimental strength values of existing commercial ferritic steels, both at room temperature and at the high service temperature, are collected from literature and compared to the values predicted by the model. The solid solution strengthening contribution at room temperature is calculated based on the equilibrium concentration in the ferritic matrix at the annealing temperature. However, to calculate the solid solution strengthening contribution at the service temperature (650 ^{o}C), the equilibrium concentration of alloying element in the ferritic matrix at 650 ^{o}C is used. As discussed before, the same strengthening coefficient K_i for each element at room temperature is applied at the high temperature, but with a common scalar a_{650}.

The chemical compositions of existing ferritic stainless steels containing no or a small amounts of precipitates are listed in Table 3.3. The phase configurations and compositions of ferritic matrix(C_i) at annealing and service temperature as calculated by Thermo-Calc® are listed in Table 3.4. As intended, at both temperatures, no significant amount of precipitates; possibly with the exception of AL 29-4-2 , AL 29-4C and E-Brite 26-1 where small amounts of precipitates may be present at the homogenisation temperature or at the intended use temperature. The total solid solution strengthening contribution was determined by using Equation 3.4. It should be noted that the solid solution strengthening due to Cu, Nb, Ce and La is neglected because 1) the concentrations of Ce, La, Cu and Nb (0-0.6%) are not high compared to those of other solid solution strengthening elements such as Ni, Mo, Al(1-5%). 2) concentrations of Cu and Nb in the solid solution are further reduced by formation of NbX carbonitride precipitates or Cu particles and, and 3) their strengthening coefficients K_i have not been determined experimentally with sufficient accuracy.

Table 3.3 Chemical composition of existing ferritic stainless steel grades (in wt.%) [42, 43].

	C	N	Si	Ni	Ti	Mn	Mo	Al	Cr	Residuals
405	0.15							0.2	13	
409	0.08				0.48				11	
429	0.12								15	
430	0.12								16	
434	0.12						1		17	
439	0.07				0.95				18.25	
444	0.025				0.6				17	
446	0.2	0.25							25	
E-Brite 26-1	0.01	0.015	0.4	0.5		0.4	1.12		26	0.2 Cu. 0.12 Nb
Type 430 Ti	0.1		1	0.75	0.625	1			17.75	
AEMCO 18SR	0.04		1		0.4	0.3		2	18	
ALFA I	0.025		0.3		0.4	0.035		3	13	
ALFA I	0.025		0.3		0.4	0.035		4	13	
AL 29-4C	0.03	0.045	1	1		1	3.9		29	0.45 Nb
AL 29-4-2	0.01	0.02	0.2	2.25		0.3	3.85		29	0.15 Cu
ALFA IV	0.015	0.014	0.24	0.14	0.004	0.23		5.4	20.8	0.04 (Ce+La)
Sea-Cure	0.025	0.035	1	2.5		1	3		26	0.55 Nb
MONIT	0.025	0.035	0.75	4		1	4		25.2	0.62 Nb

Table 3.4 Microstructure of existing ferritic stainless steels at annealing temperature (850-1000 ^{o}C) and 650 ^{o}C (in vol. %, F indicates Ferrite).

Alloy	At annealing temperature	At 650 ^{o}C
405	97.2F+2.8 $M_{23}C_6$	97.1F+2.9 $M_{23}C_6$
409	99.3F+0.72TiC	97.7F+2.3 $M_{23}C_6$
429	97.8F+2.2 $M_{23}C_6$	
430	97.8F+2.2 $M_{23}C_6$	97.7F+2.3 $M_{23}C_6$
439	99.3F+0.65TiC	
434	97.7F+2.3 $M_{23}C_6$	97.6F+2.39 $M_{23}C_6$
436	99.24F+0.65NbC+0.11 $M_{23}C_6$	
446	93.6F+3.3 $M_{23}C_6$+3.11Cr2n	93.3F+3.7 $M_{23}C_6$+3Cr2N
444	99.76f+0.23TiC	
E-Brite 26-1	99.8F+0.19TiCN	61.88F+36Sigma+2Laves+0.2TiC+ 0.054Cu
430Ti	99.1F+0.9TiC	
AEMCO 18SR	99.65F+0.35TiC	97.4F+2.28Sigma+0.36TiC
ALFA- I	99.78F+0.22TiC	99.78F+0.22TiC
ALFA- II	99.78F+0.22TiC	99.78F+0.22TiC
29-4C	89.15F+5.55Zphase+4.37Laves+0.48Sigma+0.46N bCN	
29-4-2	83.1F+16.7sigma+0.087Cr2N+0.04M23C6	
ALFA- IV	99.7F+0.2$M_{23}C_6$+0.09AlN+0.006TiC	99.6F+0.253$M_{23}C_6$+0.086AlN+ 0.0063TiCN
Sea-Cure	99.46+0.37NbCN+0.17 Z phase	
MONIT	98.1F+1.39Sigma+0.37NbCN+0.17Zphase	

The experimental minimum yield strength at room temperature as a function of the calculated solid solution strengthening contribution (use Equation 3.4 with a_{RT}=1) is plotted to validate Equation 3.4**.** As shown in **Figure 3.2**, a very good linear correlation between experiment and calculation can be observed as indicated by the two parallel dotted lines. The scalar a_{RT} is found to be 1.5, i.e. slightly above 1 which indicates there are possible positive cross effects on solid solution strengthening in multicomponent system. Nevertheless, under the current assumptions the model predicts the relative ranking of the various commercial steels grades with a sufficiently high precision.

In **Figure 3.3**, the experimental yield strength at 650 ^{o}C as a function of the calculated solid solution strengthening contribution at 650 ^{o}C (use Equation 3.4 setting a_{650}=1 initially) is plotted. Similar to the room temperature behaviour, a good linear correlation between experimental and calculated data indicated by the two parallel dotted lines can be found, with a slightly deviatory behaviour for steel grade AEMCO 18 SR. The value

for the scalar a_{650} was found to be 0.25 which is, as expected, lower than unity because of the weakened interaction of solutes with dislocations at higher temperatures.

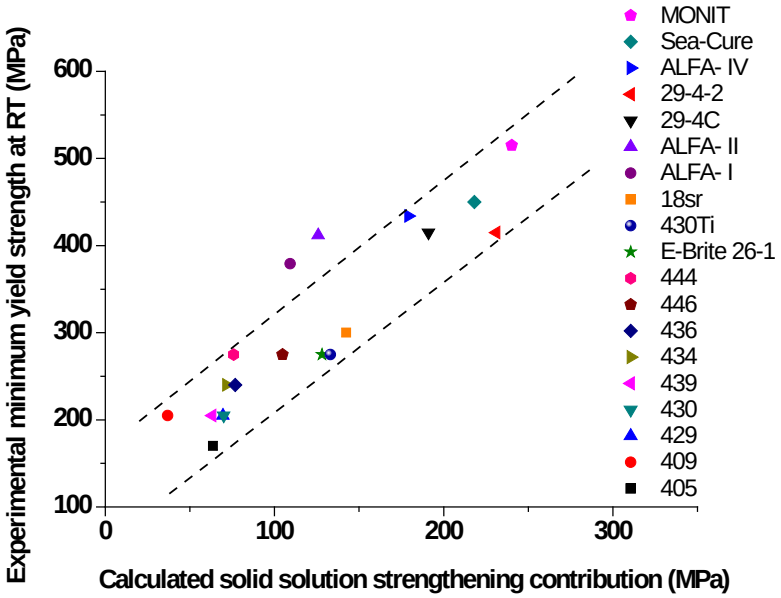

Figure 3.2 Experimental minimum yield strength at room temperature (RT) [42, 43] vs. calculated solid solution strengthening contribution (use Equation 3.4 and a_{RT}=1).

In addition, **Figures 3.2** and **3.3** show that at both room temperature and 650 ^{o}C, the yield strength is not zero when there is no calculated solid solution strengthening contribution. The intercept values reflects the base strength of a BCC iron matrix plus other strengthening mechanisms, e,g, grain size, texture, dislocations, precipitates etc. The contributions of grain size, texture and dislocation density are apparently quite similar in the selected ferritic steel grades. According to Table 3.3, each alloy generally has only one type of strengthening precipitate, either $M_{23}C_6$ or MC carbide (other precipitates are consider undesirable which would cause a decrease in strength). The amount of each precipitate is similar ($M_{23}C_6$ around 2 vol.%, and MX around 0.3vol.%). MC carbide is usually fine, yet $M_{23}C_6$ is generally coarse. Thus, they will probably have similar inter-particle spacing which is inversely proportional to the precipitation strengthening. Furthermore, according to Ref. [44], 0.3% MC carbide could probably have similar strengthening effect as 2% $M_{23}C_6$. In conclusion, it seems safe to conclude that the observed linearity is real and only due to the solid solution strengthening.

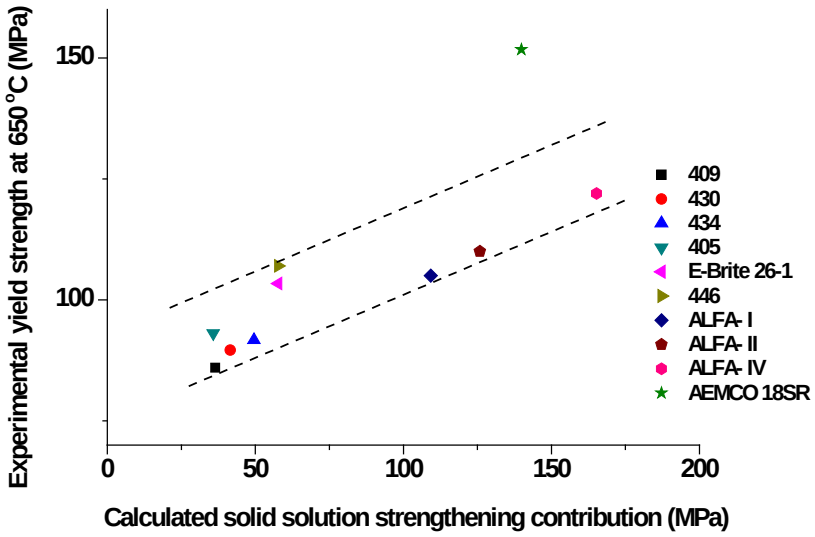

Figure 3.3 Experimental yield strength at 650 °C [42, 43] vs. calculated solid solution strengthening contribution (using Equation 3.4 and a_{650}=1), K_i in Equation 3.4 uses the room temperature value.

In conclusion, both at room temperature and at 650 °C, the calculated solid solution strengthening contributions according to Equation 3.4 fit well to experimental results. This result that the computational approach as defined can be used with some confidence to optimise the solid solution strengthening contribution in a novel multi-component ferritic steels at either room temperature and at high temperature, by applying corresponding scalar respectively.

3.4 Optimised new steel compositions

The compositions of the 6 highest ranked new solid solution strengthened ferritic steel grades to be used at 650 °C are shown in Table 3.5 and are labelled as Fer-OPT (the optimal solution), and Fer-1 to Fer-5. Although alloy Fer-OPT has numerically the highest solid solution strengthening contribution, differences with other good solutions (Fer-1 to Fer-5) are quite small and not statistically relevant. The six designed alloys have very similar solid solution strengthening contributions, indicating that the optimal solutions are located at a flat area in the solution space. Their determinations confirms the robustness of the GA optimisation procedure used.

Since alloy Fer-OPT has the highest solid solution strengthening contribution and a composition not unlike the other preferred newly designed alloys, the element levels of alloy Fer-OPT and their position with respect to the boundaries as set in the search domain are analysed in greater detail here. Firstly, the target concentrations of C and N are 0 wt.% which is not surprising since C and N promote the formation of carbide/nitride/carbonitride precipitates and their solubilities in ferrite are extremely low. Secondly, concentrations of Ti, Al and Mn reach the maximal levels set in their respective search ranges owning to their high strengthening factors and high solubilities in the ferrite, while that of Co is at the minimal level due to its low solid solution strengthening factor. The other elements have concentrations located well within their allowed search regime and must be defined by the imposed go/no-go criteria. Furthermore, concentrations of substitutional elements in the matrix of alloy Fer-OPT are shown in Table 3.5 and are almost equal to the overall composition of the alloy, indicating that all strengthening elements are effectively dissolved in the ferritic matrix and no depletion of strengthening solutes due to precipitation is predicted to take place.

Table 3.5 Chemical composition (in wt. %), annealing temperature (in ^{o}C), and calculated solid solution strengthening contributions SSSC (in MPa) of designed alloys. Concentrations of alloying element in the matrix of alloy Fer-OPT at 650 °C are also listed in the last row.

	C	N	Si	Ni	Ti	Mn	Mo	Al	Cr	Co	V	T_{anneal}	SSSC
Fer-OPT	0.00	0.00	3.35	5.53	1.86	10.69	3.79	5.25	12.27	0.00	1.75	969.00	611.76
Fer-1	0.00	0.00	3.36	5.54	1.87	10.72	3.44	5.27	12.57	0.00	2.72	800	611.01
Fer-2	0.00	0.022	3.36	5.54	1.87	10.72	3.44	5.27	12.57	0.00	2.72	1116	610.46
Fer-3	0.002	0.022	3.36	5.54	1.87	10.72	3.44	5.27	12.57	0.00	2.72	1116	610.36
Fer-4	0.002	0.022	3.36	5.55	1.87	10.73	3.26	5.24	12.58	0.00	2.73	1139	608.83
Fer-5	0.002	0.022	3.36	5.54	1.87	10.71	3.44	5.26	12.55	0.00	1.12	1116	606.86
Matrix of alloy Fer-OPT	0.00	0.00	3.31	5.56	1.88	1.74	3.65	5.38	12.01	0	1.77		

To check the thermodynamic stability, phase fractions of alloy Fer-OPT at different temperatures are plotted in **Figure 3.4**. It can be observed that at the homogenisation temperature (969 ^{o}C) only ferrite exists, while at the at service temperature (650 ^{o}C) a very small amount of Cr_3Si and MU phase coexist with ferrite matrix. Although according to the thermodynamic calculation, there are substantial amounts of non-ferritic phases present at temperature lower than 650 ^{o}C, those phases should not form during

quenching from the annealing temperature, nor heating up to the service condition due to limited diffusions in a short time, and therefore, a fully ferritic matrix with the optimal SSSC can be realized at 650°C and the alloy can be used at higher temperatures as well. In future extensions of the current model, an additional go/no-go criterion can be imposed that all go/no-go criteria are met within a predefined temperature window, e.g. 630-670 °C, rather than at a specific temperature.

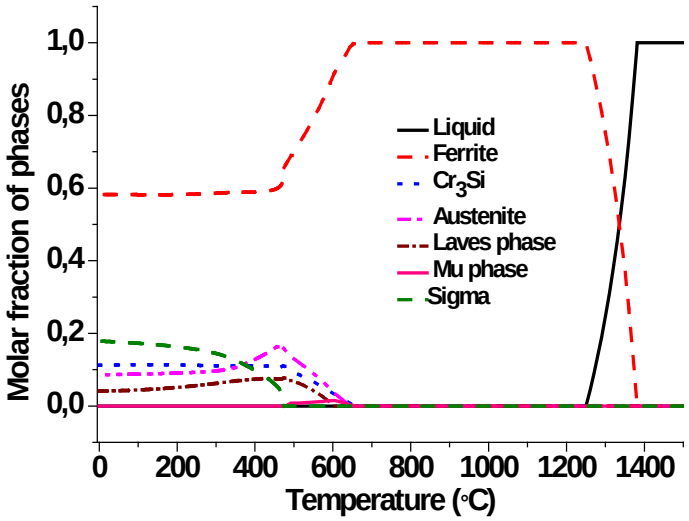

Figure 3.4 Molar fractions of phases in alloy Fer-OPT at various temperatures.

3.5 Discussion

3.5.1 Validations of go/no go criteria

To justify the validity of the go/no-go criteria employed in the alloy design, thermodynamic calculations are performed with compositions of existing alloys (see Table 3.2) at both annealing and service temperatures, and results are shown in **Figure 3.5**. The dashed black lines in **Figures 3.5a) – 3.5c** are minimum required values of go/no-go criteria for ferrite volume percent at annealing temperature (99%), service temperatures (99%) and Cr weight percent in ferrite (12 wt.%), respectively. It can be observed that most of the existing alloys meet or stand close to criteria enforced in the design exercises in this paper. The calculated amount of precipitates at the service temperature of 650 °C are indeed very low in most of cases as shown in **Figure 3.5b**. This result is in agreement with the general design concept of existing ferritic heat resistant steels that such alloys should not form precipitates to deplete Cr and other

elements. However, some exceptions can be found, such as 29-4-2, 29-4C, MONIT, Sea-Cure, E-Brite26-1. This is because those alloys all have very high Cr concentrations and are generally used at a higher temperature (around 800-900 ^{o}C), at which ferrite volume fraction will increase to a even higher value (see **Figure 3.5a**). They are not suitable for applications at lower temperature, such as 650 ^{o}C, since a significant amount of sigma phase will form.

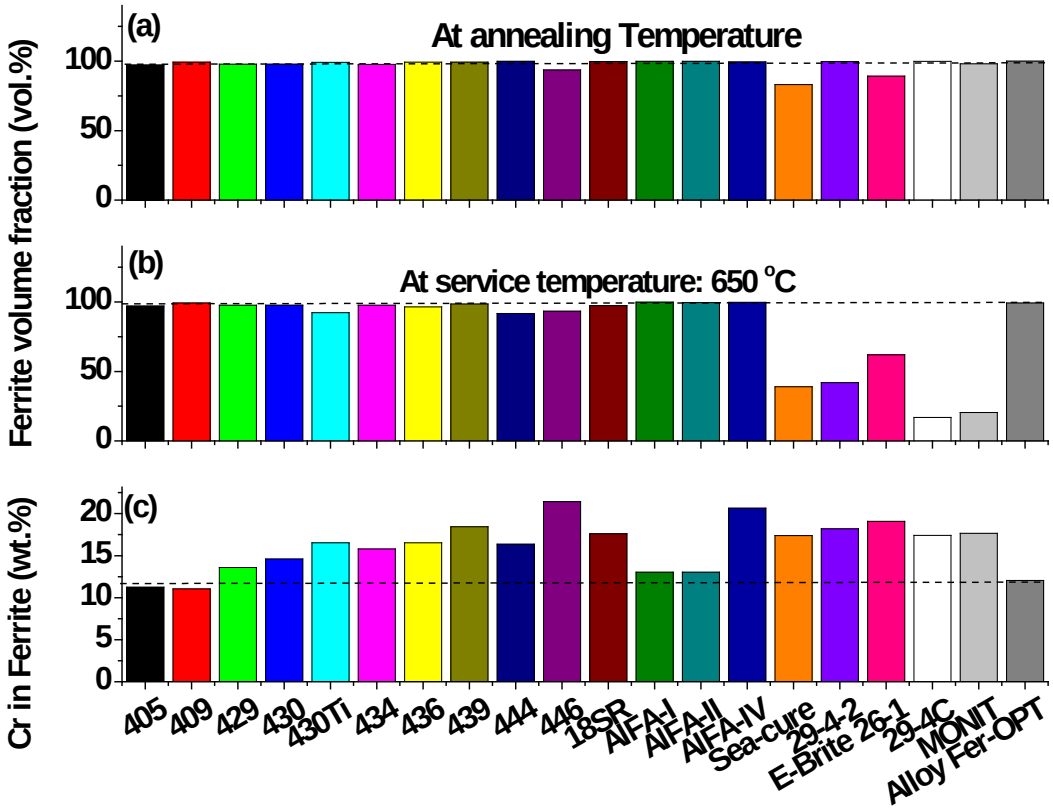

Figure 3.5 Go/no-go criteria value of existing alloys and design alloy Fer-OPT. Ferrite volume fraction at annealing temperature(a) and service temperature 650 ^{o}C (b), (c) Cr weight percentage in the ferritic matrix at 650 ^{o}C. The black dashed lines in **Figure 3.5a-3.5c** are the minimum value of go/no-go criteria.

3.5.2 Compositional effects

Figure 3.6 shows the solid solution strengthening contributions of each element and the composition as to be realised in the optimal ferritic matrix in atomic fraction. The principal solid solution strengthening contributions are attributable to Mn, Si, Ni and Al, while the other elements have more limited contributions. Moreover, although the strengthening coefficient of Mn is lower than that of Si, Mn still has a higher solid solution strengthening contribution than that of Si since higher Mn levels are allowed without meeting the restrictions imposed by the go/no-go criteria. Al being a ferrite stabilizer also increases the corrosion resistance and decrease the density in addition to its solid solution strengthening. Moreover, the high concentration of Cr is mainly required in order to obtain adequate corrosion resistance at high temperature but it also makes a notable solid solution strengthening contribution.

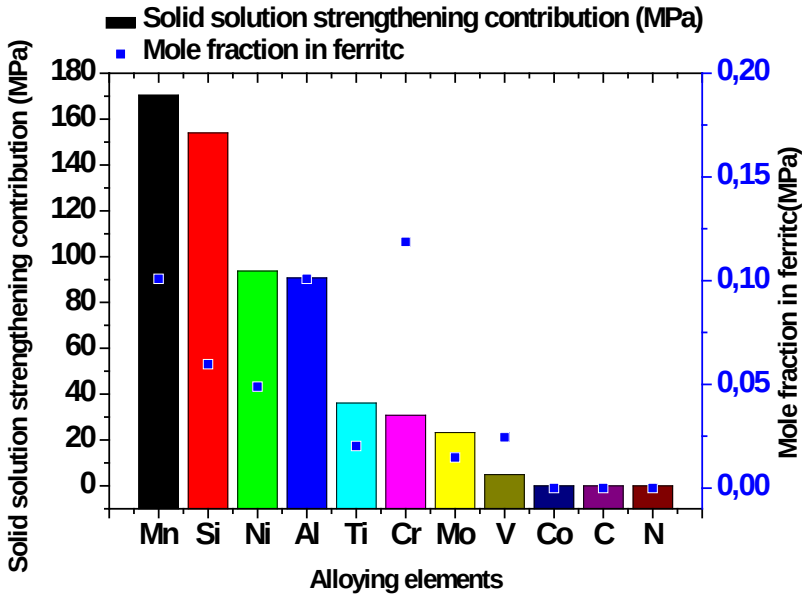

Figure 3.6 Solid solution strengthening contribution and mole fraction in ferrite of each alloying element.

To explore effects of alloying elements in relation to the pertaining go/no-go criteria, the composition of alloy Fer-OPT is taken as a baseline and concentrations of Mn, Si, Ni and Al are varied (while keeping levels of all other elements unchanged). Results are shown

in **Figure 3.7**. In this figure the search ranges of Mn and Al in **Figures 3.7a** and **3.7d** are extended beyond the original composition ranges (Table 3.2) since the early optimised solutions reached the maximal allowed value in alloy Fer (Table 3.5).The search ranges of Si and Ni are kept unchanged (Table 3.2). In each plot of **Figure 3.7** the original composition ranges of all four elements are marked by two vertical dashed lines. The backward, forward and horizontal slash patterns define areas not fulfilling the go/no-go criteria of Cr concentration in the ferritic matrix, ferrite volume fractions at service temperature (650 ^{o}C) and at annealing temperature respectively. The overlap of two or three kinds of patterns indicates that more than one go/no-go criterion is not satisfied. Only compositions located in the area without any pattern are qualified solutions. As indicated by the arrows, the original concentrations of Mn, Si, Ni and Al (in alloy Fer-OPT) fulfilled all criteria and have the highest solid solution strengthening contribution, suggesting the effectiveness of the optimisation scheme. With the exception of Ni, the solid solution strengthening contribution generally increases with the increase of concentration of the alloying element although beyond certain level, some go/no-go criteria are not satisfied any more. For Mn and Al, concentrations leading to a higher SSSC can be found beyond the original compositional ranges without breaking go/no-go criteria, which suggests a wider composition domain should be considered. However, the increase in the final solution strengthening contribution by extending the Mn and Al ranges is limited (see **Figures 3.7a** and **3.7d**). Finally, the effect of Ni on the overall SSSC, which increases first and then drops with the increase of Ni concentration, is interesting. Through the analysis of the phase configuration at different Ni concentrations, the reason for the unexpected decease can be attributed to the formation of large amounts of a Ni-rich austenite phase, a Mo-rich MU phase and Cr_3Si precipitates when Ni concentration is beyond the critical level shown in **Figure 3.7c**. The formation of these phases depletes the concentration of Ni, Mo and Si in the ferritic matrix, thus leading to a decrease in solid solution strengthening contribution.

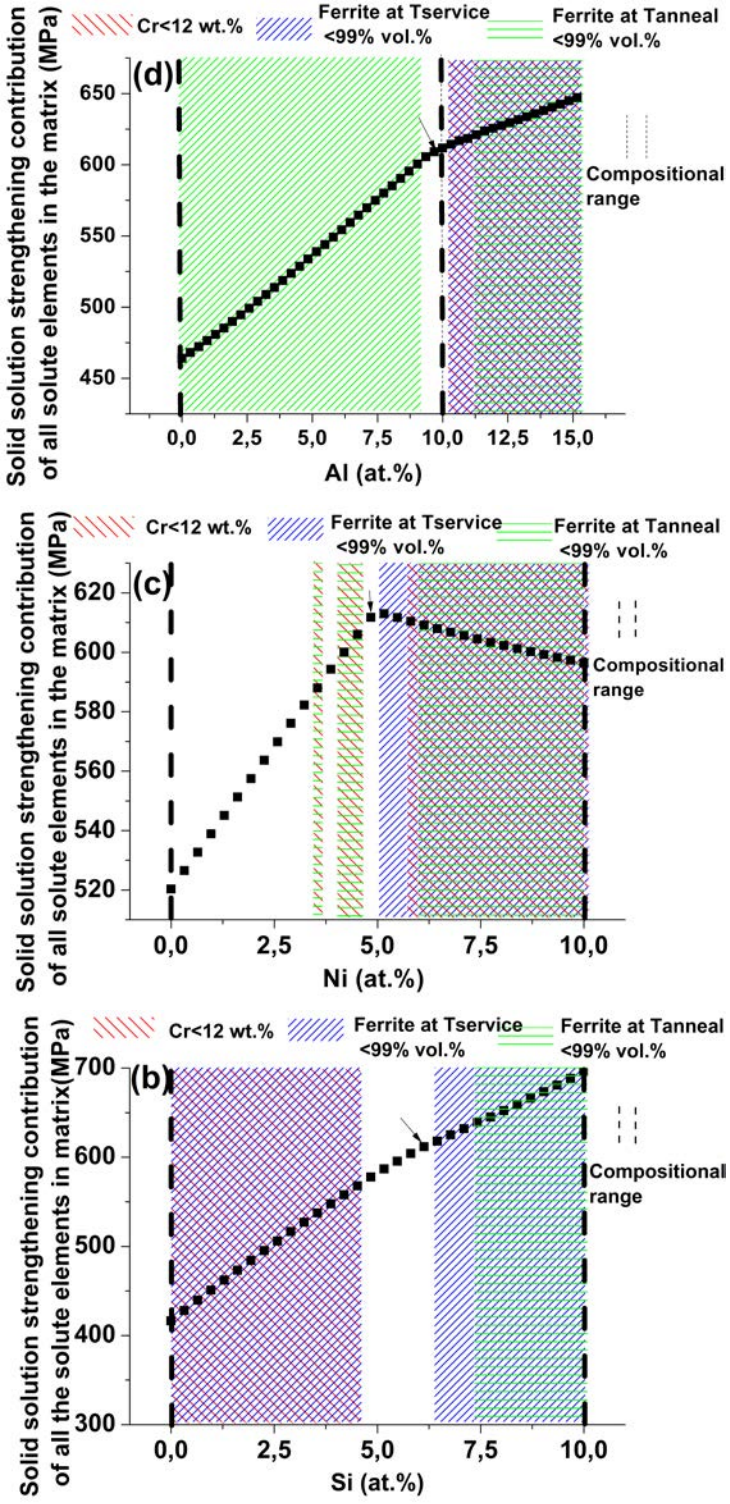
Cr<12 wt.%
Ferrite at Tservice <99% vol.%
Ferrite at Tanneal <99% vol.%
(d)
Solid solution strengthening contribution of all solute elements in the matrix (MPa)
650
600
550
500
450
0,0 2,5 5,0 7,5 10,0 12,5 15,0
Al (at.%)
Compositional range
Cr<12 wt.%
Ferrite at Tservice <99% vol.%
Ferrite at Tanneal <99% vol.%
(c)
Solid solution strengthening contribution of all solute elements in the matrix (MPa)
620
600
580
560
540
520
0,0 2,5 5,0 7,5 10,0
Ni (at.%)
Compositional range
Cr<12 wt.%
Ferrite at Tservice <99% vol.%
Ferrite at Tanneal <99% vol.%
(b)
Solid solution strengthening contribution of all the solute elements in matrix(MPa)
700
600
500
400
300
0,0 2,5 5,0 7,5 10,0
Si (at.%)
Compositional range

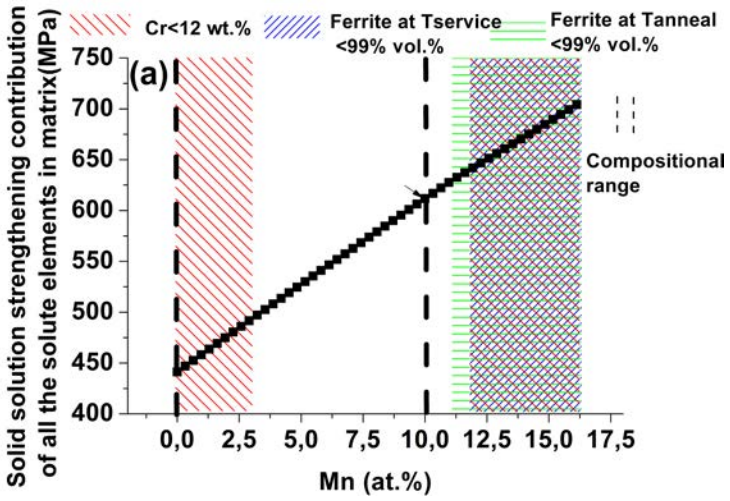

Figure 3.7 Effects of alloying elements Mn (a), Si (b), Ni (c), Al (d) on overall solid solution strengthening contribution taking the composition of alloy Fer-OPT as the baseline. The backward, forward and horizontal slash patterns demonstrate areas not fulfilling the go/no-go criteria of Cr concentration in the ferritic matrix, ferrite volume fractions at service temperature (650 ^{o}C) and at annealing temperature respectively. The two vertical dashed lines in each plot define the ranges of the alloying element applied in the optimization. The arrows indicate concentrations of Mn, Si, Ni and Al in alloy Fer-OPT.

Finally, as indicated in **Figure 3.7**, the robustness of the designed optimal alloy is quite realistic as the allowable concentration windows of Al, Ni, Si and Mn are 1.0, 0.7, 2.9 and 8.0%, respectively. However, to ensure a robust solution considering unavoidable composition deviations during manufacturing, extra calculations with predefined concentration windows for each element (e.g. ±0.01% for C, ±0.10 for Mn) around eligible solution can be performed and enforced as additional go/no-go criteria at a cost of computational effort.

3.5.3 Comparison of the predicted strength of the new alloys with existing steel grades

Figure 3.8 shows the comparison of the strengthening factor for the existing ferritic stainless steel grades and newly designed alloy Fer-OPT. Alloy Fer-OPT shows a significantly higher solid solution strengthening contribution than those of all existing ferritic stainless steel grades. According to the correlation of yield strength and SSSC, as justified in the validation section, the designed alloy would have a high yield strength at

650 ^{o}C assuming other microstructural parameters, e.g. grain size, dislocation densities etc, to be more or less identical as those of the existing ferritic steel grades. It is also interesting to mention that the validation is based on the initial yield strength at 650 ^{o}C. Given the fact that the solid solution strengthening contribution will remain constant in the absence of additional phase transformations, the new alloy is expected to perform well in long-term creep applications.

3.6 Conclusions

A computational alloy design approach, which maximizes the solid solution strengthening, is presented and successfully applied to the design of ferritic heat resistant steel.

1) The optimization and go/no-go criteria used in the computational high temperature ferritic steel design was validated successfully against existing steel grades. The optimisation process was found to be very robust.
2) The new alloys are predicted to have a significantly higher initial yield and final creep strength at 650 °C than existing ferritic steels and not to show unwanted precipitation phenomena.
3) Alloying elements Mn, Al, Si and Ni are found to give the highest strength contribution.
4) The model can be applied to other composition domains and can be expanded to take into account the uncertainties in element concentrations and operating temperatures encountered in industrial practice.

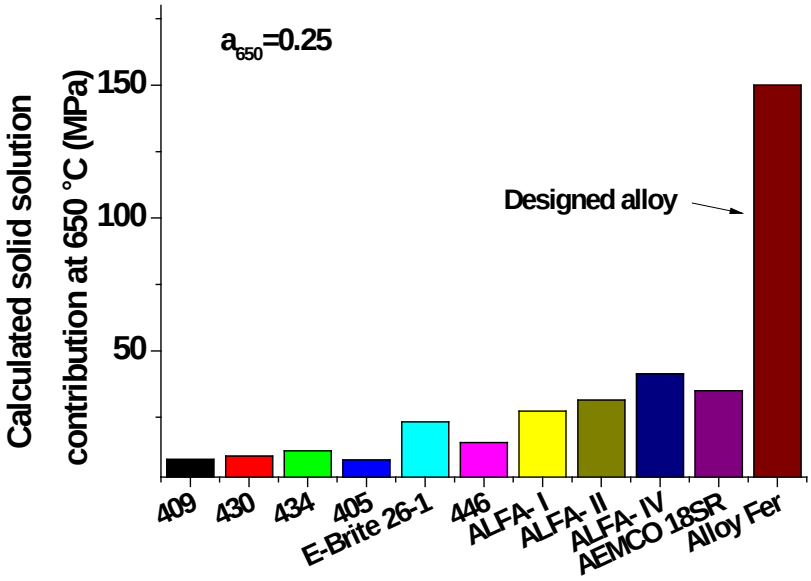

Figure 3.8 Comparison of existing ferritic stainless steel grades and designed alloy Fer-OPT assuming a_{650}=0.25.

References

[1] Masuyama F. History of power plants and progress in heat resistant steels. ISIJ Int. 2001;41:612.
[2] Labusch R. Statistical theories of solid solution hardening. Acta Mater. 1972;20:917.
[3] Labusch R. A statistical theory of solid solution hardening. Phys. Stat. Sol. A 1970;41:659.
[4] Arsenault RJ, Patu S, Esterling DM. Computer simulation of solid solution strengthening in Fcc alloys: Part I. Friedel and Mott limits. Metall. Trans. A 1989;20:1411.
[5] Fleischer RL. Substitutional solution hardening. Acta Metall. 1963;11:203.
[6] Fleischer RL. Solution hardening of BCC metals. Scr. Metall. 1968;2:573.
[7] Suzuki H. Dislocation and mechanical properties of crystals: John Wiley New York, 1957.
[8] Nabarro FRN. The theory of solution hardening. Philos. Mag. 1977;35:613.
[9] Leyson GPM, Hector Jr LG, Curtin WA. Solute strengthening from first principles and application to aluminum alloys. Acta Mater. 2012;60:3873.
[10] Raabe D, Sander B, Friák M, Ma D, Neugebauer J. Theory-guided bottom-up design of β-titanium alloys as biomaterials based on first principles calculations: Theory and experiments. Acta Mater. 2007;55:4475.
[11] Counts WA, Friák M, Raabe D, Neugebauer J. Using ab initio calculations in designing bcc Mg-Li alloys for ultra-lightweight applications. Acta Mater. 2009;57:69.

[12] Zhang H, Johansson B, Vitos L. Ab initio calculations of elastic properties of bcc Fe-Mg and Fe-Cr random alloys. Phys. Rev. B 2009;79:224201.
[13] Zhang H, Johansson B, Ahuja R, Vitos L. First-principles study of solid-solution hardening in steel alloys. Comput. Mater. Sci. 2012;55:269.
[14] Caillard D. A TEM in situ study of alloying effects in iron. II - Solid solution hardening caused by high concentrations of Si and Cr. Acta Mater. 2013;61:2808.
[15] Caillard D. A TEM in situ study of alloying effects in iron. i - Solid solution softening caused by low concentrations of Ni, Si and Cr. Acta Mater. 2013;61:2793.
[16] Terada D, Yoshida F, Nakashima H, Abe H, Kadoya Y. In-situ observation of dislocation motion and its mobility in Fe-Mo and Fe-W solid solutions at high temperatures. ISIJ Int. 2002;42:1546.
[17] Pickering FB. Physical metallurgy and the design of steels. London: Applied Science Publishers LTD, 1978.
[18] Kocks UF, Argon AS, Ashby MF. Thermodynamics and kinetics of slip (Progress in Materials Science) Oxford: Pergamon Press, 1975.
[19] Leyson GPM, Curtin WA. Friedel vs. Labusch: the strong/weak pinning transition in solute strengthened metals. Philos. Mag. 2013:1.
[20] Fleischer RL. The strengthening of metal. New York: Reinhold Press, 1964.
[21] Friedel J. Les Dislocations. Paris: Gauthier-Villars, 1956.
[22] Fleischer RL. Solution hardening by interaction of impurity gradients and dislocations. Acta Metall. 1960;8:32.
[23] Nabarro FRN. The theory of solution hardening. Philos. Mag. 1977;35:613.
[24] Jax P, Kratochvil P, Haasen P. Solid solution hardening of gold and other f.c.c. single crystals. Acta Metall. 1970;18:237.
[25] Čížek L, Kratochvíl P, Smola B. Solid solution hardening of copper crystals J. Mater. Sci. 1974;9:1517.
[26] Lukáč P. Solid solution hardening in Mg-Cd single crystals. Phys. Stat. Sol. A 1992;131:377.
[27] Suzuki H. Dislocations and Mechanical Properties of Crystals. New York: John Wiley, 1957.
[28] Mott NF, Nabarro FRN. Bristol conference of strength of solids. Lodon: Phys. Soc., 1948.
[29] Gypen LA, Deruyttere A. The combination of atomic size and elastic modulus misfit interactions in solid solution hardening. Scr. Metall. 1981;15:815.
[30] Takeuchi S. Solid-solution strengthening in single crystals of iron alloys. J. Phys. Soc. Jpn. 1969;27:929.
[31] Nakada Y, Keh AS. Solid solution strengthening in Fe-N single crystals. Acta Metall. 1968;16:903.
[32] Heslop J, Petch NJ. LXXXVIII. The stress to move a free dislocation in alpha iron. Philos. Mag. 1956;1:866.
[33] Gypen LA, Deruyttere, A. The combination of atomic size and elastic modulus misfit interactions in solid solution hardening. Scr. Metall. 1981;15 815.
[34] Butt MZ, Feltham P. Solid-solution hardening. J. Mater. Sci. 1993;28:2557.
[35] Yasi JA, Hector Jr LG, Trinkle DR. First-principles data for solid-solution strengthening of magnesium: From geometry and chemistry to properties. Acta Mater. 2010;58:5704.

[36] Zhang H, Punkkinen MPJ, Johansson B, Hertzman S, Vitos L. Single-crystal elastic constants of ferromagnetic bcc Fe-based random alloys from first-principles theory. Phys. Rev. B 2010;81:184105.
[37] Leyson GPM, Hector Jr LG, Curtin WA. First-principles prediction of yield stress for basal slip in Mg-Al alloys. Acta Mater. 2012;60:5197.
[38] Patinet S, Proville L. Depinning transition for a screw dislocation in a model solid solution. Phys. Rev. B 2008;78:104109.
[39] Proville L, Patinet S. Atomic-scale models for hardening in fcc solid solutions. Phys. Rev. B 2010;82:054115.
[40] Robert WC, P. Haasen. Physical Metallurgy. Amsterdam, North-Holland: Elsevier, 1996.
[41] Leslie WC. Iron and its dilute substitutional solid solutions. Met Trans 1972;3:5.
[42] Properties and selection: Irons, steels, and high performance alloys, ASM Handbook. Ohio: ASM International, Materials Park, 2005.
[43] Alloy Digest - Data on World Wide Metals and Alloys. Ohio: ASM International, Materials Park, 2010.
[44] Maruyama K, Sawada K, Koike J. Strengthening mechanisms of creep resistant tempered martensitic steel. ISIJ Int. 2001;41:641.

Chapter 4

The design of a compositionally robust martensitic creep resistant steel with an optimised combination of precipitation hardening and solid solution strengthening for high temperature use

4.1 Introduction

In Chapters 2 and 3, two commonly used strengthening mechanisms, precipitation hardening and solid solution strengthening, are optimized in the design of austenitic and ferritic heat resistant steels, respectively. Combining both strengthening mechanisms in one alloy will be even better to reach high strength values in real steels. In this Chapter, precipitation hardening and solid solution hardening are optimally combined in new 9- 12 % Cr martensitic steels for high temperature applications.

9-12% Cr martensitic steels are widely applied in boiler and turbine components in coal-fired ultra-supercritical power plants owing to their good performance at operating temperatures up to 600°C [1]. Nevertheless, a higher operating temperature, such as 650 °C, would be desirable to increase the efficiency of electricity generation and to decrease the CO_2 emission. However, the microstructural stability of existing creep steel grades during long term exposure at elevated temperatures is still insufficient. Much effort has been devoted to the development of new martensitic creep resistant steel with improved creep strength and a decent stability during long term use [2-11].

Kimura's research [12, 13] on ferritic creep resistant steels has shown that at very long times the creep strength reaches a constant value. This inherent strength was taken to be due to the matrix Solid Solution Strengthening (SSS) only as all Precipitation Hardening (PH) contributions (no MX carbonitrides were present in these steels) had disappeared as a result of coarsening [13]. For very long service times and high use temperatures other strengthening mechanisms such as work hardening, lath size strengthening can also be ignored [13]. Hence an ideal creep resistant steel has a matrix with a high degree of solid solution strengthening and contains a high volume fraction of precipitates with an extremely slow coarsening rate. Furthermore, such an ideal steel should have a microstructure free of undesirable phases.

Nano-sized MX carbonitrides are known to have a very slow coarsening rate and their formation and coarsening rates were shown to explain the creep behaviour of 9-10 wt% Cr ferritic steels as a function of temperature and time [14]. The optimal precipitation hardening effect is achieved mainly by tuning the precipitate forming elements and their concentrations. For example, experimental results have shown that different combinations of MX carbonitride formers, i,e, C, N, Nb, V and Ti, determine the precipitation size, volume fraction, coarsening rate and distribution of precipitates etc, which ultimately determine the microstructural stability and time dependent creep strength [3, 7, 11, 15]. However, computational investigations suggest that the coarsening rate of MX carbonitrides could be 1000 times lower by tuning all alloying elements, also those remaining in solid solution in the matrix, simultaneously [16, 17]. Other precipitates, such as $M_{23}C_6$ carbides[4], Z Phase[18], Laves Phase[19, 20] display similar strengthening effects. The initial precipitate size and coarsening rate of $M_{23}C_6$ carbides are much bigger and higher than those of MX carbonitride [21], although addition of B and Co, not being part of the precipitate itself, has been reported to moderately decrease their coarsening rate [22-24]. The Z Phase and Laves Phase generally precipitate only after long term exposure and are traditionally considered as detrimental phases in creep resistant steels. However, their formation can be accelerated by tuning the levels of Z or Laves Phase forming elements [25], such as Cr and Nb, and adjusting the heat treatment parameters. Moreover, such intentionally created Z-phase and Laves phase precipitates display more desirable morphologies and distributions, and thus strengthen the materials [18-20]. While precipitation hardening clearly is an effective way to increase the creep strength of steels, the unavoidable precipitate coarsening process invariably leads to a lowering of the creep strength with time and temperature. In contrast, solid solution strengthening depends on temperature but is essentially time independent. W and Mo are the common elements to increase the solid solution strength of martensitic creep resistant

steels [26, 27]. Addition of 2.3 wt.% W in a α iron solution with 0.001 wt.% C can decrease the creep strain rate by a factor 100 or more [26]. However, the W and Mo concentrations present in the matrix at an early stage drop considerably due to the precipitation of W and Mo enriched Lave phase after a long term exposure at high temperatures [28]. Recently Al, Ni, Mn and Si have been proposed as more stable elements to improve the strength of ferritic matrix for long term application [29]. Some early research has been done to quantify the contributions of PH and SSS separately and then to calculate their combined effects on alloy strength [30, 31]. However, such an approach does not automatically lead to optimal results as the effect of individual chemical elements on the final creep strength is far from simple because of many complex interactions between different alloying elements and the resulting influences on the two principal strengthening mechanisms PH and SS. For example: i) additions of elements contributing to SSS could thermodynamically and kinetically influence the volume fraction, size, coarsening rate of desirable precipitates; ii) additions of elements contributing directly or indirectly to PH could change the solubility of all elements in the matrix and hence the SSS; iii) additions of either PH or SSS elements could change the entire thermodynamics and may promote the formation of undesirable microstructural components. Finally, the sum of all alloying elements may be such that neither a fully austenitic homogenisation state nor a fully martensitic state upon quenching can be obtained.

Clearly, simultaneously maximizing these two strengthening mechanisms in complex multi-component 9-12% Cr martensitic steel systems by *a priori* tuning the concentration of each element concentration and ascertaining a fully martensitic microstructure with a resulting fine grain size and high dislocation density remains an unsolved scientific challenge. The coupled thermodynamic/genetic algorithm design concept explored in this thesis is used to identify the composition of a martensitic creep resistant steel grade ideally suited for long term application at a target temperature of 650 ^{o}C. The new steel has an optimal combination of significant precipitation hardening due to slowly coarsening MX carbonitrides and a high degree of solid solution strengthening. The defined composition does not lead to the formation of undesirable phase fractions and results in a steel with a fully martensitic microstructure. However, with such an ideal composition defined in high precision, it may not be possible to actually produce such a steel, as in the industrial practise it is impossible to reach the exact concentration level for each of the alloying elements simultaneously. Small compositional deviations may lead to large changes in microstructure and creep behaviour. To account for this, the model is modified such that for the final target steel composition the intended creep properties are

largely maintained if the actual steel composition deviates within the usual industrial margins from the target composition.

4.2 Methodology

4.2.1 Design methodology

A comparable design methodology as described in Chapter 2 is used in this chapter too. The required properties of creep resistant steels, such as a high creep strength after a long exposure time (> 10^5 h), good thermal stability and decent oxidation/corrosion resistance at a service temperature of 650 °C, need to be translated into microstructural features using known microstructure-property relationships. Both PH and SSS are considered and maximized simultaneously to improve the long term creep strength. Once again, the flow chart of the revised program is shown in **Figure 4.1.**

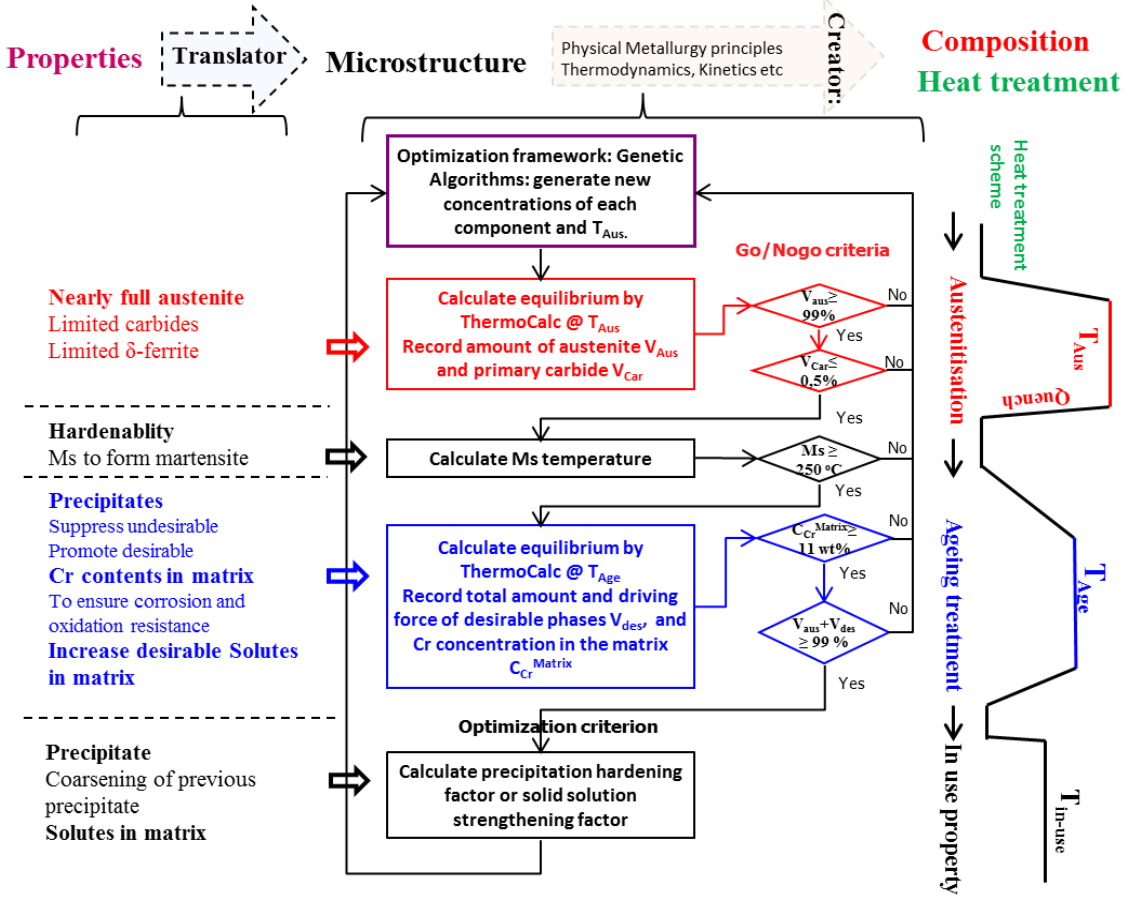

Figure 4.1 Alloy design strategy and evaluation criteria for high PH and/or SSS martensitic creep resistant steels.

Martensite is chosen as the (initial) microstructure for the matrix because of its good creep strength and its high resistance to thermal and creep fatigue during service in power plants as a result of its low thermal expansion coefficient and high thermal conductivity [27]. As mentioned in the introduction, MX carbonitrides are selected as the main strengthening particles in the new steels because of their small initial size and more importantly their extremely low coarsening rate [11]. The martensitic matrix is to be strengthened even further by SSS. Thus, the target microstructure is defined as: 1) a fully martensitic matrix with a high degree of SSS; 2) a high volume fraction of MX carbonitrides with a guaranteed very low coarsening rate over its intended life time and 3) a limited volume fraction of undesirable phases. Subsequently, the creator links the above descried microstructural features to a specific composition and related heat treatment parameters by employing various go/no-go criteria, and various thermodynamic and kinetics considerations. Finally, all qualified solutions fulfilling all go/no-go criteria are ranked according to the optimization criterion: PH factor, SSS factor or a proper combination thereof.

4.2.2 Defining the optimization criterion: PH factor and SSS factor

As the units of the PH and the SSS optimisation factors are different, the predicted strength contributions are not simply numerically additive. Hence, we first optimise the PH and SSS independently. Then all qualified solutions from the two independent optimisations are plotted together as PH versus SSS, from which a 'Pareto front' can be constructed [32]. A Pareto front is a curve where the critical information of two conflicted properties is presented graphically. From the curve one can derive the best possible trade-offs between PH and SSS.

The PH is determined by the precipitate particle size, its density and its distribution[33], and depends on the initial condition and the evolution during service. The service temperature and time considered in the present study are high and long enough to result in considerable coarsening, and hence lead to relatively large particles. For such precipitates, the climb strengthening mechanism is the most relevant and its contribution as a function of time and temperature can be estimated by Equation 2.2. The details of Equation 2.2 can be found in section 2.2.3. The time and temperature dependent inter-particle spacing of MX carbonitrides is taken as the PH optimisation parameter. In this study the service time is set at 10^5 h in order to obtain application relevant results. The factor $1/L$ (Equation 2.2) will be called the 'PH factor'.

SSS arises from the interaction of dislocations and solute atoms. Generally, SSS can be described as a function of atomic concentration of solutes [34]. the SSS contribution in the multi-component ferritic matrix is expressed by Equation 3.4. Other details about this expression can be found in section 3.2.3. In the present study, only long term creep properties are considered, and the martensitic matrix is equivalent to ferritic matrix after such a long service time. Therefore, the stress σ_{ss} from Eq. 3.4 can be used for martensitic steels and is called SSS factor.

4.2.3 Defining the go/no-go criteria

To obtain the targeted microstructure and to avoid undesirable microstructural components, various go/no-go criteria are defined and applied in the order of the (simple) thermal treatments the steels are to receive. In MX carbonitrides precipitation-hardened martensitic creep-resistant steels, the typical heat treatment includes an austenisation/solution treatment to dissolve undesirable primary carbonitrides and to achieve compositional homogeneity, followed by a tempering treatment to form desirable MX carbonitrides. In the present study we are dealing with steels for very long term applications and the final precipitate state after long term service will be much closer to the equilibrium state at the service temperature rather that at the tempering temperature. Therefore, in the present study the tempering temperature is set at the service temperature (650 °C).

Three go/no-go criteria are imposed at the start of the evaluation cycle for each candidate solution (1) the equilibrium austenite volume fraction at the austenisation temperature T_{aus} should be larger than 99%;(2) the amount of primary carbides should be less 0.5% in volume since primary carbides are known to have a very detrimental effect on the creep resistance [35];(3) liquid phase and delta phase should be absent at T_{aus}. Delta phase is taken as undesirable phase in this study since it is known to decrease the creep strength and toughness of martensitic steels [26];

After austenisation, martensitic creep steels are generally quenched to room temperature, and the austenite should completely transform to martensite. To make sure the amount of residual austenite is at a low level, the steel should have a relatively high martensite start temperature. Therefore, a fourth go/no-go criterion in the evaluation cycle is imposed: (4) the Martensite start (T_{Ms}) temperature should be higher than 250^{o}C. For each candidate alloy composition, the Ms temperature is calculated by eq. 2.5.

After quenching to room temperature, the alloy is used at its service/ageing temperature. Hence a second set of themodynamic calculations at the service temperature is performed. Three additional go/no-go criteria at this use temperature are enforced: (5) The total amount of non-desirable precipitates, i.e. all precipitates not being MX carbonitrides, Ni3Ti/NiAl intermetallic should be less than 1 vol%. Here, the Laves Phase and the Z Phase are considered as undesirable phases because of their very high coarsening rates. (6) The concentration in the matrix upon completion of the precipitation reactions should at least be 11 wt.% Cr to ascertain adequate corrosion and oxidation resistance. Existing 9 wt.% Cr steels do not have enough Cr in the matrix for the application at 650 °C, and thus a higher amount of Cr is needed to improve the corrosion and oxidation resistance. A justification of the arbitrary limit value of 11 wt.% is given in section 4.3.2.

4.2.4 Search ranges and genetic algorithm

The chemical elements to be varied within their allowed concentration ranges and the range of austenisation temperatures to be explored, are listed in Table 4.1. The service temperature is fixed at 650 ^{o}C.

Table 4.1 Search ranges (in wt.%) for 9 chemical elements and the range for the austenisation temperature T_{aus} (in ^{o}C).

	C	*Cr*	*Ni*	*Ti*	*Mo*	*Al*	*Co*	*Nb*	*N*	*V*	*Fe*	T_{aus}
Min.	0.001	8.00	0.001	0.001	0.001	0.001	0.001	0.001	0.001	0.001	Bal.	900
Max.	0,15	16.00	15.00	5.00	10.00	5.00	10.00	5.00	0.15	5.00		1250

The genetic algorithm optimisation framework is unchanged and details can be found in section 2.2.5.

4.3 Validation

4.3.1 Validation of PH and SSS factors

As stated in the introduction, in the current model the long term creep strength is taken to be solely determined by the solid solution strength SSS of the matrix plus the PH contribution of MX carbonitrides. To validate this assumption, compositions of a variety

of existing 9-12 % Cr martensitic steels, as listed in Table 4.2, were evaluated to calculate the PH factor of MX carbonitrides and the SSS contribution according to Eq. 2 and 6 respectively. The calculated results are compared with the corresponding experimental creep strength values and are shown in **Figure 4.2**. The SSS factor was calculated directly from the nominal chemical composition, as the volume fraction of ferrite at the service temperature was in excess of 0.99 according to Thermo-Calc calculations. The SSS contributions of Cu, Nb, B, Ta and Nd have been neglected for reasons stipulated earlier.

Table 4.2 Compositions of analysed 9-12% Cr martensitic steels (in wt.%)

Code	Alloy	C	Cr	Ni	Mo	Al	Cu	Co	Nb	N	V	Mn	Si	W	Others
A	9Cr1Mo	0.12	9.00	0	1.00	0	0	0	0	0	0	0.45	0.60	0	
B	9Cr2Mo	0.07	9.00	0	2.00	0.01	0	0	0	0	0	0.45	0.50	0	
C	12Cr1MoV	0.20	12.00	0.50	1.00	0	0	0	0	0	0.25	0.60	0.40	0	
D	12Cr1MoWV	0.20	12.00	0.50	1.00	0	0	0	0	0	0.25	0.60	0.40	0.50	
E	9Cr0.5Mo2WVNb	0.07	9.00	0	0.50	0	0	0	0.05	0.06	0.20	0.45	0.10	1.80	0.004 B
F	9Cr1MoVNb	0.10	9.00	0	1.00	0	0	1.00	0.08	0.05	0.20	0.45	0.40	0	
G	11Cr3W3CoVNbTaNdN	0.10	11.00	0	0	0	0	3.00	0.10	0.04	0.20	0.20	0.30	3.00	0.07Ta. 0.04Nd
H	12Cr0.4Mo2WCuVNb	0.11	12.0	0	0.40	0	1.00	0	0.05	0.06	0.20	0.60	0.10	2.00	
I	12Cr0.6Mo0.3V0.4NbN	0.15	11.50	0.75	0.55	0	0	0	0.30	0.06	0.28	0.80	0.20	0	
j	12Cr1Mo1WVNb	0.10	12.00	0	1.00	0	0	0	0.05	0.03	0.25	0.55	0.30	1.00	0.004B

Figure 4.2a shows the experimental (10^4 hour) creep strength versus the calculated SSS factors of the 9-12 % Cr martensitic steels listed in Table 4.2. It is quite clear that the data can be divided into two groups: group I at the lower right of the plot (shaded in blue) and group II at the upper left of the plot (shaded in green). Interestingly, all four alloys (A-D) in group I have no MX carbonitrides, while all six alloys (E-J) in group II are predicted to contain MX carbonitrides. Therefore, alloys in group I have only the SSS contribution, while alloys in group II have both the SSS and PH contributions. Alloys from group I show a very good linear correlation between the creep strength at 10^4 h and the calculated SSS factor, which is in agreement with the fact that SSS is the only strengthening mechanism in 9-12 % Cr martensitic creep resistant steels without MX carbonitrides after a such long service time. This also confirms the conclusion of Kimura [12]. However, other six alloys in group II do not follow the linear correlation because of the additional strength contribution from MX carbonitrides. In order to further analyse the contribution of PH due to MX carbonitrides, the calculated PH factors of MX carbonitrides after 10^4 h for all six alloys are compared to the creep strength of 10000 h after correction for the SSS contributions as indicated in **Figure 4.2a.**The results are shown in **Figure 4.2b**. With the exception of steel grade I now a very good correlation is obtained, showing that after

10^4 h PH due MX carbonitrides, on top of the basis SSS value, can still be effective. The deviation of steel grade I may originate from the transformation of the strengthening MX carbonitrides to Z phases.

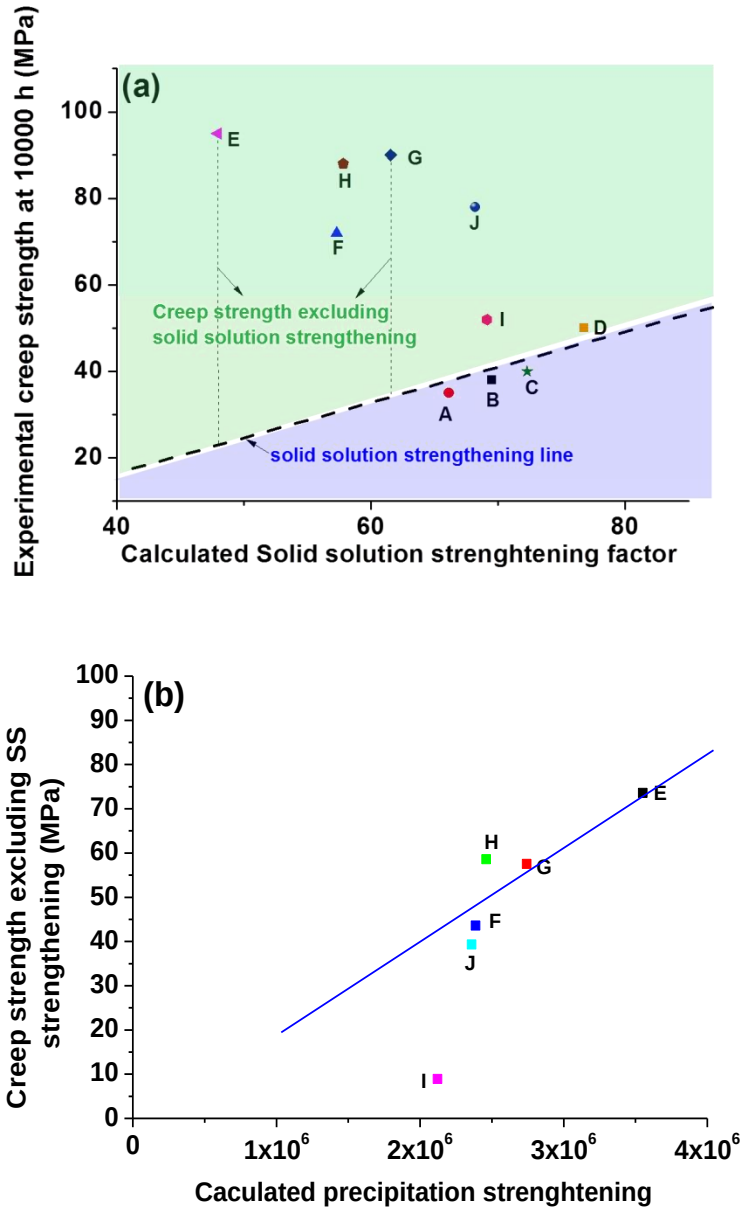

Figure 4.2 (a) Experimental creep strength at 10^4 h [36] versus calculated SSS factor of various existing 9-12% Cr martensitic steels and (b) comparison of calculated PH of MX carbonitrides at 10^4 h and corresponding creep strength excluding SSS contributions. The symbols correspond to the alloy codes given in Table 4.2.

Summarising: the long term creep strength of existing 9-12 % Cr steels can be well described as a sum of MX carbonitrides PH and SSS. The PH factor and SSS contribution as calculated by Equations 2 and 6 respectively, are able to represent the actual PH and SSS for long term creep strength in 9-12 % Cr martensitic steels.

4.3.2 Validation of the go/no-go criteria

To demonstrate the validity of the go/no-go criteria employed, thermodynamic calculations are performed for the compositions of existing alloys (see Table 4.2) both at the austenisation and the service temperature, and results are shown in **Figure 4.3**. The dashed lines in **Figures 4.3a – 4.3d** define the minimum required values of go/no-go criteria for Ms temperature, austenite volume fraction at austenisation temperature, ferrite volume fraction at service temperature and Cr concentration in the matrix, respectively. **Figures 4.3a and 4.3c** show that existing steels generally meet the go/no-go criteria for Ms temperature and ferrite volume fraction at service temperature. **Figure 4.3b** shows that some of the existing 11-12 wt.% Cr steels do not meet the go/no-go criterion for austenite volume at the austenisation temperature (due to the presence of delta phase), yet the 9% Cr steels meet the imposed go/no-go criterion very well. The presence of delta phase, consistent with experiment observations, is due to the higher Cr concentration in 11-12% Cr steels which promotes the formation of delta phase at the austenisation temperature. **Figure 4.3d** shows that the employed minimum target value for Cr content in the matrix upon completion of precipitation is generally higher than the level in existing alloys designed to operate at 600 ^{o}C or lower temperatures. The mismatch is as expected since the target value was set to a high value to obtain a decent oxidation and corrosion resistances at the higher temperature of 650°C.

4.4 Model application

As mentioned in section 2, two optimisation routes are implemented, either to solely optimise PH due to MX carbonitrides, or to optimise solely for SSS. However, for each candidate composition meeting the go/no-go criteria, also a value for the non-optimised strengthening contribution will be obtained. The PH and SSS factors of all accepted candidate solutions (around 42,000 solutions) are recorded and stored for further analysis. The results are shown in **Figure 4.4**. The black dots represent solutions obtained by optimising PH at 10^5 h, and the red dots are solutions obtained by maximizing SSS in the matrix. In addition, the dot indicated by the green rectangle is the solution of the highest PH, while the dot enclosed by the blue circle is the solution with a maximal SSS. Clearly,

neither of these two solutions meets the design target of the present study, i.e. an optimal combination of PH and SSS. To obtain the optimal combination, a 'Pareto front' can be constructed in **Figure 4.4**, which is indicated by the dashed curve. The best combination of PH and SSS can be found at the turning point of the Pareto front, indicated by the purple arrow. This solution has only slightly lower PH and SSS factors than the separate maxima respectively.

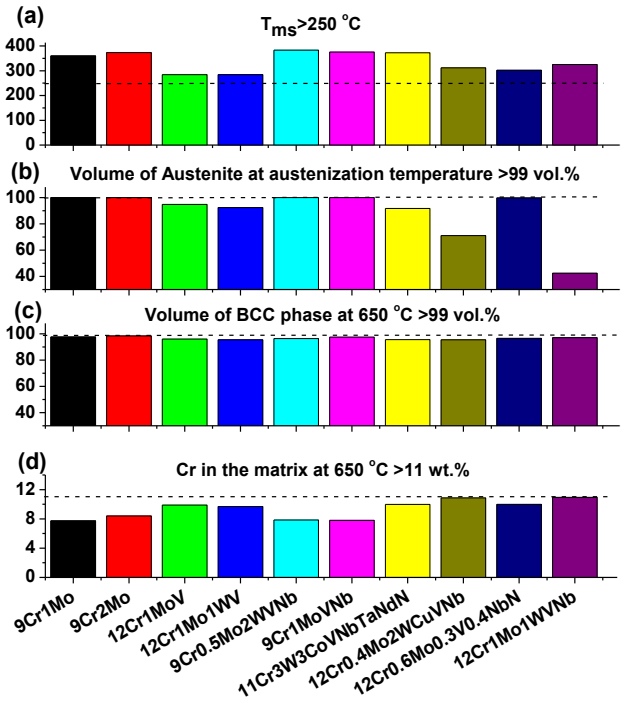

Figure 4.3 Fulfilments of go/no-go criteria of existing 9-12% Cr martensitic steel. (a) Ms temperature, (b) austenite volume fraction at their reported austenisation temperatures, (c) ferrite/martensite volume fraction at service temperature of 650°C, (d) Cr weight percentage in the ferritic/martensitic matrix at 650°C. The black dashed lines indicate the minimum values of the go/no-go criteria.

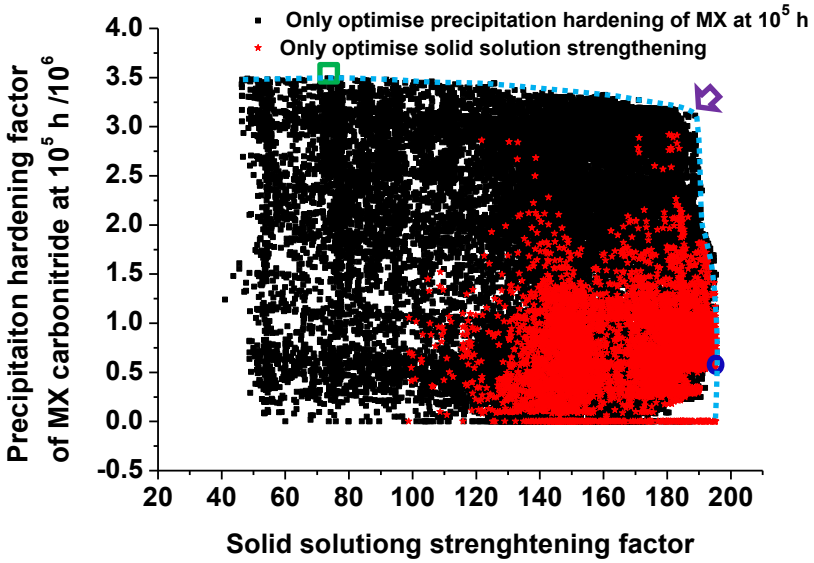

Figure 4.4 PH factor of MX carbonitrides at 10^5 h versus SSS factor of solutions meeting all go/no-go criteria from both PH and SSS driven optimisations.

The chemical compositions, austenisation temperatures and calculated strengthening factors for the three mentioned solutions are listed in Table 4.3. The alloys with the best PH, the best SSS, and the best combination are labelled as Alloy PH, Alloy SSS and Alloy PHSS, respectively. These alloys generally possess 11-12 wt.% Cr and 8-10 wt.% Co. The high Co level is necessary to keep a high Cr level in the matrix and to obtain a fully austenitic matrix at the austenisation temperature. Moreover, Alloys SSS and PHSS have much higher Ni and Al concentrations than those of Alloy PH so as to achieve a higher SSS while Alloys PH and PHSS possess similar levels of MX carbonitrides formers C, N, Ti, Nb and V in order to reach an optimal PH, and the level are have much higher than in Alloy SSS. These observations demonstrate that the current alloy design approach is capable of balancing complex interactions in a multi component system and can be used to achieve a global trade off between PH and SSS.

Table 4.3 Compositions of three designed alloys (in wt.%), austenisation temperatures T_{aus} (in °C), SSS factors (SSSF) and PH factors (PHF) at 650 °C.

	C	Cr	Ni	Ti	Mo	Al	Co	Nb	N	V	T_{aus}	SSSF	PHF
Alloy PH	0.064	11.10	0.010	0.17	0.001	1,45	10.00	0.324	0.020	0.001	1250	77.41	3.49E+6
Alloy SSS	0.097	12.39	3.88	0.010	0.97	3.71	10.00	0.485	0.001	0.001	1137	195.46	7.26E+5
Alloy PHSS	0.068	11.10	4.36	0.17	0.001	3.71	8.71	0.324	0.015	0.001	1250	188.85	3.11E+6

4.5 Discussion

4.5.1 Properties of the Pareto front

The construction of a Pareto front can guide and accelerate the optimization of two competing properties. However, the best choice is not necessarily the solution at the turning point and its actual position may vary along the Pareto front depending on the nature of the two properties. In this study, the Pareto front consists of a large number of solutions of different combinations of PH and SSS, and any of these combinations has its own chemical, thermodynamic and creep strength characteristics. The character of the data points on the Pareto front is discussed in detail in the next sections.

4.5.1.1 Evolutions of the coarsening rate, volume fraction of MX carbonitrides on the Pareto front

As shown in Equation 2, the initial volume fraction and the coarsening rate of MX carbonitrides together determine the value of the PH factor, and thus the location of the Pareto front. The values for these two parameters for data points along the Pareto front are calculated and colour coded plotted in **Figures 5a** and **5b**, respectively. On the nearly horizontal part of the Pareto front, the volume fraction and coarsening rate of MX carbonitrides are kept at the highest and the lowest values, respectively, leading to high PH factors. On the vertical part of the Pareto front, the volume fraction of MX carbonitrides doesn't change much but are significantly lower than those for data points on the horizontal part of the Pareto front. In contrast, the coarsening rate of MX carbonitrides increases significantly in the downward direction, yielding significant decrease of PH factor on the vertical part of the Pareto front. To further analyse the PH stability, the PH factors at an even longer service time, 10^6 h, are calculated for solutions on the Pareto front, and the results are shown in **Figure 4.5c**. The Pareto front retains its shape but at much lower PH values, while SSS keeps the same value as it is a time independent parameter. It is important to point out that the upper part of the Pareto front still remains nearly horizontal which indicates that the solution of the global optimization PHSS is stable and Alloy PH is also likely to be a good solution for 10^6 h. Constructing a new Pareto front by running a new optimization with a PH factor for 10^6 h may lead to a slight gain in PH factor value but is not expected to change the solution notably [17].

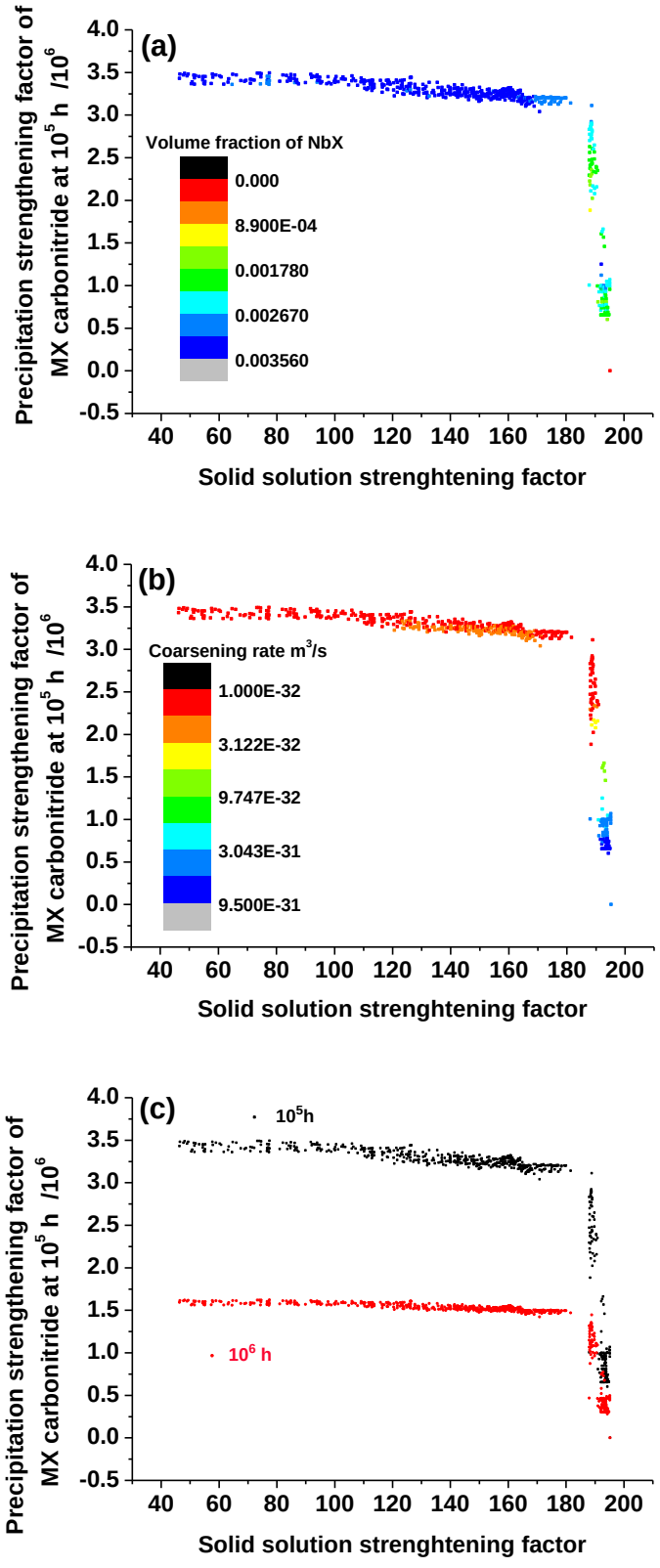

Figure 4.5 Properties values for volume fraction (a), coarsening rate (b) on the Pareto front, and the comparison of PH factors at 10^5 and 10^6 h (c).

4.5.1.2 The effect of changes in alloying element concentrations and austenisation temperature on the Pareto front

Alloying element concentrations and heat treatment parameters determine the volume fraction and coarsening rate of MX carbonitrides, and eventually the location of the Pareto front. The dependences of the Pareto front on C, Ni, Al, Mo, Nb, N concentrations and the austenisation temperature are graphically presented in **Figure 4.6**. In **Figure 4.6a**, a clear transition in C concentration can be observed around turning point: in the horizontal part of the Pareto front a slight increase of C leads to a limited decrease of PH factor. However, the PH factors drop significantly on the vertical segment of the Pareto front when the concentration of C increases further. Clearly there is an optimal concentration of C to achieve an optimal combination of PH and SSS. **Figure 4.6b** shows that the Mo concentration needs to remain low for a high PH factors while a higher concentrations is required to achieve higher SSS at the cost of a significant decrease PH. It is interesting to point out that, although Mo is quite an effective solid solution strengthening element as indicated in Table 3.1, the further increase of Mo does not increase SSS considerably as it results in the precipitation of Laves phases or Mu phase. On the contrary, Al and Ni have great capacities to improve SSS without sacrificing PH, as shown on the nearly horizontal part of the Pareto front in **Figure 4.6c** and **6d,** respectively. Higher concentrations of Al and Ni are desirable to achieve a better combination of PH and SSS. The Al effect is in agreement with reported experimental observations [37]. Fig. 4.6e shows that relative low concentrations of Nb keep PH factors at high levels on the nearly horizontal part of the Pareto front. Low concentrations of Nb stimulate positive effects on volume fraction and coarsening rate of MX carbonitrides. N does not have a simple clear effect on the Pareto front, as shown in Fig. 4.6f, owing to complex interactions with other elements. This lack of a simple clear correlation also applies to Co, Cr, Ti and V and these are not plotted here. **Figure 4.6g** shows the effect of the austenisation temperature on the Pareto front. Clearly, a high austenisation temperature is needed for potential alloys having a high PH factor, while solutions with lower PH generally require a lower austenisation temperature. The metallurgical explanation for this dependence is found in the need to dissolve a larger amount of primary carbides and/or carbonitrides at higher temperatures thereby increasing the secondary MX carbonitrides formation during ageing and service.

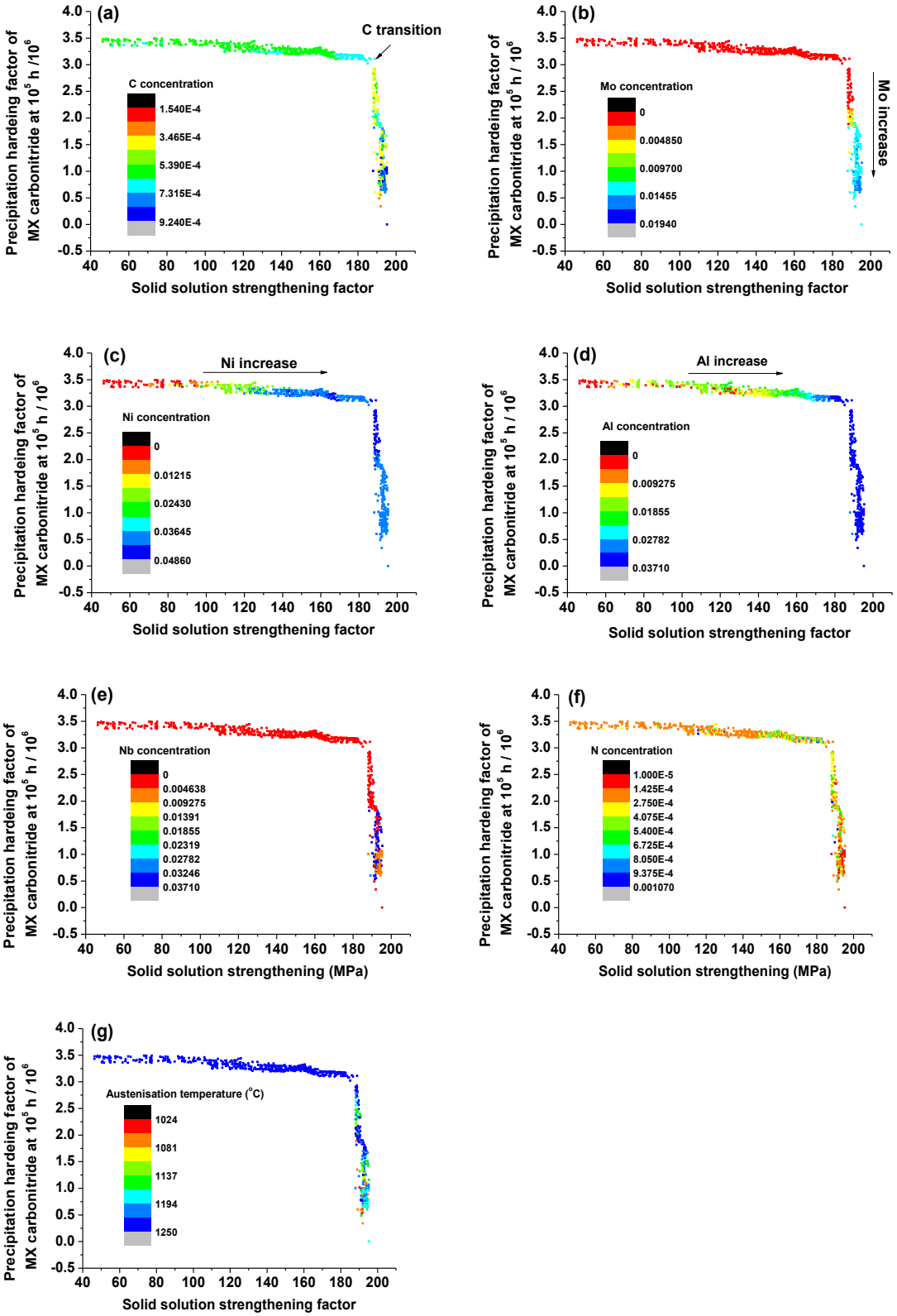
(a)
C transition
C concentration
1.540E-4
3.465E-4
5.390E-4
7.315E-4
9.240E-4
Precipitation hardeing factor of MX carbonitride at 10^5 h /10^6
Solid solution strengthening factor
(b)
Mo concentration
0
0.004850
0.009700
0.01455
0.01940
Mo increase
Precipitation hardeing factor of MX carbonitride at 10^5 h / 10^6
Solid solution strengthening factor
(c)
Ni increase
Ni concentration
0
0.01215
0.02430
0.03645
0.04860
Precipitation hardeing factor of MX carbonitride at 10^5 h / 10^6
Solid solution strengthening factor
(d)
Al increase
Al concentration
0
0.009275
0.01855
0.02782
0.03710
Precipitation hardeing factor of MX carbonitride at 10^5 h / 10^6
Solid solution strengthening factor
(e)
Nb concentration
0
0.004638
0.009275
0.01391
0.01855
0.02319
0.02782
0.03246
0.03710
Precipitation hardeing factor of MX carbonitride at 10^5 h / 10^6
Solid solution strengthening (MPa)
(f)
N concentration
1.000E-5
1.425E-4
2.750E-4
4.075E-4
5.400E-4
6.725E-4
8.050E-4
9.375E-4
0.001070
Precipitation hardeing factor of MX carbonitride at 10^5 h / 10^6
Solid solution strengthening (MPa)
(g)
Austenisation temperature (°C)
1024
1081
1137
1194
1250
Precipitation hardeing factor of MX carbonitride at 10^5 h / 10^6
Solid solution strengthening factor

Figure 4.6 Concentration effects of (a) C, (b) Mo, (c) Al, (d) Ni, (e) Nb, (f) N and the austenisation temperature T_{aus} (g) on the Pareto front. All concentrations are weight fractions.

4.5.2 Compositional robustness

Minor deviations from the intended chemical composition are unavoidable in an industrial steel production setting and hence the compositional robustness of the optimal composition is a very important, yet hitherto not yet addressed, aspect in model-based alloy design. For a robust solution all go/no-go criteria should still be fulfilled as long as the composition fluctuates within the allowed compositional scatter range and the predicted long term creep strength should not drop significantly. To explore the compositional stability of the optimal solution, we defined compositional fluctuation ranges for each of the relevant chemical elements and the austenisation temperature (see Table 4.4). Then, 20 additional calculations were performed in which one of the parameters was set to the lowest or the highest value of the scatter regime, while the other parameters were kept at the intended values. In case the combination of the optimal concentration and the allowed scatter would result in a negative concentration, the minimal concentration was set to zero. The results of such a test in which Alloy PHSS was taken as the baseline is shown in **Figure 4.7**. Blue and red symbols in the plot represent compositions meeting or not-meeting all go/no-go criteria, respectively. The positive and negative deviations of concentrations are indicated by "+" and "–" in the symbols, respectively. The figure shows that the allowed fluctuations in composition, either lead to a loss in PH factor or make the solution not meeting all requirements. All qualified solutions (blue dots) are located within the Pareto front, yet at a lower combination of both strengthening parameters, indicating the robustness of the optimisation. The effects of compositional fluctuations on the Ms temperature, the volume fractions of delta phase, the primary carbide and the austenite fraction at austenisation temperature and the volume fraction of the ferrite phase at the service temperature were calculated and results are listed in Table 4.5. For alloy PHSS, the main non-fulfilled criterion is the formation of delta phase. Its volume fraction increases significantly by either decreasing concentrations of C, N, Co and Ni, or by increasing the concentrations of Al, Cr, Mo, Nb and V. Such a result is as expected since the former elements are austenite stabilizers and the latter ones are ferrite stabilizers. The analysis clearly demonstrates that the composition of the ideal Alloy PHSS is very close to the forbidden delta phase zone. Hence, from an industrial perspective the robustness of the ideal PHSS alloy is not good and small variations in the concentrations of several

alloying elements would lead to the formation of an unwanted microstructural component and hence a marked drop in long term creep strength.

Table 4.4 The range of allowed concentration fluctuations for the alloying elements considered (in wt.%).

	C	Cr	Ni	Ti	Mo	Al	Co	Nb	N	V
Deviation(±)	0.01	0.10	0.10	0.05	0.05	0.05	0.05	0.05	0.01	0.05

The direct effect of compositional fluctuations on the values of both strengthening factors is also of great importance. As shown in **Figure 4.7**, for the allowed concentration fluctuations the resulting variations in SSS factor are relatively small (less than 1%). In contrast, very significant changes can be found in PH factor, especially caused by variations of MX carbonitrides former, i.e. C, N, Nb, Ti. To further clarify their effects on PH factor, the volume fraction and coarsening rate of MX carbonitrides are calculated and shown in Table 4.5. Clearly, the volume fraction always decreases regardless of the direction of the concentration change, which suggests that the nominal value is a local optimum. Moreover, dramatic increases of coarsening rate occur for the lower concentrations of C and N, and the higher Ti and Nb concentrations. Both a lowering of the precipitate volume fraction and that of the coarsening rate weaken the PH factor, the latter being more dominant.

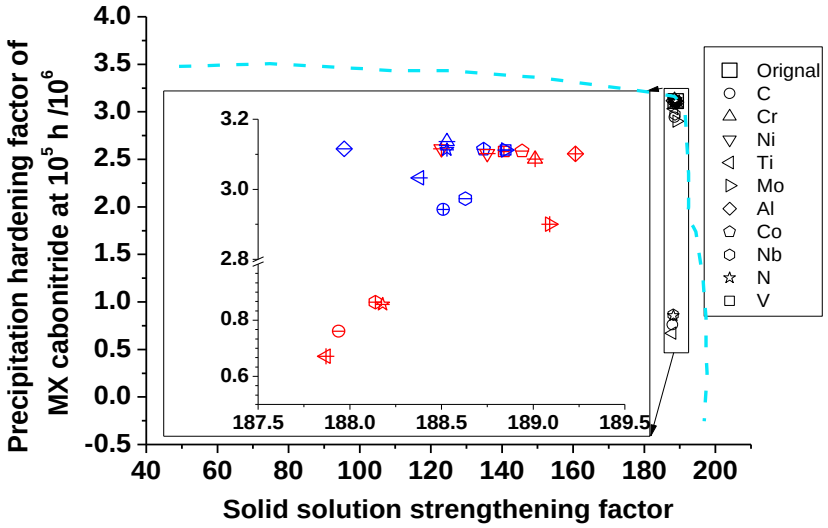

Figure 4.7 The compositional effects on PH factor, SSS factor and the fulfilment of go/no-go criteria. Blue and red symbols represent fulfilment and non-fulfilment of all go/no-go criteria, respectively. The positive and negative deviations of concentrations are indicated by "+" or "–" in the symbols respectively.

Table 4.5 Values for the various Go/nogo criteria for the composition of Alloy PHSS for minimal and maximal allowed concentration fluctuations. *at the austenisation temperature, # at service temperature, VP: volume percent, MX: MX carbonitride, CR: creep rate. The values meaning that the critical values for go/no-go criteria are not met are recorded in red.

	MS temperature (°C)	VP of Delta Ferrite*	Vp of Austenite*	VP of Carbide*	Cr in the matrix# (wt.%)	VP of ferrite#	VP of MX#	CR of MX# (m^3/s)
ORIGNAL	378.	0	99.6	0.4	11.15	99.2	0.30	1.5E-32
C+	375	0	99.5	0.5	11.05	99.0	0.26	1.5E-32
C-	381	2.6	97.1	0.4	11.12	99.0	0.29	**9.7E-31**
CR+	377	0.7	98.9	0.4	11.24	99.2	0.30	1.5E-32
CR-	379	0	99.6	0.4	11.05	99.2	0.30	1.5E-32
NI+	377	0	99.6	0.4	11.14	98.6	0.30	1.5E-32
NI-	379	2.0	97.6	0.4	11.13	99.7	0.29	1.5E-32
TI+	378	3.5	96.0	0.2	11.12	98.9	0.28	**1.3E-30**
TI-	378	0	99.6	0.3	11.09	99.1	0.28	1.5E-32
MO+	378	0.05	99.5	0.4	11.15	99.1	0.30	1.8E-32
MO-	378	0	99.6	0.4	11.15	99.2	0.30	1.5E-32
AL+	378	2.3	97.3	0.4	11.12	99.0	0.29	1.5E-32
AL-	378	0	99.6	0.4	11.15	99.2	0.30	1.5E-32
CO+	378	0	99.6	0.4	11.15	99.1	0.30	1.5E-32
CO-	378	0.1	99.4	0.4	11.15	99.2	0.30	1.5E-32
NB+	378	1.7	97.9	0.4	11.14	99.0	0.29	**6.8E-31**
NB-	378	0	99.6	0.4	11.06	99.1	0.27	1.5E-32
N+	378	0	99.5	0.4	11.15	99.2	0.30	1.5E-32
N-	378	2.4	97.2	0.4	11.13	99.0	0.29	**6.8E-31**
V+	378	0.2	99.4	0.4	11.15	99.2	0.30	1.5E-32
V-	3780	0	99.6	0.4	11.15	99.2	0.30	1.5E-32

4.5.3 **A new alloy optimization scheme taking into account the compositional robustness.**

Robust solutions should allow unavoidable composition fluctuations as encountered in the industrial practice, but make sure that all 6 go/no-go criteria are still met. To take the compositional robustness consideration into account, an extra, i.e. the 7th, go/no-go criterion is defined:

(7) The candidate solution should still meet all go/no-go criteria given compositional fluctuations as defined in Table 4.4**.**

All solutions shown in **Figure 4.4** have been recalculated by performing an additional 20 calculations per original solution. The results are shown in **Fig** 8. Robust solutions are shown as green dots **8** and the previous solutions are shown as red dots. The blue dashed line indicates the Pareto front for the original evaluation. The yellow lines indicates the Pareto front for the new optimization. Clearly, the vertical part of the new Pareto front moves to lower SSS factor values, but retains its shape. The horizontal part of the Pareto front is barely changed and retains its position and shape. This result suggests that solutions with a high SSS factor are more sensitive to composition changes. Moreover, the density of green dots in **Figure 4.8** is much lower than that in **Figure 4.4**, since only ~10,000 solutions out of the original ~42,000 solutions are robust solutions

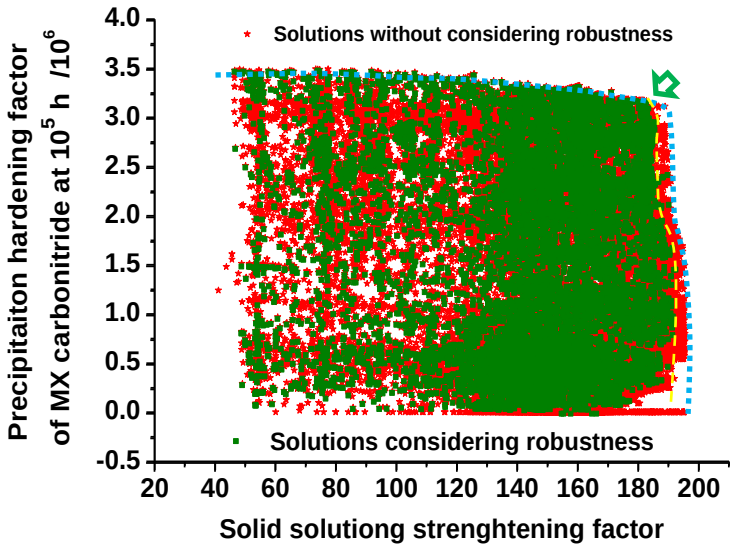

Figure 4.8 Plot of the PH versus the SSS factor with the robustness go/no-go criterion applied (green data) or without the robustness factor applied (red data). (see text)

The new optimal solution is located at the turning point of the new Pareto front. The alloy is coded Alloy PHSSR, in which R means Robustness. Its composition, SSS factor and PH factor are listed in Table 4.6. Figure 4.9 shows how compositional fluctuations for the new optimal alloy affect the predicted performance. Solid and open symbols represent higher and lower concentrations, respectively. For the new alloy, irrespective of the element to fluctuate in concentration, all go/no-go criteria are met. For most alloying elements a positive fluctuation in the concentration leads to a slight increase in the SSS

factor. However, the increase in alloying concentration generally lowers or freezes the PH factor value. Similarly to **Figure 4.7**, variations in PH factors are evident. Increases in concentrations for Ti and Nb, and a decreases of C significantly decrease the PH factor. Concentration fluctuations of the other elements do not cause significant changes in the PH factor. Therefore, for the new solution, it is preferred to have the concentrations of Ti and Nb close or slightly lower than nominal value while for C the concentration should be the target value or slightly higher.

Table 4.6 Composition of designed alloy PHSSSR considering compositional robustness (in wt.%) and corresponding austenisation temperature T_{aus} (in °C), SSS factor (SSSF) and PH factor (PHF) at 650 °C.

	C	Cr	Ni	Ti	Mo	Al	Co	Nb	N	V	T_{aus}	PHF	SSSF
Alloy PHSSSR	0.068	11.10	3.88	0.17	0.001	3.71	10.00	0.32	0.088	0.001	1523	3.17E6	182.69

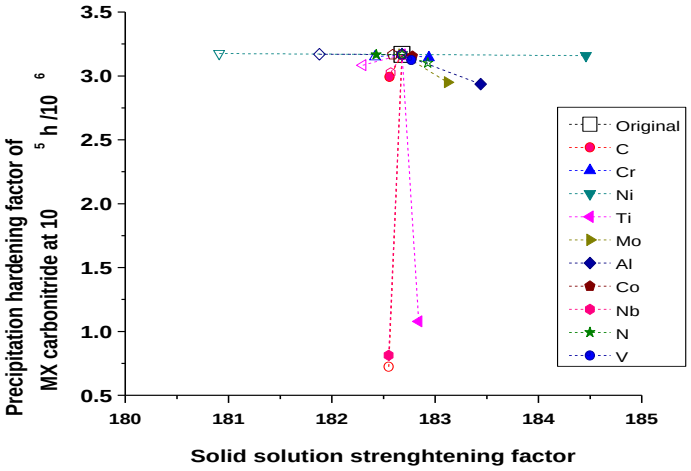

Figure 4.9 The effect of compositional fluctuations of each component on PH and SSS factors, taking alloy PHSSR as the reference point. The solid and open symbols mean higher and lower variations, respectively. (see text)

4.5.4 Comparison of the newly designed alloys and existing 9-12% Cr martensitic steels

In order to benchmark the newly designed alloys against existing alloys, the SSS and PH calculations were repeated for the compositions of the existing 9-12% Cr martensitic steels, already discussed in section 3.2. The results are shown in **Figure 4.10.** The green dots are solutions derived using the robustness criterion. All solutions on the Pareto front are predicted to outperform existing alloys not only in PH factor but also in SSS factor. Moreover, existing alloys seems to display a direct competition between the PH and SSS

factors, i.e. SSS increases at the cost of PH. It was the target of the present investigation to find a better trade off with a simultaneous optimization of both factors, leading to an optimal combination solution (PHSSSR) indicated by the arrow. Finally, the Pareto front presents a large number of attractive solutions with different combinations of SSS and PH. In future, additional criteria such as cost, weldability, processibility etc, can be added as extra criteria to filter the solutions on the current Pareto front. Whatever these additional filters, the current results as summarised in Fig. 4.10 suggest that there is still a substantial potential to improve the long term creep strength of current martensitic creep resistant stainless steels.

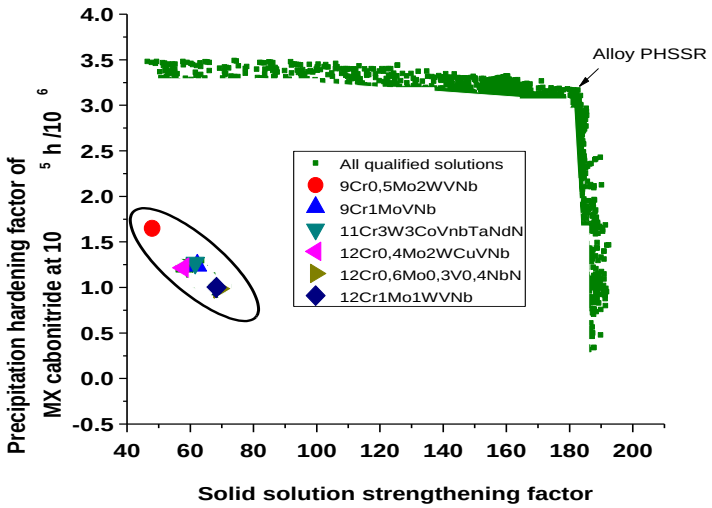

Figure 4.10 The (10^5 h, 650 °C) PH and SSS factors for the newly designed alloys and for existing 9-12% Cr martensitic steels

4.6 Conclusions

A computational alloy design approach in combination with a Pareto front analysis of the intermediate results, has led to a new high temperature ferritic/martensitic creep resistant steel with an optimal combination of relatively stable precipitation hardening even after 10^5 hours at a service temperature of 650 °C and a high solid solution strengthening. For this steel the usual fluctuations in chemical composition during steel manufacturing do not lead to substantial reductions in final creep strength. The alloy is predicted to outperform existing martensitic/ferritic creep resistant steel grades. The long term stability of the strengthening MX carbonitrides is found to be very sensitive to the concentrations of Ti, Nb, N, C. Alloying elements Al and Ni are found to have substantial solid solution strengthening effects without negatively affecting the precipitation

hardening. Mo is a less suitable solid solution hardening element for long term applications as it will be consumed by less effective precipitates.

References

[1] Abe F. Bainitic and martensitic creep-resistant steels. Curr. Opin. Solid State Mater. Sci. 2004;8:305.
[2] Rojas D, Garcia J, Prat O, Sauthoff G, Kaysser-Pyzalla AR. 9%Cr heat resistant steels: Alloy design, microstructure evolution and creep response at 650 °C. Mater. Sci. Eng., A 2011;528:5164.
[3] Abe F, Taneike M, Sawada K. Alloy design of creep resistant 9Cr steel using a dispersion of nano-sized carbonitrides. Int. J. Press. Vessels Pip. 2007;84:3.
[4] Rojas D, Garcia J, Prat O, Carrasco C, Sauthoff G, Kaysser-Pyzalla AR. Design and characterization of microstructure evolution during creep of 12% Cr heat resistant steels. Mater. Sci. Eng., A 2010;527:3864.
[5] Sachadel UA, Morris PF, Clarke PD. Design of 10%Cr martensitic steels for improved creep resistance in power plant applications. Mater. Sci. Technol. 2013;29:767.
[6] Schaffernak BC, Cerjak HH. Design of improved heat resistant materials by use of computational thermodynamics. Calphad 2001;25:241.
[7] Knežević V, Balun J, Sauthoff G, Inden G, Schneider A. Design of martensitic/ferritic heat-resistant steels for application at 650 °C with supporting thermodynamic modelling. Mater. Sci. Eng., A 2008;477:334.
[8] Knežević V, Sauthoff G, Vilk J, Inden G, Schneider A, Agamennone R, Blum W, Wang Y, Scholz A, Berger C, Ehlers J, Singheiser L. Martensitic/ferritic super heat-resistant 650 °C steels - Design and testing of model alloys. ISIJ Int. 2002;42:1505.
[9] Klueh RL, Hashimoto N, Maziasz PJ. New nano-particle-strengthened ferritic/martensitic steels by conventional thermo-mechanical treatment. J. Nucl. Mater. 2007;367:48.
[10] Brun F, Yoshida T, Robson JD, Narayan V, Bhadeshia HKDH, MacKay DJC. Theoretical design of ferritic creep resistant steels using neural network, kinetic, and thermodynamic models. Mater. Sci. Technol. 1999;15:547.
[11] Taneike M, Abe F, Sawada K. Creep-strengthening of steel at high temperatures using nano-sized carbonitride dispersions. Nature 2003;424:294.
[12] Kimura K, Kushima H, Abe F, Yagi K. Inherent creep strength and long term creep strength properties of ferritic steels. Mater. Sci. Eng., A 1997;234-236:1079.
[13] Kimura K, Toda Y, Kushima H, Sawada K. Creep strength of high chromium steel with ferrite matrix. Int. J. Press. Vessels Pip. 2010;87:282.
[14] Oruganti R, Karadge M, Swaminathan S. Damage mechanics-based creep model for 9-10%Cr ferritic steels. Acta Mater. 2011;59:2145.
[15] Yin FS, Tian LQ, Xue B, Jiang XB, Zhou L. Effect of carbon content on microstructure and mechanical properties of 9 to 12 pct Cr ferritic/martensitic heat-resistant steels. Metall. Mater. Trans. A 2012;43:2203.
[16] Lu Q, Xu W, van der Zwaag S. Computational design of precipitation strengthened austenitic heat resistant steels. Philos. Mag. 2013;93 3391.
[17] Lu Q, Xu W, van der Zwaag S. A strain-based computational design of creep-resistant steels. Acta Mater. 2014;64:133.

[18] Hald J, Danielsen HK. Z-phase strenghtened martensitic 9-12%Cr steels. 3rd Symposium on heat resistant steels and alloys for high efficiency USC power plants. Tsukuba, Japan: National Institute for Materials Science, 2009.
[19] Bhandarkar MD, Bhat MS, Parker ER, Zackay VF. Creep and fracture of a Laves phase strengthened ferritic alloy. Metall. Trans. A 1976;7:753.
[20] Abe F. Creep rates and strengthening mechanisms in tungsten-strengthened 9Cr steels. Mater. Sci. Eng., A 2001;319-321:770.
[21] Hald J, Korcakova L. Precipitate stability in creep resistant ferritic steels - Experimental investigations and modelling. ISIJ Int. 2003;43:420.
[22] Abe F, Horiuchi T, Taneike M, Sawada K. Stabilization of martensitic microstructure in advanced 9Cr steel during creep at high temperature. Mater. Sci. Eng., A 2004;378:299.
[23] Gustafson Å, Ågren J. Possible effect of Co on coarsening of M23C6 carbide and Orowan stress in a 9% Cr steel. ISIJ Int. 2001;41:356.
[24] Kipelova A, Odnobokova M, Belyakov A, Kaibyshev R. Effect of Co on creep behavior of a P911 steel. Metall. Mater. Trans. A 2013;44:577.
[25] Cipolla L, Danielsen HK, Di Nunzio PE, Venditti D, Hald J, Somers MAJ. On the role of Nb in Z-phase formation in a 12% Cr steel. Scr. Mater. 2010;63:324.
[26] Maruyama K, Sawada K, Koike J. Strengthening mechanisms of creep resistant tempered martensitic steel. ISIJ Int. 2001;41:641.
[27] Masuyama F. History of power plants and progress in heat resistant steels. ISIJ Int. 2001;41:612.
[28] Miyata K, Sawaragi Y, Okada H, Masuyama F, Yokoyama T, Komai N. Microstructural evolution of a 12Cr-2W-Cu-V-Nb steel during three-year service exposure. ISIJ Int. 2000;40:1156.
[29] Lu Q, Xu W, van der Zwaag S. Designing new corrosion resistant ferritic heat resistant steel based on optimal solid solution strengthening and minimisation of undesirable microstructural components. Comput. Mater. Sci. 2014;84:198.
[30] Wang JS, Mulholland MD, Olson GB, Seidman DN. Prediction of the yield strength of a secondary-hardening steel. Acta Mater. 2013;61:4939.
[31] de Vaucorbeil A, Poole WJ, Sinclair CW. The superposition of strengthening contributions in engineering alloys. Mater. Sci. Eng., A 2013;582:147.
[32] Hart GLW. Computational materials science: Out of the scalar sand box. Nat. Mater. 2008;7:426.
[33] Orowan E. Theory of dislocation bowing. London: Institute of Metals Symposium on Internal Stresses in Metals and alloys, 1948.
[34] Pickering FB. Physical metallurgy and the design of steels. London: Applied Science Publishers LTD, 1978.
[35] Hertzberg JL, Was GS. Isolation of carbon and grain boundary carbide effects on the creep and intergranular stress corrosion cracking behavior of Ni- 16Cr-9Fe-xC alloys in 360 °C primary water. Metall. Mater. Trans. A 1998;29 A:1035.
[36] NIMS creep data sheet, National institute for materials science, http://smds.nims.go.jp/creep/index_en.html.
[37] Mintz B, Gunawardana WD, Su H. Al as solid solution hardener in steels. Mater. Sci. Technol. 2008;24:596.

Chapter 5

A strain based computational design of creep resistant steels

5.1 Introduction

Creep resistant steels are used at very harsh conditions: elevated temperatures, high loads and long service times. During such conditions, the creep strain evolves and shows three stages: primary, secondary/steady and tertiary creep. Among these three stages, the secondary/steady stage is the most important one as it accounts for the largest part of creep life [1]. During this secondary stage, the creep rate is constant and inversely proportional to the creep life according to the Monkman-Grant relationship [2]. In industry, the stress that produces a creep rate of 10^{-7}/ hour (or 1% strain for 10^{5} hours) is generally taken as the maximum allowable stress.

In Chapter 2, a new alloy design approach was presented to design heat resistant precipitates strengthened steels [3], and the strategy focussed on the high temperature strength evolution taking into account the coarsening of precipitates. However, the creep strain during use itself, which essentially determines the creep failure, was not considered. The creep strain can be estimated by using constitutive equations which correlate the strain (rate) to the stress and the temperature. Some constitutive models have been developed based on experimental observations of strain-stress behaviour [4]. Other

models attempt to link creep behaviour to microstructural parameters, such as inter-particle spacing [5-8], leading to microstructure associated constitutive equations. These constitutive equations can be used either as an assessment of creep rupture life at a given stress, or for the prediction of the creep strength for an intended life time.

In this chapter, the genetic alloy design approach of high temperature steels is further developed by introducing a new (secondary creep) strain based optimisation criterion and taking the coarsening of the TiX carbonitrides and its effect on the creep threshold stress as the main strength determining microstructural parameter. The model is validated against experimental data for various commercial creep resistant steel grades. Using the alloy optimisation scheme, three new steel compositions are presented yielding optimal creep strength at 1% allowed strain for various intended service times (10, 10^3, 10^5 h).

5.2 Model description

5.2.1 Design methodology

A design methodology similar to that presented in previous chapters is applied, but rather than focussing on microstructural parameters the current model takes into account the effect precipitate dimensions have on the creep strain rate and it calculates the stress and time combinations leading to a fixed total strain. The tailored microstructure is chosen to be an austenitic matrix with MX carbonitride precipitates. Compositional and microstructural details of such steels are reported in Chapter 2 and our previous publication [3]. In the previous design study of heat resistant precipitation strengthened steels in Chapter 2, the maximum precipitation strengthening contribution of MX carbonitrides at the intended time of use was considered as the optimization criterion. While the method yielded interesting suggestions for optimal compositions, it can be argued that precipitate coarsening rate is an indirect optimisation parameter. Hence, it may be more appropriate to take the creep strain development itself as the direct optimisation parameter.

Creep behaviour can be divided into diffusional and dislocation creep depending on the service temperature and applied stresses. According to Harnold and Ashby's deformation map for 316 austenitic stainless steel [9], advanced austenitic creep resistant steels will undergo dislocation creep at the intended service condition i.e. a service temperature of 650 ^{o}C and an applied stress higher than 60 MPa. For this type of creep mechanism

various failure models have been proposed. Some researchers focused on the rupture due to void, grain boundary wedge accumulation [10, 11] and tried to correlate the damage with the rupture time/strength in creep resistant steels [12, 13] accordingly. Alternatively, others focused on investigating the effects of stress and temperature on strain rate and accumulated strain [14, 15], especially in the secondary / steady stage [1, 16]. Our work will follow the latter approach, and the choice of equations to describe strain-stress and other new the model features are presented in the following.

Based on numerous experimental results involving various types of pure metals and precipitate free alloys [1], a power law equation of dependence of strain rate upon applied stress has been proposed and is now commonly accepted for estimating the strain rate during the steady stage [1]:

$$\dot{\varepsilon}_{ss} = C\exp(-Q/RT)(\frac{\sigma}{G})^n \tag{5.1}$$

where $\dot{\varepsilon}_{ss}$ is creep rate of steady stage. C is a constant, Q is activation energy, R is gas constant, T is temperature, σ is applied stress, G is shear modulus, component n is a constant normally ranging from 4 to 6. However, in the case of precipitate strengthened alloys the creep rate is not properly described by Equation 5.1 and a threshold stress σ_{th} has been introduced [17, 18]. If the applied stress is lower than the threshold stress, the strain rate is negligible and can be ignored. When it reaches the threshold stress, the strain rate will increase significantly with further increase of the applied stress. Thus, for precipitate strengthened alloys, Equation 5.1 is reformulated as,

$$\dot{\varepsilon}_{ss} = C\exp(-Q/RT)(\frac{\sigma-\sigma_{th}}{G})^n \tag{5.2}$$

In Equation 5.2, the component n will again be in the range 4 to 6. In our further analysis a fixed value for n, n=5, is imposed.
According to Ref. [1], the threshold stress can be expressed as,

$$\sigma_{th} = \alpha G b / L \tag{5.3}$$

where, α is a constant, G the shear modulus and L the average inter-particle spacing. For general dislocation climb, α varies from 0.004 to 0.02, for local climb, α=0.19 [1].

According to the detachment model [19, 20] α is not a constant but changes with the mechanism of dislocations passing the particle. However, as a first order approximation α can be taken as being constant and equal for alloys with a common dislocation-precipitate interaction mode. In this work, the dimensionless factor α is taken as a constant, $\alpha = 0.02$. The validity of this assumption will be tested and demonstrated in the results section using a range of commercial steel grades.

In precipitation strengthened creep resistant steels, the precipitates evolve in time and hence the inter-particle spacing increases and threshold stress decreases with service time due to the coarsening of precipitates [21, 22]. The inter particle spacing L is determined by both the volume fraction of particles, f_p, and the average particle radius, r. Assuming that a (spherical) particle can only act as an obstacle to the dislocation motion in a glide plane if its centre is within a distance r from the plane, then [5, 23],

$$2rL^2N = 1 \tag{5.4}$$

where N is the number of particles per unit volume, which can be calculated using

$$f_p = \frac{4}{3}\pi r^3 N \tag{5.5}$$

Combining Equations 5.4 and 5.5 it yields,

$$L = (\frac{2\pi}{3})^{1/2} r / f_p^{1/2} \approx r / f_p^{1/2} \tag{5.6}$$

Equation 5.6 has been widely used to estimate the inter-particle spacing in order to calculate the precipitation strengthening contribution [5, 23, 24].

Furthermore, according to LSW law [25, 26] dealing with the evolution of particle size during coarsening, the inter-particle spacing L [24] after a certain time t can be expressed by equation 2.2. Details about this equation can be found in section 2.2.3.

The creep strain ε during the secondary stage therefore can be calculated by integrating Equation 5.2 over time, while taking into account that the threshold stress is time dependent, as shown in equation 5.7:

$$\varepsilon = \int \dot{\varepsilon}_{ss} dt = \int C_1 \exp(-Q/RT)(\frac{\sigma - \sigma_{th}}{G})^5 dt = C_2 \int (\sigma - \frac{\alpha G b \sqrt{f_p}}{\sqrt[3]{(r_0^3 + Kt)}})^5 dt \qquad (5.7)$$

Where C_2 is expressed as,

$$C_2 = \frac{C_1 \exp(-Q/RT)}{G^5} \qquad (5.8)$$

C_2 is a constant for a certain temperature.

We are aware of the fact that the threshold stress not only depends on the initial size, coarsening rate and volume fraction of TiX carbonitride (Equation 5.7), but also changes with applied stress/creep rate [21]. In the current model, this second order effect has not been taken into account as there is not enough experimental data for precipitation hardened austenitic steels of different compositions available to numerically include the effect in the optimisation process in a proper manner.

From Equation 5.7, it can be deduced that, for a certain creep strain ε, a higher volume fraction of precipitate f and/or a smaller initial size r_0 and/or a smaller coarsening rate K will result in a higher allowable stress σ (i.e. in a higher creep strength). Since Equation (5.7) is only suitable for the secondary stage, the selected strain level should be located within secondary creep range. According to the literature, the maximum strain for the secondary stage is up to around 1% for MX carbonitride strengthened austenitic heat resistant steels. Once it enters the tertiary stage, creep rate increases dramatically and the sample fails rapidly. This is also in agreement with the practical rule that the stress leading to 1% strain for the intended service time should be used as the allowable stress in its design. As a result, in this work we chose the maximal stress for a given combination of time and temperature to reach 1% strain as the optimisation parameter. At a given temperature, time and strain, for a given steel composition, the applied stress can be determined by solving Equation 5.7 and be further optimised by the genetic algorithm. The actual algorithm and the positions of various go/no-go criteria (to be explained in the next section) are indicated in **Figure 2.1** (with a different optimisation criterion in this chapter, i.e. applied stress at 1% strain). As in previous chapters the metallurgical justification of each step in the algorithm is explained below.

5.2.2 Defining the go/no-go criteria

For MX carbonitride precipitation strengthened steels, the size, density and spatial distribution of precipitates together influence the threshold stress and affect the creep strength. In order to achieve the most desirable combination of threshold strength and stability of TiX carbonitrides, a proper heat treatment scheme is necessary. A typical heat treatment of precipitation strengthened steel includes an austenisation / solution treatment for dissolving undesirable primary carbonitrides and achieving compositional homogeneity, followed by a proper ageing treatment to form desirable precipitates. For creep resistant steels strengthened by TiX precipitates, a pre-ageing process to form the strengthening precipitates is usually not imposed as the desirable secondary strengthening MX carbonitrides will form during creep at elevated temperature anyway. Therefore, the ageing temperature and service temperature are considered to be the same. Same go/no-go criteria as described in Chapter 2 are employed. Details can be found in section 2.2.4.

The candidate solutions which fulfil all go/no-go criteria, are then further evaluated by the optimisation criteria according to Equation 5.7, so as to maximize the allowed maximal stress leading to 1% strain at the predefined service temperature in the predefined (minimal) service time.

5.2.3 Searching condition and optimization framework

The composition ranges, heat treatment parameters and service times applied in the alloy design calculations are summarized in Table 5.1. In this analysis the ageing/service temperature is set at 650 ^{o}C. For this temperature, three service times (10 h, 10^3 h, 10^5 hours) are considered.

Table 5.1 Search ranges of composition (in mass%) and austenitisation temperature T_{aus} (in ^{o}C), service temperature T_{ser} = Ageing temperature T_{Age} (in ^{o}C). Mn level and Si level are fixed at 1.00 and 0.5 mass% respectively. Service strain fixed at 1%. Solutions to be found for 10, 10^3 and 10^5 hours respectively. Service temperature is fixed at 650 ^{o}C.

	C	*Cr*	*Ni*	*Ti*	*Mo*	*Cu*	*N*	T_{aus}	*Fe*
MIN	0.01	15.00	8.00	0.01	0.10	0.01	0.01	1000	Bal.
MAX	0.15	25.00	25.00	1.00	3.00	5.00	0.15	1250	

The genetic algorithm optimisation framework is unchanged, taking into account 8 variables (7 alloying elements and the austenitization temperature), and details can be found in section 2.2.5.

5.3 Validation and application

5.3.1 Validation against reported experimental data

First of all, we like to reproduce experimental creep data at a fixed temperature of 650 ^{o}C for a well-known creep steel 321H [27] and to justify the use of the time to reach 1% strain as the appropriate creep resistance indicator. The experimental data are shown in **Figure 5.1**. **Figure 5.1a** clearly shows that the time to reach 1 % strain (indicated by dashed line) forms a substantial and more or less constant fraction of the total creep life time, irrespective of the imposed stress level, in accordance with the Monkman-Grant relationship [2]. Taking the composition of 321H and calculating the initial precipitate size (Equation 2.3) and the coarsening rate (Equation 2.4) and inserting the appropriate values into the final creep strain equation (Equation 5.7) the time to reach 1% creep strain was calculated. The calculated time to reach 1% strain (using a value of $C_2 = 2.23*10^{47}$ as the calibration factor) is compared to the experimental value in **Figure 5.2b** and a very good agreement over the entire stress range of 53-216 MPa is obtained.

Secondly, in **Figure 5.2a** the relationship between the experimental life time (creep rupture time) at fixed temperature of 650 ^{o}C and the applied stress is plotted for 5 commercial precipitation hardened austenitic creep steels. The compositions of the 5 steel grades are listed in Table 5.2.

Table 5.2 Chemical compositions of the 5 commercial steels presented in **Figure 5.2** (in mass%)

	C	*Cr*	*Ni*	*Ti*	*Mo*	*Nb*	*N*	*Mn*	*Si*
16-13Nb	0.07	16.00	11.00			0.70		1.00	0.50
321H	0.07	18.50	11.00	0.30				1.00	0.50
347H	0.08	18.50	11.00			0.64		1.00	0.40
NF709	0.04	22.29	24.87	0.02	1.42	0.23	0.18	0.97	0.40
TEMPALOY-1	0.12	18.00	10.0	0.08		0.10		1.00	0.60

It is clear that the compositions of all 5 steel grades are well within the final compositional space to be explored in this optimisation (see Table 5.1) except for the N level for NF 709, which is only a little greater than the maximum value set. For all alloys except TEMPALOY A-1, there is only one type of MX carbonitride (as is assumed in the present design study). For TEMPALOY A-1, there are two types of MX (TiX and NbX) carbonitrides, and the coarsening behaviour of each of them are completely different. Therefore, the time-stress curve of TEMPALOY A-1 crosses that of the other grades.

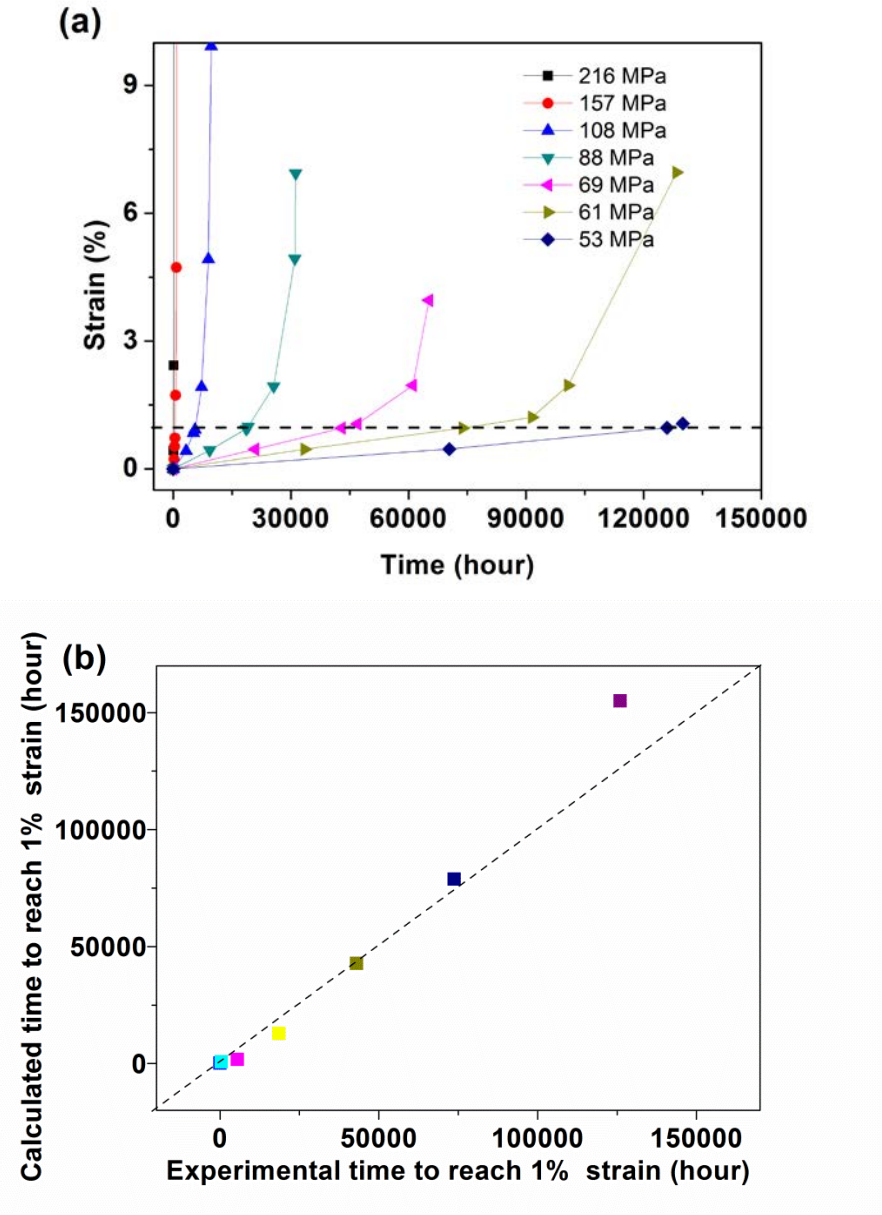

Figure 5.1 a) Actual creep strain evolution with time at various stress levels for 321H after [27]. b) model predictions for the time to reach 1% strain versus the experimentally determined time to reach 1% strain at various stress levels.

In **Figure 5.2b**, the calculated stress for these 5 steel grades to reach 1% strain after 10^4 hours' service at 650 ^{o}C is compared to the experimental rupture stress values. There is a very good correspondence. As is to be expected the rupture stress is slightly greater than the predicted stress for 1% strain for the same service time, since the rupture strain is normally greater than 1%. For other service times the prediction of the relative ranking of

the 5 steel grades is equally good, albeit that the relative behaviour of TEMPALOY A-1 sometime deviates a bit due to the role of its NbX carbonitrides, which are not taken into account in the model. It should be noted that the same C_2 value (calibrated by using data from 321H) was used for all 5 steel compositions, suggesting that in the optimisation over the composition domain defined in Table 5.1, the use of a constant calibration factor C_2 is likely to be an acceptable simplification.

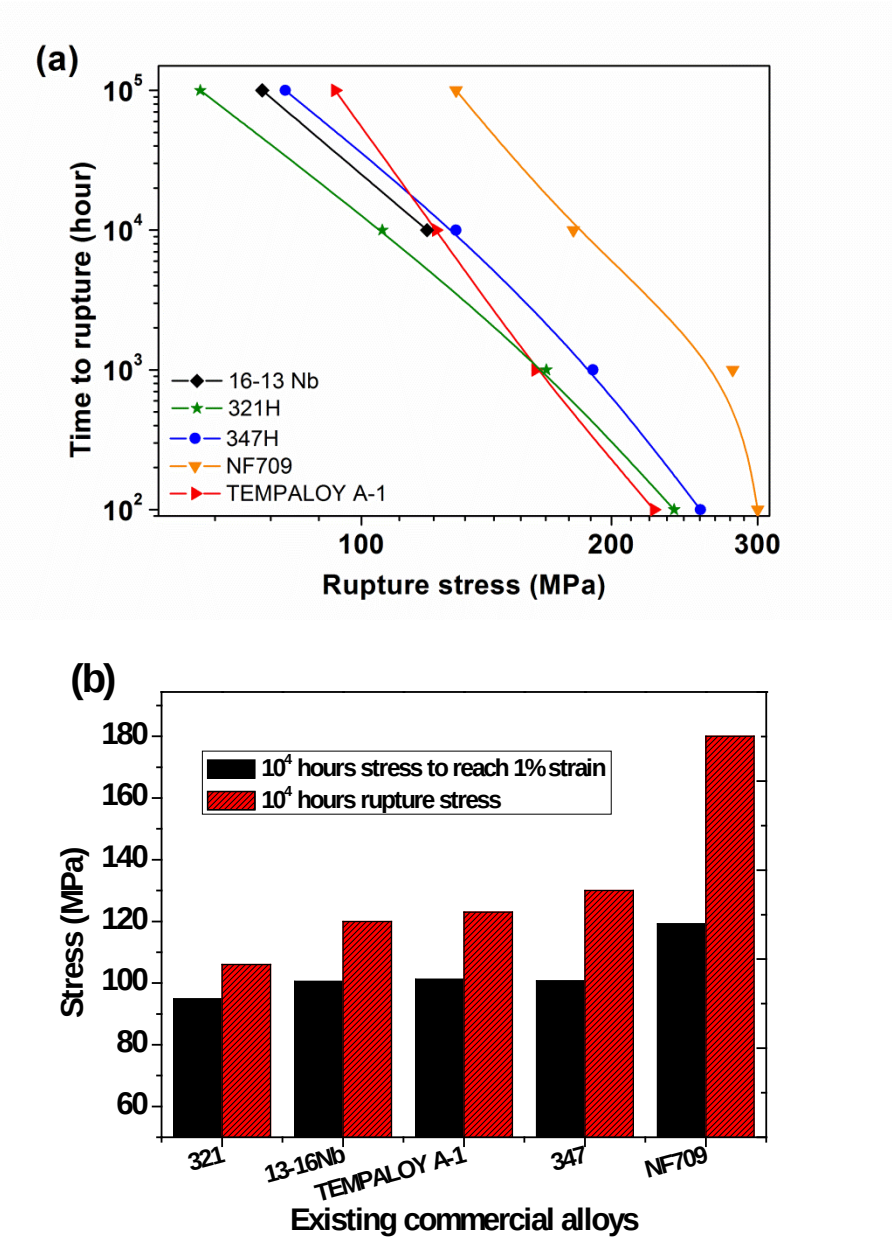

Figure 5.2 (a) Experimental rupture time dependence of (applied) stress for various existing commercial steel grades[27]. (b) Comparison of experimental rupture stress and the calculated stress to reach 1% strain in 10^4 hours.

The very good agreement between predicted and experimental data for industrial grades demonstrated in **Figures 5.2** and **5.3** should give some credibility to the predictions to be made with the model for steel compositions not yet explored experimentally.

5.3.2 Design results

To design alloys suitable for different service conditions, three values for the intended service time (i.e. the time to reach 1% strain) were selected according to practical service conditions, i.e. 10h - 10^3 h - and 10^5 h respectively. The three selected time scales correspond to short, intermediate and long term creep conditions respectively. The resulting optimized alloy compositions for the three creep conditions are named alloy1, alloy2 and alloy3 respectively, and their compositions are listed in Table 5.3. For each of the alloying elements the three predicted optimal values are located well within search region except for the molybdenum concentration which is at the lower boundary value. The low Mo concentration value coming out of the optimisation is attributed to the tendency of Mo to promote the formation of the undesirable Sigma phase (go/no-go criterion No. 6).

Table 5.3 The composition (in mass%), austenitisation temperature T_{aus} (in ^{o}C), Service temperature T_{age} = Ageing temperature T_{ser} (in ^{o}C), service time (in hours). Maximum allowed creep strain 1%.

	C	*Cr*	*Ni*	*Ti*	*Mo*	*Cu*	*N*	*Mn*	*Si*	$T_{age}=T_{ser}$	T_{aus}	$t_{service(hour)}$
Alloy1	0.015	16.29	24.45	0.23	0.10	1.05	0.06	1.00	0.50	650	1250	10
Alloy2	0.019	16.29	22.81	0.20	0.10	0.89	0.064	1.00	0.50	650	116	10^3
Alloy3	0.051	17.58	17.87	0.17	0.10	0.10	0.055	1.00	0.50	650	1178	10^5

In order to visualize the differences in time dependent behaviour of the three alloys, the stresses leading to 1 % strain as a function of time are plotted in **Figure 5.3**. The figure clearly indicates that each steel grade outperforms the other two grades at its designed lifetime (indicated by arrows) which demonstrates the effectiveness of the GA optimisation procedure as such. Alloy1 designed for 10 h shows the fastest reduction in allowed stress as a function of the service time. Alloy2 and alloy3 have more or less the same degradation behaviour, and the maximal stresses for short time services are only slightly lower than that of alloy1. Nevertheless, the maximum imposable stresses decrease much more slowly than that for alloy1, and have a much higher value at a service time of 10^3 h and beyond. The predicted relative 'strength' of alloy2 and alloy3 at

the intended service times of 10^3 and 10^5 hours are in their intended mutual position, but the difference in absolute value is small.

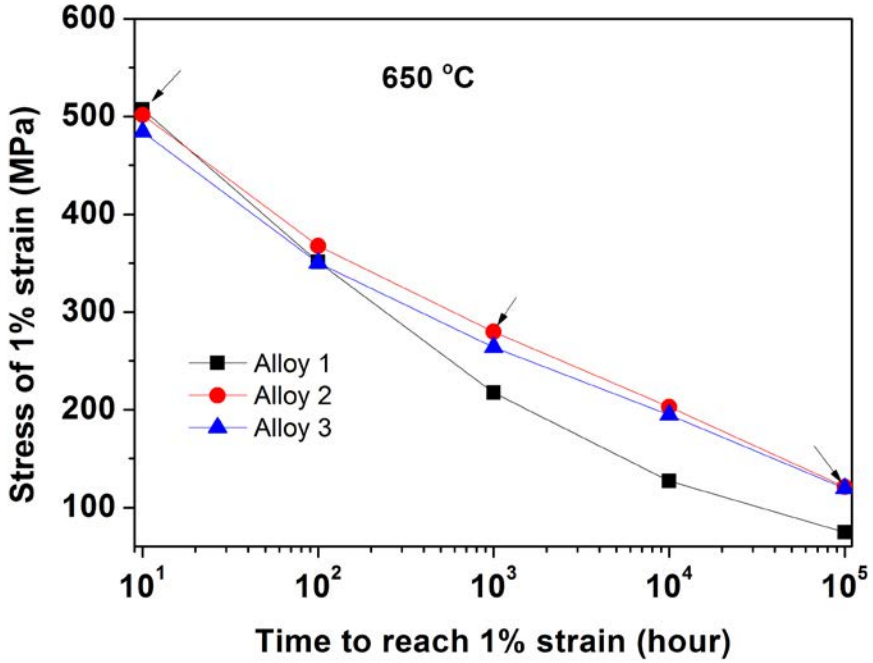

Figure 5.3 The calculated stress of 1% strain versus time to reach 1% strain for the three alloys designed to give optimal strength at 0, 10 and 10^5 hour at 650 °C respectively.

3 Discussion

3.1 validation of go/no-go criteria

To validate all pre-defined go/no-go criteria, we analysed five commercial austenitic creep resistant steels and determined to which degree multiple go/no-go criteria are fulfilled commercial creep resistant alloys. **Figure 5.4** shows corresponding values of all six go/no-go criteria on five existing and three designed alloys calculated in the same way by Thermo-Calc. The backward slashes in the figure define the area that satisfies one particular go/no-go criterion. It can be found that almost every alloy satisfies both go/no-go criteria concerning austenitization, i.e. the a) primary carbide and b) austenite volume fraction. However, for the other four go/no-go criteria, which are c) martensitic starting temperature (T_{Ms})< 25 °C, d) Sigma phase < 4 vol.%, e) Cr in the matrix > 16 mass% and f) undesirable phase (Sigma phase excluded) < 1 vol.%, commercial alloys mostly do not

fulfil the requirement strictly. This result indicates that those four go/no-criteria employed here are rather strict and completely ensure the formation of desirable microstructures, i.e. a more stable austenitic matrix, less undesirable phases and an acceptable corrosion and oxidation resistance. Notwithstanding the very demanding criteria set, the genetic algorithm is still robust enough to find solutions fulfilling all requirements, and simultaneously an even better performance (allowed maximal stress, to be discussed later). Moreover, the go/no-go performance levels of all designed alloys are located well within the backward slashed areas marking the 'safe' domains.

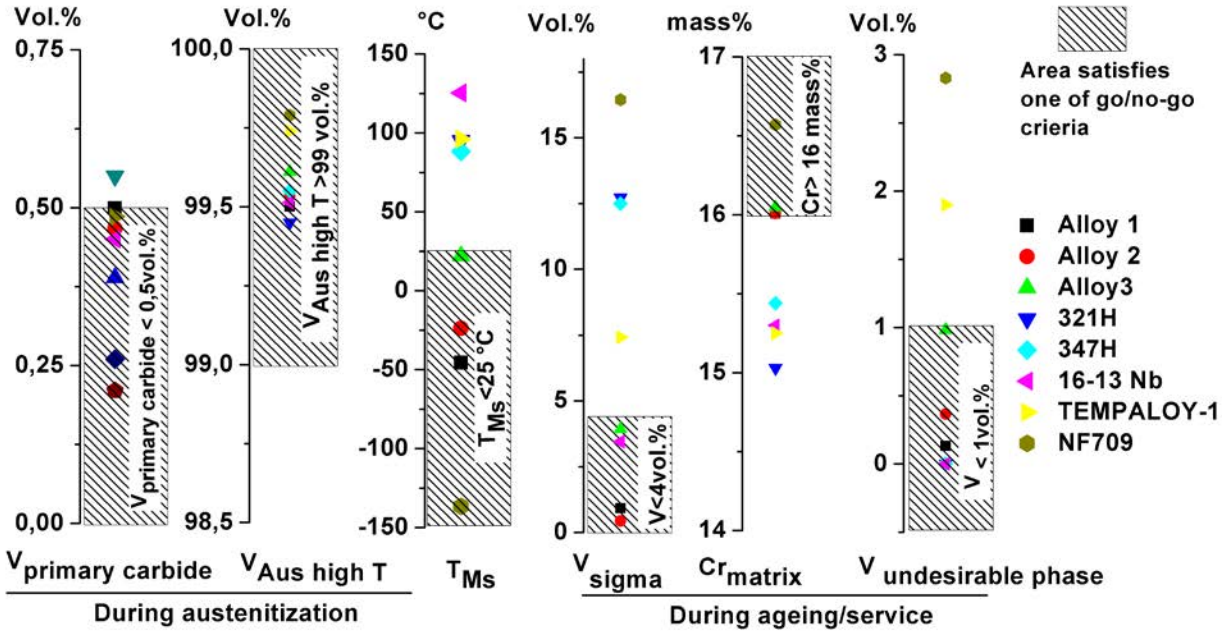

Figure 5.4 Fulfilments of go/no-go criteria on various MX carbonitrides precipitation strengthened steel grades and designed alloys. The backward slash describes the region where a particular criterion is met.

5.3.3 Compositional effect

To screen effects of alloying elements on fulfilments of all go/no-go criteria, alloy2 is taken as a baseline and the concentrations of major elements are varied one by one while keeping levels of all other components constant. Fulfilments of all go/no-go criteria are calculated and shown in **Figure 5.5**. Concentrations ranges not fulfilling any go/no-go criteria are displayed by symbols referring to the corresponding go/no-go criterion. The vertical dashed lines define original searching ranges of each alloying element. Backward slashed areas define the area that satisfies all go/no-go criteria. The composition of alloy2 is indicated by a blue triangle which apparently fulfils all the go/no-go criteria as required. Furthermore, the allowable stress for 10^3 h in the valid zones for all elements is plotted,

as indicated by the solid line. Different slopes of allowable stress indicate different decreasing speeds for various elements. **Figure 5.5** clearly shows that alloy2 meets all criteria.

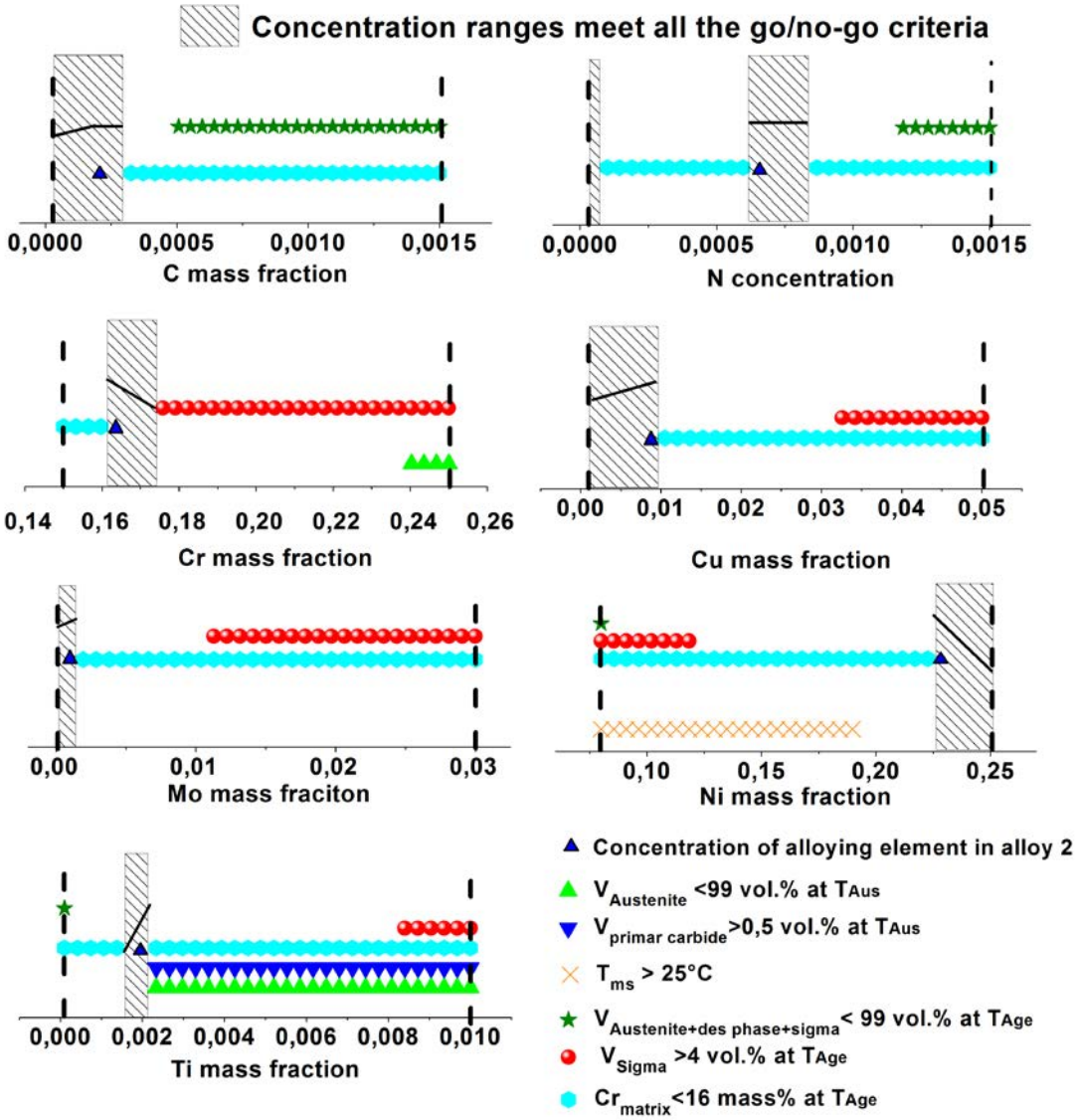

Figure 5.5 Effects of concentrations of major alloying elements on fulfilments of go/no-go criteria. The composition of alloy2 is taken as the baseline and indicated by blue triangles in each plot. The double vertical dashed lines form the original searching range. Backward slashes define the area that satisfies all go/no-go criteria, in which the trend of allowable stress for 10^3 h is indicate by the solid lines. The concentration of which any go/no-go criterion is not fulfilled is marked with corresponding symbols.

Deviations of the target concentration beyond a certain level (depending on the element), results in one or multiple go/no-go criteria not being met anymore. To show this effect, all alloying elements are classified into four groups, which are C/N, Cr/Mo/Cu, Ni, and Ti. For C and N, the system requires some C and N to be present to form strengthening MX precipitates. However, if their concentrations are increased but still within the allowed range, the allowable stress reaches to a platform due to the compromise between volume fraction and coarsening rate of MX carbonitride. A further increase of either will significantly decreases the austenite volume fraction and the Cr concentration in the matrix since C and N promote the formation of Cr rich precipitates such as $Cr_{23}C_6$ or Sigma. Therefore, these two criteria are not satisfied anymore if C/N concentrations exceed critical levels. For Cr, Cu and Mo levels, a further increase will generally promote the precipitation of Sigma phase, which subsequently depletes Cr from the matrix. Therefore, their 'safe' zones are generally on the lower side of their allowed search ranges. Cr should be at the lower end of the valid zone since it increase the coarsening rate of MX carbonitrides leading to a decrease in threshold stress, while Cu and Mo have an opposite effect giving rise in a location at the upper end of the 'safe' zone. The optimum is reached at the best trade-off among maximal allowable stress, risk of formation of Sigma phase and Cr concentration in the matrix. For Ni, an austenite stabilizing element, a decrease of the Ni level will increase the Ms temperature (Equation 5.12) and promote formation of Sigma phase resulting in the depletion of Cr in the matrix. A slight increase in the Ni concentration still within the 'safe' zone will not cause a breach in the fulfilment of the criterion but does not make the allowable stress to increase due to the increase of coarsening rate of MX carbonitrides. Finally, Ti is found to be the most sensitive element in the system and a subtle change of concentration will affect all go/no-go criteria except T_{Ms}. In case of a decrease of the Ti concentration from the optimum value, due to the lack of Ti, Cr_2N instead of TiN will form leading to a decrease in the Cr concentration in the matrix below the set critical level. An increase in the Ti concentration with respect to the target value will promote the precipitation of Sigma phase and primary MX carbonitrides which subsequently break four go/no-criteria as indicated in the figure. Clearly the allowable creep stress is most sensitive to the concentration of Ti and Ni.

All qualified compositions were further evaluated according to the optimization criterion which is the evolution of the threshold stress over time, as discussed in the following section.

5.3.4 The evolution of threshold stress with time

The variation of the threshold stress influences the strain rate in a very strong and non-linear manner and eventually have a strong effect on the allowed maximal applied stress. The threshold stress is determined by the precipitate size, its coarsening rate and volume fraction (Equations 5.3 and 5.7). Therefore, the particle size evolution of MX carbonitride as a function of time, its coarsening rate and equilibrium volume fraction are calculated at 650^{o}C for the commercial grades discussed before, as well as for 3 designed alloys. Results are presented in **Figures 5.7a** and **5.7b.** It can be observed in **Figure 5.6a** that the critical nuclei sizes of MX carbonitride (Equation 2.3) of commercial alloys are generally larger than those of three newly designed alloys. The small size of MX precipitates in the designed alloys represents a good initial microstructure against coarsening. During the service, MX carbonitrides in all alloys will grow and coarsen over time with different coarsening rates. In alloy1, designed for short time applications, the growth/coarsening of precipitates is slow in the first 10 hours and then increase significantly, similarly to other commercial alloys (except NF709), but precipitates in alloy1 still have a smaller average size. However, MX carbonitrides in alloy2 and alloy3 designed for longer term applications, have significantly slower coarsening rates than those in almost all commercial alloys with the exception of NF709. The combination of a smaller initial precipitate size and a slower coarsening kinetics leads to a significant reduction of precipitate size during the entire service time. The volume fractions and coarsening rates of MX carbonitrides of all alloys are plotted in **Figure 5.6b.** The figure shows that a higher precipitate volume fraction generally is associated with a higher coarsening rate. Such a correlation is as such undesirable because ideally a higher precipitate volume fraction is desirable from a strengthening perspective while a slower kinetics is required to control the strength degradation over time. However, the designed alloy2 and alloy3 display the desired combination of properties: a relative high volume fraction and a low coarsening rate. As indicated in Equation 2.5, the coarsening rate of precipitates is determined by interfacial energy, diffusion coefficients and concentration gradients at the precipitate/matrix interface. In the present analysis, the first two are fixed as constants for a given temperature and independent of the alloy composition. Therefore, the low coarsening rates of alloy2 and alloy3 originate from the tailored precipitate/matrix interface conditions, where the concentration gradient $(x_i^p - x_i^{mp})$ is maximized and the matrix concentration x_i^{mp} is minimized, especially for those elements involved in precipitation but possessing low diffusion coefficient values, such as Ti, V. The low value of the diffusion coefficients, the steep concentration gradients and the low matrix solid solution concentrations all contribute to a low coarsening rate of precipitates.

Finally, the variation of threshold stress with time is calculated and shown in **Figure 5.6c.** Generally, all designed alloys have higher threshold stresses than existing alloys. Alloy1, which is designed for a short service time, displays the highest initial value but decrease the fastest among designed alloys, nevertheless still possesses a higher threshold stress compared to existing alloys up to 10^5 hours. Alloy2 and alloy3 display very low degradation rates due to the combination of a slow coarsening rate and a high precipitate volume fraction. Alloy3 designed to have the longest life time exhibits the lowest initial threshold stress value, but the value is still significantly higher than that of existing alloys. After 10^5 hours there is almost no difference between alloy2 and alloy3, but alloy3 can be expected to outperform alloy2 at a service time of 10^6 hours and beyond due to its slower coarsening rate.

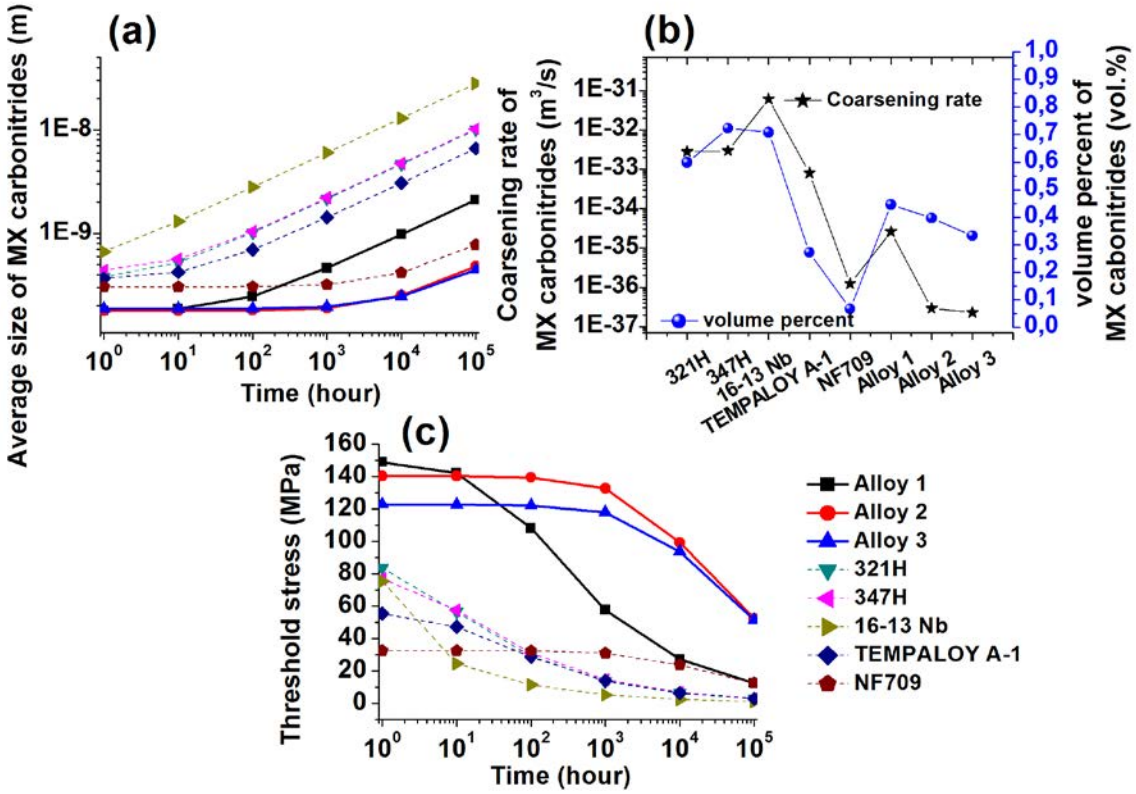

Figure 5.6 (a) Evolution of average size of MX carbonitrides with time, (b) coarsening rate and volume fraction (c) the variation of threshold stress with time for all the selected commercial alloys and three designed alloys at 650 ^{o}C.

5.3.5 The comparison of designed alloys and existing commercial steel grades

To appreciate the times predicted to reach 1% strain at a fixed stress of 150 MPa and a fixed temperature of 650 °C, the life time extension factors for the newly designed alloys (all data normalised to the experimental life time of alloy 321H) are plotted in **Figure 5.7** for both commercial steels and the newly designed alloys. As shown in **Figure 5.7**, the predicted life time extensions factors of two newly designed alloys clearly indicate a significant increase of creep life time over that of commercial alloys, especially for alloy3 which is designed for long term use.

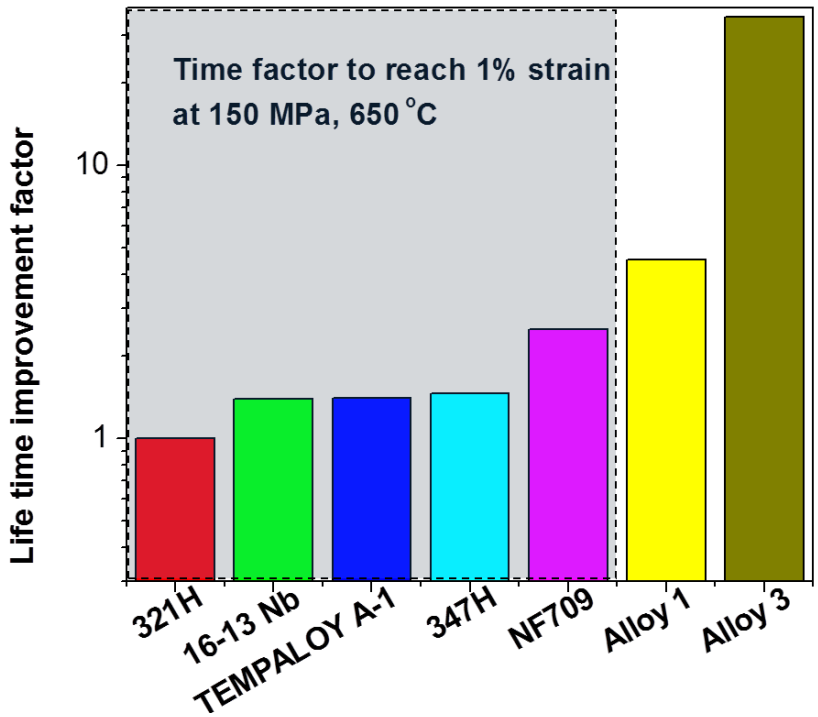

Figure 5.7 Life time improvement to reach 1% strain at 150 MPa for existing alloys and alloy1 and alloy3 designed for short time and long term usage respectively. The life time of alloy 321H is taken as the reference.

To show the predicted improvement in maximum allowed stress for the two new alloys (alloy2 and alloy3), the maximum allowable stresses and the experimentally determined creep strength values [27, 28] at both 10^4 and 10^5 hours are plotted in **Figure 5.8**. As shown in **Figure 5.8**, the experimental allowable stresses for the 5 reference steels can be well predicted using Equation 5.7 and the fixed C_2 value presented earlier. Given the excellent agreement between predictions and experimental data for the commercial steels, we conclude that the newly designed alloy2 and alloy3, with intended service lifetimes of

10^3 and 10^5 hours are likely to have substantially higher creep strength values than the currently existing precipitation hardened austenitic steels.

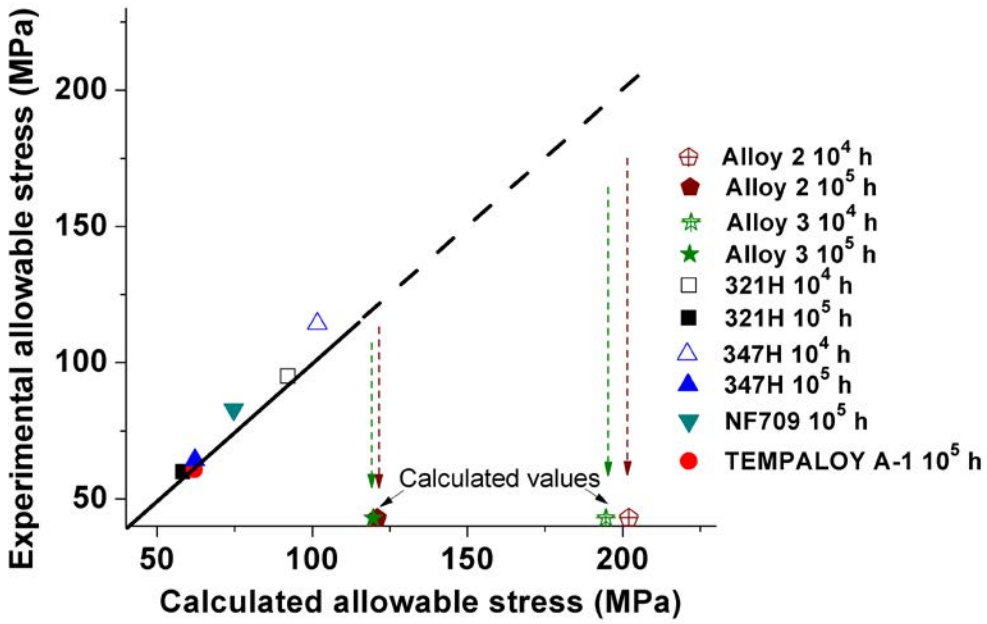

Figure 5.8 Comparison of predicted and experimental maximal allowable stress values for existing steel grades [27, 28] at 10^4 and 10^5 hours. The predicted maximal allowable stresses of designed alloy2 and alloy3 at both 10^4 and 10^5 hours are also indicated.

5.4 Conclusions

A strain based computational model for the design of creep resistant steels, which takes into account the coarsening of TiX carbonitride precipitates and its effect on threshold stress, was able to reproduce the properties of existing precipitation hardened austenitic creep resistant steels with very good accuracy. The wider exploration of the compositional domain involving 7 alloying elements and an adjustable austenisation temperature led to the definition of new alloy compositions predicted to have substantially better properties at 650 °C both for short, medium and long service times than the existing commercial steel grades.

References

[1] Kassner ME, Pérez-Prado M-T. Fundamentals of creep in metals and alloys. Amsterdam,: Elsevier, 2004.
[2] Monkman FC, Grant NJ. An empirical relationship between rupture life and minimum creep rate in creep-rupture tests. Proc. ASTM 1956;56:593.
[3] Lu Q, Xu W, van der Zwaag S. Computational design of precipitation strengthened austenitic heat resistant steels. Philos. Mag. 2013;93 3391.
[4] Merckling G. Long-term creep rupture strength assessment: Development of the European Collaborative Creep Committee post-assessment tests. Int. J. Press. Vessels Pip. 2008;85:2.
[5] Reichert B, Estrin Y, Schuster H. Implementation of precipitation and ripening of second-phase particles in the constitutive modelling of creep. Scr. Mater. 1998;38:1463.
[6] Zhu Z, Basoalto H, Warnken N, Reed RC. A model for the creep deformation behaviour of nickel-based single crystal superalloys. Acta Mater. 2012;60:4888.
[7] Dyson BF. Microstructure based creep constitutive model for precipitation strengthened alloys: Theory and application. Mater. Sci. Technol. 2009;25:213.
[8] Ma A, Dye D, Reed RC. A model for the creep deformation behaviour of single-crystal superalloy CMSX-4. Acta Mater. 2008;56:1657.
[9] Frost HJ, Ashby MF. Deformation-Mechanism Maps: The Plasticity and Creep of Metals and Ceramics. Oxford: Pergamon press, 1982.
[10] Lin J, Liu Y, Dean TA. A review on damage mechanisms, models and calibration methods under various deformation conditions. Int. J. Damage Mech 2005;14:299.
[11] Othman AM, Dyson BF, Hayhurst DR, Lin J. Continuum damage mechanics modelling of circumferentially notched tension bars undergoing tertiary creep with physically-based constitutive equations. Acta Metall. Mater. 1994;42:597.
[12] Mahesh S, Alur KC, Mathew MD. A creep model for austenitic stainless steels incorporating cavitation and wedge cracking. Modell. Simul. Mater. Sci. Eng. 2011;19.
[13] Nam SW. Assessment of damage and life prediction of austenitic stainless steel under high temperature creep-fatigue interaction condition. Mater. Sci. Eng., A 2002;322:64.
[14] Takahashi Y, Shibamoto H, Inoue K. Development of inelastic constitutive model for austenitic stainless steel for design use. Nucl. Eng. Des. 2008;238:368.
[15] Estrin Y, Mecking H. A unified phenomenological description of work hardening and creep based on one-parameter models. Acta Metall. 1984;32:57.
[16] Garofalo F. Fundamentals of creep and creep-rupture in metals. New York: The Macmillan Company, 1965.
[17] Pharr GM, Nix WD. A comparison of the Orowan stress with the threshold stress for creep for Ni20Cr2ThO2 single crystals. Scr. Metall. 1976;10:1007.
[18] Lund RW, Nix WD. High temperature creep of Ni-20Cr-2ThO2 single crystals. Acta Metall. 1976;24:469.
[19] Arzt E, Rölsler J. The kinetics of dislocation climb over hard particles-II. Effects of an attractive particle-dislocation interaction. Acta Metall. 1988;36:1053.
[20] Rösler J, Arzt E. A new model-based creep equation for dispersion strengthened materials. Acta Metall. Mater. 1990;38:671.

[21] Stevens RA, Flewitt PEJ. The dependence of creep rate on microstructure in a γ' strengthened superalloy. Acta Metall. 1981;29:867.
[22] Williams KR, Cane BJ. Creep behaviour of 1/2Cr 1/2Mo 1/4V steel at engineering stresses. Mater. Sci. Eng., A 1979;38:199.
[23] Ardell AJ. Precipitation hardening. Metall. Trans. A 1985;16:2131.
[24] Robert WC, P. Haasen. Physical Metallurgy. Amsterdam, North-Holland: Elsevier, 1996.
[25] Lifshitz IM, Slyozov VV. The kinetics of precipitation from supersaturated solid solutions. J. Phys. Chem. Solids 1961;19:35.
[26] Wagner C. Theorie der Alterung von Niederschlägen durch umlösen. Zeitschrift für Elektrochemie 1961;65:581.
[27] NIMS creep data sheet, National institute for materials science, http://smds.nims.go.jp/creep/index_en.html.
[28] ASM metals handbook, properties and selection irons - irons, steels, and high performance alloys, Specialty steels and heat-resistant alloys. Ohio: ASM International, Materials Park, 2005.

Chapter 6

The computational design of W and Co containing creep resistant steels with barely coarsening Laves phase and $M_{23}C_6$ as the strengthening precipitates

6.1 Introduction

Generally, alloy designers are inclined to select alloying elements and at such concentrations that desirable microstructural components (in particular slowly coarsening precipitates) are formed and they avoid alloying elements and higher concentrations which will lead to the formation of undesirable phases. The same strategy has been used in the alloy design in previous chapters. In this Chapter, we will relax this approach and explore modification of the negative characteristics of undesirable phases such that the nominally undesirable phases can be used to make a positive contribution to the steel properties at elevated temperatures. Precipitates that have large initial sizes and are unstable during service at elevated temperatures are generally regarded as undesirable components. Laves phase and $M_{23}C_6$ are two of such examples. They have a very high coarsening rate, which is 10-100 times faster than that of MX carbonitrides [1-3]. Their growth and coarsening not only lead to a loss of strengthening but also lead to depletion of useful elements, such as Mo and Cr, from the matrix. A common solution to prevent the formation of such undesirable phases is to decrease the Mo and Cr levels to a level at which such precipitates do not form. However, these two elements themselves are crucial for a desired creep performance: Mo increases the solid solution strengthening and

stabilizes the microstructure, while a high amount of Cr is necessary to obtain a material with a good corrosion and oxidation resistance. The alternative approach explored in this chapter is to tailor the characteristics of such potentially detrimental phases by adding some other alloying elements in order to slow down the coarsening. In the literature it has been reported that the coarsening rate of $M_{23}C_6$ can be decreased moderately by adding B, Co or W [4-8]. Abe [9, 10] reported that the coarsening rate of Laves phase can also be effectively reduced by substituting W for Mo. The shape of W enriched Laves phases is also near spherical, which is more coherent and stable than needle-shaped precipitates [11]. In addition to the more stable feature of Laves phase in W-containing alloys, a high Laves phase volume fraction, which is beneficial in order to reach a high precipitation strengthening level, can be achieved by increasing the W level. As a consequence, several researchers now use Laves phase as the principal strengthening precipitate in the design of new creep resistant alloys [12, 13]. Recently, a high W (6 wt.%) ferritic creep resistant steel has been designed which has an extraordinary creep strength [14, 15] well beyond that of conventional alloys. This alloy is mainly strengthened by W enriched Laves phase (Fe_2W) precipitate, which are very stable even after 10,000 hours' service at 650 ^oC.

In order to reach the design target and to avoid the usual obstacles, a computational design approach coupling thermodynamic and kinetic data is developed in combination with a genetic algorithm to search the multi-element search domain for optimal stability and high volume fraction of Laves phase and $M_{23}C_6$ precipitates. In this work the search space covers 10 regular alloying elements demonstrating our intention to explore the full potential of Laves phase and $M_{23}C_6$ for new creep and corrosion resistant martensitic steels with an intended use time of 10^5 hours and a fixed operating temperature of 650 ^oC.

6.2 Model descriptions

As mentioned in the introduction, either Laves phase or $M_{23}C_6$ precipitates are selected as the phase to be optimised as the main, long time – high use temperature strengthening phase in martensitic creep steels. Martensite is chosen as the (initial) microstructure of the matrix because of its good creep strength and its high resistance to thermal and creep fatigue during service in power plants [16]. Thus, the target microstructure is: 1) a fully martensitic matrix; 2) a high volume fraction of Laves phase or $M_{23}C_6$ with a tuned ultra low coarsening rate throughout its intended life time and 3) a limited volume fraction of undesirable phases.

The main concept of the model is as follows: Firstly, random compositions and heat treatment parameters are generated by the GA from the predefined parameter ranges listed in Table 1. Eleven variables are taken into account (10 alloying elements and the austenisation temperature) each uniformly spaced at 32 levels between predefined minimal and maximal values. As mentioned in the introduction, W and Mo are expected to have similar effects on the strengthening phase, but may have different overall effects. To illustrate this difference as clearly as possible, the search domains were specified either for Mo or for W. Alloy compositions involving both W and Mo were evaluated but did not yield interesting results and they are not presented here. The intended service temperature in all simulations is fixed at 650 ^{o}C and the intended service time for continuous operation is set to a high value of 10^5 hours.

Table 6.1 Search ranges (in wt.%) for 10 chemical elements and the austenisation temperature T_{aus}.

	C	*Cr*	*Ni*	*Ti*	*Mo/W*	*Al*	*Co*	*Nb*	*N*	*V*	*Fe*	T_{aus}
Min.	0.001	8.00	0.001	0.001	0.001	0.001	0.001	0.001	0.001	0.001	Bal.	900 ^{o}C
Max.	0.15	16.00	20.00	3.00	10.00	10.00	10.00	5.00	0.15	1.00		1250 ^{o}C

To check if a candidate combination of composition and heat treatment conditions can lead to the desired microstructure, various go/no-go criteria are defined and applied in the sequence of the thermal treatments to which such steels intended for long life- high load applications are subjected. In precipitation-hardened martensitic creep-resistant steels, the typical heat treatment includes an austenisation/solution treatment to dissolve undesirable primary precipitates and to achieve compositional homogeneity, followed by quenching and a tempering treatment to form desirable precipitates in the martensitic matrix. The present study deals with Laves phase or $M_{23}C_6$ strengthened steels for very long term applications and hence the final precipitate state after long term service will be close to the equilibrium condition at the service temperature rather that at the tempering temperature. Therefore, in the present study the tempering temperature is set equal to the service temperature (650 °C). In the order of the actual heat treatment sequence, thermodynamic calculations are performed at the (variable) austenisation temperature and three go/nogo criteria are defined: (1) the equilibrium volume fraction of austenite should be larger than 99%; (2) the amount of primary carbides should be less than 0.5% in volume. (3) liquid and delta phase should be absent. After austenisation, such steels are quenched to room temperature, and the austenite should completely transform to martensite. Therefore, a fourth go/no-go criterion is imposed: (4) the Martensite start (T_{Ms}) temperature should be higher than 250 ^{o}C. The T_{Ms} is obtained by calculating the chemical composition using the formula proposed by Ishida [17]. After quenching to

room temperature, the alloy is used at its service/ageing temperature. Hence a second set of thermodynamic calculations at the service temperature is performed. Two additional go/no-go criteria at this use temperature are enforced: (5) the amount of precipitates other than Laves phase/$M_{23}C_6$ should be less than 1 vol% as Laves phase or $M_{23}C_6$ are defined as the principal and property determining strengthening phases. (6) The Cr concentration in the matrix upon completion of the precipitation reactions should at least be 11 wt.% to assure adequate corrosion and oxidation resistance. Other residual Cr concentrations could have been chosen, but the current level is selected on the basis of discussions with industrial experts. The appropriate minimal Cr level obviously depends on the operating conditions in the installation.

Finally, the aim of this study is to tailor the undesirable Laves phase or $M_{23}C_6$ to a desirable phase by tuning the chemical composition, so as to drastically reduce their coarsening rates. Therefore, the time dependent precipitation hardening effect (PH) of Laves phase or $M_{23}C_6$ is considered to be the sole optimisation criteria to rank all qualified solutions fulfilling all above 6 go/no-go criteria. The PH is determined by the average precipitate particle size, its volume fraction and its spatial distribution [18]. The actual values for the three parameters depend on their initial condition and evolution during service. Given the extremely long service time, Laves phase and $M_{23}C_6$ will grow and coarsen considerably during the exposure at high temperatures, and in doing so change the inter-particle spacing. The precipitation hardening contribution σ_p is inverse proportional to inter-particle spacing, which is estimated by considering the coarsening kinetics only [19-21]. σ_p is described by Equation 2.2. The computational details can be found in Chapter 2.2.3.

The coarsening rate of precipitates is generally very well described by Equation 2.4 [2, 22], and is used in the simulations performed to calculate the coarsening rate for the Laves phase and $M_{23}C_6$ precipitates at a fixed temperature of 650 ^{o}C. Prior to the design study it was verified for a number of existing 9-12% Cr steels that the coarsening rate of Laves phase and $M_{23}C$ as predicted by Equation 2.4 indeed drops with increasing W level. The result is shown in **Figure 6.1**. The coarsening rate of the Laves phase is much lower than that of $M_{23}C_6$. Moreover, the coarsening rate of Laves phase or $M_{23}C_6$ both decreases when the level of W is increased. A similar shift, not shown, occurs with increasing Co level. The calculated behaviour agrees well with the practical experience.

At very long times the strengthening contributions of the dislocations accompanying the formation of Laves phases will have dropped to a low level due to recovery. Furthermore,

there are no indications that this final dislocation level varies with type of Laves phase or matrix composition. Moreover the strengthening contribution of lath boundaries is also negligible owing to their significant growth after long term service. Hence, the dislocation and lath boundary contributions in the strength model for the steels analysed in the present work were ignored. Precipitate hardening of Laves phase and/or or $M_{23}C_6$ is taken as the principle strengthening source for long term creep strength in this study. Effectively, the time and temperature dependent inter-particle spacing of Laves phase or $M_{23}C_6$ is taken as the PH optimisation parameter. In this study the service time is fixed at 10^5 h. The factor $1/L$ (Equation 2.2) is called the 'PH factor' and is to be maximised by tuning the chemical composition and heat treatment parameters.

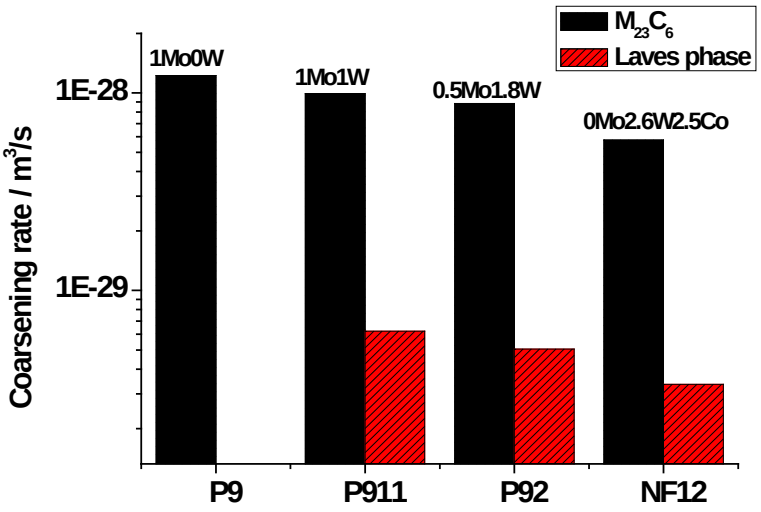

Figure 6.1 Calculated coarsening rates of $M_{23}C_6$ and Laves phase at 650 ^oC in existing 9-12% martensitic steels.

6.3 Model predictions

The GA based search covered about 10^6 unacceptable or less well performing variants finally leading to four alloys with the highest long term precipitation strengthening effect. Their composition, austenisation temperatures, volume percent, coarsening rate of Laves phase or $M_{23}C_6$ and the PH factors determined are listed in Table 6.2. The alloys strengthened by Laves phase with either W or Mo as the modifying element, and those strengthened by $M_{23}C_6$ with either W or Mo as the modifying element are labelled as Alloy LavesW, Alloy LavesMo, Alloy $M_{23}C_6$W and Alloy $M_{23}C_6$Mo, respectively. These alloys have a high Cr level and a Co level equal to the upper limit set in Table 6.1. The

high Co level is required so as to keep a high Cr level in the matrix and hence to stabilize the austenite and to suppress the ferrite. This is necessary to obtain a fully austenitic matrix at a reasonable austenisation temperature within the search range. For the LavesW alloy the W level equals the imposed maximum level. In contrast, for the LavesMo alloy the Mo level is well below the maximum allowed level. In both $M_{23}C_6$ alloys the C and Cr levels are equal to the maximal values, but the Mo and W levels are substantially lower than the maximum allowed level. The lower recommended concentration levels are the result of strict go/no-go constraint boundaries being met in the optimisation cycles. The concentration of Ni in Laves phase strengthened alloys LavesW and LavesMo is much higher (3-5 wt.%) than that in $M_{23}C_6$ hardened steels to further stabilize austenite at the austenisation temperature, since the content of ferrite stabilizer elements W in alloy LavesW or Mo, Al and Nb in alloy LavesMo are much higher than those in $M_{23}C_6$ hardened steels.

Table 6.2 Composition of four designed alloys (in wt.%), austenisation temperature T_{aus} (in °C), volume percent (vol.%), coarsening rate, PH factors (PHF) of Laves phase or $M_{23}C_6$ at 650 °C.

	C	*Cr*	*Ni*	*Ti*	*Mo*	*W*	*Al*	*Co*	*Nb*	*N*	*V*	*Taus*/K	*vol.*% of laves/$M_{23}C_6$	*K* / m^3/S Laves/$M_{23}C_6$	PH factor at 10^5 h
LavesW	0.001	10.84	3.23	0.11	0.00	10.00	0.001	10.00	0.32	0.03	0.001	1239 °C	11.30	8.57E-31	4.98E+06
$M_{23}C_6$W	0.15	16.00	0.01	0.01	0.00	1.61	0.001	10.00	0.001	0.006	1.00	1069 °C	3.05	7.39E-30	1.26E+06
LavesMo	0.001	10.07	3.23	0.11	4.19	0.00	0.001	10.00	1.78	0.001	0.001	1250 °C	9.50	6.10E-29	1.11E+06
$M_{23}C_6$Mo	0.15	16.00	0.01	0.01	0.97	0.00	0.001	10.00	0.001	0.006	0.39	1182 °C	3.02	1.46E-29	1.00E+06

It is interesting to note that the coarsening rate of Laves phase or $M_{23}C_6$ in W containing alloys is much slower than that in Mo containing alloys. Clearly W has the higher capacity to stabilize the precipitates. To further visualize its effect on coarsening rates, the PH factor evolution with time for the optimal alloys defined is shown in **Figure 6.2**. The PH factor invariably decreases with time but with a different rate. In Laves phase strengthened alloys, the degradation kinetics of alloy LavesW is much slower, leading to a much higher PH factor at the long intended service time. The W effect is also observed in $M_{23}C_6$ strengthened alloy but the effect is less pronounced. Moreover, the coarsening rate of Lave phases in alloy LavesW is close to that of the well accepted very stable MX carbonitride [1, 22], proving that indeed undesirable Laves phase can be turned into desirable precipitates. While being equally stable, the volume percentage of Laves phase (11.3 vol%) is much higher than the maximum volume percent of MX carboniride (0.5 to 1 vol%) which increases the nett strengthening contribution of the Laves precipitates significantly.

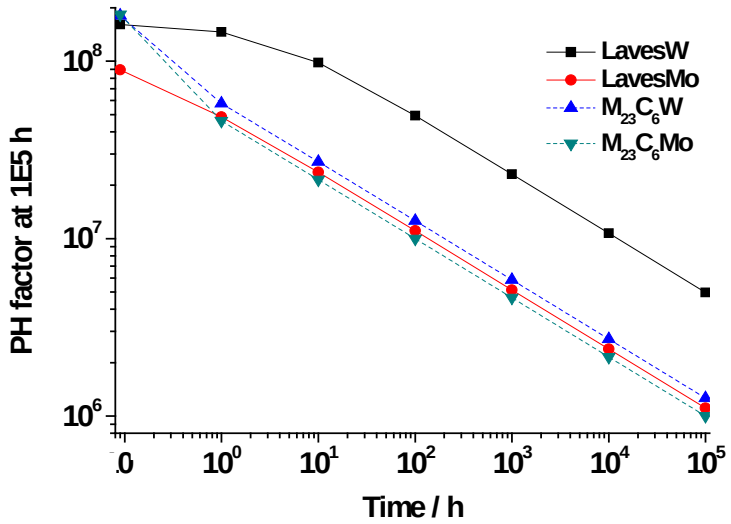

Figure 6.2 The degradation behaviour of the PH factor with service time for the four designed alloys.

6.4 Discussion

6.4.1 Effects of alloying elements on the precipitate configuration

As demonstrated in the previous sections, the type of alloying element can significant influence the precipitate characteristics. To further explore this effect, the alloy compositions LavesW and LavesMo are taken as baselines and the concentrations of Co, W/Mo in each alloy are varied while keeping the levels of all other elements unchanged by adjusting the Fe level. The results are shown in **Figure 6.3**. The two vertical dashed lines represent the allowed ranges of alloying elements (as Table 6.1). The green box defines the concentrations that meet all the go/nogo criteria. The black arrows indicate the original composition of alloys LavesW or LavesMo, which, as expected, always shows the highest PH factor in the predefined ranges, confirming the robustness of the GA optimisation model. As demonstrated in **Figure 6.3a and 6.3c,** the addition of Co in both alloys can significantly decrease the coarsening rate (by ~10 times in Alloy LavesW and by ~5 times in Alloy LavesMo) as well as increase the volume fraction of Laves phase, leading to a substantial increase in PH factor (Equation 2.2). The difference between **Figure 6.3a and 6.3c** is that the volume fraction of Laves phase in Alloy LavesMo reaches a maximum value at 10 wt.% Co and then decrease with further addition of Co. The effect of W is similar to that of Co, as shown in **Figure 6.3b**. When

the concentration of W is low (<0.3 wt.%), there is no Laves phase formation since W is the principal Laves forming element. At a further increase in W concentration, the Laves phase begins to form and its concentration increases almost linearly and reaches a maximum PH at the upper limit of 10wt%. At the same time, the coarsening rate of Laves phase is significantly decreased. On the contrary, addition of Mo in alloy LavesMo increases the coarsening rate provided the Mo content is lower than 5 wt.% as shown in **Figure 6.3d**. A further increase in Mo level will not decrease the coarsening rate. This trend explains why the Mo containing alloy LavesMo has a much higher coarsening rate than the W added alloy LavesW. The effects of both Co and W on the coarsening rate of Laves phase agree qualitatively very well with existing experimental results. By analysing the coarsening rate as defined in Equation 2.4, it is found that the coarsening rate mainly depends on the diffusion coefficients and concentration gradients of alloying elements at the interface. The diffusion coefficient of W at the set temperature of 650 ^{o}C is very low, close to 10^{-20} m^2/s, while those of other elements (including Mo) are higher than 10^{-19} m^2/s. As shown in **Figure 6.3b**, the coarsening rate decreases rapidly with the addition of W when its content is lower than 2.5 wt.%. This is the combined effect of concentration gradient at the interface and the low diffusion coefficient of W. The addition of a small amount of W can significantly change the gradient concentration at the interface. Furthermore, the diffusion coefficient of W is very small which increase the effect of concentration gradient at the interface (Equation 2.4). The W atom is bigger than Fe atom and can cause lattice misfit, which can possible explains the decrease of the diffusion rate of other Laves phase forming elements. A further addition of W only decreases the coarsening rate slightly, suggesting there is no significant change in interface concentration gradient. This phenomenon is not so pronounced in Co modified alloys, since an increase in the Co level also decreases the diffusion coefficients of other alloying elements [5].

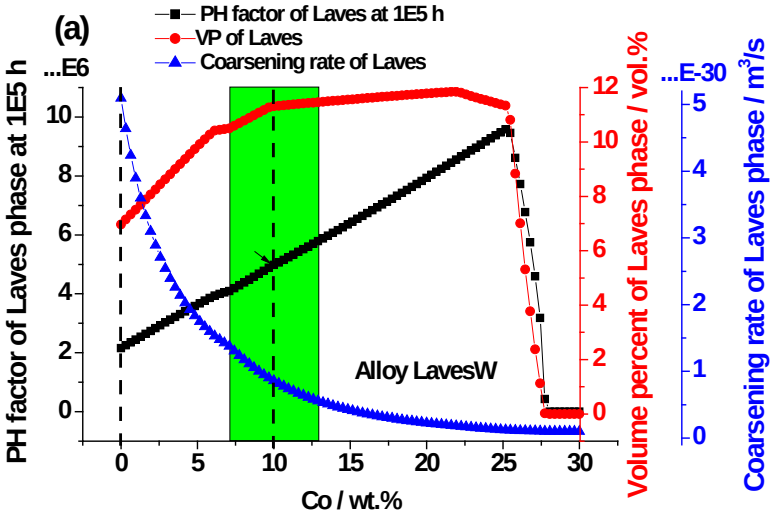
(a)
PH factor of Laves at 1E5 h
VP of Laves
Coarsening rate of Laves
...E6
...E-30
PH factor of Laves phase at 1E5 h
Volume percent of Laves phase / vol.%
Coarsening rate of Laves phase / m³/s
Alloy LavesW
Co / wt.%

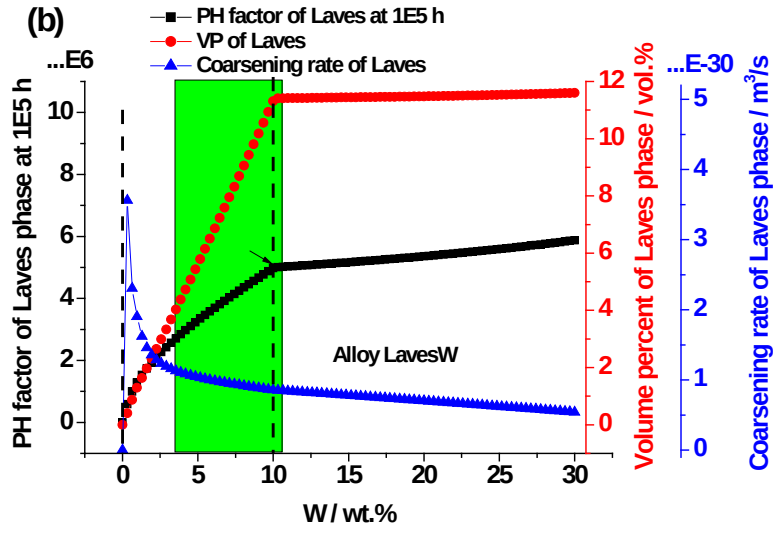
(b)
PH factor of Laves at 1E5 h
VP of Laves
Coarsening rate of Laves
...E6
...E-30
PH factor of Laves phase at 1E5 h
Volume percent of Laves phase / vol.%
Coarsening rate of Laves phase / m³/s
Alloy LavesW
W / wt.%

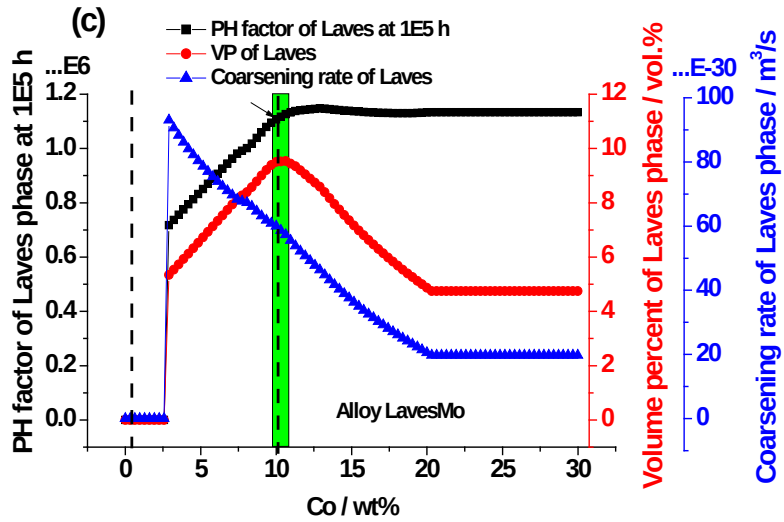
(c)
PH factor of Laves at 1E5 h
VP of Laves
Coarsening rate of Laves
...E6
...E-30
PH factor of Laves phase at 1E5 h
Volume percent of Laves phase / vol.%
Coarsening rate of Laves phase / m³/s
Alloy LavesMo
Co / wt%

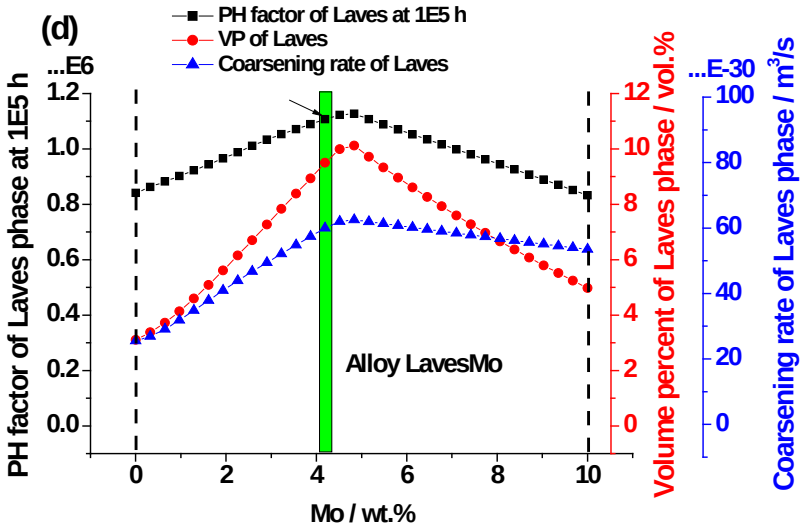

Figure 6.3 Effect of concentration variation of alloying element on the volume percent (VP), coarsening rate and PH factor of Laves phase. (a) Co, (b) W in alloy LavesW and (c) Co and (d) Mo in alloy LavesMo. The two vertical dashed lines mark the predefined range of alloying elements. The green box defines the concentration that meets all the go/nogo criteria, and the concentration in other areas do not fulfil one or multiple go/nogo criteria. The black arrows indicate the original composition in alloy LavesW or LavesMo.

6.4.2 Comparison of designed alloys and existing alloys

The coarsening rates, volume fraction and PH factors after 10^5 h exposure at 650 °C for Laves phase, $M_{23}C_6$ and MX carbonitride in existing alloys are calculated using their compositions and are compared to those of designed alloys. The results are listed in Table 6.3. In the two designed Mo enriched alloys, LavesMo and $M_{23}C_6$Mo, the volume fraction of Laves phase and $M_{23}C_6$ are slightly higher and their coarsening rates are similar to those in existing alloys. Hence the two newly designed alloys have a PH factor at 10^5 h similar to that of existing alloys (Equation 2.2). In contrast, in the two W containing alloys LavesW and $M_{23}C_6$W, not only the volume fraction of Laves phase and $M_{23}C_6$ is higher, but also their coarsening rates are much slower than those in existing alloys, leading to a much higher PH factor at 10^5 h (Equation 2.2). The strongly reduced coarsening rates in the two W containing alloys are mainly attributed to the high levels of W and Co (see Table 6.2), which are much higher than those in existing alloys. Although the coarsening rate of Laves phase is still faster than that of MX carbonitride in existing and previous designed alloys, the volume percent of Laves phase (11.3 vol.%) can be much higher than that of MX carbonitride (~0.3 vol.%). As a consequence, the PH factor

of Laves phase at 10^5 h in alloy LavesW is even greater than the predicted PH of existing stable MX carbonitride reinforced (1.3-1.8 E+06) alloys.

Similar to the optimisation of $M_{23}C_6$ or Laves in the W containing system, the alloy compositions using MX carbonitride as the main strengthening precipitate have been optimised and the best candidate is labelled as MXW. The composition of alloy MXW is listed in Table 6.4, and the coarsening rate and volume percent of MX carbonitride are listed in Table 6.3. The coarsening rate of MX carbonitride in alloy MXW is slower than that of MX carbonitrides in known alloys, which is in agreement with the prediction. However the volume fraction of MX carbonitride in alloy MXW is still similar to those of existing alloys. Combining the effects of coarsening rate and volume fraction, the PH factor of alloy LavesW based on conventionally undesirable Laves phase remains higher than that of alloy MXW which is based on optimising the conventionally precipitate MX carbonitrides. Therefore, in the newly designed alloy LavesW the Laves phase has become a truly desirable component.

Table 6.3 The coarsening rate *K* (in m^3/s), volume percent (vol.%), PH factor at 10^5 h of Laves phase, $M_{23}C_6$ and MX carbonitride of existing alloys and designed alloys at a service temperature of 650 ^oC. MXW is a new alloy based on the optimisation of MX carbonitride in W concept alloy using the model of this study.

Alloys	*K* of $M_{23}C_6$	*K* of laves	K of MX	Vol.% of $M_{23}C_6$	Vol.% of Laves	Vol.% of MX	PH factor at 1E5 h of $M_{23}C_6$	PH factor at 1E5 h of Laves	PH factor at 1E5 h of MX
P9 (9Cr1Mo)	1.23E-28	-	-	2.38	-	-	0.45E+06	-	-
P911 (9Cr1Mo1WVNb)	9.91E-29	6.23E-30	7.46E-32	2.15	0.45	0.31	0.45E+06	0.51E+06	1.87E+06
P92 (9Cr0.5Mo2WvNb)	8.85E-29	5.05E-30	7.88E-32	1.39	0.99	0.32	0.37E+06	0.81E+06	1.85E+06
NF12 (11Cr2.6W2.5CoVNbBN)	5.78E-29	3.34E-30	9.52E-32	1.55	1.68	0.31	0.45E+06	1.22E+06	1.72E+06
SAVE12 (11Cr3W3CoVNbTaNdN)	3.18E-29	2.41E-30	1.40E-31	1.90	1.95	0.24	0.61E+06	1.46E+06	1.33E+06
lavesW	-	**8.57E-31**	-	-	**11.30**	-	-	**4.98E+06**	-
$M_{23}C_6W$	**7.39E-30**	-	-	**3.05**	-	-	**1.26E+06**	-	-
LavesMo	-	**6.1E-29**	-	-	**9.50**	-	-	**1.11E+06**	-
$M_{23}C_6Mo$	**1.46E-29**	-	-	**3.02**	-	-	**1.00E+06**	-	-
MXW	-	-	**1.53E-32**	-	-	**0.34**	-	-	**3.29E+06**

Table 6.4 Composition of the designed alloy MXW (in wt.%), austenisation temperature T_{aus} (in °C).

	C	*Cr*	*Ni*	*Ti*	*Mo*	*W*	*Al*	*Co*	*Nb*	*N*	*V*	*Taus*
MXM	0.06	11.10	0.01	0.20	0.00	0.65	0.97	9.35	0.32	0.04	0.001	1250

6.4.3 Combining $M_{23}C_6$ and Laves phase in one alloy

Generally $M_{23}C_6$ precipitates are located at lath boundaries and have a positive effect on creep strength by pinning the lath boundaries during creep [23], while the W-enriched Laves phase can be found both in the grain interior and boundaries [10, 12, 24] and only restricts the movement of dislocations. Both effects decrease the creep rate, especially if the coarsening rates of both types of precipitates can be kept at a low value during the service. It will be very interesting to combine both types of precipitates in one alloy to further optimise the creep resistance. However, the optimisation procedure as used in this thesis can only deal with one PH factor per optimisation cycle. In order to optimise both PH factors simultaneously in one alloy, two optimisations are performed respectively: either only for Laves, or only for of $M_{23}C_6$ at 10^5 h, while the PH factors of both precipitates are recorded for all eligible solutions that fulfil all the go/no-go criteria in both optimisations. Such a dual precipitate optimisation search was only performed for the search space containing W. Putting all the qualified solutions together, the property map **Figure 6.4** can be constructed. The best combination of two precipitates can be found as indicated within the circle at the upper right corner. The new alloy, which has only slightly lower PH factors than those from dedicated single optimizations, is labelled as Alloy LavM. Its composition, austenisation temperature and PH factor are listed in Table 6.5.

Table 6.5 Composition of the designed alloy LavW (in wt.%), austenisation temperature T_{aus} (in ^{o}C), PH factors of Laves and $M_{23}C_6$ at 650 °C.

	C	*Cr*	*Ni*	*Ti*	*Mo*	*W*	*Al*	*Co*	*Nb*	*N*	*V*	*Taus/K*	PH factor of Laves at 10^5 h	PH factor of $M_{23}C_6$ at 10^5 h
LavM	0.15	12.39	1.30	0.01	0.00	10.00	0.001	10.00	0.001	0.07	1.00	1216	4.59E+06	1.32E+06

To benchmark the newly designed alloy against existing alloys, the PH factor after 10^5 h of exposure to 650 ^{o}C was calculated for a number of commercial 9-12Cr% martensitic creep resistant steels (other precipitates than Laves phase and $M_{23}C_6$ were not considered in their analysis). Their results are shown in **Figure 6.4**, and are indicated by stars. The PH values for all existing alloys are located in the lower left corner, indicating that in existing alloys Laves phase and $M_{23}C_6$ indeed have no significant strengthening effects for long time exposure due to the high coarsening rate. By the simultaneous optimisation of the volume fraction and the coarsening rate, not only alloy LavM itself but also many other solutions with different combinations of PH factors of Laves phase and $M_{23}C_6$, as shown in **Figure 6.4**, are identified which are predicted to significantly outperform existing alloys. This clearly demonstrates that an undesirable phase can indeed be changed into a desirable phase by tuning the composition and austenitization temperature.

While the current analysis and optimisation route only take into account the precipitation strengthening factor and present an idealised solution, the procedure employed here can be extended to take into account other criteria such as cost, weldability, processibility etc. [25], provided the new design parameters can be captured in quantitative parameter values. Such additional considerations are likely to eliminate some solutions included in the figure, but even then it is clear that there is a substantial potential to improve the long term creep strength of current martensitic creep resistant stainless steels by employing this new alloy design concept.

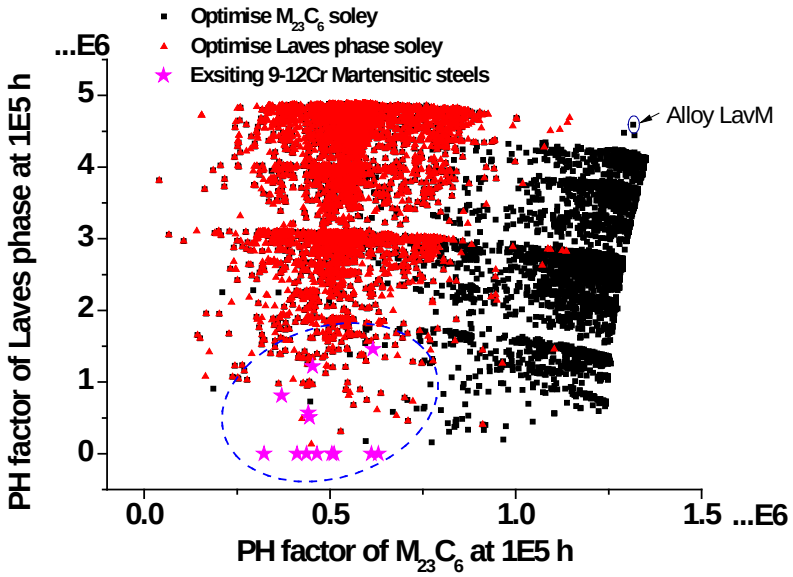

Figure 6.4 Simultaneous optimisation of PH factors of Laves phase and $M_{23}C_6$. The values of existing alloys, as indicated by star symbols, are also put on the plot to compare to the designed solutions.

Finally, a similar analysis of the possibility to combine the contributions of two different sets of precipitates in a single alloy has been performed for the W containing steel grades. As shown in **Figure 6.5**, a significant difference can be found between on the one hand the MX/$M_{23}C_6$ and on the other hand the Laves/$M_{23}C_6$ systems. Most notably, there is no best combination point in MX/$M_{23}C_6$ system. The main reason for this phenomenon is that these two precipitates are competing for the same alloying elements. For MX and $M_{23}C_6$ strengthening, a high amount of C (~0.15 wt.%) ensures a high volume fraction of MX and $M_{23}C_6$. For $M_{23}C_6$, the coarsening rate does not change significantly with the C level, and thus a high initial PH factor is obtained if the C level is high. However a high level of C (> 0.08 wt.%) will dramatically increase the coarsening rate of MX carbonitride since the C gradient at the interface of MX and Matrix (Equation 2.4) will be changed. Therefore, if the PH factor of $M_{23}C_6$ is high (a high C level), that of MX will be low, and vice versa. There is no such counteracting effect in the Laves/$M_{23}C_6$ system.

Moreover, the highest PH factor for MX is still lower than that of the best combination alloy LavM. Therefore, the Laves/ $M_{23}C_6$ system offers a higher probability of success in obtaining new martensitic steel grades with very long life times at very high temperatures

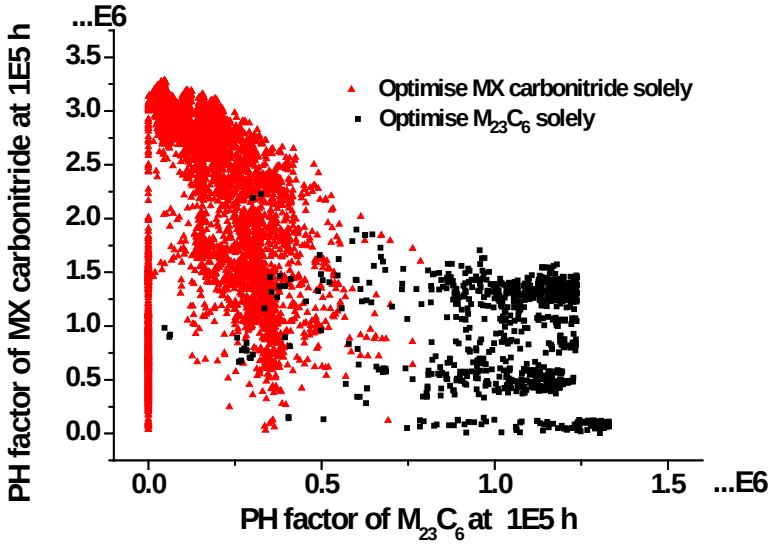

Figure 6.5 Simultaneous optimisation of PH factors of MX carbonitrides and $M_{23}C_6$.

6.5 Conclusions

A computational alloy design approach has been developed to design W or Mo containing martensitic creep resistant steels strengthened by Laves phase and/or $M_{23}C_6$ precipitates by tuning the coarsening rate of the strengthening phase to a minimum value and by simultaneously tuning their volume fraction to a maximum level. The coarsening kinetics of both precipitates can be significantly lowered by changes in the overall alloy composition and the precipitation hardening contributions are hence substantially increased by tuning the composition. Addition of Co can significantly reduce the coarsening rate of Laves phase. The main Laves phase forming elements W and Mo have different effects on the coarsening rates. Addition of W significantly decreases the coarsening rate and the effect increases with W level. In contrast, Mo shows an optimum low-coarsening level at 4-5 wt% Mo. For W-based creep steels, the combination of Laves phase and $M_{23}C_6$ strengthening precipitates shows great potential for creating new alloys outperforming existing martensitic creep resistant steel grades. Successfully combining MX and $M_{23}C_6$ as strengthening precipitates was found to be impossible.

References

[1] Prat O, Garcia J, Rojas D, Carrasco C, Kaysser-Pyzalla AR. Investigations on coarsening of MX and M23C6 precipitates in 12% Cr creep resistant steels assisted by computational thermodynamics. Mater. Sci. Eng., A 2010;527:5976.
[2] Gustafson Å, Hättestrand M. Coarsening of precipitates in an advanced creep resistant 9% chromium steel—quantitative microscopy and simulations. Mater. Sci. Eng., A 2002;333:279.
[3] Rojas D, Garcia J, Prat O, Sauthoff G, Kaysser-Pyzalla AR. 9%Cr heat resistant steels: Alloy design, microstructure evolution and creep response at 650 °C. Mater. Sci. Eng., A 2011;528:5164.
[4] Abe F, Horiuchi T, Taneike M, Sawada K. Stabilization of martensitic microstructure in advanced 9Cr steel during creep at high temperature. Mater. Sci. Eng., A 2004;378:299.
[5] Gustafson Å, Ågren J. Possible effect of Co on coarsening of M23C6 carbide and Orowan stress in a 9% Cr steel. ISIJ Int. 2001;41:356.
[6] Kipelova A, Odnobokova M, Belyakov A, Kaibyshev R. Effect of Co on creep behavior of a P911 steel. Metall. Mater. Trans. A 2013;44:577.
[7] Sherif MY, Mateo CG, Sourmail T, Bhadeshia HKDH. Stability of retained austenite in TRIP-assisted steels. Mater. Sci. Technol. 2004;20:319.
[8] De Carlan Y, Murugananth M, Sourmail T, Bhadeshia HKDH. Design of new Fe-9CrWV reduced-activation martensitic steels for creep properties at 650 °C. J. Nucl. Mater. 2004;329-333:238.
[9] Abe F. Creep rates and strengthening mechanisms in tungsten-strengthened 9Cr steels. Mater. Sci. Eng., A 2001;319-321:770.
[10] Abe F. Effect of fine precipitation and subsequent coarsening of Fe2W laves phase on the creep deformation behavior of tempered martensitic 9Cr-W steels. Metall. Mater. Trans. A 2005;36 A:321.
[11] Yamamoto Y, Takeyama M, Lu ZP, Liu CT, Evans ND, Maziasz PJ, Brady MP. Alloying effects on creep and oxidation resistance of austenitic stainless steel alloys employing intermetallic precipitates. Intermetallics 2008;16:453.
[12] Kuhn B, Talik M, Niewolak L, Zurek J, Hattendorf H, Ennis PJ, Quadakkers WJ, Beck T, Singheiser L. Development of high chromium ferritic steels strengthened by intermetallic phases. Mater. Sci. Eng., A 2014;594:372.
[13] Tarigan I, Kurata K, Takata N, Matsuo T, Takeyama M. Novel concept of creep strengthening mechanism using grain boundary Fe 2Nb Laves phase in austenitic heat resistant steel. Mater. Res. Soc. Symp. Proc., vol. 1295. p.317.
[14] Shingledecker J, Purgert R, Rawls P. Current status of the U.S. DOE/OCDO A-USC materials technology research and development program. Advances in Materials Technology for Fossil Power Plants - Proceedings from the 7th International Conference, 2014. p.41.
[15] Toda Y, Tohyama H, Kushima H, Kimura K, Abe F. Improvement in creep strength of precipitation strengthened 15Cr ferritic steel by controlling carbon and nitrogen contents. JSME International Journal, Series A: Solid Mechanics and Material Engineering 2005;48:35.

[16] Masuyama F. History of power plants and progress in heat resistant steels. ISIJ Int. 2001;41:612.
[17] Ishida K. Calculation of the effect of alloying elements on the Ms temperature in steels. J. Alloys Compd. 1995;220:126.
[18] Orowan E. Theory of dislocation bowing. London: Institute of Metals Symposium on Internal Stresses in Metals and alloys, 1948.
[19] Kelly A. The strength of aluminium silver alloys. Philos. Mag. 1958;3:1472.
[20] Ågren J, Clavaguera-Mora MT, Golczewski J, Inden G, Kumar H, Sigli C. Applications of Computational Thermodynamics: Group 3: Application of computational thermodynamics to phase transformation nucleation and coarsening. Calphad-Computer Coupling of Phase Diagrams and Thermochemistry 2000;24:41.
[21] Robert WC, P. Haasen. Physical Metallurgy. Amsterdam, North-Holland: Elsevier, 1996.
[22] Hald J, Korcakova L. Precipitate stability in creep resistant ferritic steels - Experimental investigations and modelling. ISIJ Int. 2003;43:420.
[23] Kostka A, Tak KG, Hellmig RJ, Estrin Y, Eggeler G. On the contribution of carbides and micrograin boundaries to the creep strength of tempered martensite ferritic steels. Acta Mater. 2007;55:539.
[24] Shibuya M, Toda Y, Sawada K, Kushima H, Kimura K. Effect of nickel and cobalt addition on the precipitation-strength of 15Cr ferritic steels. Mater. Sci. Eng., A 2011;528:5387.
[25] Xu W, van der Zwaag S. Property and cost optimisation of novel UHS stainless steels via a genetic alloy design approach. ISIJ Int. 2011;51:1005.

Chapter 7

A comparison of the design space for creep resistant steels with an austenitic, ferritic or martensitic matrices

7.1 Introduction

Precipitation Hardening (PH) and Solid Solution Strengthening (SSS) are the two principal strengthening mechanisms to improve the strength in the design of new metallic alloy. Different matrices, such as ferritic, austenitic and martensitic, will influence the maximal strengthening and may favour certain strengthening mechanisms. For instance, ferritic steels have a much higher optimal SSS value than martensitic steels. If the full potential of each matrix for both PH and SSS is known, a better solution can be chosen depending on the conditions of the practical application. In Chapter 4, PH and SSS are optimally combined in martensitic steels via the construction of a “Pareto front” of PH and SSS contributions for all qualified solutions (composition and heat treatment). This concept can also be also applied in the design of ferritic and austenitic steels. In this chapter, we summarize the previous design strategies for ferritic, austenitic and martensitic steels and then simultaneously optimise PH and SSS for ferritic, austenitic and martensitic steels. The results are put together to show the impact of the matrix on the optimisation.

7.2 Alloy by design Methodology

The design methodology follows the same philosophy as stated in previous chapters. The performance of such a design process highly relies on two key steps as shown in **Figure 7.1**: the 'translator' for the correlation from mechanical properties to the required microstructures, and the 'creator' to link desirable microstructures to alloy composition (genome) and heat treatments (experience) employing established metallurgical principles [1]. The criteria are defined by the creator as indicated in **Figure 7.1** and classified either as go/no-go or as optimization criteria reflecting different considerations/requirements. The go/no-go criteria were evaluated to eliminate non-eligible solutions and then the optimization criteria were assessed to obtain an optimal performance factor. In order to avoid local optimization, a genetic algorithm using a single optimisation parameter is employed to search the entire multi-parameter space and to achieve the optimal solution effectively and efficiently.

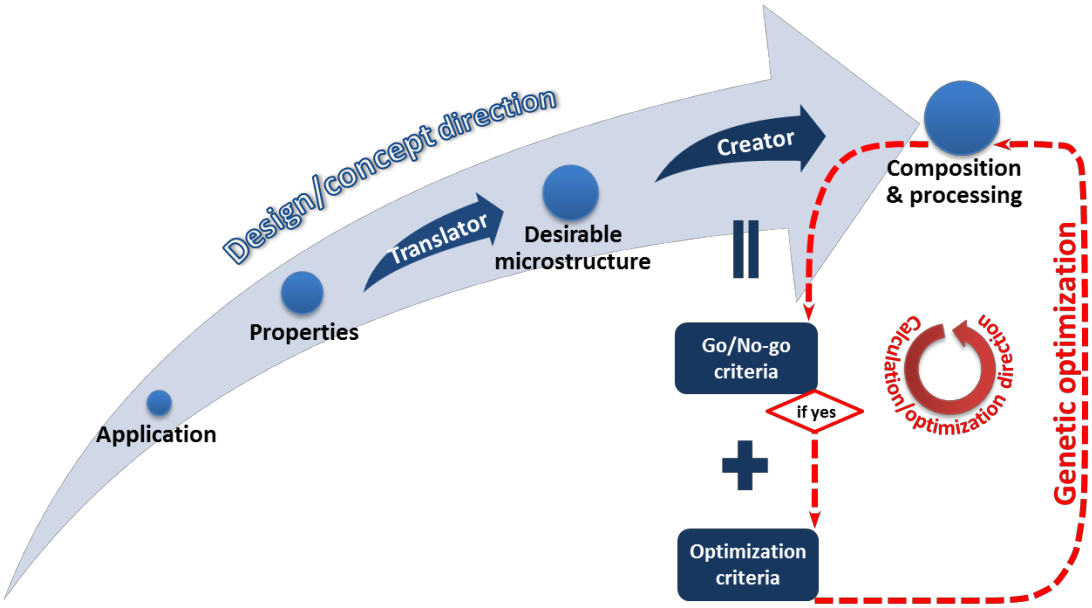

Figure 7.1 Flow chart of the alloy design strategy and optimization.

The actual optimisation route follows the direction of the red arrows (right hand side of **Figure 7.1**). The genetic algorithm generates random solutions (combinations of composition and heat treatment parameters), over wide ranges which were set considering the physical and practical constraints. Necessary calculations to evaluate the

go/no-go criteria can therefore be performed accordingly and only for those fulfilling all go/no-go criteria, which suggests that desirable microstructure is obtained, are eligible for further extra calculations to evaluate and optimize the performance factor as listed in Table 7.1.

To obtain the microstructure strategy and strengthening mechanisms, the translator has to consider the microstructure evolution and detail its evolution throughout the entire heat treatment, as summarized in Table 7.1. The creator therefore generates quantitative criteria associated with each microstructure requirement based on physical metallurgical principles. The quantities calculated in the creator as shown in Table 7.1 are calculated either by thermodynamics (via ThermoCalc®) at the corresponding temperatures or physical metallurgy formulas, e.g. all phase fractions/compositions are calculated by equilibrium thermodynamics and T_{Ms} is martensite starting temperature, which is calculated by an empirical formula as a function of austenite composition and used to ascertain the occurrence of the martensitic transformation upon cooling to room temperature.

Table 7.1 Key parameters in the Translator and Creator for each type of the target alloy:

	Translator: desirable microstructure			Creator: link the microstructure to composition and heat treatment				
	Austenitization/ annealing temperature	Room Temperature	Ageing/Service temperature	**Go/nogo criteria**				**Optimisation criteria/ Performance factor**
				Austenitization/annealing temperature		T_{Ms} (K)	Ageing/Service temperature	
FCS	Ferrite	Ferrite	Ferrite with sufficient Cr and best solid solution in matrix	$V_{Ferrite}$ > 99 vol.%	No liquid $V_{primary\ carbide}$ < 0.5 vol.%	None	Cr in matrix> 12 mass % Undesirable phase< 1 vol.%	σ_{ss}
ACS	Austenite	Austenite	Austenite with sufficient Cr + optimal precipitates (MX carbonitride)	$V_{Austenite}$ > 99 vol.%		<298	Cr in matrix>16 mass% Sigma< 4 %vol.%, Undesirable phase (Sigma phase excluded)<1vol. %	$\sigma_{p(t)}$
MCS	Austenite	Martensite	Martensite with sufficient Cr + best solid solution + optimal precipitates (MX carbonitride)	$V_{Austenite}$ > 99 vol.%		>473	Cr in matrix>11 mass% Undesirable phase<1 vol.%	σ_{ss} & $\sigma_{p(t)}$

The details of the performance factors defined for the different alloy types listed in Table 7.1 are introduced in the following. The PH values in creep resistant steels vary with time and temperature due to the significant growth and coarsening of precipitates during service. Considering the coarsening kinetics [2-4], as explained in more detail in Chapter 2, the PH contribution $\sigma_{p(t)}$ is estimated from

$$\sigma_{p(t)} \propto 1/L = \sqrt{f_p}/r = \sqrt{f_p}/\sqrt[3]{r_0^3 + Kt} \tag{7.1}$$

where L, r_0 and f_p are the average inter-particle spacing, critical precipitate nucleus size and volume fraction of MX carbonitride, respectively. K is the coarsening rate depending on the equilibrium interfacial concentrations gradient of the relevant chemical elements on both the matrix and the precipitate sides, corresponding diffusion coefficient of these elements, interfacial energy and the service temperature. The involved thermodynamic values are obtained via Thermo-Calc® using the TCFE6 and Mob2 databases.

Despite the evolution of the PH factor during the service, the composition of the matrix remains constant once the thermodynamic equilibrium is achieved and hence the SSS in the matrix also remains stable. As stated in Chapter 3, in both ferritic/martensitic [5, 6] and austenitic steels [7], the SSS value depends linearly on concentrations of elements in the matrix, as described by the following equation,

$$\sigma_{ss} = a_1 \sum K_i C_i \tag{7.2}$$

where K_i is the strengthening coefficient for 1 at.% of alloying element i, C_i is the atomic percentage of the alloying element i in solution, a_1 is a temperature dependent scalar.

The strengthening coefficient values per at% alloying element for austenitic and ferritic/martensitic matrices are listed in Table 7.2 [4, 7, 8].

Table 7.2 Strengthening coefficient for alloying elements at room temperature (MPa per at.%) for ferritic/martensitic and austenitic matrices.

Element	C	N	Si	Ni	Ti	Mn	Mo	Al	Cr	Co	V	W	B	Cu
K_i *(ferrite/martensite)*	1103	1103	25.8	19.2	17.9	16.9	15.9	9.0	2.6	2.1	2.0	31.8		
K_i *(austenite)*	73.7	198.2	6.7	-1.0		2.6	18.0			1 .7	10.7	25.0	50.0	5.7

7.3 Results and discussion

The design of advanced creep resistant steels for high-temperature use is presented taking into account the three matrix types possible (Ferritic (FCS), Martensitic (MCS), Austenitic (ACS). Each matrix may effectively employs different (combinations of) specific strengthening mechanisms, i.e., FCS utilizes primarily solid solution strengthening (SSS); MAS and ACS primarily apply precipitation hardening (PH) while MCS combines both SSS and PH mechanisms. In the steel grades to be optimised the grain size, a non-thermodynamically addressable quantity, only plays a minor role in achieving the required performance level.

In order to validate the PH and SSS formulas employed, the calculated PH and SSS values of various existing ferritic, martensitic and austenitic creep resistant steels on the basis of alloy composition and use time are compared to experimental values. The results are shown in **Figure 7.1**. Notwithstanding the different matrix types and in strengthening mechanisms, a very good agreement between the calculated strength and existing experimental results was obtained, which indicates that the computational evaluations of the strengthening contributions of various types were appropriate and can be implemented in discovering new alloys.

Applying the approach, the optimal compositions and heat treatment parameters of FCS, MCS and ACS steels were optimised. To demonstrate the potential of newly designed alloys, they are benchmarked against the existing high-end counterparts. **Figure 7.2** shows the separate contributions of SSS and PH in both newly designed creep resistant steels FCS, MCS, ACS and in their existing commercial counter-partners. Alloy FCS, which is designed to be strengthened by SSS only has a significantly higher SSS contribution than existing ferritic creep resistant steels. Similarly, Alloy ACS, which is optimized solely for PH, has a much higher PH than that of existing austenitic ones. Finally alloy MCS which optimally combines PH and SSS, a Pareto front consisting of new solutions substantially superior to existing counterparts both in SSS and PH contributions. To construct this Pareto front, two separated optimisations were performed respectively: either only for PH factor, or only for SSS factor, and then all the qualified solutions were put together. The turning point in the Pareto front indicates the optimal composition (alloy MCS). Moreover, other compositions on the Pareto front can also have better PH and SSS values than those of existing steels. Therefore, the current model can design alloys with exceptional SSS or PH values, or combinations thereof.

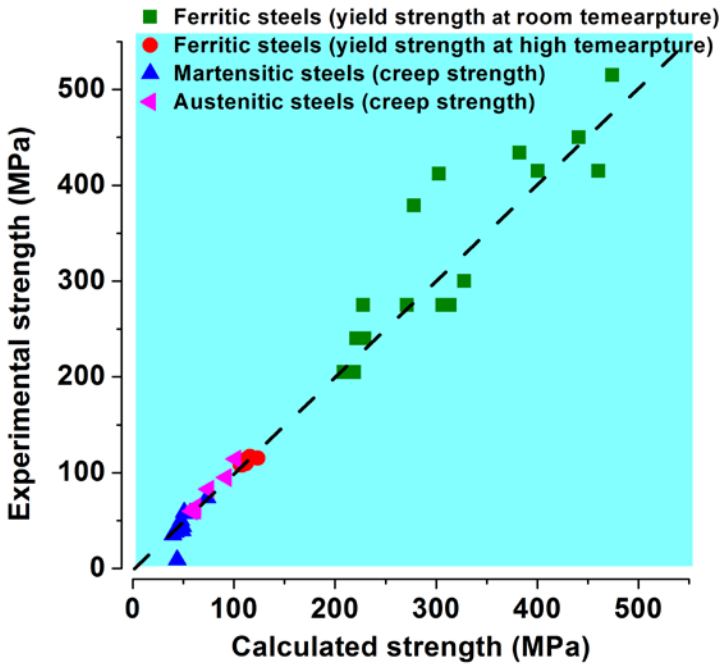

Figure 7.1. Calculated strength vs. experimental strength for the four different types of stainless steels considered

The above study of simultaneous optimisation of PH and SSS was applied to creep steels having a (tempered) martensitic matrix. We can extend the approach to other systems, for instance, by simultaneously optimising PH and SSS in austenitic or ferritic matrices. Moreover, MX carbonitride is not the only option for the precipitate family, intermetallics such as Ni_3Ti can also used as the desirable phases,. The results for austenitic, ferritic and martensitic matrices are presented in **Figure 7.3a** and **7.3b**. Significant differences between three matrices can be found. Austenitic matrices offer the highest PH contribution of MX carbonitrides, but the lowest SSS. Ferritic steels have the greatest capacity for SSS, but have a low PH contribution. The martensitic steels allow the best combination of both strengthening sources. These observations also apply to the Ni_3Ti strengthened variants, albeit to a lesser degree as the options to create Ni_3Ti particles at high volume fractions are limited. In summary, the plots of **Figure 7.3** clearly indicate the design space given the nature of the matrix.

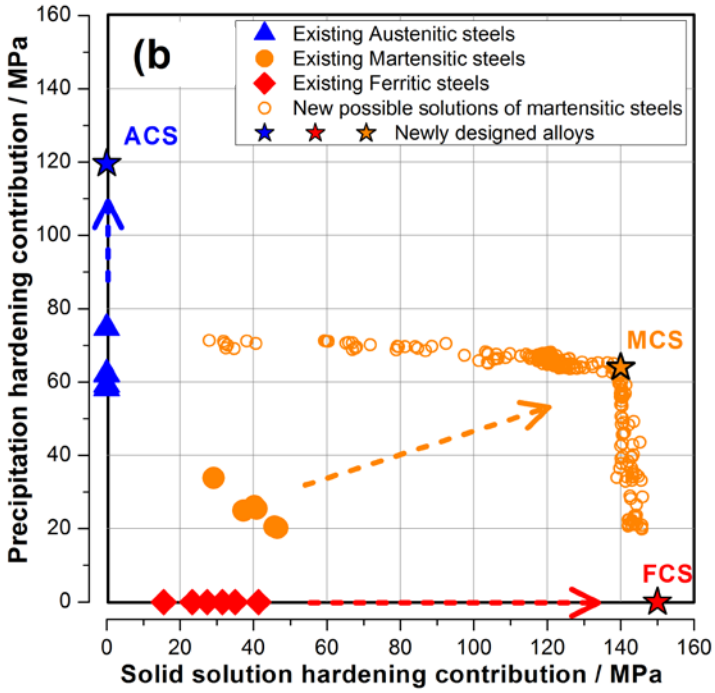

Figure 7.2. Comparison of designed and existing creep resistant alloys.

Precipitate coarsening has a significant effect on the PH contribution in particular when the intended service time becomes 10^5 h or even longer. To demonstrate the effect of coarsening rates on the strength, the solutions in **Figure 7.3b** are taken as examples and each solution (dot) is mapped with its own coarsening rate, as shown in **Figure 7.3c**. Clearly, Ni_3Ti has the lowest coarsening rate in an austenitic matrix, followed by that in martensitic and ferritic matrices, respectively. This is due to the low diffusion rate of alloying elements in an austenitic matrix. A lower coarsening rate also leads to a higher PH factor at the end of the service time. In addition, the solutions of NbX carbonitride strengthened martensitic steels on the Pareto front are also chosen and mapped with coarsening rates, as indicated in **Figure 7.3c**. The coarsening rates of NbX carbonitride are much slower than those of Ni_3Ti in martensitic matrix, indicating that carbonitrides are the preferred precipitate family for applications with ultra-long service time

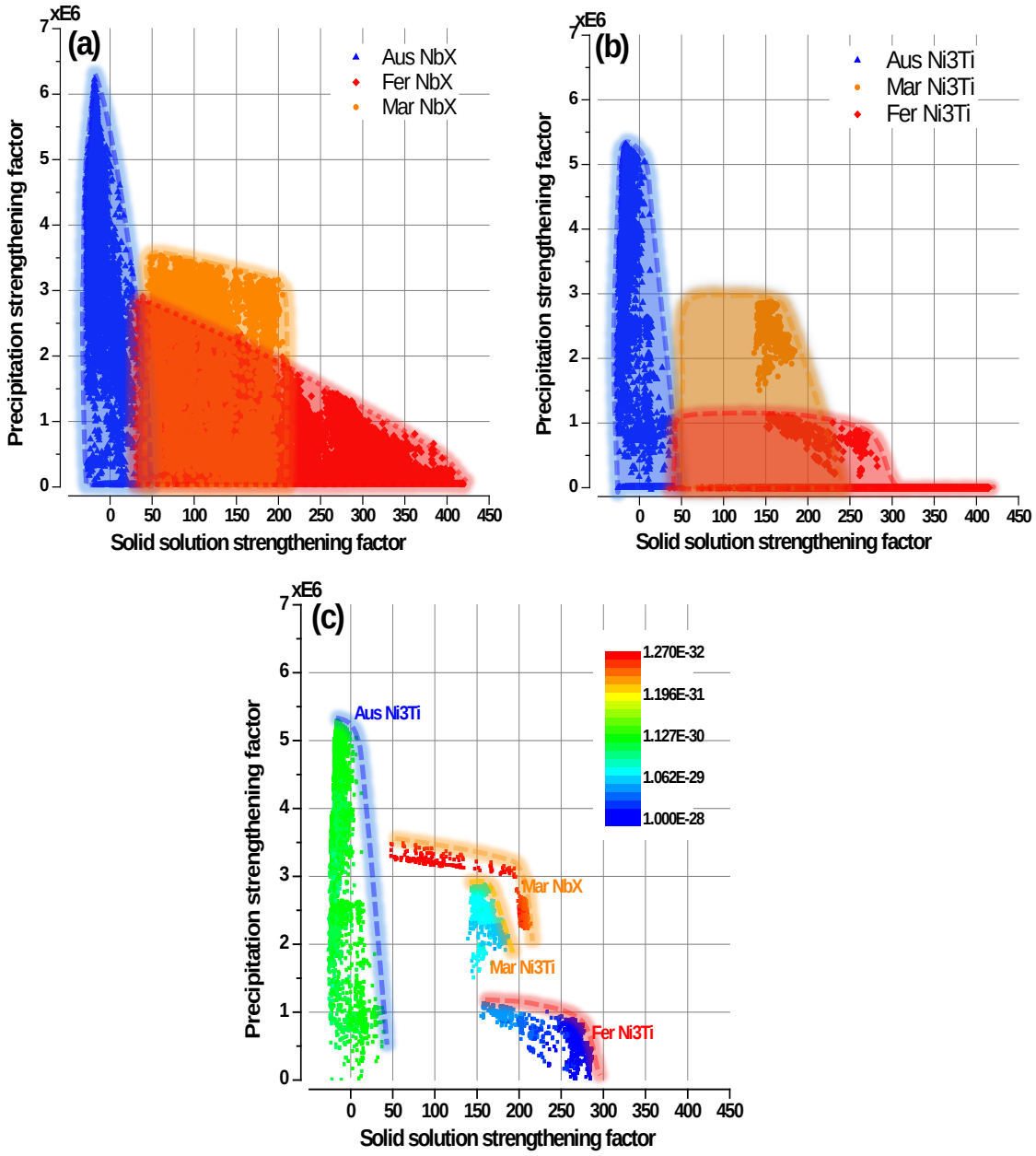

Figure 7.3. (a) optimisation of PH of NbX carbonitride and SSS in austenitic, martensitic and ferritic matrices, (b) optimisation of PH of Ni_3Ti and SSS in austenitic, martensitic and ferritic matrices, (c) mapping the solutions in Ni_3Ti strengthened systems with coarsening rates. In addition, the solutions on the Pareto front of NbX carbonitride strengthened martensitic steels are also mapped with coarsening rate and shown in (c) to compare to Ni_3Ti with the same matrix.

7.4 Conclusions

The alloy design approach works well for the three types of creep resistant steels and presents well-defined compositions and heat treatment parameters ideally suited to start

experimental development programs aimed at validation of the predicted high performance levels while at the same time addressing all pertinent technological challenges. The predicted optimal compositions are unlikely to be found in a realistic time via an empirical approach and the results as presented here clearly demonstrate that the computational alloy design approach holds great promise of substantially shortening the development time of new high-performance steel grades.

References

[1] Xu W, Lu Q, Xu X, van der Zwaag S. The structure of a general materials genome approach to the design of new steel grades for specific properties. Comput. Methods in Mater. Sci. 2013;13:382.
[2] Kelly A. The strength of aluminium silver alloys. Philos. Mag. 1958;3:1472.
[3] Ågren J, Clavaguera-Mora MT, Golczewski J, Inden G, Kumar H, Sigli C. Applications of Computational Thermodynamics: Group 3: Application of computational thermodynamics to phase transformation nucleation and coarsening. Calphad-Computer Coupling of Phase Diagrams and Thermochemistry 2000;24:41.
[4] Robert WC, P. Haasen. Physical Metallurgy. Amsterdam, North-Holland: Elsevier, 1996.
[5] Gypen LA, Deruyttere A. The combination of atomic size and elastic modulus misfit interactions in solid solution hardening. Scr. Metall. 1981;15:815.
[6] Takeuchi S. Solid-solution strengthening in single crystals of iron alloys. J. Phys. Soc. Jpn. 1969;27:929.
[7] Pickering FB. Physical metallurgy and the design of steels. London: Applied Science Publishers LTD, 1978.
[8] Leslie WC. Iron and its dilute substitutional solid solutions. Met Trans 1972;3:5.

Chapter 8

Experimental validations

8.1 Alloy compositions

In order to validate the computational alloy design approach as described in the previous chapters, five prototype alloys with ferritic, martensitic or austenitic matrix were fabricated and tested at Institute of Metal Research, Chinese Academy of Science. These alloys were either optimised by Solid Solution Strengthening (SSS), Precipitation Hardening (PH) via MX carbonitrides, or a combination thereof. The austenitic steel, solely optimised on the PH factor by applying the model in Chapters 2 and 6, is termed APH. Another alloy having a ferritic matrix was designed with an optimal SSS using the model in Chapter 3, which is called FSSS. The other three alloys are all martensitic steels, and had compositions based on the application of the model developed in Chapter 4. These alloys have different combinations of SSS and PH, and are labelled as MSSI, MPHI and MPHS. Their calculated positions with respect to the existing corresponding high end creep resistant steels are indicated in **Figure 8.1.** Alloy MSSI has an optimal SSS factor but a low PH factor, alloy MPHI is designed to possess a high PH factor but a relatively low SSS factor, while alloy MPHS holds the best combination of PH and SSS factors. Besides optimised strengthening features, all five alloys have a acceptable (low) amount of undesirable phases. The designed and actual steel compositions and heat

treatment schemes are listed in Table 8.1. The composition of an existing very well performing high-end martensitic steel P92 is also listed in Table 8.1 to benchmark the designed martensitic steels.

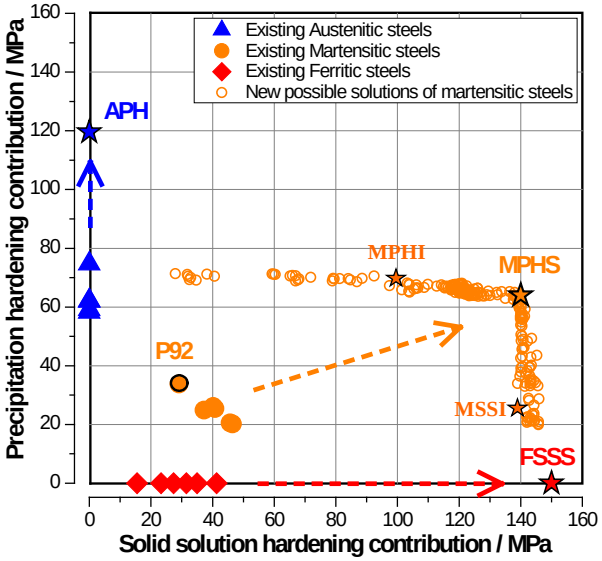

Figure 8.1 Location of the five steels produced in the PH-SSS domain, as well as the position of important commercial steels and the industrial reference steel P92.

Table 8.1 The designed and actual alloy compositions (in wt.%) and austenitization/ annealing temperatures (in °C) of alloys APH, FSSS, MPHI, MPHS and MSSI. The actual composition and austenitization temperature of reference alloy P92 is also listed.

		C	Cr	Ni	Ti	Mo	Al	W	Co	Nb	N	V	Mn	Si	Taus/ Tanneal
APH	design	0.060	17.58	21.16	0.15						0.047		1.00	0.50	1234
	actual	**0.050**	**16.77**	**20.20**	**0.087**						**0.053**		**1.04**	**0.55**	**1200**
MSSI	design	0.044	11.36	3.88		1.29	2.74		7.42	0.16	0.020				1239
	actual	**0.043**	**11.30**	**4.80**		**1.22**	**2.68**		**6.99**	**0.18**	**0.015**				**1200**
MPHI	design	0.064	11.1	2.91	0.15		0.16		4.84	0.30	0.025				1250
	actual	**0.061**	**10.65**	**3.05**	**0.15**		**0.34**		**4.78**	**0.30**	**0.019**				**1200**
MPHS	design	0.073	11.36	3.88	0.15		3.55		9.68	0.30	0.035				1250
	actual	**0.068**	**10.89**	**3.82**	**0.16**		**3.39**		**9.14**	**0.30**	**0.019**				**1200**
FSSS	design		12.27	2.10	1.86	3.79	5.25					1.75	10.69	3.35	1200
	actual		**12.77**	**2.25**	**2.06**	**3.99**	**5.52**					**1.82**	**6.90**	**3.55**	**1200**
P92 [1]	actual	0.07	9.00			0.50		1.80		0.05	0.06	0.2	0.45	0.1	1050

8.2 Experimental procedures

All prototype alloys were fabricated, processed and tested at Institute of Metal Research, Chinese Academy of Science. The alloys were prepared in a vacuum induction melting furnace as ingots of approximately 10 kg. The ingots were produced using high purity ingredients to achieve the best cleanliness. Phosphorus, Sulphur, Arsenic, Boron and Tin were controlled to the lowest possible levels. The melting temperature was kept relatively low at about 1773 K and the chamber was flushed with Argon. Alloy FSSS ingot was found to be too brittle to be rolled, and even fractured spontaneously before rolling as indicated in **Figure 8.2a**. The ingots of the other four alloys were ground to smoothen their surface and to remove the oxide scale, soaked at 1473 K for 2 h and subsequently forged into a slab at a finishing temperature above 1173 K. The slabs were reheated to 1473 K for 2 hours, and subsequently hot rolled into plates of 7 mm thickness, as shown in **Figure 8.2b**, by 6 consecutive passes in the temperature range of 1323-1073 K, followed by air cooling. The heat treatment scheme for as hot rolled material is shown in **Figure 8.3**. To dissolve undesirable precipitates or phases formed during casting and hot rolling, and to achieve a homogeneous matrix, solution treatments were performed on the rolled sheets of prototype alloys and P92, followed by a water quench. Then, the ageing treatments were conducted at 923 K from 5 minutes up to 1000 h, followed by natural cooling. The Vickers hardness was measured with a load of 0.2 N. The microstructures were investigated by optical microscopy (OM), scanning electron microscopy (SEM). X-ray Diffraction (XRD) was also applied to identify phases. Optical microscopy and SEM were carried out on specimens etched with Villela's reagent. Carbon replica’s containing the strengthening precipitates were prepared at OCAS and investigated by TEM with energy dispersive X-ray detector (EDX) to analyse the chemical composition of specific areas.

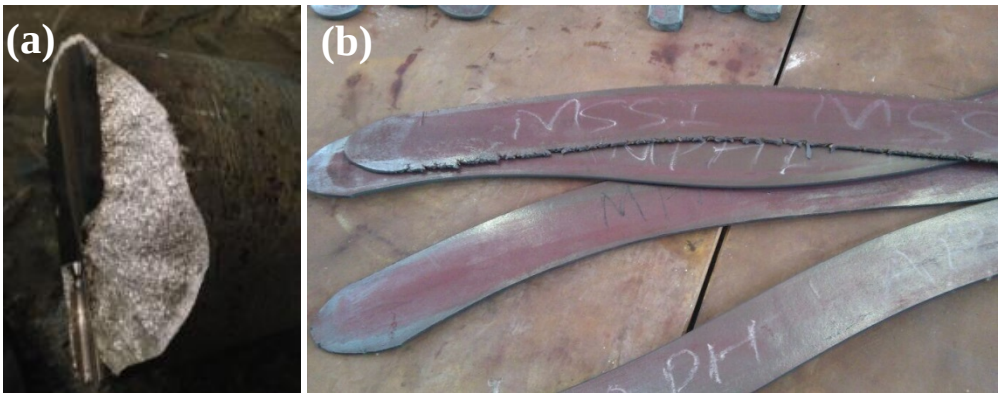

Figure 8.2 (a) As casted alloy FSSS, (b) hot rolled plates with a thickness of 7 mm of alloys MPHI, MPHS, MSSI and APH.

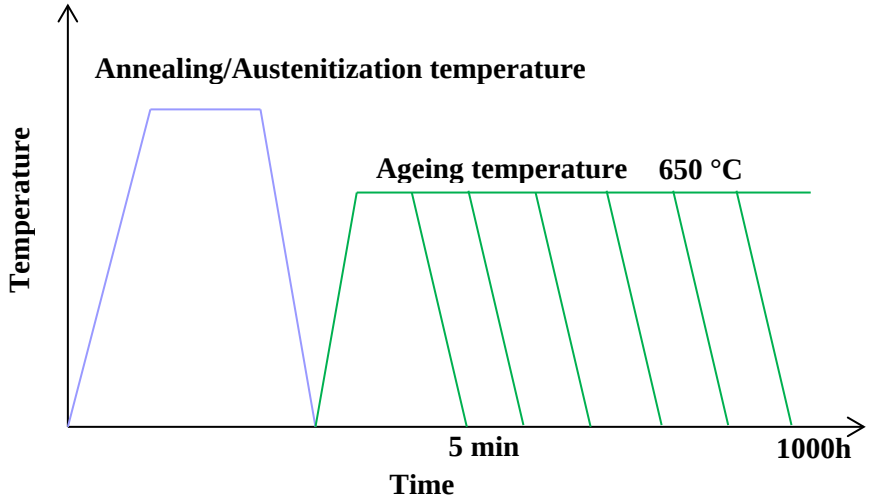

Figure 8.3 Heat treatment schemes of all designed alloys

8.3 Results

8.3.1 Solution treatment

8.3.1.1 Microstructures after solution treatment of all designed alloys and P92

The microstructure after solution treatment of all experimental alloys and the reference steel P92 are shown in **Figures 8.4-8.9**. Alloy APH has a homogeneous microstructure

and a significant amount of twins (**Figure 8.4a**). Some big primary TiN were found as indicated by white arrows. Furthermore, the XRD pattern in **Figure 8.4b** confirmed a fully austenitic matrix as intended.

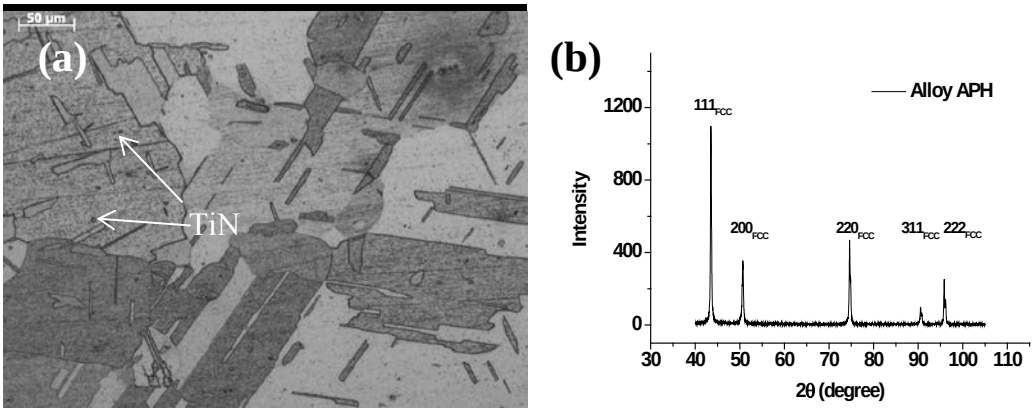

Figure 8.4 Optical micrographs (a) and XRD pattern (b) of alloy APH after solution treatment at 1200 °C for 2 h followed by water quench.

Figure 8.5a shows some large precipitates along the grain boundaries and inside the grains in alloy FSSS after its solution treatment at 1200 °C for 2 h. The results of the EDS analysis plotted in **Figure 8.5c** indicate that the precipitates have a composition $Fe_{50}(Si_{13.29}Ti_{8.12}Mo_{3.56})$, i.e. $Fe_2(Si, Ti, Mo)$, which is a typical composition for the Laves phase. The XRD pattern in **Figure 8.5d** further confirms that this phase has a Laves phase structure, i.e. has an HCP structure. The other diffraction peaks all belong to the BCC matrix. To dissolve the undesirable Laves phase, which may cause the room temperature brittleness, a second solution treatment at a higher temperature (1250 °C) and for a longer time (5 h) was performed on alloy FSSS, and the resulting microstructure is shown in **Figure 8.5b**. Unfortunately, although the amount of precipitates was reduced, still a large amount of Laves phases was present both in the grains and along the grain boundaries.

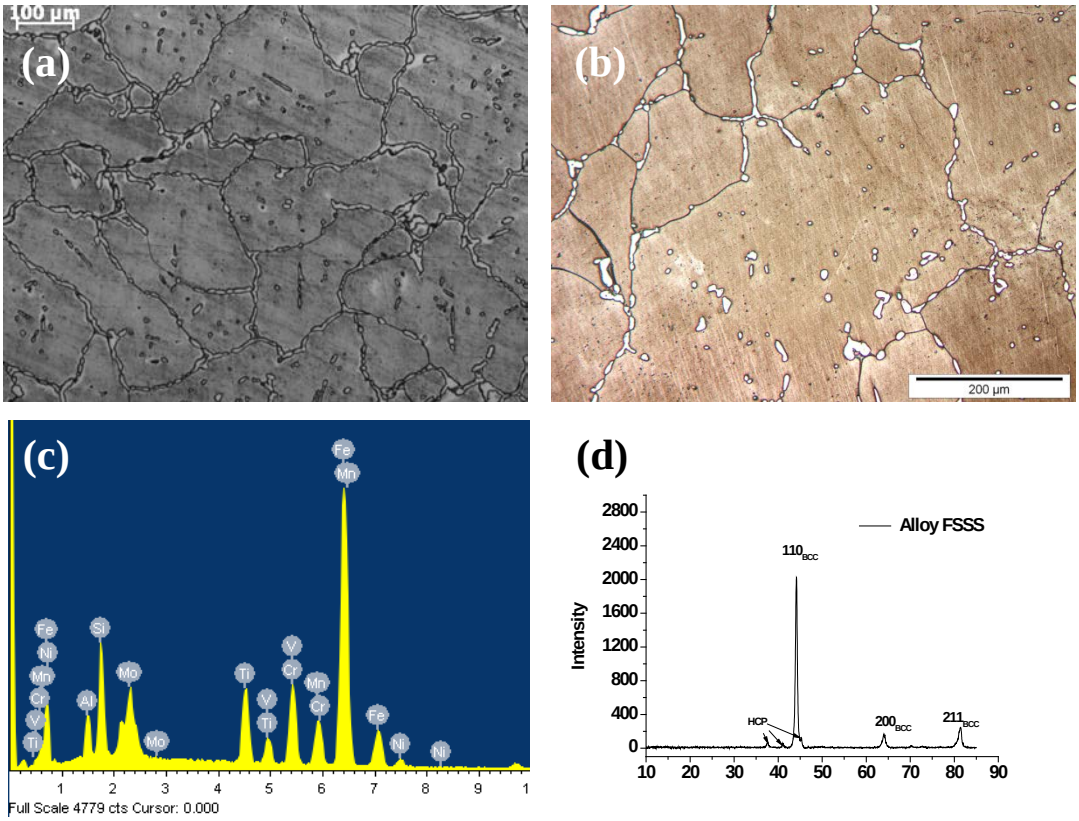

Figure 8.5 Optical micrographs of alloy APH after solution treatments at (a) 1200 °C for 2 h, (b) 1250 °C for 5 h, followed by water quench. (c) The EDS analysis of the precipitate on the grain boundary and (d) XRD pattern of condition (a).

Figure 8.6a shows that alloy MSSI had a partial martensitic matrix, rather than the intended fully martensitic structure after the solution treatment at 1200 °C for 2 hours. The XRD pattern of this alloy shown in **Figure 8.6b** only displays the BCC peaks as XRD cannot distinguish between martensite and ferrite at low carbon steels.

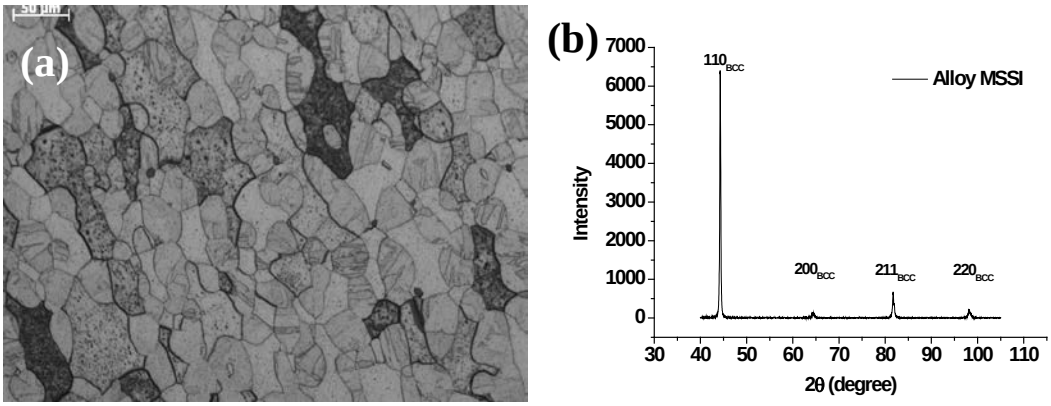

Figure 8.6 Optical micrographs (a) and XRD pattern (b) of alloy MSSI after the solution treatment at 1200 °C for 2 h followed by water quench.

Similarly, alloy MPHS also had a martensite-ferrite matrix instead of the intended fully martensitic matrix after the same solution treatment, as indicated in **Figure 8.7a and 8.7b.** The only difference is that alloy MPHS displays a lower amount of martensite than alloy MSSI.

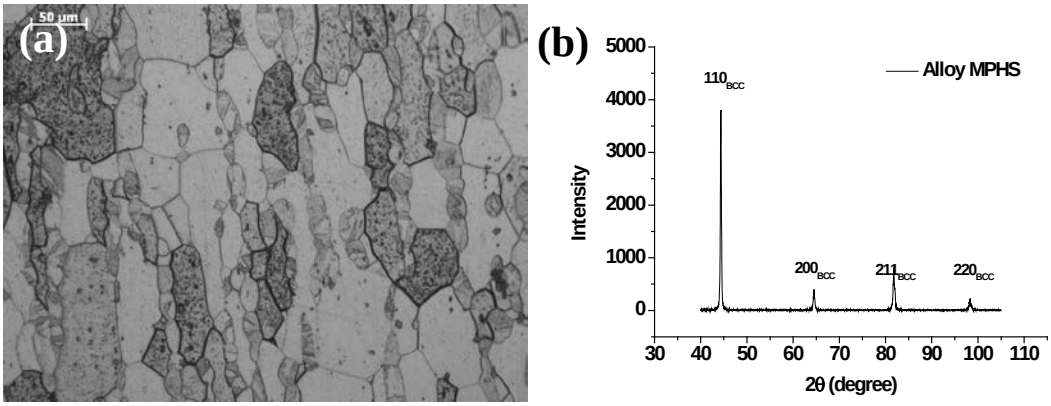

Figure 8.7 Optical micrographs (a) and XRD pattern (b) of alloy MPHS after the solution treatment at 1200 °C for 2 h followed by water quench.

Unlike alloys MPHS and MSSI, **Figure 8.8a** shows the exactly intended fully martensitic matrix in alloy MPHI after the solution treatment at 1200 °C for 2 h. In **Figure 8.8b,** the XRD pattern of alloy MPHI confirms the absence of retained austenite. In addition, **Figure 8.8a and 8.8c** shows some remaining undissolved large particles after solution treatment, which were identified as primary carbonitrides (TiNb)(CN), on the basis of their morphology and the EDS analysis shown in **Figure 8.8d**.

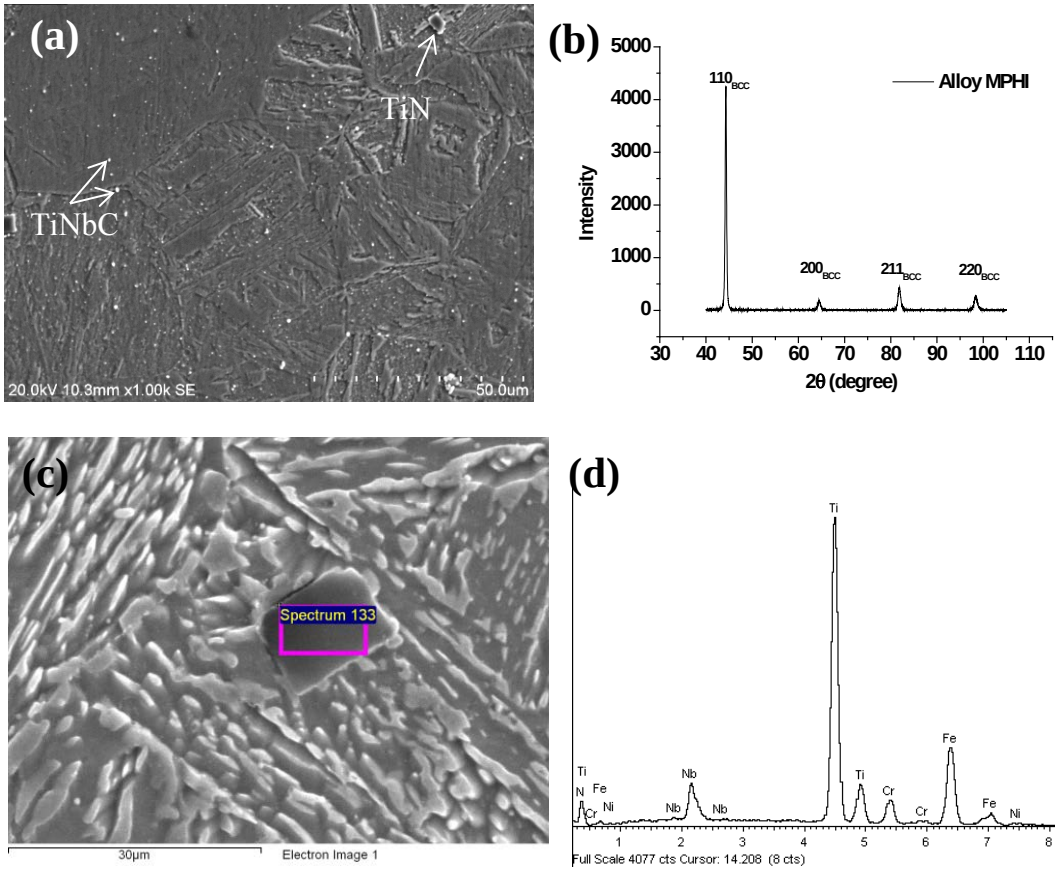

Figure 8.8 SEM Micrographs (a), (c), and XRD pattern (b) of alloy MPHS after the solution treatment at 1200 °C for 2 h followed by water quench. The EDS analysis (d) is performed in the indicated area in (c).

In **Figure 8.9a**, a fully lath martensitic structure was found in the reference alloy P92 after solution treatment at 1050 °C for 2 h, which is in accordance with existing reports. In addition, a small amount of undissolved primary carbonitrides, indicated by arrows in **Figure 8.9b**, was observed

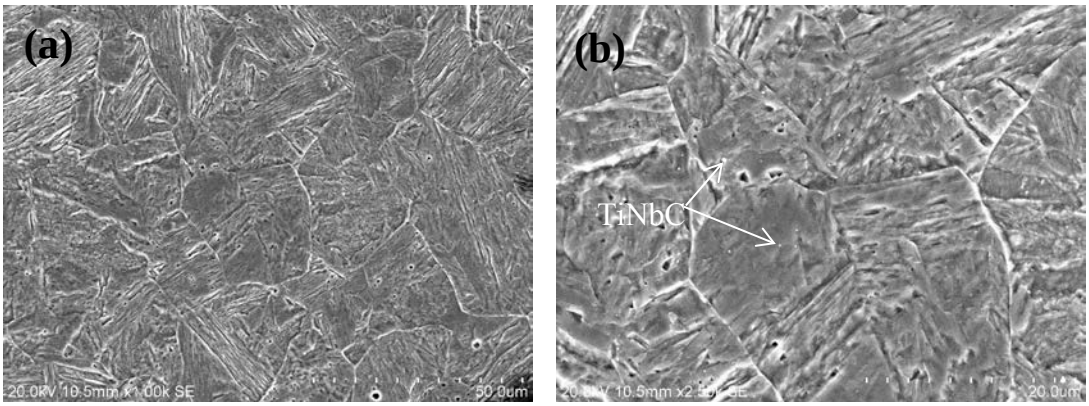

Figure 8.9 SEM micrographs of alloy P92 after the solution treatment at 1050 °C for 2 h followed by water quench.

In summary, alloys APH, MPHI and FSSS did achieve the intended matrix structure after the imposed solution treatments. A few primary carbonitrides were observed in alloys APH and MPHI while a large amount of Laves phase was present in alloy FSSS. Alloys MPHS and MSSI have a duplex (martensite-ferrite) matrix rather than the intended fully martensitic matrix. The solution treatments applied for them were not effective enough to reach the full austenitic state , and contained a significant amount of ferrite. Analysis of the compositions of alloys achieving (or not achieving) the target microstructure shows that the alloys can be separated according to the Al content. For alloys FSSS, MPHS and MSSI with high Al contents, the prediction clearly deviates from experimental results while the alloys with low Al contents achieve desirable microstructures. This suggests the thermodynamic database for higher Al level needs to be improved.

8.3.1.2 Hardness of all alloys after solution treatments

The initial hardness of all designed alloys in the as quenched condition (with corresponding optimal soaking condition as listed in Table 8.1) was measured and the results are shown in **Figure 8.10**. Interestingly, alloy FSSS has an exceptional high hardness, (the data point was taken taken from an area free of Laves precipitates) compared to other steels. This implies that solid solution contributes very significantly to the strength while the ductility is limited. The austenitic alloy APH has the lowest hardness since austenite is softer than martensite by nature. Moreover, alloys MPHS and MSSI having a combination of soft ferrite and harder martensite still show comparable hardnesses with respect to the fully martensitic steels MPHI and P92. This indicates that

the SSS contributions in alloys MPHS and MSSI are significant, resulting in a much stronger martensitic matrix than those of MPHI and P92, which is exactly the design strategy, i.e. combining the PH and SSS.

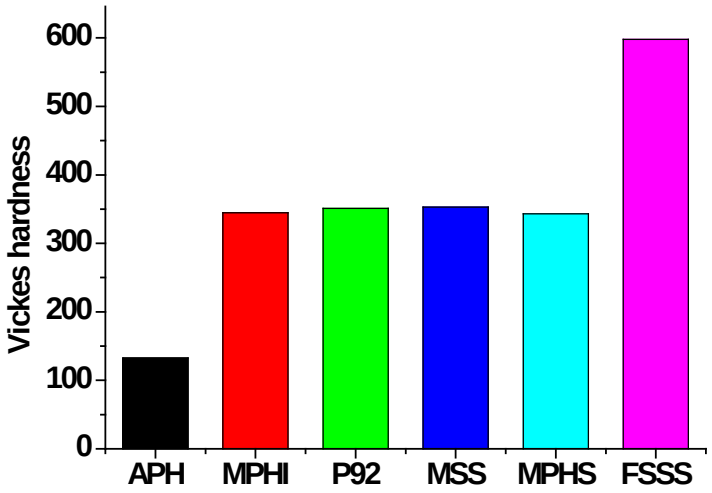

Figure 8.10 Hardness of alloys APH, MPHS, MSSI, MPHI and P92 after solution treatments for 2 h followed by water quench.

8.3.2 Hardness and microstructure evolution during ageing treatment

To show the microstructural and mechanical stability of all experimental alloys except alloy FSSS (which could not be rolled), the as quenched materials were subjected to ageing at the intended service temperature, i.e. 650 °C for various length of time ranging from 5 minutes to 1000 hours. The same ageing treatment was performed for alloy P92. In **Figure 8.11**, the hardness evolution of all alloys during ageing is shown (0 s refers to the as quenched condition). The austenitic alloy APH has the lowest as-quenched hardness due to the soft matrix compared to that of martensitic one. However, the hardness of alloy APH is very stable until 300 h, and then increases notably. This phenomenon will be discussed later. The other four martensitic steels show a similar hardness in the as-quenched condition.The hardness of alloys MPHS and MSSI increases significantly after ageing for 1 h, and then decreases upon further aging but still remains higher than those of alloys MPHI and P92 annealed for the same time. The hardness of alloy MPHI and P92 does not have a notable increase during ageing, and gradually

decreases with ageing time at different kinetics. The hardness degradation rate of alloy MPHI is much slower than that of alloy P92, resulting in a higher hardness at the longest annealing time of 1000 h.

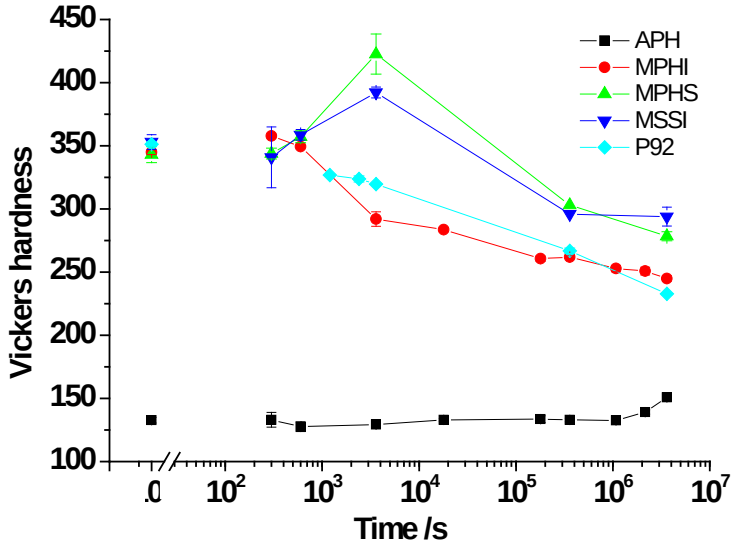

Figure 8.11 Hardness evolution of alloys APH, MPHS, MSSI, MPHI and P92 during ageing at 650°C.

The microstructures of all alloys after ageing were studied to interpret the hardness evolution. **Figure 8.12** shows the microstructure of alloy APH after different ageing times. At short ageing times there are only primary nitrides in the matrix (**Figure 8.12a**). The needle-shaped particles can be found in twin boundaries and in the grain interiors after ageing for 100 h, as shown in **Figure 8.12b**. The twin boundaries seem to be preferential sites for the formation of this needle-shape particle since the particles located there are larger than those within the grain. This may be due to a relative fast diffusion rate of elements at twin boundaries. **Figures 8.12c** and **8.12d** show that the needle shape particles become larger with increasing ageing time. This needle-shaped particle may explain the increase of hardness after 300 h (**Figure 8.11**).

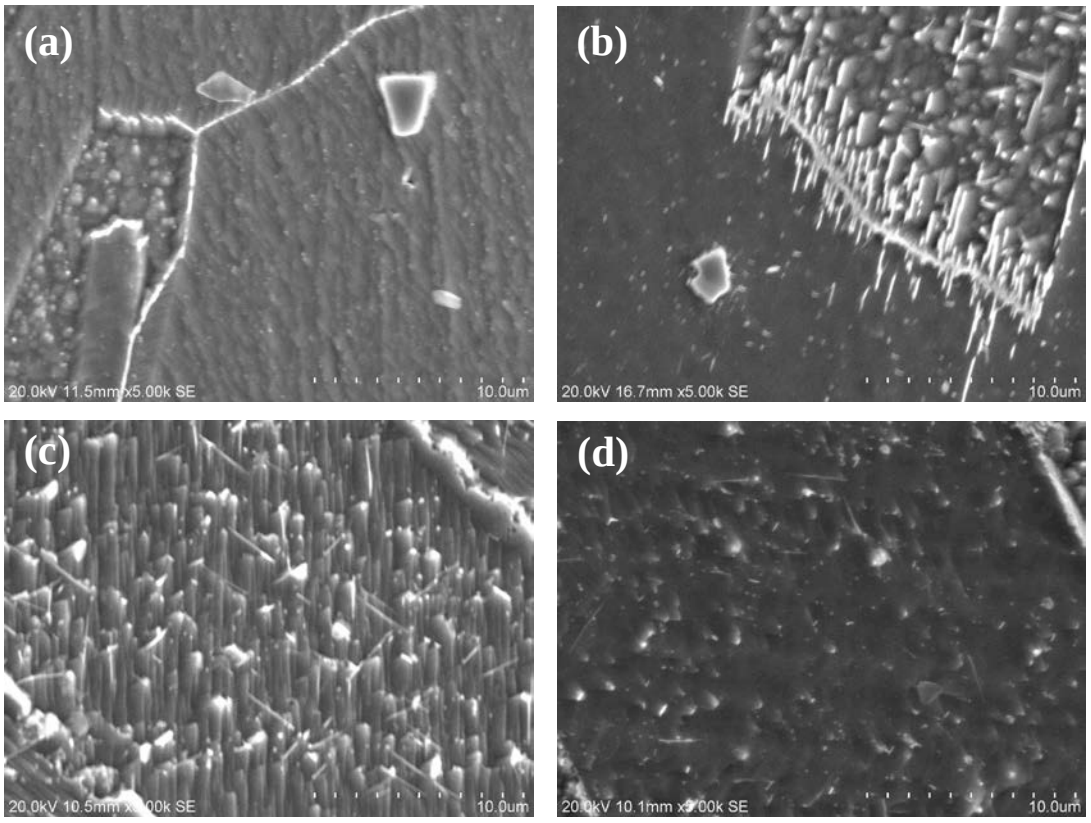

Figure 8.12 SEM micrographs of alloy APH after ageing at 650 ^{o}C for (a) 5 h, (b) 100 h, (c) 600 h and (d) 1000 h.

Figure 8.13 shows the microstructure evolution of alloy MPHS during ageing at 650 °C. A mixture of martensite and ferrite in alloy MPHS was observed in **Figure 8.13a**. Besides the large primary carbonitrides, very fine and evenly distributed particles in both martensite and ferrite can be identified after ageing for 100 h and longer time (**Figure 8.13b, 8.13c and 8.13d**). The size of these homogeneous particles increases significantly with ageing time.

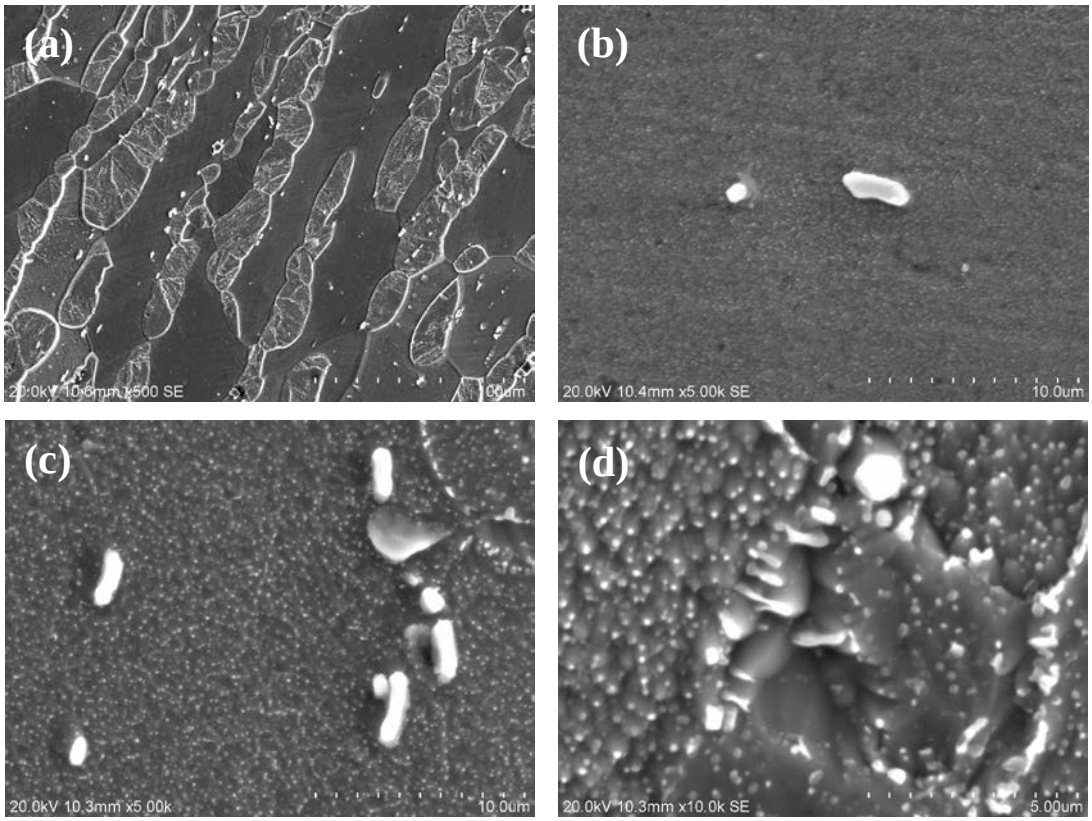

Figure 8.13 SEM micrographs of alloy MPHS after ageing at 650 ^{o}C for (a) 1 h, (b) 100 h, (c) 1000 h and (d) 1000 h at a higher magnification.

Similarly, **Figure 8.14** shows that alloy MSSI also has fine and even distribution of strengthening particles. The average particle size after ageing of 1000 h is similar to that of alloy MPHS. The presence of these particles explains the increase of hardness after a short ageing time resulting in a much higher hardness than those of other alloys. These strengthening particles will be further detailed in the next section.

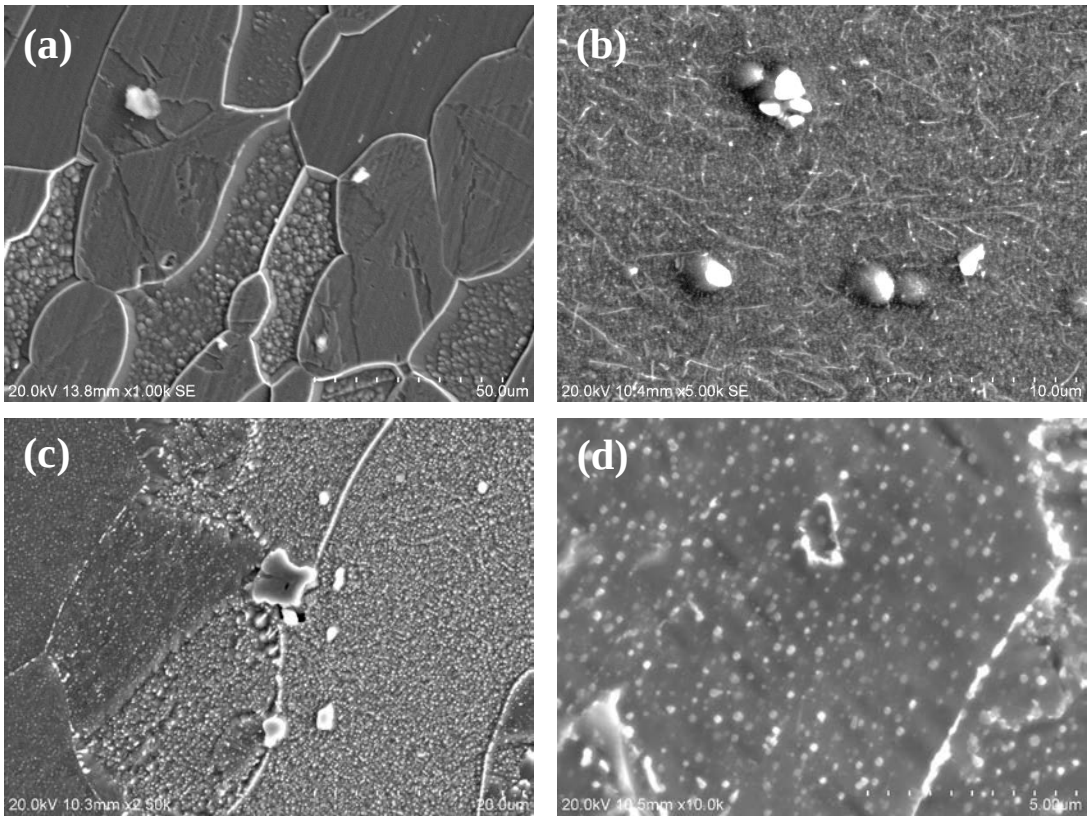

Figure 8.14 SEM micrographs of alloy MSS after ageing at 650 ^{o}C for (a) 1 h, (b) 100 h, (c) 1000 h and (d) 1000 h in a higher magnitude.

In the fully martensitic steel MPHI, only some primary NbTiCN carbonitrides and a small amount of $M_{23}C_6$ were found along the lath and prior boundaries after ageing for different times. Fine and homogenous precipitates as found in alloy MPHS and MSSI were not present (**Figure 8.15**). The average size of $M_{23}C_6$ carbides increases with ageing time, and reaches 500 nm after 1000 h. At the same time, the lath width increases from 1 to 3 μm.

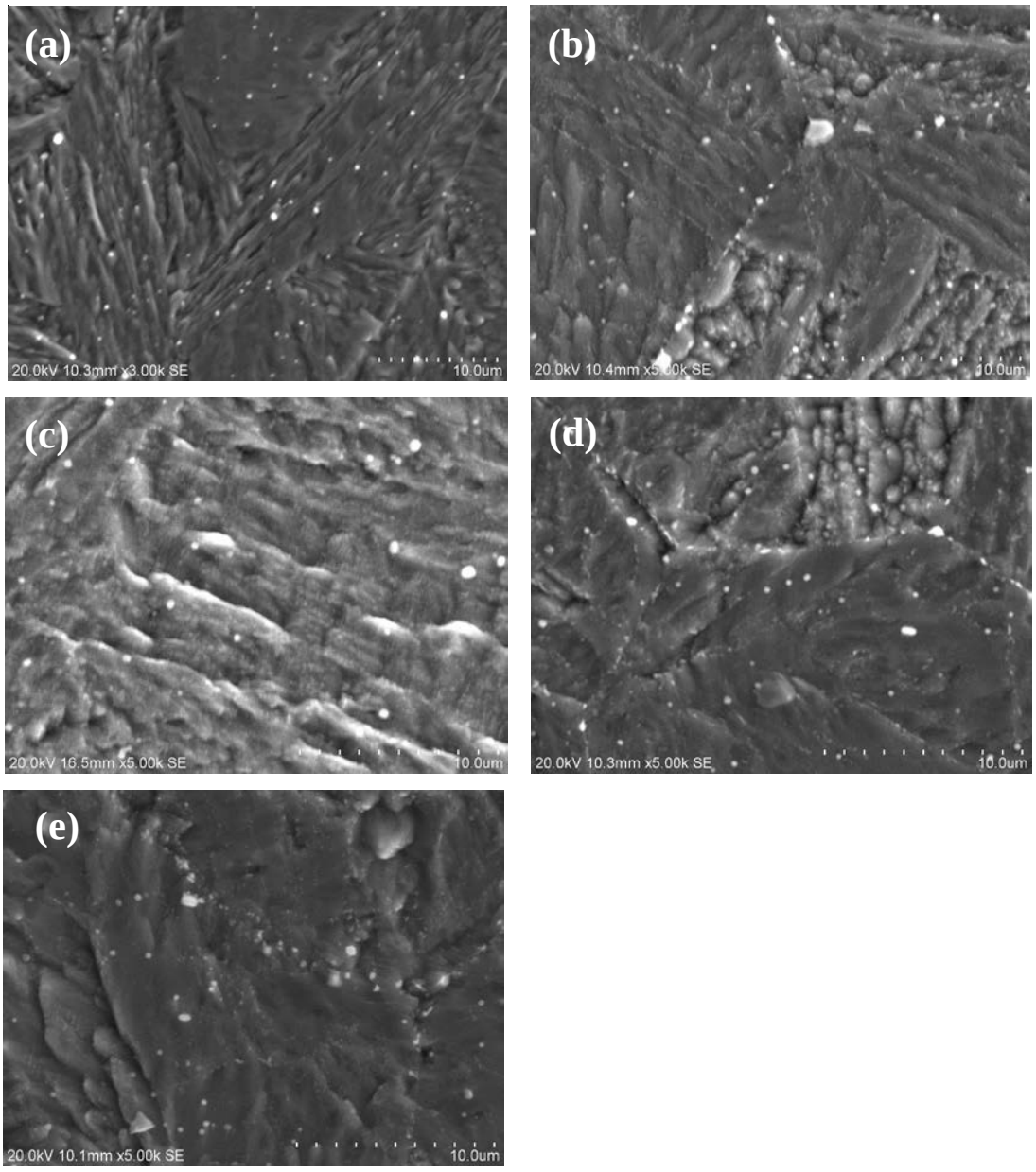

Figure 8.15 SEM micrographs of alloy MPHI after ageing at 650 ^{o}C for (a) 1 h, (b) 50 h, (c) 100 h, (d) 600 h and (e) 1000 h.

In Figure 8.16, the microstructure evolution of alloy P92 after ageing for 1, 100 and 1000 h is shown. Large precipitates along the prior austenite grain boundaries in **Figure 8.16c** are identified as $M_{23}C_6$ carbides according to EDS analysis plotted in **Figure 8.16d**. After annealing for 1 h, $M_{23}C_6$ carbides mainly precipitate along the prior austenite grain boundaries while only a few along the lath boundaries (**Figure 8.16a**). Both the size and

amount of $M_{23}C_6$ carbides increase with ageing time, as shown in **Figures 8.16b** and **8.16c**. The average size of $M_{23}C_6$ carbides in P92 is around 500 nm which is similar to that in MPHI. Clearly, the amount of $M_{23}C_6$ carbide in P92 is much more than that in alloy MPHI.

The main strengthening precipitates, secondary MX carbonitride, in alloys MPHI and P92 cannot be observed in SEM due to their very fine size, estimated to be around 20 nm. These occurrence and behaviour of the fine precipitates will be discussed in the next section.

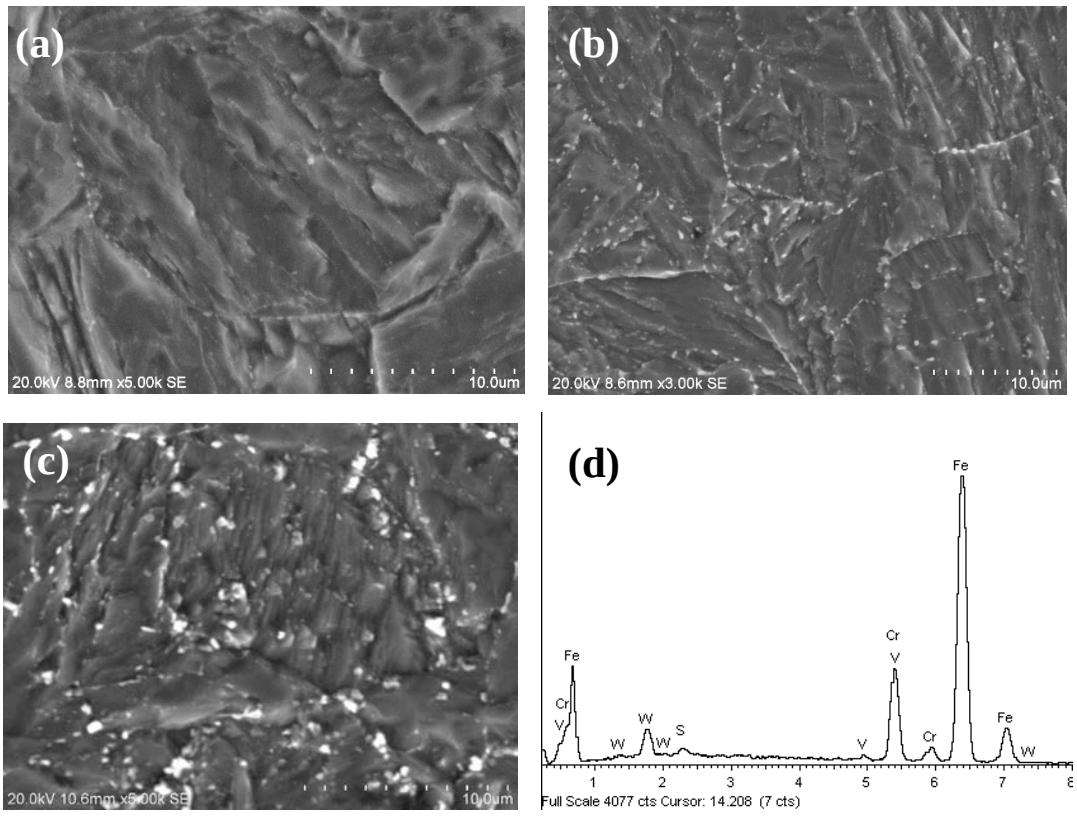

Figure 8.16 SEM micrographs of alloy P92 after ageing at 650 ^{o}C (a) 1 h, (b) 100 h and (c) 1000 h, (d) EDS analysis of large precipitate along prior grain boundary in condition (c).

8.4 Discussion

8.4.1 Effect of composition and heat treatment temperature deviations on phase constitution and coarsening rates of strengthening precipitates

As listed in Table 8.1, the composition of designed and actual steels are slightly different. To demonstrate the effect of minor deviations in the chemical composition, additional thermodynamic calculations of both target and actual compositions at both the solution treatment temperatures and the ageing temperature (650 °C) were performed with ThermoCalc linked to the TCFE6 and MOB2 databases. For practical reasons, the actual solution treatment temperature is fixed at 1200 °C (the experimental value), which deviates from the intended homogenisation temperatures. All results are listed in Table 8.2. It should be noted that the effect of composition and austenisation temperature deviations are investigated only thermodynamically, rather than on the mismatch of experimental results and thermodynamic calculation.

For alloy FSSS, both the designed and actual compositions can achieve a fully ferritic matrix at an annealing temperature of 1200 °C. At the ageing temperature, the volume fractions of ferrite in both designed and actual alloys are over 99%, which matches the go/no-go criteria applied in Chapter 3. Therefore, the designed and actual alloys have similar equilibrium phases notwithstanding the 3.79 wt.% deviation in Mn level (Table 8.1).

In alloy APH, the designed and actual compositions fulfil all go/no-go criteria as defined in Chapter 2, both at the austenitization and the ageing temperature. However, the amount of strengthening precipitate TiX in the actual alloy is much lower than that in the designed alloy due to a much lower factual Ti concentration. Nevertheless, the coarsening rates of both alloys are very low and nearly identical. The calculated Ms temperature of designed and actual alloys are different but still well below room temperature as required.

Table 8.2 Equilibrium phase fractions (in vol.%) calculated by ThermoCalc on designed and actual compositions at both the solution treatment and the ageing temperatures. Coarsening rate of MX carbonitride (in m^3/s) and Ms temperature (in °C) are calculated by applying our approach describes in previous chapters. Aus and Fer indicate austenite and ferrite respectively.

Alloy		@Taus	@Tage 923K	K of TiNbX /VX	Ms from model
FSSS	design	100%Fer	99.37%Fer+0.36%Cr_3Si+0.19%Mu Phase	N/A	N/A
	actual	100%Fer	99.29%Fer+0.71%Cr_3Si		
APH	design	99.74%Aus+0.26%MX	97.12%Aus+0.0075%TiN+0.023%CR_2N+1.1%$M_{23}C_6$+1.65%Sigma	1.90 E-37	-22.2
	actual	99.84%Aus+0.16%MX	98.78%Aus+0.0015%TiX+0.95%$M_{23}C_6$+0.027%Cr2N	1.61E-37	3.6
MPHS	design	99.65%Aus+0.35%MX	99.55%Fer + 0.26%(NbTi)C + 0.187%$M_{23}C_6$ +0.0006%AlN	1.49E-32	385.5
	actual	99.57%Aus+0.43%MX	99.69%Fer + 0.22%(NbTi)C + 0.087%$M_{23}C_6$ +0.0004%AlN	1.34E-32	390.5
MSS1	design	99.87%Aus+0.13%AlN	99.27%Fer+0.19%(NbTi)C+0.44%$M_{23}C_6$+0.0013AlN+0.039%M_6C	7.6E-32	371.4
	actual	99.90%Aus+0.10%AlN	95.64%Fer+3.74%Aus+0.19%(NbTi)C+0.43%$M_{23}C_6$+0.0009%AlN	2.97E-31	357.7
MPHI	design	99.70%Aus+0.30%MX	99.45%Fer+0.31%NbCN+0.23 $M_{23}C_6$+0.003%AlN	1.45E-32	364.1
	actual	99.63%Aus+0.37%MX	99.65%Mar+0.25%(NbTi)CN +0.099% $M_{23}C_6$+0.0012%AlN	1.31E-32	369.5
P92	actual	99.83%Aus+0.17%MX	97.21%Fer+0.18%VN+0.082%Cr_2N+0.98%Laves phase+1.38%$M_{23}C_6$	6.96E-32	382.9

With respect to the martensitic alloy MSSI, the phase constitutions are almost the same in the designed and actual alloys at the solution treatment temperature. However, at the ageing temperature, no austenite should be found in the designed alloy but in the realized alloy around 3.7% retain austenite is predicted, owning to a higher amount of austenite stabilize Ni in the actual composition. Moreover, the realized alloy has a higher coarsening rate of strengthening precipitate MX carbonitrdes (Table 8.2), which is less desirable as compared to the ideal composition.

In the precipitation hardened alloy MPHI, the slight composition deviation does not lead to different microstructures at either the solution treatment or the ageing temperatures. Both alloys meet all the go/no-go criteria as defined in Chapter 4, and have identical (MPHI) or similar (MPHS) coarsening rates of MX carbonitrides. The newly designed martensitic steels have a similar phase constitution as the commercial P92 steel grade.The main difference is that the strengthening precipitate is VN in alloy P92 and NbX in the newly designed three martensitic steels. The coarsening rate of VN in alloy P92 is much higher than that of NbX in alloy MPHS and MPHI which are designed to have a low coarsening rate of MX carbonitrides.

8.4.2 Precipitates identification in alloys MPHS, MSSI and MPHI

As discussed in the results section, homogenously distributed fine particles were found in both alloys MPHS and MSSI. However, these particles are not the intended strengthening precipitate MX carbonitrides because not only their volume fraction is much higher than of MX carbonitrides, but also their morphologies are quite different from of the typical MX carbonitrides. The phase diagrams of alloys MPHS and MSSI with their actual compositions were re-calculated to further identify the particles in these two alloys, shown in **Figure 8.17**. From the phase diagram, only $M_{23}C_6$ and MX carbonitrides are in equilibrium at 650 °C. However, at lower temperatures, a large amount of α-Cr and NiAl intermetallics are predicted to form in both alloys. According to the literature, α-Cr generally has a rod shape [2] and NiAl has a spherical or cubic shape [3]. The morphology of the precipitates observed (**Figures 8.13 and 8.14**), suggests that these particles are most likely NiAl intermetallics. However, more detailed characterization is required to further confirm the species of this precipitates.

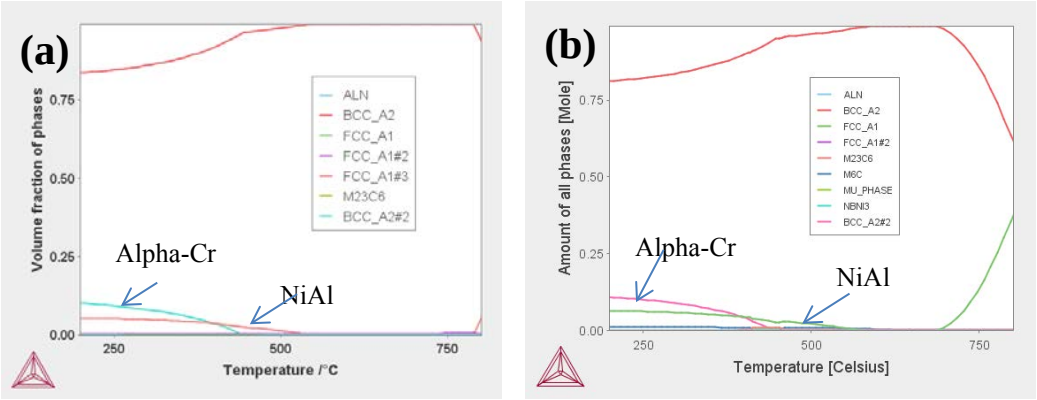

Figure 8.17 Phase diagrams of alloys MPHS (a) and MSSI (b) calculated by ThermoCalc using their actual compositions.

The phase diagram of alloy MPHI was also re-calculated for the actual composition, as shown in **Figure 8.18**. At a lower temperature than 650 °C, a significant amount of alpha-Cr could be present, but the NiAl phase should be absent . The SEM data suggested that no alpha-Cr was present in alloy MPHI. To further prove that the precipitate species in MPHI is indeed MX carbonitrides other than alpha-Cr or others, TEM experiment on replica samples was carried out on using a sample aged for 1000 h. The results are shown in **Figures 8.20** and **8.21**.

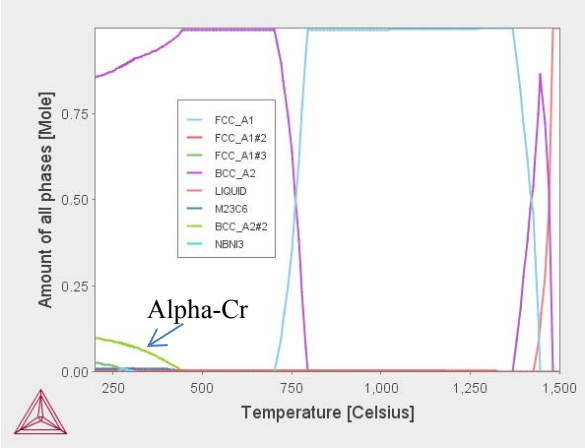

Figure 8.18 The phase diagram of alloy MPHI calculated by ThermoCalc using its actual composition.

In **Figure**s **8.20a** and **8.20b**, two types of precipitates can be readily identified. One is a Cr-enriched particle of a large size (200-500 nm), and the other one are Nb and Ti enriched carbonitrides of a small size (10-50 nm) according to the EDX analysis (see**Figures 8.20c** and **8.20d)**. Combining the thermodynamic calculation (see Table 8.2), the big precipitate should be $M_{23}C_6$ and the smaller one is (Nb,Ti)X carbonitride. The big size of $M_{23}C_6$ particles results from its much higher coarsening rate than MX carbonitrides. Consequently, the precipitates characterisation confirms that alloy MPHI indeed has exactly the intended microstructure (as listed in Table 8.2).

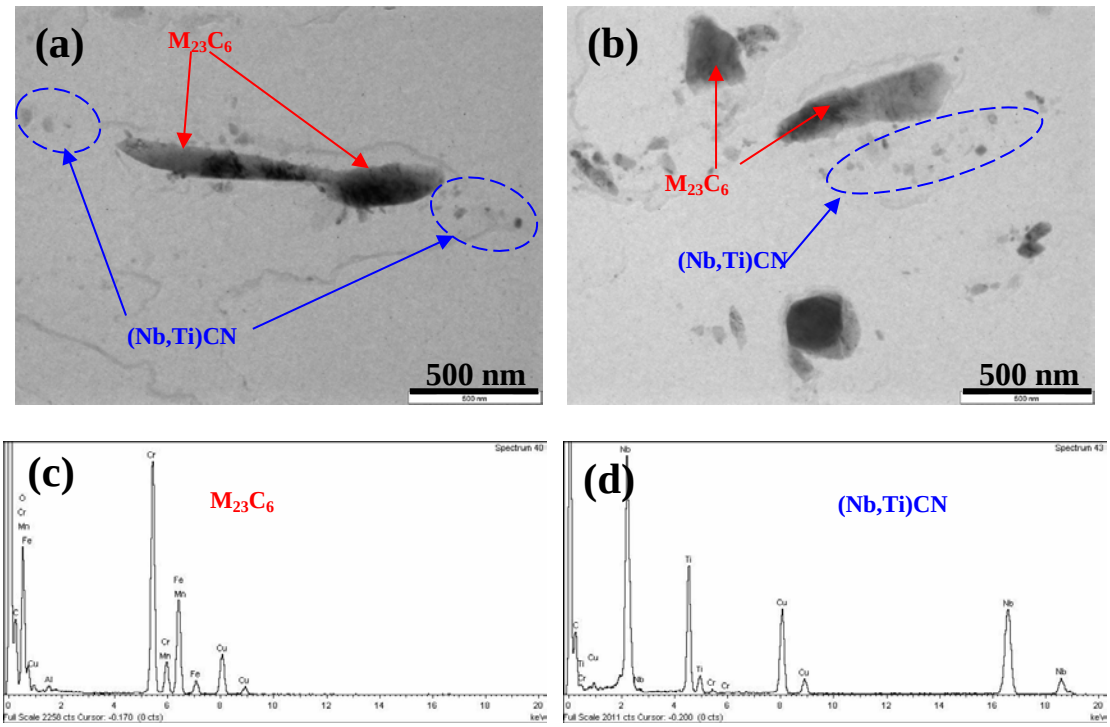

Figure 8.20 (a) and (b) TEM images of the C-replica for alloy MPHI ageing for 1000 h. The EDX analysis for big particle (c) and small particle (d) in **Figure 8.20a** and **8.20b**.

Figure 8.21 shows that MX carbonitrides have a variety of sizes, from 10 nm (**Figure 8.21d**) to 50 nm (**Figures 8.21a**, **8.21b**, and **8.21c**). They can precipitate along the grain/lath boundaries (**Figure 8.21b** and **8.21c)**, or within the laths (**Figure 8.21a** and **8.21d)**. After ageing of 1000 h, MX carbonitrides still keep a small size, suggesting that alloy MPHI successfully achieves an intended low coarsening rate of MX carbonitrides.

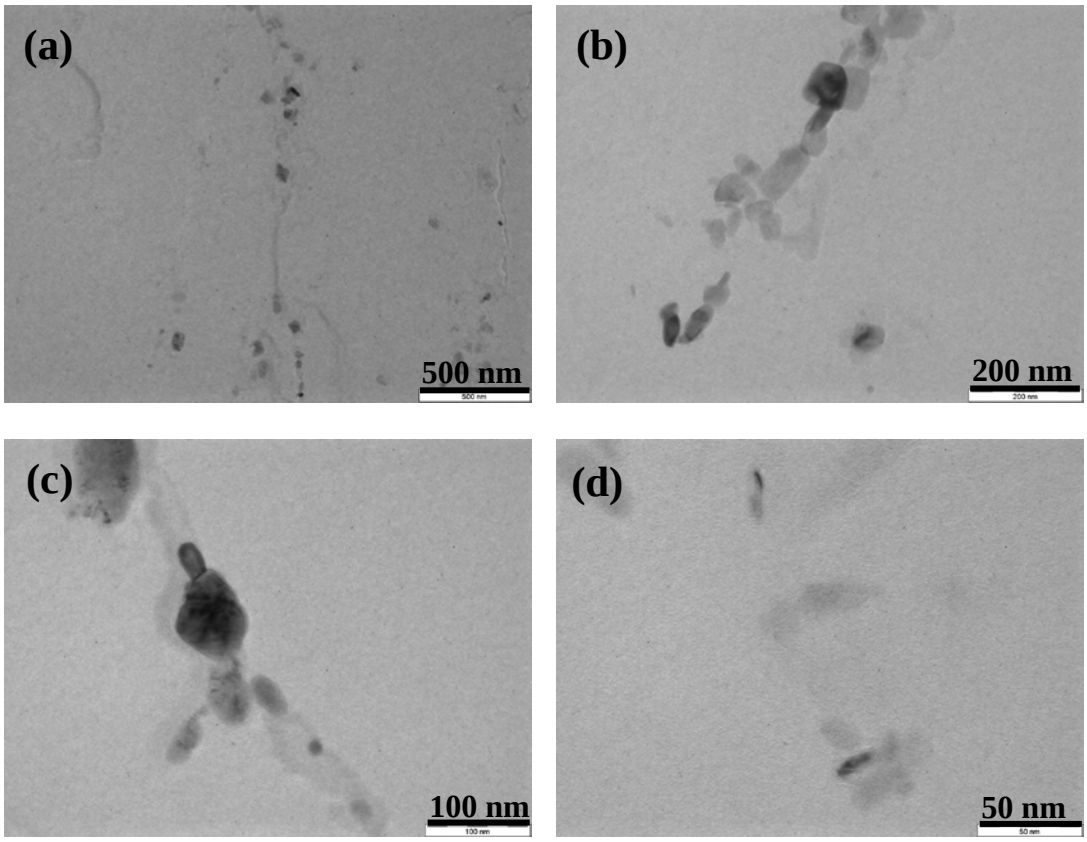

Figure 8.21 TEM images of the C-replica for alloy MPHI ageing for 1000 h (a), (b), (c) and (d).

8.4.3 A comparison between the new alloy MPHI and the existing steel P92

The fully martensitic alloy MPHI is chosen to be compared to the existing commercial steel P92. Alloys MPHS and MSSI are not considered since they do not have a fully martensitic matrix. Although both MPHI and P92 use MX carbonitrides as the strengthening precipitate, the main difference is that P92 utilizes VN while MPHI relies on (NbTi)CN. Precipitates of the (NbTi)CN family, instead of those from the VN family were chosen in the design strategy of MPHI because of the tendency of VN to transform into Z phase upon prolonged ageing (e.g. several thousand hours). The Z phase is known to have a deleterious effect on the creep strength [4]. Generally, VN has a lower coarsening rate than (NbTi)CN. However, by tuning the concentrations of Nb, Ti, C, N and other alloying elements, the coarsening rate of (NbTi)CN can be lower than that of VN. As listed in Table 8.2, the volume fraction of MX carbonitrides in both alloys are similar, but the coarsening rate of (NbTi)CN in MPHI is 1.31E-32m^3/s, which is five

times lower than that of VN in P92, i.e. 6.96E-32 m^3/s. In contrast, the coarsening rate of the other precipitate $M_{23}C_6$ in alloys P92 and MPHI are nearly identical, 0.94E-28 m^3/s and 1,00E-28 m^3/s respectively, which explains the similar size in both alloys after ageing of 1000 h. In line with the experimental observations, their volume fractions are around 1.38% and 0.099% respectively. Therefore, the strengthening contribution of $M_{23}C_6$ in alloy P92 is higher than that in alloy MPHI according to Equation 4.2. From the hardness evolution in **Figure 8.11a,** a good correspondence of the hardness and precipitation evolutions can be established, assuming that the lath widening and dislocation recovery processes proceed in a similar way in both steels. After a short annealing time, the hardness of P92 is higher than that of alloy MPHI owing to a higher strengthening contribution from $M_{23}C_6$. Upon further ageing, $M_{23}C_6$ coarsens very fast with its very high coarsening rate while MX carbonitrides with their extremely low coarsening rate start to play a more dominant role. Their difference in coarsening rate as derived from the resulting particle sizes have been confirmed by TEM experiments shown **Figure 8.20**. A higher hardness at the prolonged ageing in alloy MPHI is probably because of the lower coarsening rate of MX carbonitrides in alloy MPHI than that in P92, given the fact that the volume fractions of MX carbonitrides in both steels were similar.

8.5 Summary and Conclusions

Five prototype alloys with optimised SSS (ferritic steel FSSS and martensitic steel MSSI), PH (austenitic steel APH and martensitic steel MPHI) and combination of PH and SS (martensitic steel MPHS) were designed applying the models in chapters 2 to 5. These alloys have been fabricated, processed, and characterized in different service conditions. Alloys APH and MPHI were found to have the intended matrices. Alloy MPHS and MSSI contained a martensite-ferrite duplex microstructure instead of a fully martensitic matrix. Alloy FSSS showed a ferritic matrix with a large amount of Laves phase being present. The mismatch between the thermodynamic (ThermoCalc) predictions and the experimental observations may correlate to the high Al content in alloys FSSS, MPHS and MSSI. All alloys designed to have full or partially SSS have reached a high SSS. On the other hand, only alloy MPHI contained just the desired strengthening precipitates.

The microstructure stability and resulting hardness during annealing at 650 °C were investigated. Alloy MPHS and MSSI display a significant increase in hardness after ageing for 1 h, owing to the precipitation of fine and evenly distributed NiAl particles. Their hardness was always higher than that of alloys P92 and MPHI for the same service

time. All newly made martensitic steels have a similar hardness as alloy P92 after quenching. Although alloy MPHI has a relative lower initial hardness, its hardness decreased even slower than that of P92 owing to a lower coarsening rate of MX carbonitride, resulting in a higher hardness after long exposure. The slow coarsening kinetics is confirmed by the TEM experiments which show the eventual fine size (10-50 nm) of MX carbonitrides after 1000 h ageing. The performance of MPHI is expected to further outperform that of P92 at longer times than the maximum 1000 h available in this testing campaign.

References

[1] Masuyama F. History of power plants and progress in heat resistant steels. ISIJ Int. 2001;41:612.
[2] Semba H, Okada H, Hamaguchi T, Ishikawa S, Yoshizawa M. Development of Boiler Tubes and Pipes for Advanced USC Power Plants. Technical report of Nippon Steel & Sumitomo Metal 2013:71.
[3] Teng ZK, Zhang F, Miller MK, Liu CT, Huang S, Chou YT, Tien RH, Chang YA, Liaw PK. New NiAl-strengthened ferritic steels with balanced creep resistance and ductility designed by coupling thermodynamic calculations with focused experiments. Intermetallics 2012;29:110.
[4] Sawada K, Kushima H, Kimura K. Z-phase formation during creep and aging in 9-12% Cr heat resistant steels. ISIJ Int. 2006;46:769.

Chapter 9

Process-time optimisation of vacuum degassing using a genetic alloy design approach

9.1 Introduction

In previous chapters, the alloy design approach has been applied to develop novel creep resistant steels for components used in fossil-fired or nuclear power plants. In this chapter efforts are made to expend the genetic alloy design concept and the GA model to the steel making process, in particular the vacuum degassing part. In early studies the process was analysed generically and a detailed understanding on how individual process parameters influence the vacuum degassing process was not gained. No attempt was made to optimise the vacuum degassing time systemically. The present work is a first step to implement the genetic alloy design approach [1] on the steel making process. More specifically, self-consistent CALPHAD-type thermodynamic multi-component databases and empirical kinetic relations are coupled with genetic algorithms to predict the optimal set-up for degassing. Since this work focusses on demonstrating how genetic algorithms can be used to optimize the steelmaking process it should be emphasized that little effort has been spent on the physical and kinetic models called upon in the optimisation process. This could affect the results but the chapter will still demonstrate the effectiveness of the methodology presented.

The steel plant's objective is to efficiently produce high quality steels at maximal rates. Profit is made if the cost can be reduced while strictly fulfilling the demands for a specific steel grade. One way to reduce the cost of the steel making process is to minimise the time needed for one of the most expensive process steps, namely the vacuum degassing operation which is part of the secondary metallurgy processing. It is performed after deoxidation and alloying, and involves low pressure and high stirring rates. It has been shown to be a very efficient way to reduce the sulphur, nitrogen and hydrogen content in liquid steel [2, 3], and to reduce the inclusion content. More information regarding vacuum degassing can be found elsewhere [2, 3].

9.2 Model description

In order to optimise the process it is necessary to have a model that describes the vacuum degassing for all possible set-ups. Since the objective of the present work is to minimise the time, t_{min}, needed to reach target composition, the model should return this value for a certain set-up, i.e. as given by Equation 9.1.

$$t_{min} = degassing(v_1, v_2, \dots) \dots \quad (9.1)$$

where v_i denotes variables of a set-up generated by the optimisation algorithm. The equilibrium information is obtained using the thermodynamic software Thermo-Calc [4], as described in Section 9.2.1, and the time is obtained using an empirical relationship for the mass transfer, as described in Section 9.2.2. It should be mentioned that not all solutions explored during the genetic algorithm search are meaningful from a metallurgical perspective. In other words, solutions that violate the physical constraints for vacuum degassing should be discarded. The following constraints are considered in the present work: too high a slag viscosity, too high a foaming height, too low a fraction of liquid slag, and too high a temperature drop. The flow chart of the model for the process-time optimisation of vacuum degassing using the GA approach is given in **Figure 9.1**. For each candidate solution the first step is to calculate and confirm that the viscosity and foaming height are within the allowed ranges. The next step is to calculate the thermodynamic equilibrium for the set-up. Using the equilibrium information it is possible to check that the amount of liquid slag is high enough and that the equilibrium content of O, S, N, Al and Si is below the critical composition. The final step is to calculate the time needed to reach the target composition of O, S, N, Al and Si but also to

check that the temperature remains high enough. Detailed descriptions of all the steps indicated in the flow chart are given in the following sections.

9.2.1 Thermodynamic calculations

Thermodynamic calculations are performed using software, such as Thermo-Calc, together with self-consistent thermodynamic databases for multicomponent alloy systems. Such databases have been developed using the so-called CALPHAD approach, see[5-7]. The idea of the CALPHAD approach is to determine Gibbs energy expressions for each individual phase as a function of constitution, temperature and pressure. The determination is performed through an optimization procedure in which model parameters are fitted to experimental, as well as ab initio information. Thermodynamic models based on the crystallography are assigned to each phase, and the majority of models used are found within the Compound Energy Formalism [8]. CALPHAD-type thermodynamic databases have predictive power if all important binary and most ternary sub-systems have been described. It may then reasonably well predict properties such as phase composition, phase fractions and thermochemical properties such as heat capacity. In the present case the equilibrium state is calculated by considering all elements both in steel and slag to obtain the fraction of impurities in the steel as well as the fraction of liquid slag.

All thermodynamic calculations are performed with the commercial software Thermo-Calc [4] using a custom-made database using the liquid steel phase as well as solid oxide and sulphide phases from the steel database TCFE6 [9], the liquid slag phase from the database SLAG3 [10] and the gas phase from the database SSUB3[11]. The custom-made database contains a description of the chemical system Fe-Al-Ca-Mg-Mn-N-O-S-Si.

Although in reality the system is not expected to reach full equilibrium during vacuum degassing the thermodynamic description will provide vital information concerning elemental distribution between the steel and the slag. In many cases the system may be considered to be reasonably close to equilibrium after vacuum degassing, which can be seen as reduced mass transfer in the earlier work [12]. During vacuum degassing the desulphurisation is the major reaction that occurs between steel and slag. In the desulphurisation the reaction between S, O and Ca dominates. However, Al and Si are also of importance since they react with oxygen that is dissolved in the liquid steel as a result of the desulphurisation. Another important reaction during vacuum degassing is the

metal-gas reaction through the assembling of N and H from the steel into the gas. In this work only nitrogen is taken into consideration since the current thermodynamic databases do not include hydrogen. The lining of the ladle walls consists of MgO which may dissolve into the slag depending on the MgO activity. Even though some MgO is expected to be dissolved during vacuum degassing the effect on the overall equilibrium is likely to be limited since this reaction mostly occurs before the vacuum degassing. The mass fraction of liquid slag is important to take into consideration since a low fraction of liquid slag results in a higher effective viscosity as well as in a lower mass transfer rate. The amount of liquid slag is obtained from the thermodynamic calculation.

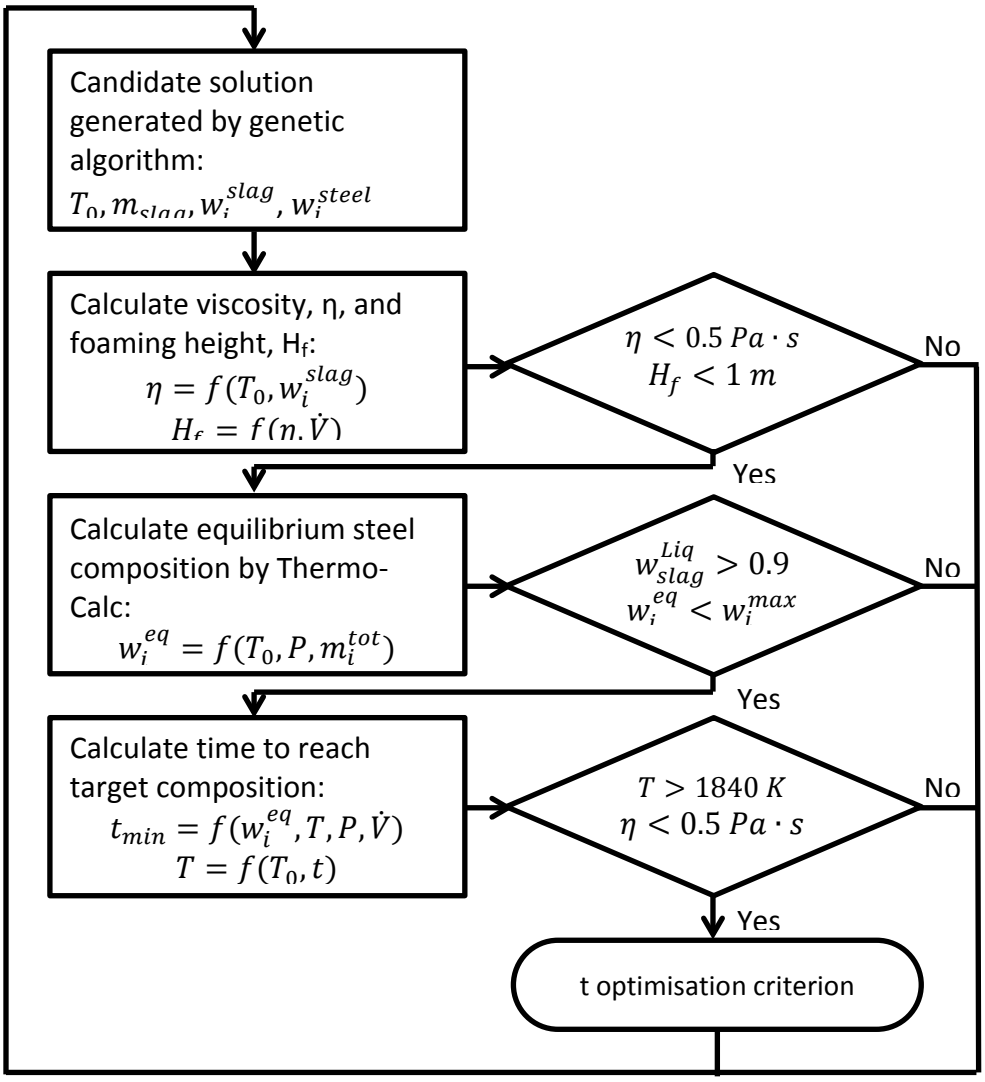

Figure 9.1 Flow chart of a model for optimising the minimum time to reach target composition during vacuum degassing.

9.2.2 Kinetic considerations

The kinetics of the steel making process is complex and involves phenomena such as turbulent flow and heat gradients. This means that the kinetics is more or less unique for every steel plant. Several studies have been conducted to investigate these phenomena in detail, see e.g. [13]. Unfortunately, these complex models need too long computational times to be coupled with genetic algorithms. Moreover the aim of this work is to develop a method to optimize the process over a wide range of various set-ups rather than describing one particular set-up in detail. However, in order to be able to control the process at the steel plants, simpler analytical process models may be used [13]. Although the exact nature of these models is considered trade secrets it is possible to use a similar approach by assuming reasonable kinetic relationships. The mass fraction of element *i* in the steel at time *t*, $w_{i,steel}(t)$, may be calculated using Equation 9.2.

$$w_{i,steel}(t) = \left(w^0_{i,steel} - w^{eq}_{i,steel}\right)e^{-k_i t} + w^{eq}_{i,steel} \ldots \quad (9.2)$$

where $w^0_{i,steel}$ and $w^{eq}_{i,steel}$ denotes the initial and equilibrium mass fraction of element *i* in the steel, respectively, and k_i the mass transfer coefficient of element *i*. The reaction rate decreases exponentially with time since the driving force decreases as the reaction progresses. If instead the objective is to calculate the time needed to reach a specific composition, $w^{max}_{i,steel}$, this is done by setting $w_{i,steel}(t) = w^{max}_{i,steel}$ and rearranging the equation into Equation 9.3. Of course, both $w^{eq}_{i,steel}$ and k_i depend on external conditions, such as temperature. Constant values of these parameters are used for simplification. These values are calculated 20 K below the start temperature which yields an average value, assuming a 20 min process time and temperature drop of 2 K/min. Since the process time of a good solution is expected to be less than 20 min this approximation will not generate too optimistic times. Using water models it has been shown that the mass transfer coefficient strongly depends on the stirring energy, $\dot{\varepsilon}$, according to Equation 9.4 [14].

$$t = -\frac{1}{k_i} ln \frac{w^{max}_{i,steel} - w^{eq}_{i,steel}}{w^0_{i,steel} - w^{eq}_{i,steel}} \quad (9..3)$$

$$k_i = C\dot{\varepsilon}^{\,n} \ldots \quad (9.4)$$

where *C* is a constant and *n* the exponential factor, which from experimental practice is known to be 2.1, if the stirring energy is above 60 W/tonne, and 0.25, if the stirring energy is lower [2, 3]. The reason for the abrupt change around 60 W/tonne is considered to be the result of slag and steel mixing at the higher stirring energies while at lower stirring energies only the steel is circulated [3]. In the latter case there is much less steel

and slag interaction. In the current paper *C* is estimated to be around $2.7 \cdot 10^{-8}$ s^{-1} for all elements involved in slag and steel reactions, using results from CFD calculations [13]. These calculations were performed in order to develop an on-line process model for vacuum degassing. Since the nitrogen removal does not rely on the steel and slag reaction, but rather on the steel and gas reaction, it does not follow the same relation. However, lacking a better description of the nitrogen transfer, and since nitrogen removal has approximately the same order of magnitude as desulphurisation, it is assumed to have the same value. The assumption that nitrogen would behave as sulphur is unphysical but will demonstrate how the equilibria involving different impurity elements will impact the minimum time needed to reach the target composition. In this work the stirring energy, $\dot{\varepsilon}$, is calculated using an empirical relation [2], as shown in Equation 9.5, that have been derived from [15].

$$\dot{\varepsilon} = 14200 \frac{\dot{V}T}{m_{steel}} log\left(\frac{1+h}{1.48P}\right) \ldots \quad (9.5)$$

where $\dot{V}$ denotes the gas flow rate (m^3/min), *T* the temperature (K) , m_{steel} the steel mass (kg), *h* the depth of the steel bath (m), and *P* the pressure (Pa).

9.2.3 Constraints/go/no-go criteria

Even though the effect of physical properties on the mass transfer rate is neglected in the present optimisation model, each candidate solution generated by genetic algorithm still has to fulfil some physical constraints. The constraints considered here are the slag viscosity and foaming height. In addition, the temperature drop will change the equilibrium steel composition and thus dynamically change the mass transfer coefficient. The effect of the temperature change during the degassing process is neglected but the temperature drop is checked so that the process does not end up at unreasonable low temperatures.

9.2.3.1 Viscosity

The viscosity will influence how efficient the vacuum degassing will be. A high viscosity is expected to have a negative influence on the reaction rate. The viscosity is not included in the kinetic relationship. Instead a constraint is used which does not allow the viscosity to be above 0.5 Pa·s. Although this assumption might generate an incorrect minimum time it discards solutions that are too slow due to high viscosity. The viscosity, η, is

calculated using the Urbain model [16]. In the Urbain model the viscosity is obtained from Weymann type equation [17] as is seen in Equation 9.6

$$\eta = a_1 T exp\left(\frac{1000 a_2}{T}\right)[Pa \cdot s] \ldots \quad (9.6)$$

where T denotes the temperature and a_1 and a_2 are composition dependent parameters, see [16, 18] for details about a_1 and a_2.

9.2.3.2 Foaming height

If the steel is subjected to a gas flow or gas formation, slag foaming will occur. In some cases, like in an electric arc furnace, this is desirable because the foam acts as thermal insulation. In vacuum degassing, however, slag foaming is undesirable since too high a slag rise may cause damage to the equipment. The foaming height, H_f, is calculated by using Equation 9.7 derived from [19].

$$H_f = 1150 \frac{\eta}{\sqrt{\sigma \rho}} \frac{\dot{V}}{A}[m] \ldots \quad (9.7)$$

where η denotes the viscosity (Pa·s), σ the surface tension (N/m), ρ the density of the slag (kg/m^3), $\dot{V}$ the volumetric flow rate (m^3/min), and the A the area of the steel bath (m^2).

9.2.3.3 Temperature drop

The temperature drop is mainly due to heat transfer from the steel to the ladle walls. Some heat will be lost heating the slag which is colder than the steel. However, this neglected since the steel amount is much higher than slag and also because the slag foaming. Which is expected to be higher during vacuum degassing and this will reduce the heat loss through the slag. It is easily understood that the temperature drop will be more severe with increased stirring. Due to the high stirring energy during vacuum degassing the temperature drop is expected to be higher than during other ladle operations. It is assumed that the temperature decrease due to stirring may be described as $C\dot{\varepsilon}^{\,n}$, just like the mass transfer, since stirring will make new steel come into contact with the ladle wall or slag continuously. Given the similarity n is set to 0.25 which is the relationship between the mass transfer coefficient and the stirring energy when no mixing between slag and steel occurs[3]. Hence, the temperature drop is estimated using the following Equation 9.8

$$\frac{dT}{dt} = -1 - 0.25\dot{\varepsilon}^{\,0.25}[K/min] \ldots \quad (9.8)$$

where the constants in the equation are obtained by assuming a temperature drop of about 1 K/min under normal ladle operations (assuming atmospheric pressure and no or very low gas flow) and about 2 K/min during vacuum degassing (assuming 50 Pa pressure and 0.2 m^3/min gas flow). Details about the estimation of the temperature drop can be found in [3].

9.2.4 Parameter settings

In order to minimise the process time needed to reach the target composition both the steel and slag compositions should be optimised such that the driving force for reducing impurities is as favourable as possible. The eight variables used as optimising variables for degassing are listed in Table 9.1. The values result from the operations performed before degassing while pressure and flow rate are process parameters for the degassing process. The two major process parameters during vacuum degassing are flow rate and pressure. Using the current kinetic relationship the flow rate will only affect the time needed to reach the target composition and not the optimal set-up. The pressure will have a similar effect as the flow rate, meaning that lower pressures will result in shorter times. In addition, the pressure also has an effect on the equilibrium. The optimisations are performed at four different pressures (50, 75, 100 and 200 Pa).

Table 9.1 Ranges for all variables used in the optimisation.

	Al (mass %)	Ca (mass %)	Si (mass %)	Fe (mass %)	Slag (kg)	Al_2O_3 (mass %)	MgO (mass %)	SiO_2 (mass %)	CaO (mass %)	Temp. (K)
min	0.0	0.0	0.0	Bal.	1000	20	5	5	Bal.	1913
max	0.04	0.005	0.3		2000	40	10	20		1973

The initial composition of the steel is fixed to 1.5 mass% Mn, 10 ppm O, 50 ppm N and 200 ppm S. Additionally a fixed amount of 20 kg FeO is added to the slag and the amount of steel per heat, m_{steel}, is set to 10^5 kg. The depth of the steel bath, h, is set to 2 m, the upper surface area, A, is set to 7 m^2, the density of the slag, ρ, is set to 3000 kg/m^3 and the flow rate, $\dot{V}$, is set to 0.2 m^3/min. These values are needed to calculate the stirring energy, $\dot{\varepsilon}$, and thus the time needed to reach the critical composition. The surface tension of the slag, σ, varies with composition and temperature but should be above 0.4 N/m, for a slag consisting mostly Al_2O_3-CaO-SiO_2 and with 20 mass% SiO_2 in the temperature range 1800-2000 K [20]. Given that the surface tension does not exceed this value and that the

viscosity condition is fulfilled the foaming height will not exceed 0.15 cm. The degassing is considered as completed when the conditions listed in Table 9.2 have been reached.

Table 9.2 Target composition of steel after vacuum degassing.

	S (ppm)	N (ppm)	O (ppm)	Al (mass%)	Si (mass%)
max	100	30	5	0.02	0.25

The temperature used in the thermodynamic calculations as well as the calculation of the viscosity and the mass transfer, is set to 20 K below the temperature generated by the genetic algorithm in order to take temperature drop into consideration. The final temperature is used to check that the viscosity is below the critical value when the degassing has finished. The temperature is not allowed to drop below 1840 K and the viscosity should never be allowed to reach above 0.5 Pa·s and the foaming height should not be above 1 m.

As in the previous chapters, the optimisation is performed using genetic algorithms. More details on the optimisation procedure can be found elsewhere [21] and details about the genetic algorithm program used are reported in [22].

9.3 Results and discussion

All the results from the optimisations are listed in Table 9.3 together with normal values used by industry. One interesting feature is that the optimal set-up seems to depend highly on the pressure. With increasing the pressure the content of Al in the steel, the SiO_2 in the slag and the temperature increase monotonically, while the opposite behaviour is seen for Al_2O_3. The result obtained at 50 Pa pressure is within the range expected from industrial practice with two major exceptions, the slag amount and the SiO_2 content. The difference in slag amount, however, is expected since it is known that a higher slag content promotes desulphurisation, see e.g. a CFD study of vacuum degassing [12]. In a steel plant the amount of SiO_2 is expected to be relatively high since some SiO_2 remains from earlier production stages as well as from the Si-deoxidation. The fact that industrial practice suggests higher pressure indicates that the model used cannot fully reproduce the true nature of vacuum degassing. One likely reason is that the transfer

coefficient of nitrogen may be under-estimated. However, the result obtained at 50 Pa can be used to demonstrate the methodology.

To investigate the evolution of concentrations of critical alloying elements during degassing, their variation with time at various pressures are calculated and plotted in **Figure 9.2**. In all cases the Si content is below the critical composition during the whole process stage. At lower pressures (50 and 75 Pa) the Al content is below the critical content from the beginning while this is not the case at higher pressures (100 and 200 Pa). Al is not limiting the optimal time in any of the optimal set-ups. In all cases, particularly at lower pressures, the content of S and O almost overlap. The reason for this is that the equilibrium content of both O and S is only a small fraction of their maximum allowed content. Interestingly, the positions of the cross points of N and S change with pressures giving rise to the change of the dominant factor in

Table 9.3 Results from the optimisations. Values according to industrial practice are shown in the bottom row.

Pressure (Pa)	Time (s)	Al (mass %)	Ca (mass %)	Si (mass %)	Slag (kg)	Al_2O_3 (mass %)	MgO (mass %)	SiO_2 (mass %)	Temp. (K)
50	429	0.010	0.005	0.243	1571	25.7	7.14	5.00	1922
75	479	0.019	0.005	0.243	1143	22.9	7.86	7.14	1964
100	562	0.023	0.005	0.243	1000	20.0	9.29	11.43	1973
200	1002	0.036	0.005	0.243	1286	20.0	8.57	15.71	1973
100	900-1200†	0.020 - 0.050	0-0.0010	0.20-0.30	1000	25.0-30.0	5.0-10.0	8.0-12.0	1950

†Indicates normal process time, i.e. longer than the minimum time.

optimal degassing time. At the lowest pressure (50 Pa), the intersection is below the critical line. Therefore, it takes more time for the concentration of S to reach its critical level, indicating that the removal of S is the determining factor. At pressures of 75-100 Pa, the intersections are located right on the critical line. Thus N and S removal lead to the same minimal degassing time. Finally, at the higher pressure (200 Pa) the intersections of the N and S lines are above the critical line and thus N becomes the determining factor for the degassing time. These trends are expected since low pressures promote nitrogen removal both via thermodynamics and by increased stirring while desulphurisation is only affected by the stirring. It should be stated that irrespective of the

pressure level, the positions of cross point are always close to the critical line indicating that the system is generally tailored such that N and S nearly simultaneously reach the intended minimal values.

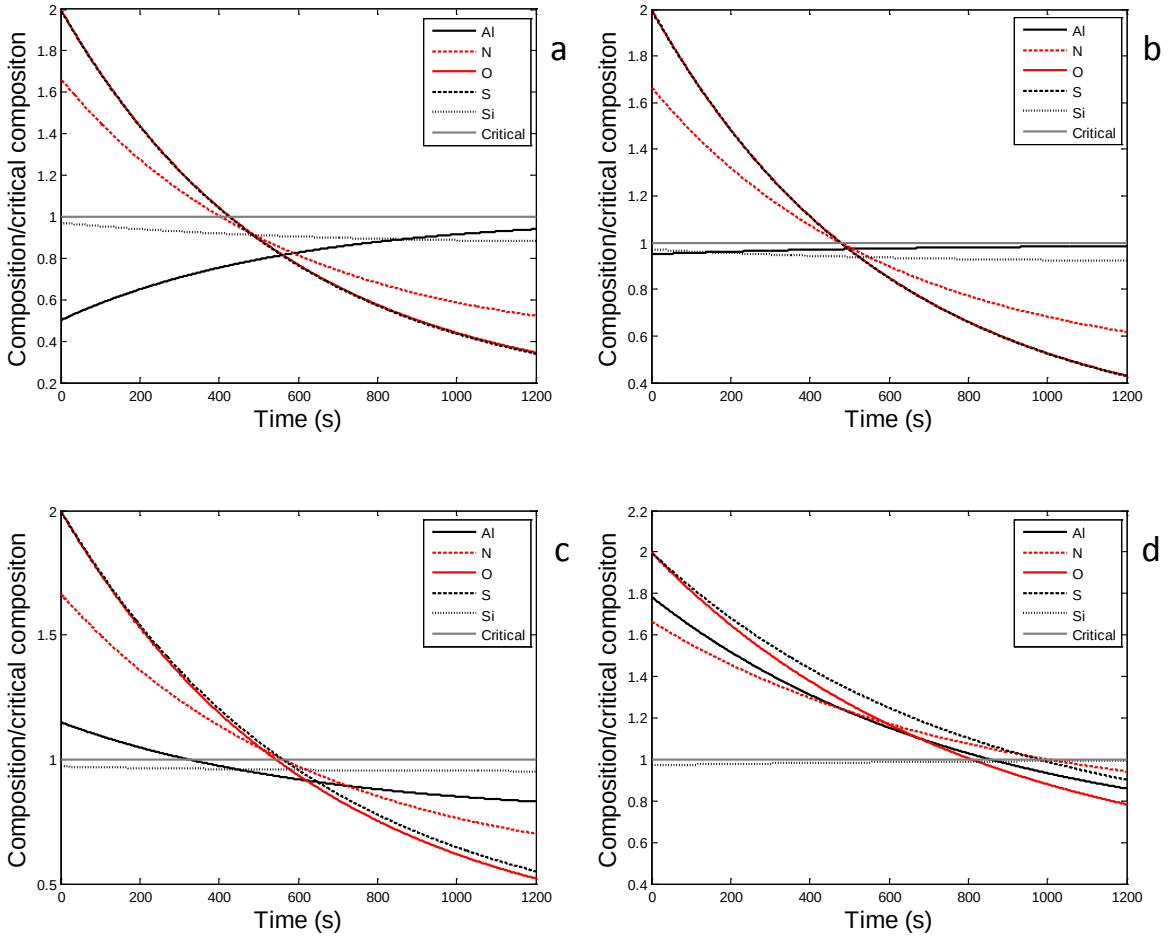

Figure 9.2 Composition of the Al, N, O, S and Si normalised to critical level vs time. Calculated for solutions obtained at pressures of a) 50 Pa, b) 75 Pa, c) 100 Pa and d) 200 Pa.

Since different pressures yield considerably different optimal set-ups, the optimized process time at various pressures and corresponding set-ups is analysed in more detail and the results are shown in **Figure 9.3**. In the figure the times needed to reach both the maximum allowed content of S and N are compared. Again it can be seen that the sulphur level is the limiting factor at lower pressures. It is interesting to note that the pressure at which the critical content of N and S are reached simultaneously is close to the pressure where the corresponding optimal set-up is found. This again demonstrates how the

optimal set-up takes both desulphurisation and nitrogen removal into consideration. However, the optimal set-up obtained at 200 Pa is only slightly better considering nitrogen removal, while it is disadvantageous considering desulphurisation as the pressure decreases.

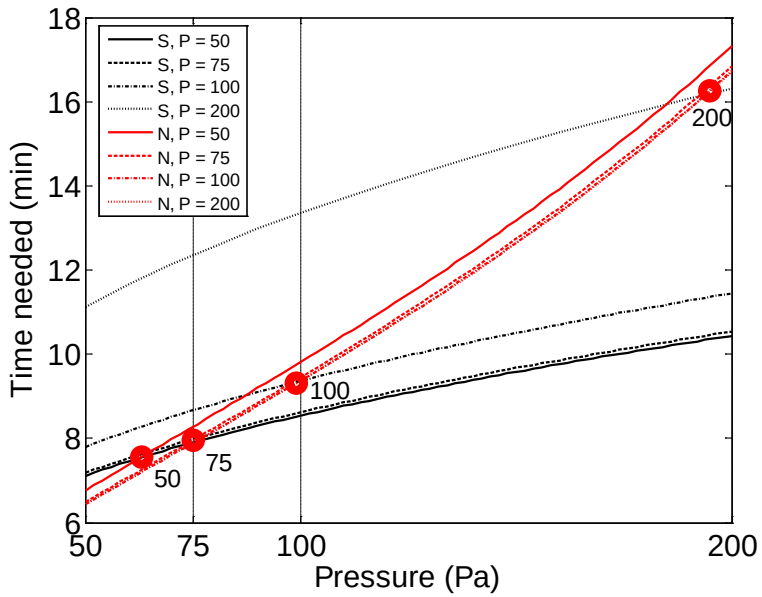

Figure 9.3 Time needed to reach target composition of S and N as function of pressure, using optimal set-ups found at P = 50, 75, 100 and 200 Pa. The circles indicate the pressure above which the time to reach the nitrogen composition is limiting.

For all solutions the optimal amounts of the refining elements in the steel (Al, Ca and Si) reach the highest possible value, defined by the constraints imposed. The optimal solution obtained at 50 Pa indicates that some Al is dissolved from the slag into the steel, while the opposite is seen at higher pressures. In **Figure 9.4** the optimal set-ups found at 50 Pa and 200 Pa are varied with respect to some critical variables. As can be seen in **Figure 9.4a** and **9.4b** desulphurisation is most effective if the SiO_2 content is below a certain value while the nitrogen removal is more or less unaffected. However at a high pressure the nitrogen removal is limiting which indicates that the SiO_2 content will be optimised with respect to the nitrogen removal as seen in **Figrue 9. 4b**. Al_2O_3 on the other hand has one optimal value which strongly depends on the remaining parameters as shown in **Figure 9.4c** and **9.4d**, again the nitrogen removal is limiting at higher pressures. The time needed to reach the critical content of nitrogen, sulphur and oxygen in the steel depends on temperature as shown in **Figure 9.4e** and **9.4f**. However, while nitrogen removal simply is enhanced with increasing temperature, the effect on sulphur and oxygen depends on other parameters as well. Thus, since different pressures yield different

optimal set-ups, particularly regarding the slag composition, the temperature effect is different for sulphur and oxygen. In **Figure 9.4g** and **9.4h** the positive effect of increasing the slag amount on desulphurisation is clearly demonstrated. However, using the optimal set-up found at 200 Pa the time needed to reach the critical oxygen content increases with the slag amount which has a negative effect on the desulphurisation as seen at higher pressures in **Figure 9.4h**. In general, it is shown that the nitrogen removal becomes limiting as the pressure increases.

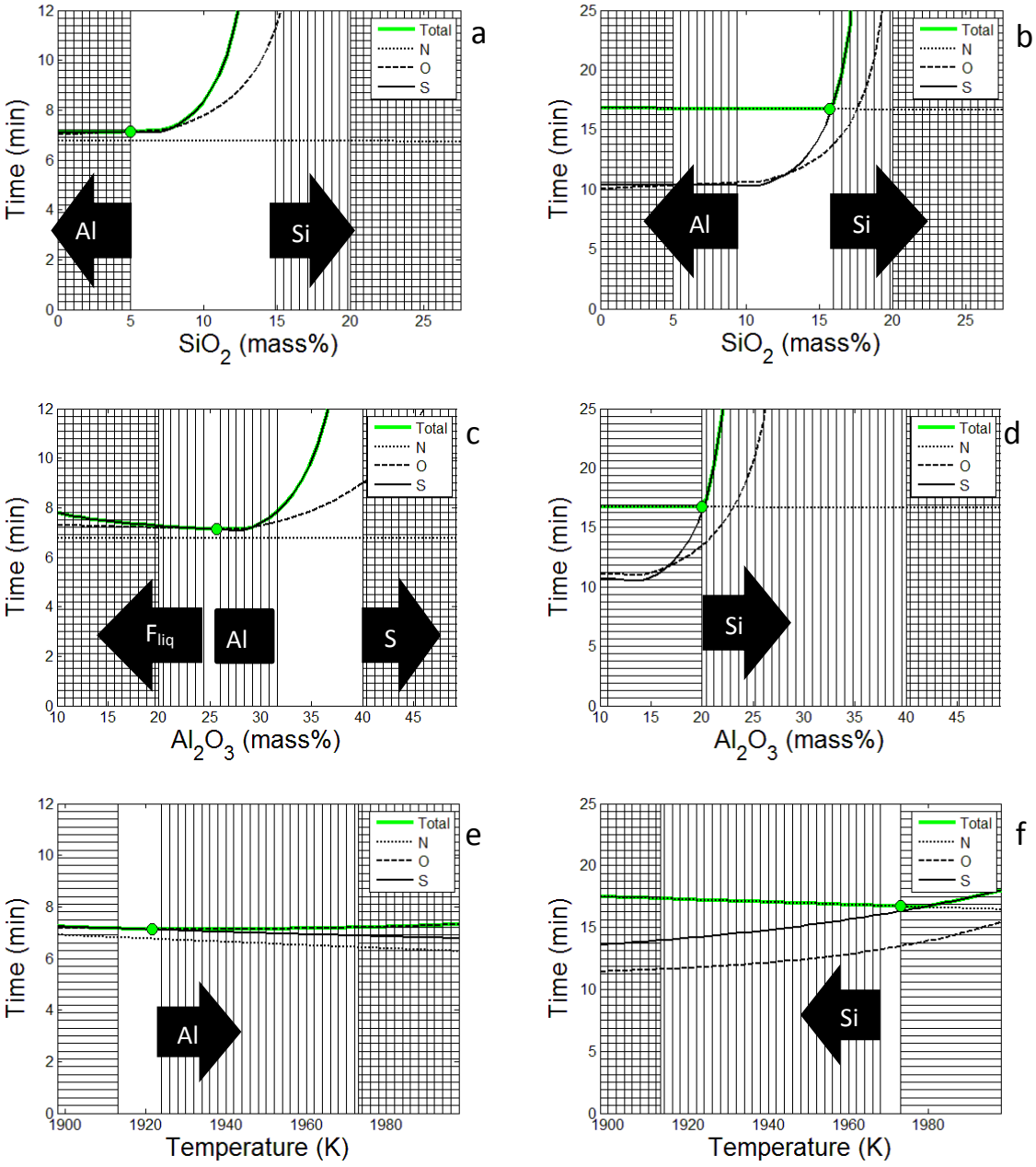

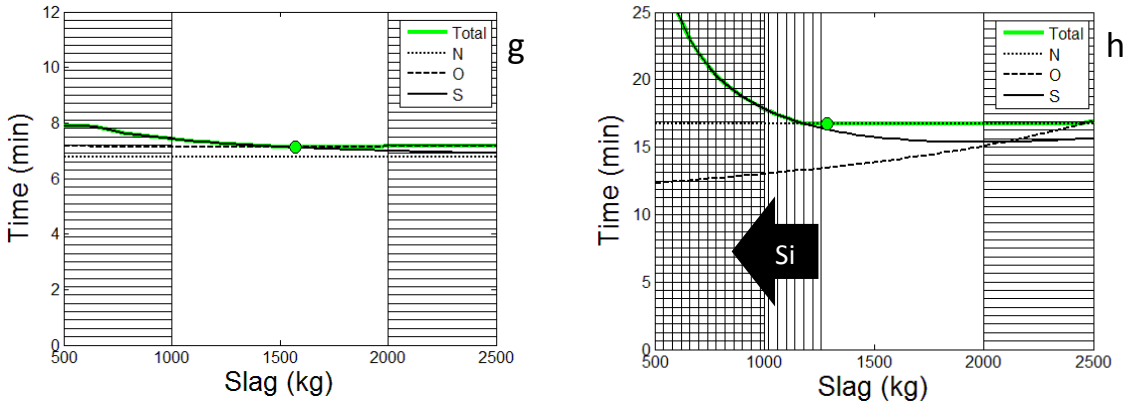

Figure 9.4 Time to reach target composition in total, N, S and O plotted against optimization variables. All other optimisation variables are fixed to the optimal set-up. The left side is using the solution at 50 Pa and the right side is the solution at 200 Pa. Vertical lines means that some criterion has not been met and horizontal lines means that the variable is outside the search domain. The arrows show which constraint that is broken.

The fact that the optimal set-up at low pressures is close to industrial practice shows that the methodology can reproduce what is known to be good slag and steel compositions. The fact the agreement with industrial practice is observed at lower pressures than expected indicated that the current description of nitrogen transfer should be improved. Using this approach it should be possible to predict a good slag composition as well as the amount of refining elements needed to produce a certain steel grade. In principle the process optimisation approach as described in this paper, which originally was developed for alloy design, could be extended and applied on other process steps as well, e.g. decarburisation of stainless steel, melting of scrap in an electric arc furnace or even on multi-stage processes.

9.4 Conclusions

By using a ‘materials-by-design’ approach in which a genetic algorithm, computational thermodynamics and analytical process models are combined, a model has been developed to minimise the vacuum degassing time as a function of the steel and slag compositions. Despite the simple analytical descriptions for the mass transport kinetics, the predicted optima are close to industrial practice. A lower pressure than expected on the basis of industrial practice generates the optimal set-up, which is due to the (too) simple relationship for the nitrogen mass transfer. For the optimal set-up the target

contents of sulphur, nitrogen and oxygen are reached almost simultaneously. The predicted optimal slag amount is larger than used in normal industrial operation. However, it has previously been established that an increased slag amount is beneficial for desulphurisation. At lower pressures the optimal set-up is stable; in most cases the process time decreases until the variable hits one of the physical constraints. At higher pressures there are some cases where the optimal results are almost unaffected by a change in the value of the variable, the reason being that the nitrogen content becomes limiting.

References

[1] Xu W, Rivera-Díaz-Del-Castillo PEJ, van der Zwaag S. Computational design of UHS maraging stainless steels incorporating composition as well as austenitisation and ageing temperatures as optimisation parameters. Philos. Mag. 2009;89:1647.
[2] Kor G, Glaws P. Ladle refining and vacuum degassing. The Making, Shaping and Treating of Steel 1998:661.
[3] Szekely J. The fundamental aspects of injection metallurgy. Ladle Metallurgy. Springer, 1989. p.27.
[4] Andersson JO, Helander T, Höglund L, Shi P, Sundman B. Thermo-Calc & DICTRA, computational tools for materials science. Calphad: Computer Coupling of Phase Diagrams and Thermochemistry 2002;26:273.
[5] Kaufman L, Bernstein H. Computer calculation of phase diagrams. With special reference to refractory metals. 1970.
[6] Saunders N, Miodownik AP. CALPHAD (Calculation of Phase Diagrams): A Comprehensive Guide: A Comprehensive Guide: Elsevier, 1998.
[7] Lucas GE. The evolution of mechanical property change in irradiated austenitic stainless steels. J. Nucl. Mater. 1993;206:287.
[8] Hillert M. The compound energy formalism. J. Alloys Compd. 2001;320:161.
[9] Thermo-Calc A. TCFE6, Thermo-Calc Software AB Steel Database, Version 6.2. Stockholm: Thermo-Calc AB 2009.
[10] SLAG3 - TCS Fe-containing Slag Database v3.1 as supplied by Thermo-Calc Software AB, Thermo-Calc, Stockholm. 2010.
[11] SSUB3 - SGTE Substances Database v3.3 as supplied by Thermo-Calc Software AB, Stockholm. 2008.
[12] Jonsson L, Sichen D, Jönsson P. A New Approach to Model Sulphur Refining in a Gas-stirred Ladle–A Coupled CFD and Thermodynamic Model. ISIJ Int. 1998;38:260.
[13] Hallberg M, Jonsson TLI, Jonsson PG. A New Approach to Using Modelling for On-line Prediction of Sulphur and Hydrogen Removal during Ladle Refining. ISIJ Int. 2004;44:1318.
[14] Asai S, Kawachi M, Muchi I. Mass transfer rate in ladle refining processes. SCANINJECT III, Refining of Iron and Steel by Powder Injection 1983:12.

[15] Pluschkell W. Grundoperation pfannenmetallurgischer Prozesse. Stahl und Eisen 1981;101:97.
[16] Urbain G. Viscosity of silicate melts. Trans. J. Br. Ceram. Soc. 1981;80:139.
[17] Weymann H. On the hole theory of viscosity, compressibility, and expansivity of liquids. Kolloid-Zeitschrift und Zeitschrift für Polymere 1962;181:131.
[18] Mills K, Sridhar S. Viscosities of ironmaking and steelmaking slags. Ironmaking & steelmaking 1999;26:262.
[19] Jiang R, Fruehan R. Slag foaming in bath smelting. Metall. Trans. B 1991;22:481.
[20] Keene BJ. Surface tension of slag systems. in Verein Deutscher Eisenhüttenleute (Ed.), Slag Atlas, 2nd ed. Düsseldorf, 1995. p.403.
[21] Xu W, Rivera-Díaz-del-Castillo PEJ, van der Zwaag S. Designing nanoprecipitation strengthened UHS stainless steels combining genetic algorithms and thermodynamics. Comput. Mater. Sci. 2008;44:678.
[22] Carroll DL. FORTRAN genetic algorithm driver. CU Aerospace 2001.

Summary

Alloy design by the traditional trial and error approach is known to be a time consuming and a highly cost procedure, especially for the design of heat resistant steel where the feedback time is intrinsically long. The significant developments in computational simulation techniques in the last decades have made a theory-guided computational alloy design possible. Such a computational approach can substantially decrease the development time costs. In this thesis a computational alloy design approach coupling thermodynamics, kinetics and a genetic algorithm has been developed to design the non-corroding ferritic, martensitic and austenitic heat resistant steels for use at a high service temperature. In the design of heat resistant steels, the evolution of the microstructure and hence properties, depends on service time and temperature and should be considered carefully. For heat resistant steels deriving part of their high strength on precipitates the coarsening of the precipitates at high temperature is considered as the most important factor and this process features highly in the design. Novel steel compositions (involving typically 9 alloying elements) and associated key heat treatment parameters are considered and optimised. The calculated optimal compositions are unlikely to be perfect and free of experimental problems but form an excellent start to initiate experimental development programs and to substantially shorten the development time of new high performance steel grades.

In Chapter 2, this alloy design approach is applied to the design of precipitation strengthened austenitic heat resistant steel. Three alloys dedicating to three service time of 0 h (for comparison), 10 h (optimised for fire resistance) and 10^5 h (optimised for creep resistance), are designed to have the best precipitation hardening contribution of MX carbionitride at their designed times, respectively. For short service times, the optimal composition has a high volume fraction of MX carbonitride with a relatively high coarsening rate. The optimal composition for a long use time has a relative low volume fraction of MX carbonitride yet an extremely low coarsening rate. The kinetics of precipitate coarsening forms the basis for the time and temperature dependence of the creep strength for MX carbonitrides precipitation strengthening austenitic creep resistant steels. A validation of the designed alloys against existing commercial precipitation strengthened austenitic steels indicates that the model is quite reliable and suggests that the newly defined alloy compositions are likely to be stronger at longer use times than the existing austenitic creep resistant steels currently on the market.

As stated in Chapter 2, precipitation hardening contributions decrease with time owing to coarsening of precipitates, while strength control via solid solution strengthening is stable once thermodynamic equilibrium is achieved. Solid solution strengthening is the main strengthening source in existing ferritic heat resistant steels. Consequently, ferritic heat resistant steels are designed with optimised solid solution strengthening and minimised undesirable microstructural components in Chapter 3. The solid solution strengthening model in the design was validated successfully against existing steel grades. Alloying elements Mn, Al, Si and Ni are found to have the highest solid solution strengthening contribution in ferritic steels. The ferritic alloy designed has been compared to existing ferritic steels and is predicted to deliver a better performance.

In Chapter 4, this computational alloy design approach is extended to simultaneously optimise the precipitation hardening and solid solution strengthening in martensitic creep resistant steels via constructing a “Pareto front” of precipitation hardening and solid solution strengthening contributions for all qualified solutions. From the Pareto front analysis, a new alloy is found with an optimal combination of a relatively stable precipitation hardening even after 10^5 hours at a service temperature of 650 °C and a high solid solution strengthening. However, minor deviations in composition lead to significant reductions in the precipitation hardening contribution but small effects on the solid solution strengthening contribution. The robustness of composition is thus considered and improved by adding a new criteria. For the new design steels considering the robustness of composition, the usual fluctuations in chemical composition do not lead

to substantial reductions in final creep strength. In the newly constructed Pareto front, a large amount of alloys that are predicted to outperform existing martensitic/ferritic creep resistant steel grades, can be found. Alloying elements have a significant impact on precipitation hardening and solid solution strengthening. Unplanned variations in the concentrations of Ti, Nb, N and C can change the coarsening rate of the strengthening MX carbonitrides significantly. Alloying elements Al and Ni are found to have substantial solid solution strengthening effects without negatively affecting the precipitation hardening. Mo is a less suitable solid solution hardening element for long term applications as it will be consumed by less effective precipitates.

In the previous chapters, the creep strain rate, ultimately determining the creep life time, is not taken into account. In Chapter 5, a strain based model takes into account the coarsening of TiX carbonitride precipitates and its effect on threshold stress is presented, and it was able to reproduce the properties of existing precipitation hardened austenitic creep resistant steels with very good accuracy. 1% creep strain is taken as the maximum strain and alloys with best combination of applied stress and intended life time are designed. The new alloy compositions are predicted to have substantially better properties at 650 °C (both for short, medium and long service times) than the existing commercial steel grades.

Laves phase and $M_{23}C_6$ are conventionally regarded as undesirable precipitate families in heat resistant steels owing to their very high coarsening rates. In Chapter 6, the concept is challenged and it is shown that these two precipitate families can achieve low coarsening rate by tuning the alloy composition. Among all the alloying elements, Co and W are the most effective elements that can significantly reduce the coarsening rate of Laves phase, and the effect increases with Co and W level. Furthermore, an increase in the level of W can lead to a higher volume of Laves phase since W is the main Laves phase forming elements. Another Laves phase forming element, Mo, has a different effect on the coarsening rate of Laves phase. An optimum low-coarsening level is achieved at 4-5 wt% Mo. The alloy composition with optimal combination of Laves phase and $M_{23}C_6$ is designed by construction a Pareto front of precipitation hardening contriubutions of Laves phase and $M_{23}C_6$. It was found to be impossible to effectively combine MX and $M_{23}C_6$ as strengthening precipitates.

An optimal combination of precipitation hardening and solid solution strengthening has been achieve in the design of martensitic creep resistant steel by constructing a Pareto fronts. Similar to the approach used in martensitic steels, In Chapter 7 the design of

ferritic, martensitic and austenitic steels is presented with optimal combinations of precipitation hardening and solid solution strengthening. The constructed Pareto fronts and other qualified solutions of all the three types of alloys are summarized and positioned in one plot. Martensitic steels can have the best combination of precipitation hardening and solid solution strengthening, while ferritic steel have the greatest solid solution strengthening potential but a low precipitation hardening. Austenitic creep steels have the highest precipitation hardening potential but a low solid solution strengthening capability

In Chapter 8, prototype alloys, as developed in chapters 2 to 4, with optimised SSS (ferritic steel FSSS and martensitic steel MSSI), PH (austenitic steel APH and martensitic steel MPHI) and combination of PH and SS (martensitic steel MPHS) are fabricated, heat treated and tested. The microstructures are characterised and hardness values are measured at solution treatment and ageing stages, respectively. Alloys APH and MPHI were found to have the the intended matrices. Alloys MPHS and MSSI were found to have ferrite-martensite matrix instead of the intended fully martensitic matrix. Alloy FSSS has a ferritic matrix but with the presence of a large amount of Laves phases. The mismatch between the thermodynamic (Thermo-Calc) predictions for the matrix structure and the experimental results may be related to the high Al content. The precipitate stability during ageing at 650 °C was investigated for the solution treated alloys. Alloy MPHS and MSSI gain a significant increase in hardness after ageing for 1 h due to the precipitation of fine and evenly distributed particles, which are probably NiAl according to ThermoCalc calculations. The other martensitic alloy MPHI shows no significant increase in hardness during ageing and the hardness decreases slowly with time. Alloys MPHI and P92 are of similar hardness after quenching, but the hardness decrease in the new alloy decreases more slowly than for P92 owing to a low coarsening rate MX carbonitride. As confirmed by TEM replica experiments, the MX carbonitride still has a small size of around 10-50 nm even after a long time at 650 ^{o}C. This proves that alloy MPHI successfully achieves the design target of a martensitic creep resistant steel strengthened by MX carbonitrides with a very low coarsening rate. The hardness of austenitic alloy almost keep constant for about 300 h and then increase due to the precipitate of some intermetallic phase.

In Chapter 9, the alloy design approach was reformulated to optimise the time for a liquid steel degassing process. The combination of the genetic algorithm, thermodynamics and analytical process models, leads to a realistic prediction of the vacuum degassing time as

a function of the steel and slag compositions. Despite the simple analytical description of the mass transport kinetics, the predicted optima are close to industrial practice. A lower pressure than expected on the basis of industrial practice is required to generate the optimal set-up. For the optimal set-up the target concentrations of sulphur, nitrogen and oxygen are reached almost simultaneously. At lower pressures the optimal set-up is stable; in most cases the process time decreases until the variable hits one of the physical constraints. At higher pressures there are some cases where the optimal results are almost unaffected by varations in the variable values, the reason being that lowering the nitrogen content becomes rate limiting.

Samenvatting

De ontwikkeling van nieuwe metaallegeringen via een ‘trial en error’ methode is een langzame en zeer kostbare zaak, zeker in het geval van kruipstaalsoorten waarbij de evaluatie van de verkregen eigenschappen onvermijdelijk pas na lange tijd afgerond kan worden. Dankzij belangrijke ontwikkelingen op het gebied van modelmatige materiaalbeschrijving is het nu mogelijk nieuwe metaallegeringen te bedenken en optimaliseren op basis van computermodellen en de resultaten als aanzet voor de experimentele programma’s te gebruiken. Deze aanpak heeft belangrijke financiële voordelen. In dit proefschrift wordt een modelmatige aanpak gepresenteerd voor het ontwerpen van corrosie-vaste austenitische, ferritische of martensitische kruipstaalsoorten. De te presenteren modellen zijn gebaseerd op thermodynamica, thermo-kinetiek en metaalkundige concepten en maken gebruik van een genetisch algoritme. In het ontwerpen van de nieuwe legeringen moet rekening gehouden worden met het feit dat de microstructuur verandert tijdens langdurig gebruik op hoge temperatuur. Voor kruipstaalsoorten die hun sterkte grotendeels ontlenen aan precipitaten is de kinetiek van de precipitaatvergroving de meest belangrijke optimalisatiefactor. In de te presenteren modellen worden typisch 9 legeringselementen en tenminste 1 procestemperatuur in rekening gebracht, welke alle binnen redelijk ruime marges gevarieerd kunnen worden. De optimale samenstelling zoals die volgt uit de ontwikkelde computermodellen is vast niet volledig vrij van experimentele problemen maar biedt een

uitstekend startpunt voor het technische ontwikkelprogramma en dit zal zeker leiden tot belangrijke verkorting van het totale ontwikkeltraject.

In hoofdstuk 2 wordt het model ontwikkeld voor en toegepast op het ontwerp van nieuwe precipitatiegeharde austenitische kruipstaalsoorten. In de optimalisatie worden drie beoogde gebruikstijden (0, 10 en 10^5 uur) beschouwd en voor elke gebruikstijd is de bijdrage van de MX-carbonitride precipitaten aan de uiteindelijke sterkte geoptimaliseerd door gerichte aanpassing van de staalsamenstelling. Het staaltype voor kortstondig gebruik op hoge temperatuur heeft een hoog volume percentage precipitaten maar deze vergroven met een relatief hoge snelheid. Het staaltype met de beoogde zeer lange gebruikstijd heeft minder precipitaten maar deze zijn uitermate stabiel en leveren ook na zeer lange tijd nog een belangrijke bijdrage aan de hoge-temperatuursterkte. Vergelijking van de eigenschappen van de nieuwe staalsoorten met die van bestaande kruipstaalsoorten suggereert dat het ontwikkelde model de belangrijkste processen goed in rekening brengt. De nieuwe staalsamenstelling zou tot betere eigenschappen moeten leiden dan de austenitische kruipstaalsoorten nu op de markt.

In precipitatie hardende kruipstaalsoorten neemt de sterkte in de loop van de tijd af door de vergroving van de precipitaten. In het geval van oplosharding is de sterktebijdrage echter tijdsonafhankelijk. Ferritische kruipstaalsoorten ontlenen hun sterkte grotendeels aan deze oplosharding. In hoofdstuk 3 is het model aangepast om te komen tot nieuwe ferritische staalsoorten met een hogere oplosharding en een zeer laag gehalte aan ongewenste uitscheidingen. De voorspellingen van het model zijn getoetst aan de eigenschappen van bestaande ferritische staalsoorten en bleken zeer betrouwbaar. De legeringselementen Mn, Al, Si en Ni spelen een belangrijke rol in de verhoging van de sterkte. De berekende optimale staalsamenstelling zou tot hogere sterktes moeten leiden dan nu op de markt verkregen worden.

In hoofdstuk 4 wordt het model gepresenteerd waarin zowel de precipitatieharding als de oplosharding geoptimaliseerd worden voor een beoogde levensduur van 10^5 uur op een vaste temperatuur van 650 ^{0}C. Hierbij werd gebruik gemaakt van de zogenaamde Pareto-front benadering en de optimale oplossing zou een duidelijke verhoging van de sterkte moeten geven. De samenstelling van dit nieuwe staal is echter heel kritisch en kleine variaties in samenstelling leiden tot grote veranderingen in eigenschappen. Dit geldt vooral voor de legeringselementen Ti, Nb, N en C die betrokken zijn bij de vorming van MX-carbonitrides. De legeringselementen Al en Ni leveren een relatief stabiele bijdrage aan de sterkte. Ter voorkoming van de ongewenste gevoeligheid ivoor kleine afwijkingen in de exacte samen stelling is het model aangepast om te komen tot de berekening van robuuste staalsamenstellingen waarbij kleine samenstellingsvariaties slechts een gering effect op de uiteindelijke hoge sterkte hebben.

In de voorgaande hoofdstukken is alleen gekeken naar de stabiliteit van de sterkte-verhogende componenten, maar is geen rekening gehouden met de eigenlijke kruipverlenging die bepalend is voor het bezwijken van het materiaal. In hoofdstuk 5 wordt een nieuw model gepresenteerd waarin het effect van de vergrovende precipitaten op de spanningsafhankelijkheid van de kruipsnelheid kwantitatief in rekening gebracht. Het model bleek het gedrag van bestaande precipitatiegeharde austenitische staalsoorten goed te beschrijven indien uitgegaan wordt van een constante maximaal toegestane kruipverlenging van 1%. Toepassing van het optimalisatie model voor de geselecteerde 9 legeringselementen geeft aan dat er diverse samenstellingen zijn die tot belangrijke verbeteringen in de combinatie van maximaal toepasbare spanning en levensduur kunnen leiden.

Traditioneel worden Laves fases en $M_{23}C_6$ uitscheidingen niet gebruikt in kruipstaalsoorten omdat ze aanleiding geven tot een relatief snel verlies van eigenschappen. In hoofdstuk 6 wordt dit uitgangspunt verlaten en wordt aangetoond dat er ook heel stabiele Laves fases en $M_{23}C_6$ uitscheidingen bestaan. De legeringselementen Co en W hebben het meest gunstige effect op de stabiliteit van Laves fases en het effect neemt toe met toenemend gehalte. Een verhoging van het W gehalte heeft ook een aanvullend positief effect op de volumefractie. Het effect van Mo op de stabiliteit van Laves fases is optimaal bij 4-5 gewichtsprocent. Een Pareto-front benadering werd gebruikt om nieuwe staalsamenstellingen leidend tot een optimale combinatie van stabiele Laves fases en $M_{23}C_6$ uitscheidingen te verkrijgen. Het bleek niet mogelijk MX en $M_{23}C_6$ uitscheidingen op soortgelijke wijze effectief te combineren.

In hoofdstuk 7 wordt een bredere studie naar de optimalisatie van austenitische, ferritische en martensitische kruipstaalsoorten gepresenteerd waarin voor alle drie matrixvarianten de maximale sterktewinst door precipitatieharding en oplosharding bij hoge temperatuur onderzocht en vergeleken wordt. Uit het onderzoek blijkt dat martensitische staalsoorten de beste mogelijkheden bieden voor een succesvolle combinatie van precipitatie- en oplosharding. Ferritische staalsoorten zijn meer geschikt voor optimalisatie van de oplosharding. Austenitische staalsoorten bieden de beste mogelijkheden voor precipitatieharding maar hebben beperkte kansen op oplosharding.

Hoofdstuk 8 beschrijft de resultaten verkregen aan de 5 legeringen die op basis van de berekeningen gepresenteerd in hoofdstukken 2 tot 4 geproduceerd zijn. Het zijn een ferritische legering met optimale oplosharding (FSSS), een martensitische legering met optimale oplosharding (MSSI), een precipitatie hardende austenitische legering (APH), een precipitatie-hardende martensitische legering (MPHI) en een martensitische legering met zowel oplos- als precipitatieharding (MPHS). Alleen de legeringen APH en MPHI hadden de beoogde matrix structuur. Legering FSSS had wel de beoogde structuur maar bevatte veel Laves fase. De afwijking wordt gedeeltelijk toegeschreven aan het onvermogen van ThermoCalc om goed om te gaan met het hoge Al gehalte in de

legering. Legering MPHI en het commerciële referentiestaal NH92 hadden een vergelijkbare aanvangshardheid maar de hardheid van MPHI als gevolg van gloeien op 650 °C nam nog langzamer af dan NH92 als gevolg van de hoge stabiliteit van de gevormde MX-carbonitrides. TEM replica studies lieten zien dat ook na lang gloeien de precipitaat afmetingen niet verder toegenomen waren dan tot 10-50 nm. Van alle geproduceerde legeringen voldoet legering MPHI het beste aan het beoogde gedrag. De hardheid van de austenitische proeflegering bleef 300 uur constant en nam toen langzaam toe als gevolg van de uitscheiding van een intermetallische fase.

Tot slot beschrijft hoofdstuk 9 hoe het concept achter de bovengenoemde modellen gebruikt kan worden voor de constructie van een nieuwe model ter minimalisatie van de procestijd tijdens vacuüm-ontgassen van vloeibaar ijzer. Het nieuwe model, gebaseerd op het genetisch algoritme, thermodynamica en een aantal analytische procesmodellen, geeft een realistische voorspelling van de benodigde procestijd als een functie van de samenstelling van het staal en de slak. Voor de optimale instellingen worden de beoogde concentraties van zwavel, stikstof en zuurstof min of meer gelijktijdig bereikt. Bij lage druk in de installatie is het proces behoorlijk stabiel en wordt de procestijd bepaald door de tijd waarbij een van de variabelen de gestelde grenswaarde bereikt. Bij hogere druk in de installatie wordt de procestijd vrijwel onafhankelijk van de instellingen. In dat geval is de verlaging van het stikstofgehalte de enige procestijdbepalende stap.

Appendix A

The impact of intended service temperature on the optimal composition of Laves and $M_{23}C_6$ precipitate strengthened ferritic creep resistant steels

A.1 Introduction

In Chapter 6, Laves phase and $M_{23}C_6$ in martensitic creep resistant steels are tuned to have a low coarsening rate and a high volume fraction at a fixed service temperature so as to reach a desirable high precipitation hardening contribution. In this appendix, Laves phase and $M_{23}C_6$ will again be tuned to strengthen ferritic creep resistant steels, but the emphasis will focus on the impact of intended service temperature on the optimal compostion.

The operation temperatures in power plants are continually increased in order to improve the efficiency of power generation and to reduce CO_2 emissions. This trend put increasing demands on the performance of creep resistant steels used to construct boiler and steam turbine components in power plants. For instance, at operation temperatures of 500-620 ^{o}C, martensitic creep resistant steels are a good choice owing to their excellent creep strength and their low thermal fatigue behavior originating from a low thermal expansion coefficient [1]. However, if the operation temperature exceeds 650 ^{o}C for extended periods, martensitic creep resistant steels are intrinsically unsuitable due to a significant microstructural degradation (recovery of dislocations and lath structures) [2]. Austenitic creep resistant steels could be of interest as they have a high creep strength at

temperatures up to 700 ^{o}C. However their thermal expansion coefficient and cost are not favorable relative to martensitic creep resistant steels. The third family of creep steels, ferritic creep resistant steels, generally have a desirable low thermal expansion coefficient but their creep strength is relatively low. Relative recently it has been discovered that their very long term-high temperature strength can be significantly improved by introducing PH of intermetallics, such as Laves phase [3-6].

Kimura and Toda et. al recently developed a super strong 15Cr ferritic creep resistant steel (hereafter referred as alloy 15Cr) through the use of PH of Laves phase (Fe_2W) [4, 7-13], which remains stable over long term service at temperature up to 700 ^{o}C. Moreover, the time dependence of the strengthening via Laves phase can be further improved through the modification of alloying elements, such as Co and W [14] so as to increase volume fraction and decrease the coarsening rate. This would open the possibility of using such an alloy at even higher service temperatures, such as 750 ^{o}C. However, when the service temperature changes, the thermodynamic and kinetics of ferritic creep steels (typically containing at least 8 alloying elements) are also changed, and thus the optimal composition (the composition leading to a maximal concentration of slowly coarsening precipitates) may also vary. The present computational alloy design study aims at designing optimal ferritic steel compositions for 10^5 hour use at their intended service temperatures, i.e. 650, 700 and 750 ^{o}C, by coupling thermodynamics, thermokinetics and PH theories. The predicted effect of service temperature on the optimization of new alloy composition is discussed and compared to that experimentally recorded for a 15Cr steel. In the discussion, it is also shown how the model can be used to modify the steel composition to have a ferritic creep steel with a high short term and a long term strength by the superposition of two strengthening precipitates: $M_{23}C_6$ and Laves phase.

A.2 Model description

First, a desirable microstructure will be defined that can be used at high temperatures in power plant applications. As discussed in the introduction, given the right overall steel composition Laves phase can be used to yield significant precipitation strengthening. The microstructure of the matrix is chosen to be ferrite because of its high resistance to thermal fatigue and good capacity to dissolve Cr causing an improved oxidation resistance. Therefore, the desirable microstructure is: 1) a nearly fully ferritic matrix; 2) a low volume fraction of undesirable phases and 3) a high volume fraction of Laves phase

with a tailored low coarsening rate. In order to obtain the microstructure defined above, a computational alloy design model has been developed, coupling a Genetic Algorithm (GA) optimisation protocol [15-18]. More information on the genetic algorithm used can be found in Ref. [19].

The real alloy design process in the model is as follows: Firstly, the GA generates random composition and heat treatment parameters from the predefined parameter ranges, which is listed in table A.1. We consider nine variables (8 alloying elements and the annealing temperature) each equally spaced at 32 levels between predefined lowest and highest values. As the thermodynamic equilibrium state for multicomponent systems depends on the temperature, the compositional optimisation is done for three predefined temperatures, 650, 700 and 750 ^{o}C. For each optimisation run, the intended service time is fixed at a high value of 10^5 hours.

Table A.1 Search ranges (in wt.%) of 8 chemical elements and the annealing temperature T_{anneal}.

	C	*Cr*	*Mo*	*W*	*Co*	*Nb*	*N*	*V*	*Fe*	T_{anneal}
Min.	0.001	8.00	0.001	0.001	0.001	0.001	0.001	0.001	Bal.	900 ^{o}C
Max.	0.10	20.00	2.00	10.00	10.00	1.00	0.15	1.00		1250 ^{o}C

Then, a candidate solution (composition and heat treatment conditions) is fed to the heat treatment in practise. The typical heat treatment precipitation-hardened ferritic creep-resistant steels consists of an annealing/solution treatment and a followed fast cooling. After fast cooling and mild stress relieving the steels are subjected to the service temperature directly [11]. To check if the candidate solution can lead to the desirable microstructure defined above, various go/no-go criteria are defined according to the order of the heat treatments. Following the heat treatment sequence, the first set of thermodynamic calculations are performed at the (variable) annealing temperature and three go/no-go criteria are imposed: (1) the equilibrium ferrite should be at least 99% in volume; (2) no liquid should be present; (3) the volume fraction of primary carbides should be less than 0.5%. Then, at the intended service temperature, a second set of thermodynamic calculations are performed and two additional go/no-go criteria are defined: (4) the volume fraction of precipitates excluding Laves phase should be no more than 1 %; (5) The equilibrium Cr concentration in the matrix should at least be 15 wt.% to assure high corrosion and oxidation resistance (a different residual Cr concentration level could have been chosen, but this level is selected on the basis of existing literature).

The aim of this study is to design ferritic steels only strengthened by Laves phase for different service temperatures. Therefore, all solutions fulfilling all above 5 go/no-go criteria is further ranked by the time and temperature dependent PH effect of Laves phase which is considered to be the sole optimisation criterion. The PH is affected by the inter-particle spacing [20]. Considering the ultra-long service time (up to 10^5 h), the precipitate would grow and coarsen significantly at high temperatures, and thus the inter-particle spacing (L) changes. Given the precipitate coarsening, the precipitation hardening contribution inverse proportional to inter-particle spacing, is descried by Equation 2.2. Other details can be found in section 2.2.3.

Precipitates of the Laves phase in ferritic steels generally have a disk shape [8, 21], and the coarsening rate of disk precipitate is around 5/e time higher than that of spherical precipitate [22], where e is the aspect ratio of thickness and diameter of a disk. This ratio e is generally constant for existing ferritic alloys and the value is around 0.5, thus the coarsening rate of disk Laves phase is expressed as [23]

$$K = 80\gamma {V_m}^p / \sum_{i=1}^{n} \frac{9(x_i^p - x_i^m)^2}{x_i^m D_i / RT} \qquad \text{(A.1)}$$

where V_m^p is the molar volume of Laves phase, x is the equilibrium interfacial mole fraction of the relevant alloying element on both the matrix (m) or the precipitate (p) sides, D is corresponding diffusion coefficient and T is the service temperature. the interfacial energy γ is set to a value of 0.1 J/m^2 for lack of data on the actual impact of chemical composition on surface tension. The thermodynamic values, such as D_i, V_m^p, x_i^p and x_i^m, are obtained via Thermo-Calc® using the TCFE7 and Mob2 databases.

The factor 1/L, which for a particular steel has a temperature and time dependent value, is called the PH factor and is to be optimised depending on the service temperature and the service time. The intended service time in this study is fixed at 10^5 h reflecting the long period of service in power plant applications. From an optimised factor 1/L at 10^5 h, one can on only get the maximising PH contribution at the end of that time, but also the PH power throughout the whole service life. Laves phase (Fe2W) is formed by consuming W, which can also decrease the coarsening rate in the meantime [24]. So a high PH power is obtained at a high volume fraction and a low coarsening rate of Laves Phase (Equation 2.2).

A.3 Model validation

In order to validate the model, its power to back 'predict' the properties of one of the most advanced ferritic creep steels currently on the market, alloy 15Cr, is examined. To this aim the PH factors of Laves phase in alloy 15Cr at service temperatures of 650, 700 and 750 ^{o}C are calculated on the basis of its composition, which is listed in Table A.2. In **Figure A.1**, these factors are compared to experimental creep strength [21] in order to validate the use of the factor 1/L (Equation 2.2) for ranking solutions (compositions and annealing temperature) at different service temperatures. The good linear relationship between calculated and experimental values validates the use of the factor 1/L and indicates that PH effect of Laves phase is the main contribution to the creep strength since the large grain size (200-500 μm) and the low dislocation density in alloy 15Cr barely contribute to the strength. In addition, research has shown that there is a good linear correlation between logarithm of rupture strength and high temperature strength at the same temperature for various stainless steels in the annealed and cold-worked conditions at temperatures range from 538 to 816 ^{o}C and for test times approaching 10^4 h [25]. The intercept of the fit line and the x-axis indicates the (solid solution) strength of the ferritic matrix.

There are two things which need to be clarified to further validate the model. First, the highest point in **Figure A.1** has the largest deviation from the linear line. This point is the sample with a short service time (4900 h) at 650 ^{o}C. For this condition, precipitate growth cannot be ignored, but in our model aiming to predict the behaviour at the end of the service time of 10^5 h coarsening is far more important and growth is in fact ignored. Second, the PH contribution is usually presented as αGb/L (α is a constant, b is the Burgers vector). In the model αGb is taken as constant. For ferritic steels G actually is not a constant but changes about 10% when the temperature changes from 650 to 750 ^{o}C [26]. The small change of G would not influence the final validation compared to significant change of the inter-particle spacing L, which can be suggested from the good linear relationship shown in **Figure A.1**. In summary, the factor 1/L can be taken as an decent first order optimizing/performance factor to rank all qualified solutions for next generation Laves phase strengthened ferritic creep steels.

Table A.2 Composition (in wt.%) and annealing temperature T_{anneal} (in ^{o}C) of existing alloy 15Cr.

	C	*Cr*	*Mo*	*W*	*Co*	*Nb*	*N*	*V*	*Mn*	*Si*	*B*	T_{anneal}
Alloy 15Cr	0.05	15	1.0	6.00	3.0	0.05	0.03	0.2	0.5	0.2	0.003	1200

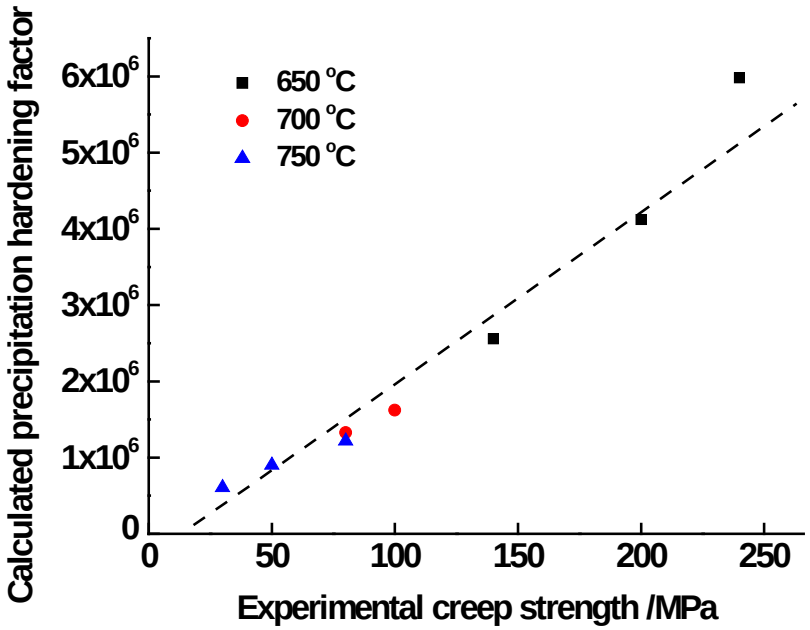

Figure A.1 Calculated precipitation hardeing factor vs. experimental creep strength at different temperatures.

A.4 Model application

The composition and annealing temperature for the three selected service temperatures are optimized and the results are listed in Table A.3. These alloys are labeled as Alloy 650, Alloy 700 and Alloy 750 according to their service temperatures. In all alloys the concentrations of W and Nb reach their maximum level in the search space which will lead to a high volume fraction of Laves phase. Table A.3 also shows that the MX carbonitride forming elements C and V have their minimal levels as the current optimization only focused on maximizing the influence of the Laves phase. The slight difference in Alloys 700 and 750 is in the N concentration and the annealing temperature. Lower Mo, Co and N contents can be found in Alloy 650 compared to those in Alloys 700 and 750. The observations mentioned above will be further analyzed in the discussion section.

Table A.3 Composition (in wt.%) and annealing temperature T_{anneal} (in ^{o}C) of alloys designed for 650, 700 and 750 ^{o}C applications, respectively.

	C	*Cr*	*Mo*	*W*	*Co*	*Nb*	*N*	*V*	T_{anneal}
Alloy 650	0.001	13.80	1.23	10.00	8.06	1.00	0.001	0.001	1250
Alloy 700	0.001	13.80	2.00	10.00	10.00	1.00	0.0058	0.001	1250
Alloy 750	0.001	13.80	2.00	10.00	10.00	1.00	0.035	0.001	1239

The PH factor of Laves phase will decrease with service time owing to the coarsening of Laves phase. The predicted degradation behaviors in the three designed alloys at their correspond service temperatures are shown in **Figure A.2**. Clearly, the PH factor drops with increasing service temperature, since the increase of temperature will significantly increase the coarsening rate of Laves phase.

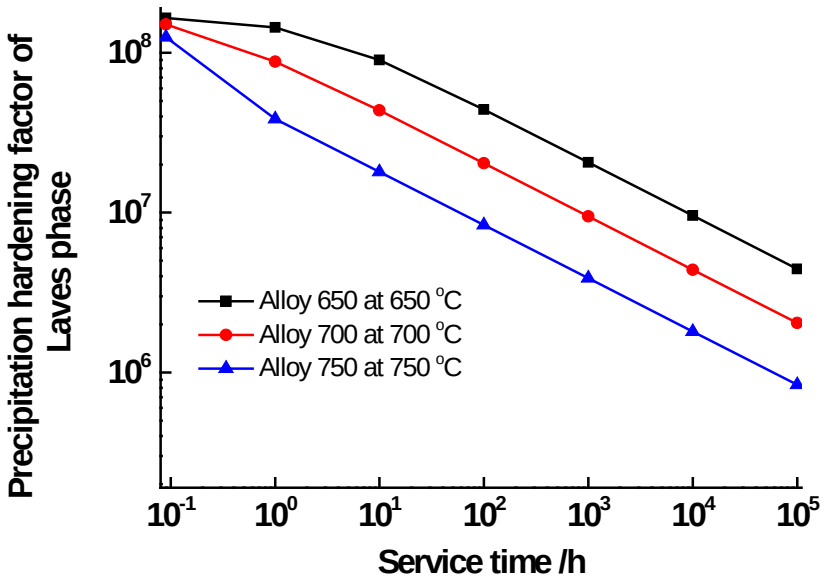

Figure A.2 Degradation of precipitation hardening factor with service time for three designed alloys at their corresponding service temperature 650, 700 and 750 °C, respectively.

A.5 Discussion

A.5.1 Effect of service temperature on the optimization results

In order to compare the three new designed alloys, the Laves phase PH factors at 10^5 h of all designed alloys at 650, 700 and 750 °C are calculated, and the results are shown in **Figure A.3**. PH factors of Alloy 700 and Alloy 750 are almost the same and are higher than those of Alloy 650 both at 700 and 750 °C. This result agrees well with the optimization target that the designed alloy should have the best performance at its designed service temperature. The PH factor of Alloy 650 at 650 °C is less than those of Alloy 700 and Alloy 750 at 650 °C, which at first sight seems to be against expectation.

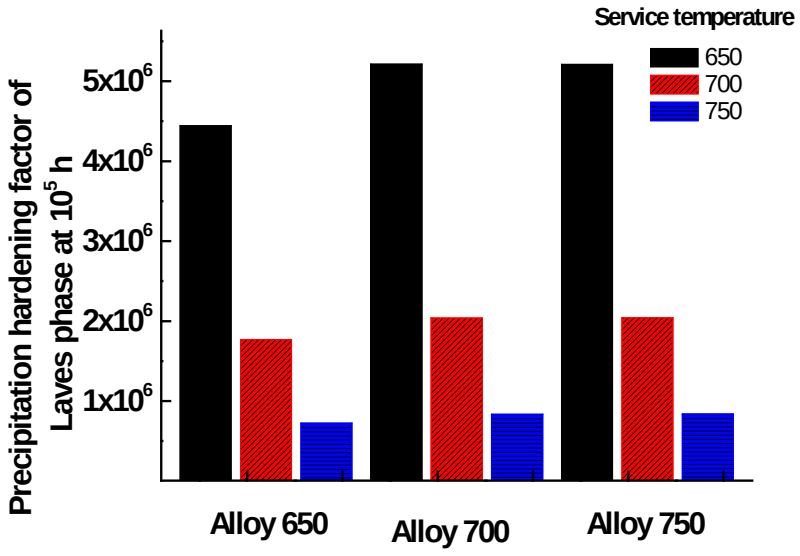

Figure A.3 Precipitation hardening factors of Alloy 650, Alloy 700 and Alloy750 at 650, 700 and 750 ^{o}C three service temperatures

To investigate the reason for this latter seemingly inconsistent result, the phase constitutions at all three temperatures for all three designed alloys are calculated and listed in table A.4. Generally, all three designed alloys contain Sigma phase, NbX carbonitride, Z phase and Laves phase. The volume fraction of undesirable phases in Alloy 650, such as Sigma and Z phase, meet all the go/no-go criteria at all three service temperature. However, the volume fractions of undesirable Sigma phase in Alloy 700 and Alloy 750 at 650 ^{o}C are higher than 5 vol.%, which itself is much higher than maximum allowed amount (1%) as defined in the go/no-go criteria. Therefore compositions of Alloy 700 and Alloy 750 are not acceptable solutions for application at 650 ^{o}C, while Alloy 650 remains the best solution at 650 ^{o}C among all candidate solutions fulfilling all go/no-go criteria. This result also explains the different Mo levels between Alloy 650 and Alloy 700/Alloy 750 since the addition of Mo promotes the formation of Sigma phase. The promotion effect of Mo on the formation of Sigma phase at temperature higher than 650 ^{o}C, such as 700 and 750 ^{o}C, decreases as indicated in tables A.4. Thus Alloy 700 and Alloy 750 are qualified solutions at their intended service temperature. The difference of these two alloy are such that both at 700 and 750 ^{o}C, the phase fraction of Laves phase in Alloy 700 is higher than that of Alloy 750, but the coarsening rate of Laves phase in Alloy 700 is faster than that of Alloy 750 (see table A.4). These two factors lead to a more or less identical PH factor of Laves phase at 700 and 750 ^{o}C. The identical PH factor suggests that Alloy 700 and Alloy 750 can both be used at temperatures of 700 and

750 ^{o}C.

In summary, the simulation clearly identified optimal alloys with metallurgically understandable compositions and also revealed that alloys designed for a very high temperature could be unsuitable for lower temperature use.

Table A.4 Phase constitutions of three designed alloys (in vol.%), coarsening rate (in m^3/s), precipitation hardening factor (PHF) of Laves phase at 650, 700 and 750 ^{o}C

		Sigma phase	NbX carbonitride	Z phase	Laves Phase	Coarsening rate of laves phase	PHF of Laves phase
650 ^{o}C	Alloy 650	0.2	0.0125	0.009	14.60	1.77E-30	4.44E+06
	Alloy 700	**5.1**	0.007	0.04	15.40	1.19E-30	5.21E+06
	Alloy750	**5.07**	0.005	0.05	14.99	1.14E-30	5.21E+06
700 ^{o}C	Alloy 650	0	0.013	0.0078	14.32	2.72E-29	1.77E+06
	Alloy 700	0.86	0.008	0.04	15.60	2.02E-29	2.04E+06
	Alloy750	0.83	0.005	0.05	15.20	1.94E-29	2.04E+06
750 ^{o}C	Alloy 650	0	0.014	0.0064	13.82	3.79E-28	0.72E+06
	Alloy 700	0	0.008	0.039	15.22	2.82E-28	0.84E+06
	Alloy750	0	0.005	0.049	14.80	2.70E-28	0.84E+06

A.5.2 Comparison of newly designed alloys and the existing 15Cr alloy

To compare the designed alloys with existing 15Cr alloy, volume fraction, coarsening rate and PH factor of Laves phase in alloy 15Cr at 650, 700 and 750 ^{o}C were calculated. The results together with those of Alloy 650 at 650 ^{o}C, Alloy 700 at 700 ^{o}C and Alloy 750 at 750 ^{o}C are shown in **Figure A.4**. All three designed alloys have a significantly higher volume fraction and lower coarsening rate of the Laves phase at their intended temperatures relative to alloy 15Cr. The high volume fraction is the result of the high level of W, which is the main constitution of Laves phase (Fe_2W). The low coarsening rate is attributable to the high level of Co and W [27]. Both factors lead to a much higher PH factor or corresponding creep strength in the newly designed alloys.

A.5.3 Combining $M_{23}C_6$ with Laves phase at three service temperatures

The main precipitate family in the designed Alloy 650, Alloy 700 and Alloy 750 is the Laves phase, and other kinds of precipitates were found to be present in very low amounts (table A.4) as they were not part of the optimization routine. The absence of

non-Laves phase precipitates in the designed alloys would give them a low initial strength as the Laves phase takes quite some time to develop. While hard to quantify with the current creep strength models, such a low initial strength is likely to be undesirable for the final creep lifetime. So, it would be desirable to have a certain fraction of other precipitates forming (and coarsening) during the early stages of creep loading as well as the slowly changing Laves phase during the final stage. Calculations show that the alloy 15Cr contains about 1 vol.% $M_{23}C_6$, while the $M_{23}C_6$ precipitates are absent in the designed alloys. Combining both types of precipitates in one alloy would be very promising further improve the creep property. The alloy design approach as described above can only work with one PH factor in one optimisation cycle. To simultaneously

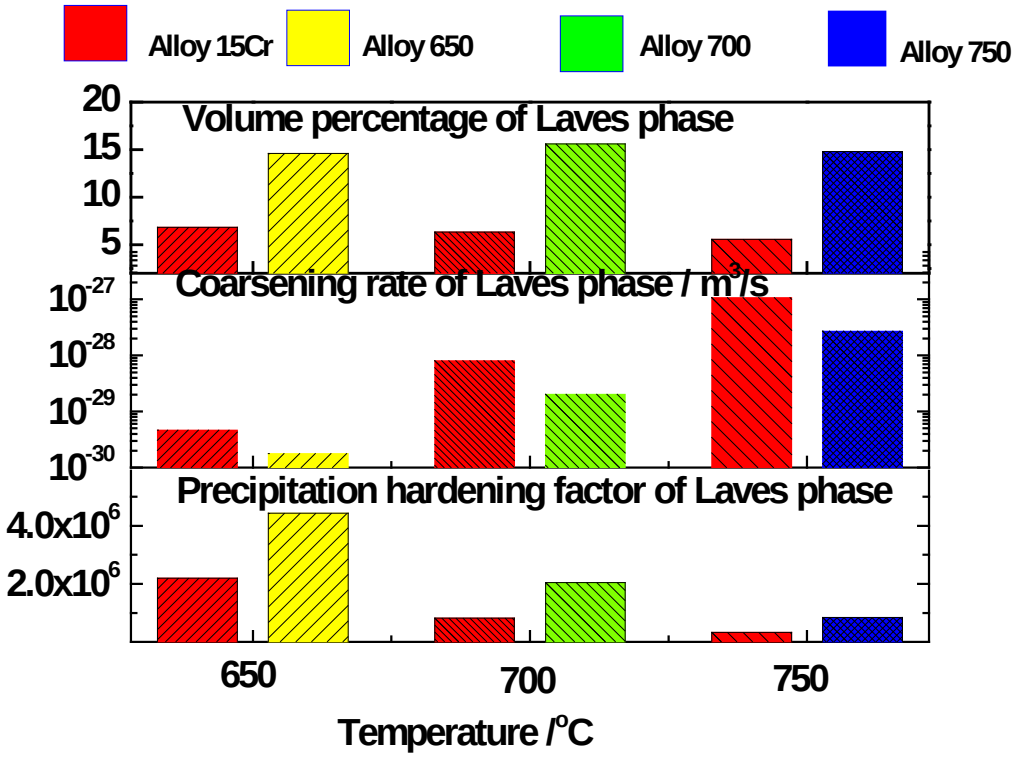

Figure A.4 Comparison of volume percentage, coarsening rate, precipitation hardening factor of Laves phase in Alloy 15Cr with those of Alloy 650, Alloy 700, Alloy 750 at service temperatures of 650, 700 and 750 ^{o}C, respectively

optimise PH factors of Laves phase and $M_{23}C_6$ in single alloy, two separated optimisations are implemented respectively: either solely Laves phase at 10^5 h, or solely $M_{23}C_6$ at 10^5 h (to be comparable with the PH factor of laves phase at 10^5 h, the PH factor of $M_{23}C_6$ at 10^5 h is chosen in the optimization since it is proportional to that of $M_{23}C_6$ at

a short serivce time), while both PH factors are recorded. Then the property maps for 650, 700 and 750 ^{o}C can be constructed through putting all the qualified solutions together, as shown in **Figure A.5**. Black dots stand for the solutions solely optimizing Laves phase, and red dots indicate the solutions solely optimizing $M_{23}C_6$. A "Pareto front" can thus be found at the border in the upper right direction. At 650 ^{o}C. A best solution with a combination of a PH factors for $M_{23}C_6$ and Laves phase not too different from their respective maximal values can be found in the upright corner. However, such an attractive dual solution could not be found at 700 and 750 ^{o}C since the right border of the solutions of two optimization become more separated at a higher temperature, as shown in **Figures A.5b** and **A.5c**. This suggests that $M_{23}C_6$ and Laves phase have a mutually, albeit limited competing effect at high service temperatures. Besides the above strategy to obtain optimized combination of two properties, there are multi-objective algorithms which can optimize two different properties in one optimization run [28, 29]. In principle multi-objective algorithm are quite identical to single-objective algorithm, but the latter can optimize more than one fitness parameters by extend the searching space. The bigger searching spacing results in a longer computational time so that an non-dominated sorting process is further added in these multi- objective algorithm to construct a Pareto front [4]. In this study, the "Pareto front" of PH hardening of Laves phase and $M_{23}C_6$ for each temperature is not solely from two single objective optimisations, but validated by further optimizations only focus on the area close to optimal position. These process is actually identical to the multi-objective algorithm. Furthermore, for one of two properties, the result from single-objective algorithm should always be better or equal to that of multi- objective algorithms.

The solutions with the best trades off of PH factors of Laves phase and $M_{23}C_6$ in all three temperatures are indicated by black arrows in **Figure A.5**. These newly designed alloys are labeled as Alloy LaM650, Alloy LaM700 and Alloy LaM750 according to their optimization temperature, and their compositions are listed in table A.5. The main difference between newly designed and previous designed alloys is a higher concentration of C, which could increase the amount of $M_{23}C_6$. In addition, lower amounts of Mo and higher levels of V/Nb in the newly designed alloys are required to achieve a slower coarsening rate of $M_{23}C_6$.

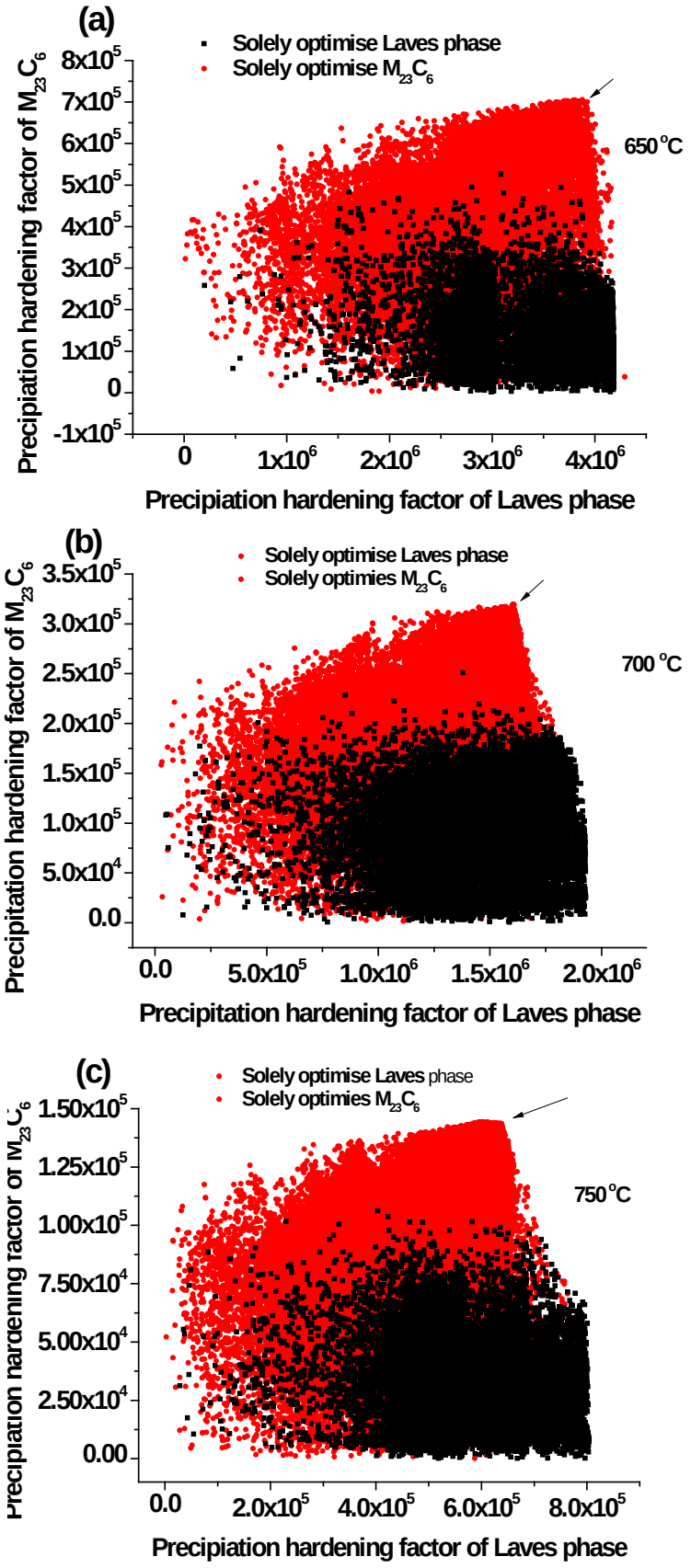
(a)
Solely optimise Laves phase
Solely optimise $M_{23}C_6$
650 °C
Precipiation hardening factor of $M_{23}C_6$
Precipiation hardening factor of Laves phase
(b)
Solely optimise Laves phase
Solely optimies $M_{23}C_6$
700 °C
Precipitation hardening factor of $M_{23}C_6$
Precipitation hardening factor of Laves phase
(c)
Solely optimise Laves phase
Solely optimies $M_{23}C_6$
750 °C
Precipiation hardening factor of $M_{23}C_6$
Precipiation hardening factor of Laves phase

Figure A.5 Simultaneous optimizations of Laves phase and $M_{23}C_6$ in one alloy at different service temperatures.

Table A.5 Composition (in wt.%), annealing temperatures T_{anneal} (in ^{o}C) and precipitation hardening factor (PHF) of Laves phase and $M_{23}C_6$ of designed alloys combining Laves phase and $M_{23}C_6$ at 650, 700 and 750 ^{o}C, respectively

	C	*Cr*	*Mo*	*W*	*Co*	*Nb*	*N*	*V*	T_{anneal}	*PHF of* $M_{23}C_6$	*PHF of Laves phase*
Alloy LaM650	0.046	15.40	0.01	10.00	8.06	0.066	0.001	0.87	1228	0.71E+06	3.88E+06
Alloy LaM700	0.046	15.70	0.14	10.00	9.35	0.23	0.0058	0.90	1250	0.28E+06	1.64E+06
Alloy LaM750	0.046	17.30	0.14	10.00	10.00	0.098	0.001	0.87	1250	0.14E+06	6.44E+05

A.6 Conclusions

A computational alloy design approach has been successfully developed to design novel ferritic steels strengthened by optimized Laves phase dedicating to different service temperatures. The composition for the applications at 700 and 750 ^{o}C are similar, but is different from the alloy designed for 650 ^{o}C. This is caused by the higher tendency of formation of detrimental Sigma phase at 650 ^{o}C, while such tendency is not so significant at 700 and 750 ^{o}C. For very long service times all three newly designed alloy have much higher PH contributions than those in the existing alloy 15Cr irrespective of temperautre. To create steels with decent hardening at short and long service times, the Laves phase and $M_{23}C_6$ phase are also optimally combined in one alloy using a dual optimization approach at 650, 700 and 750 ^{o}C, respectively.

References

[1] Masuyama F. History of power plants and progress in heat resistant steels. ISIJ Int. 2001;41:612.
[2] Sawada K, Kushima H, Tabuchi M, Kimura K. Microstructural degradation of Gr.91 steel during creep under low stress. Mater. Sci. Eng., A 2011;528:5511.
[3] Yamamoto Y, Brady MP, Lu ZP, Liu CT, Takeyama M, Maziasz PJ, Pint BA. Alumina-forming austenitic stainless steels strengthened by laves phase and MC carbide precipitates. Metall Mater Trans A 2007;38A:2737.
[4] Toda Y, Seki K, Kimura K, Abe F. Effects of W and Co on long-term creep strength of precipitation strengthened 15Cr ferritic heat resistant steels. ISIJ Int. 2003;43:112.
[5] Takeyama M. Novel concept of austenitic heat resistant steels strengthened by

intermetallics. Mater. Sci. Forum, vol. 539-543. Vancouver, 2007. p.3012.
[6] Kuhn B, Talik M, Niewolak L, Zurek J, Hattendorf H, Ennis PJ, Quadakkers WJ, Beck T, Singheiser L. Development of high chromium ferritic steels strengthened by intermetallic phases. Mater. Sci. Eng., A 2014;594:372.
[7] Toda Y, Tohyama H, Kushima H, Kimura K, Abe F. Influence of chemical composition and heat treatment condition on impact toughness of 15Cr ferritic creep resistant steel. JSME International Journal, Series A: Solid Mechanics and Material Engineering 2006;48:125.
[8] Toda Y, Tohyama H, Kushima H, Kimura K, Abe F. Improvement in creep strength of precipitation strengthened 15Cr ferritic steel by controlling carbon and nitrogen contents. JSME International Journal, Series A: Solid Mechanics and Material Engineering 2005;48:35.
[9] Toda Y, Kushima H, Abe F, Kimura K. Improvement in creep strength and impact toughness of high Cr heat resistant steel based on ferrite matrix. Proceedings of the 4th International Conference on Advances in Materials Technology for Fossil Power Plants, vol. 2005, 2005. p.1136.
[10] Toda Y, Iijima M, Kushima H, Kimura K, Abe F. Effects of Ni and Heat treatment on long-term creep strength of precipitation strengthened 15Cr ferritic heat resistant steels. ISIJ Int. 2005;45:1747.
[11] Shibuya M, Toda Y, Sawada K, Kushima H, Kimura K. Effect of precipitation behavior on creep strength of 15%Cr ferritic steels at high temperature between 923 and 1023K. Mater. Sci. Eng., A 2014;592:1.
[12] Shibuya M, Toda Y, Sawada K, Kushima H, Kimura K. Effect of nickel and cobalt addition on the precipitation-strength of 15Cr ferritic steels. Mater. Sci. Eng., A 2011;528:5387.
[13] Kimura K, Seki K, Toda Y, Abe F. Development of high strength 15Cr ferritic creep resistant steel with addition of tungsten and cobalt. ISIJ Int. 2001;41:S121.
[14] Qi Lu, Wei Xu, Zwaag Svd. The computational design of W and Co containing creep resistant steels with barely coarsening Laves phase and M23C6 as the strengthening precipitates. Materials and Metallurgy Transactions A 2014.
[15] Xu W, Rivera-Díaz-del-Castillo PEJ, Wang W, Yang K, Bliznuk V, Kestens LAI, van der Zwaag S. Genetic design and characterization of novel ultra-high-strength stainless steels strengthened by Ni3Ti intermetallic nanoprecipitates. Acta Mater. 2010;58:3582.
[16] Lu Q, Xu W, van der Zwaag S. Designing new corrosion resistant ferritic heat resistant steel based on optimal solid solution strengthening and minimisation of undesirable microstructural components. Comput. Mater. Sci. 2014;84:198.
[17] Lu Q, Xu W, van der Zwaag S. A strain-based computational design of creep-resistant steels. Acta Mater. 2014;64:133.
[18] Lu Q, Xu W, van der Zwaag S. The design of a compositionally robust martensitic creep-resistant steel with an optimized combination of precipitation hardening and solid-solution strengthening for high-temperature use. Acta Mater. 2014;77:310.
[19] Xu W, Rivera-Díaz-del-Castillo PEJ, van der Zwaag S. Designing nanoprecipitation strengthened UHS stainless steels combining genetic algorithms and thermodynamics. Comput. Mater. Sci. 2008;44:678.
[20] Orowan E. Theory of dislocation bowing. London: Institute of Metals Symposium

on Internal Stresses in Metals and alloys, 1948.
[21] Y. Toda MS, K. Sawada, H. Kushima, K. Kimura. Improvement in Creep Strength of Precipitation-strengthened 15Cr Ferritic Steel at Temperatures above 973 K. Creep and Fracture of Engineering Materials and Structures, 2012.
[22] Boyd JD, Nicholson RB. The coarsening behaviour of θ″ and θ′ precipitates in two Al-Cu alloys. Acta Metall. 1971;19:1379.
[23] Ågren J, Clavaguera-Mora MT, Golczewski J, Inden G, Kumar H, Sigli C. Applications of Computational Thermodynamics: Group 3: Application of computational thermodynamics to phase transformation nucleation and coarsening. Calphad-Computer Coupling of Phase Diagrams and Thermochemistry 2000;24:41.
[24] Lu Q, Xu W, van der Zwaag S. The Computational Design of W and Co-Containing Creep-Resistant Steels with Barely Coarsening Laves Phase and M23C6as the Strengthening Precipitates. Metall. Mater. Trans. A 2014;45:6067.
[25] ASM Handbook: 2000 ASM International, 2000.
[26] Frost HJ, Ashby MF. Deformation-Mechanism Maps: The Plasticity and Creep of Metals and Ceramics. Oxford: Pergamon press, 1982.
[27] Gustafson Å, Hättestrand M. Coarsening of precipitates in an advanced creep resistant 9% chromium steel—quantitative microscopy and simulations. Mater. Sci. Eng., A 2002;333:279.
[28] Datta S, Pettersson F, Ganguly S, Saxén H, Chakraborti N. Designing high strength multi-phase steel for improved strength-ductility balance using neural networks and multi-objective genetic algorithms. ISIJ Int. 2007;47:1195.
[29] Mahfouf M, Jamei M, Linkens DA. Optimal design of alloy steels using multiobjective genetic algorithms. Mater. Manuf. Processes 2005;20:553.

Acknowledgments

Like most PhD students, the journey of my PhD study is full of pains and happiness, ups and downs. It is the support and help from many people that makes this journey possible and joyful. Hereby, I want to express my sincere gratitude to them.

First, I want to sincerely thank my promotor, Prof. dr.ir. Sybrand van der Zwaag and daily supervisor, Dr. Wei Xu, for their helpful and inspiriting supervision and continuous support. Sybrand is always enthusiastic and high efficient, especially on revising manuscripts. He gave me enough freedom to do what I preferred during my PhD study while keeping the research on the right track. He is very good at explaining a concept or an idea, and is a master of making a presentation. These skills is beneficial to me and will be valuable throughout my life. Dr. Xu is always willing to help and give me encouragement. His detailed guidance and useful suggestion significantly improved the quality of my thesis work. I have learned a lot from him, especially the spirit of never giving up and embracing the challenge. Besides the work, He helped me and my family a lot. He is also good at cooking and I really enjoyed the beers and food made by him.

I also want to express my sincere gratitude to the collaborators during my PhD study. I want to thank Dr. Toda Yoshiaki for his hospitability during my three month internship at

National Institute of Materials Science, Japan. I learned lots of experimental details on creep test from him. Naomichi Harada's help on my experiments is also much appreciated. I also would like to thank Prof. Ke Yang and his group at Institute of Metal Research, Chinese Academy of Science, China. Prof. Ke Yand is very kind and willing to provide valuable support. Dr. Wei Yan and Wenjia Ma's excellent experimental work on fabricating and characterising of all prototype alloys make this thesis more attractive. My sincere acknowledgment also goes to David Dilner from KTH, Seweden. During his stay in Delft we had a lot of interesting discussion and successfully applied our alloy design approach to optimise the steel making process. He is also the main author of Chapter 9.

I would express my sincere gratitude to Prof. dr. Annika Borgenstam (KTH Royal Institute of Technology, Sweden), Prof. dr. Serge Claessens (University of Gent, Belguim), Prof. dr. Suzana.G. Fries, (Ruhr-Universität-Bochum, Germany), Prof. dr. Richard Thackray (University of Sheffield, UK), Prof. dr. ir. Fred van Keulen (Technische Universiteit Delft) and Prof. dr. ir. Ekkes H. Brück (Technische Universiteit Delft) for being my PhD committee members.

NovAM group is a very international group and has a nice working atmosphere. It's a great pleasure to spend four year with my nice group members, whom I want to thank here. I want to thank Mina and Johan, who are very nice officemates and make a very good office environment. Thank Xiaomin, Jie, Jianwei, Xiaojuan, Nijesh, Željka, Qingbao, Huiyu, Shasha, Zenan, Hussein, Le, Lie, Theo, Santiago, Ugo, Jesus, Marek, Ranjita, Michiel, Srikanth, Matino, Maruti, Daniella, Hamideh, Arijana, Nan, Jimmy, Hongli, Mladen, Pim, Antonio, Wouter(P), Wouter(V), Marianella, Jibran, Casper, Jeroen, Christian, Maarten, Fre, Kevin, Renee, Frederick…. for the interesting discussion during coffee, lunches during my PhD life.

Last but not the least, I want to thank my family for their love and always support. The most sincere thank goes to Xiaojuan, my beloved wife, for her persistent support, sacrifice her own career. She always believe in me, and never complain about the tough time. Without her, I cannot fully concentrate on the thesis work, which cannot be finished such smoothly. During the last year of my PhD study, the coming of my little baby daughter also make my life more colourful.

Curriculum Vitae

CV of Qi Lu

Sept. 2011-Sept. 2015
PhD candidate, Group of novel aerospace materials, Faculty of aerospace engineering, Delft university of technology. Supervisors: Professor Sybrand van der Zwaag and Dr. Wei Xu

May 2014 – Aug. 2014
Internship at National Institute of Materials Science (NIMS), Tsukuba, Japan. Supervisor: Senior researcher Dr Yoshiaki Toda

Sept. 2008-June 2011
Master of Engineering in Materials Science, Institute of Metal Research, Chinese Academy of Science, Supervisors: Professor Tao Jin and Professor Jinguo Li.

Sept. 2004-June 2008
Bachelor of Engineering in Materials Science and Engineering, College of Material and Metallurgy, Northeastern University, China.

List of Publications

REFEREED JOURNAL PUBLICATIONS

1. **Lu Q**, Blaauw M, van der Zwaag S, Xu W, High through-put design of low activation high strength creep resistant steel for nuclear reactor applications, to be submitted to **Journal of Nuclear Materials.**

2. **Lu Q**, van der Zwaag S, Xu W, Alloy by design - A materials genome approach to advanced high strength stainless steels for low and high temperature applications, to be submitted to **Materials & Design**.

3. **Lu Q**, Ma WJ, Yan W, Yang K, Toda Y, van der Zwaag S, Xu W, A novel martensitic creep resistant steel strengthened by MX carbonitrides with extremely low coarsening rates: design and characterization, submitted to **Metall. Mater. Trans. A**

4. **Lu Q**, Toda Y, Harada N, Xu W, van der Zwaag S, The impact of intended service temperature on the optimal composition of Laves and $M_{23}C_6$ precipitate strengthened ferritic creep resistant steels, **Comp. Mater. Sci**., 2015;107:110

5. **Lu Q**, Xu W, van der Zwaag S. The computational design of W and Co-containing creep-resistant steels with barely coarsening laves phase and $M_{23}C_6$ as the strengthening precipitates. **Metall. Mater. Trans. A**,. 2014;45:6067. *Selected as Editors' choice article.*

6. **Lu Q**, Xu W, van der Zwaag S. The design of a compositionally robust martensitic creep-resistant steel with an optimized combination of precipitation hardening and solid-solution strengthening for high-temperature use, **Acta Mater.** 2014, 77, 310.

7. **Lu Q**, Xu W, van der Zwaag S. Designing new corrosion resistant ferritic heat resistant steel based on optimal solid solution strengthening and minimisation of undesirable microstructural components. **Comput. Mater. Sci.** 2014;84:205.

8. **Lu Q**, Xu W, van der Zwaag S. A strain based computational design of creep resistant steels. **Acta Mater**. 2014;64:133.

9. **Lu Q**, Xu W, van der Zwaag S. A material genomic design of advanced high performance, non-corroding steels for ambient and high temperature applications. **Mater. Sci. Forum** 2014. 1201.

10. **Lu Q**, Xu W, van der Zwaag S. Computational design of precipitation strengthened austenitic heat resistant steels. **Philos. Mag.** 2013;93:3391.

11. Dilner D, **Lu Q**, Mao H, Xu W, van der Zwaag S, Selleby M. Process-time optimisation of vacuum degassing using a genetic alloy design approach, **Materials** 2014;7:7997.

12. Xu W, **Lu Q**, Xu X, van der Zwaag S. The structure of a general materials genome approach to the design of new steel grades for specific properties. **Computer method in materials science** 2013;13:382.

13. Meng XB, **Lu Q**, Zhang XL, Li JG, Chen ZQ, Wang YH, Zhou YZ, Jin T, Sun XF, Hu ZQ. Mechanism of competitive growth during directional solidification of a nickel-base superalloy in a three-dimensional reference frame. **Acta Mater.** 2012;60:3965.

14. Meng X, **Lu Q**, Li J, Jin T, Sun X, Zhang J, Chen Z, Wang Y, Hu Z. Modes of grain selection in spiral selector during directional solidification of nickel-base superalloys. **J. Mater. Sci. Technol.** 2012;28:214.

15. **Lu Q**, Li J, Jin T, Zhou Y, Sun X, Hu Z. Competitive growth in bi-crystal of Ni-based superalloys during directional solidification. **Jinshu Xuebao/Acta Metallurgica Sinica** 2011;47:641.

CONFERENCE PROCEEDINGS

1. **Lu Q**, Ma WJ, Yan W, Yang K, Toda Y, Xu W, van der Zwaag S, A New Martensitic Creep Resistant Steel Strengthened by MX Carbonitrides with an Extremely Low Coarsening Rate, PTM 2015(International Conference on Solid-Solid Phase Transformations in Inorganic Materials), June, 2015, Whistler, Canada.

2. **Lu Q**, Xu W, van der Zwaag S, Alloys by design - a 'materials genome' approach to high strength stainless steels for low and high temperature applications, PTM 2015(International Conference on Solid-Solid Phase Transformations in Inorganic Materials), June, 2015, Whistler, Canada.

3. **Lu Q**, Xu W, van der Zwaag S, Turning laves phase and $M_{23}C_6$ into desirable phases in novel martensitic creep resistant steels, proceedings of 10th Liège Conference on Materials for Advanced Power Engineering 2014, 14-17 Sep.,2014, Liege, Belgium.

4. **Lu Q**, Xu W, van der Zwaag S, Computational design of martensitic creep resistant steels with stable precipitation strengthening and high solid solution strengthening, proceedings of 3rd International ECCC- Creep & Fracture Conference. Creep & Fracture in High Temperature Components, Design & Life Assessment. 5-7 May, 2014, Rome, Spain.

5. **Lu Q**, Xu W, van der Zwaag S, A computational design study of novel heat resistant steels for fossil power plant applications, proceeding of Seventh International Conference on Advances in Materials Technology for Fossil Power Plants, 21-25, October, 2013, Hawaii, USA

6. **Lu Q**, Xu W, van der Zwaag S. Model based redesign of MX carbonitrides strengthened austenitic heat resistant steels, proceedings of TMS 2013 142nd Annual Meeting and Exhibition: Linking Science and Technology for Global Solutions, 3-7 March 2013. p.327, San Antonio, United States

CONFERENCE PRESENTATIONS

1 Accepted for Oral presentation**: Lu, Q**, Xu, W, van der Zwaag, S (Sep., 2015). Alloys by design - A 'materials genome' approach to high strength creep resistant steels. Euromat 2015 European Congress and Exhibition on Advanced Materials and Processes, Warsaw, Poland.

2 **Lu Q**, Ma WJ, Yan W, Yang K, Toda Y, Xu W, van der Zwaag S,(June, 2015), A New Martensitic Creep Resistant Steel Strengthened by MX Carbonitrides with an Extremely Low Coarsening Rate, PTM 2015(International Conference on Solid-Solid Phase Transformations in Inorganic Materials), Whistler, Canada. (Oral presentation).

3 **Lu Q**, Ma WJ, Yan W, Yang K, Toda Y, Xu W, van der Zwaag S, (May, 2015). Design and first evaluation of new martensitic creep resistant steel with an ultra-high MX precipitate stability at 650 °C, Creep 2015 (13^{th} International Conference on Creep and Fracture of Engineering Materials and Structures), Toulouse, France. (Oral presentation).

4 **Lu, Q**, Xu, W, van der Zwaag, S (Sep., 2014). A strain based computational design of austenitic creep resistant steel with an improved precipitation hardening. Materials Science Engineering , MSE 2014. Darmstadt, Gernany. (Oral presentation).

5 **Lu, Q**, Xu, W, van der Zwaag, S (Sep., 2014). Designing the composition of a high strength martensitic creep resistant steel. Materials Science Engineering (MSE 2014). Darmstadt, Germany. (Oral presentation).

6 **Lu Q**, Xu W, van der Zwaag S, (Sep., 2014). Computational design of martensitic creep resistant steels. 10th Liège Conference on Materials for Advanced Power Engineering 2014, Liege, Belgium. (Poster presentation).

7 **Lu Q**, Xu W, van der Zwaag S, (May, 2014). Computational design of martensitic creep resistant steels with stable precipitation strengthening and high solid solution strengthening. 3rd International ECCC- Creep & Fracture Conference. Creep &

Fracture in High Temperature Components, Design & Life Assessment. Rome, Spain. (Oral presentation).

8 **Lu Q**, Xu, W, van der Zwaag, S (Nov. 2013). A computational design study of novel creep resistant steels for fossil fuel power. 7th Advances in Materials Technology for Fossil Power Plants Waikoloa, HI; United States. (Poster presentation).

9 **Lu Q**, Xu W, van der Zwaag S, (Sep., 2013). Designing the composition of improved precipitation hardened austenitic creep steels, Euromat 2013 European Congress and Exhibition on Advanced Materials and Processes. Seville, Spain. (Oral presentation).

10 **Lu Q**, Xu W, van der Zwaag S, (Mar., 2013). Design of MX strengthened austenitic creep resistant steels via a combined artificial intelligence-thermodynamics approach, TMS 2013, San Antonio, USA. (Oral presentation).

11 **Lu Q**, Xu W, van der Zwaag S, (Sep., 2012). Design of creep resistant steels via a combined artificial intelligence-thermodynamics approach. Materials Science Engineering (MSE 2012), Darmstadt, Germany. (Oral presentation).

12 **Lu Q**, Xu W, van der Zwaag S, (June, 2012). Genetic design of heat resistant steels, National Student Conference in Metallic Materials, Manchester, UK. (Oral presentation).

13 **Lu Q**, Li JG, Jin T, Zhou YZ, Sun XF, Hu ZQ (May, 2010). Competitive growth during directional solidification in a bi-crystal Ni-based superalloy. Sixth national conference of solidification and phase transformation, Ningbo, China. (Oral presentation).